buildings

Special Issue Reprint

Recent Studies in Static and Dynamic Behaviour of Engineering Structures

Edited by
Xinzhi Dang, Zhihao Wang, Junfeng Jia, Xinxin Wei and Murat Dicleli

mdpi.com/journal/buildings

MDPI

Recent Studies in Static and Dynamic Behaviour of Engineering Structures

Recent Studies in Static and Dynamic Behaviour of Engineering Structures

Guest Editors

Xinzhi Dang
Zhihao Wang
Junfeng Jia
Xinxin Wei
Murat Dicleli

MDPI

Basel • Beijing • Wuhan • Barcelona • Belgrade • Novi Sad • Cluj • Manchester

Guest Editors
Xinzhi Dang
School of Civil Engineering
Tongji University
Shanghai
China

Zhihao Wang
School of Civil Engineering
and Communication
North China University of
Water Resources and Electric
Power
Zhengzhou
China

Junfeng Jia
Faculty of Architecture, Civil
and Transportation
Engineering
Beijing University of
Technology
Beijing
China

Xinxin Wei
Faculty of Civil and
Environmental Engineering
Ruhr-Universität Bochum
Bochum
Germany

Murat Dicleli
Department of Engineering
Sciences
Middle East Technical
University (METU)
Ankara
Turkey

Editorial Office
MDPI AG
Grosspeteranlage 5
4052 Basel, Switzerland

This is a reprint of the Special Issue, published open access by the journal *Buildings* (ISSN 2075-5309), freely accessible at: https://www.mdpi.com/journal/buildings/special_issues/MF4S4911XB.

For citation purposes, cite each article independently as indicated on the article page online and as indicated below:

Lastname, A.A.; Lastname, B.B. Article Title. *Journal Name* **Year**, *Volume Number*, Page Range.

ISBN 978-3-7258-5729-6 (Hbk)
ISBN 978-3-7258-5730-2 (PDF)
https://doi.org/10.3390/books978-3-7258-5730-2

Contents

About the Editors

Xinzhi Dang

Xinzhi Dang is a research professor at Tongji University and Chief Scientist of the National Key Research and Development Program. He also serves as the permanent Secretary-General of the Organizing Committee of the International Conference on Engineering Innovation and Seismic Mitigation of Bridges. He has long focused on the field of bridge engineering seismic resistance and achieved fruitful results. He has published more than 100 academic papers, obtained 22 authorized invention patents and 86 utility model patents, and also compiled 4 standards as well as 1 academic monograph. In addition, he has won 2 first prizes and 4 second prizes of provincial and ministerial scientific and technological progress awards and been awarded the title of Municipal Leading Talent in Science, Technology, Innovation and Entrepreneurship; and his achievements have been selected to be placed among the "Top 10 Most Transformative Potential Scientific and Technological Achievements" of Tongji University. At the same time, he serves as a review expert for scientific research projects and science and technology awards of the Ministry of Science and Technology, Shanghai Municipality. As a project leader, he has completed the presided over vertical projects such as National Key Research and Development Program projects and the General Program of the National Natural Science Foundation of China. He has also carried out special seismic research for major projects such as the Lingdingyang Bridge of the Shenzhen-Zhongshan Link, providing scientific research support for the construction of super projects.

Zhihao Wang

Zhihao Wang is a Full Professor and Dean at the School of Civil Engineering and Transportation, North China University of Water Resources and Electric Power, China. His research mainly focuses on the inerter-based damper and eddy current damper as well as structural health monitoring and vibration control. He has published over 100 journal papers indexed by SCI/EI, obtained 25 authorized national invention patents, and won 3 first prizes and 4 second prizes for scientific research at the provincial and ministerial levels, as well as 3 first prizes for teaching achievements at the provincial level.

Junfeng Jia

Junfeng Jia is a full Professor at the College of Architecture and Civil Engineering, and Vice President of the Department of Civil Engineering, Beijing University of Technology. He received his PhD degree in disaster mitigation and prevention from Harbin University of Technology in 2011 and then joined BJUT. He has published over 120 journal papers and books, and authorized more than 30 Chinese patents. His research interests includes the seismic design and analysis of bridges, seismic resilient bridges, accelerated bridge construction, and advanced materials and structures in bridges. Professor Jia is an young Editor of the *China Journal of Highway and Transport* and *Smart Construction*. He is a reviewer for over 20 renowned international journals, such as *Earthquake Engineering and Structural Dynamics*, *Engineering Structures*, *Bulletin of Earthquake Engineering*, and so on. His awards include an governmental award for science and technology for two provinces (Rank 1 and 2), three awards from associations (Rank 1, 3 and 12), and a Young Talents of Science and Technology of MOT award from the P.R.C.

Xinxin Wei

Xinxin Wei received his engineering education, academic training, and professional experience in China (e.g., Tongji University in Shanghai) and Europe (e.g., KU Leuven in Belgium and RUB in Germany). His research interests mainly include crowd dynamics, human–structure interaction, structural dynamics (e.g., human-induced vibrations), vibration serviceability evaluation, the structural system identification and vibration control of civil structures, uncertainty quantification and propagation, etc. His research results are published in top-tier journals, e.g., *Mechanical Systems and Signal Processing*, *ASCE-Journal of Bridge Engineering*, *Structural Control & Health Monitoring*, and *the International Journal of Structural Stability and Dynamics*, etc. One of his papers is the 'Most Read' paper in the *Journal of Bridge Engineering*. He has been developing several research toolboxes and patents for applications. He serves as reviewer for international journals, is a session chair and organizer for international conferences, is a working group member for an international association, and is a supervisor for master thesis. He has been an invited speaker for several international conferences and seminars. He has also had many opportunities to be involved in engineering projects. He has been recognized by being awarded the IAAM Young Scientist Medal, Best Paper Award, Excellent Scholar Award, Excellent Presentation Award, State Scholarship Fund, etc.

Murat Dicleli

Murat Dicleli is a Professor and Head of the Department of Engineering Sciences at Middle East Technical University in Turkey, with a Doctor of Engineering degree. He obtained his doctoral degree from the University of Ottawa in Canada and is a Professional Engineer (P.Eng.). He holds several important positions in the academic field: he is not only a member of the Canadian Bridge Seismic Isolation Code Writing Committee and the Seismic Effects Committee, but also an Editorial Board Member of journals such as the *International Journal of Structural Engineering and Mechanics* and *Frontiers in Earthquake Engineering*. Meanwhile, he is the founder and Editor-in-Chief of the journal *Sustainable and Resilient Infrastructure*. In terms of research, he focuses on fields such as structural seismic resistance and bridge seismic isolation, devoting himself to research on new hysteretic dampers and seismic isolation devices. He has successfully developed various torsional hysteretic dampers for structural seismic protection, such as the Multi-Directional Torsional Hysteretic Damper (MT HD), and has obtained relevant patents.

buildings

Article

Numerical Simulation Analysis of Twin-PBL Rubber-Ring Shear Connector

Jun Wei [1], Peiwen Chen [2,*] and Qiaowen Hu [1]

[1] Zhejiang Institute of Communications, Hangzhou 310030, China; weijun@zjvtit.edu.cn (J.W.); qiaowenhu@zjvtit.edu.cn (Q.H.)
[2] School of Marine Engineering Equipment, Zhejiang Ocean University, Zhoushan 316022, China
* Correspondence: chenpeiwen@zjou.edu.cn; Tel.: +86-189-7652-5973

Abstract: In recent years, a growing number of studies have focused on improving shear distribution and mitigating stress concentration in PBL shear connectors through the incorporation of composite materials. However, research on Twin-PBL shear connectors remains limited. Therefore, this study employed the finite element method to develop 23 finite element models to evaluate the shear performance of the Twin-PBL rubber-ring shear connector. The results indicate that the Twin-PBL rubber-ring shear connector with a 4 mm thick rubber ring exhibits a 7.5% decrease in shear force and a 71.1% reduction in shear stiffness compared to the conventional Twin-PBL shear connector. Furthermore, parametric analysis reveals that increasing the thickness of the rubber ring reduces both shear capacity and shear stiffness, while higher concrete strength, greater perforated rebar strength, and larger perforated rebar diameter enhance both shear capacity and stiffness. In contrast, the strength of the perfobond steel plate has minimal influence. Based on these findings, a predictive formula is proposed to estimate the shear capacity of the Twin-PBL rubber-ring shear connector.

Keywords: composite structure; shear resistance; shear behavior; PBL shear connector; rubber ring; finite element analysis; parametric study

1. Introduction

Recent engineering practices have shown that composite material structures, owing to their excellent mechanical properties, ease of construction, and significant economic advantages, are widely applied in the fields of large-scale building structures and bridge engineering [1–3]. As a critical load-bearing component in composite material structural systems, the performance of shear connectors directly affects the overall load-bearing capacity of the structure. PBL shear connectors, derived from perfobond steel plates, have increasingly become vital load-transmitting elements in steel–concrete composite structures due to their outstanding shear capacity, reliable fatigue performance, and superior ductility characteristics. Especially in the domain of large-span bridge engineering, with the growing adoption of new structural types such as steel–concrete composite beams and hybrid cable-stayed bridges, the optimization of the mechanical performance and durability design of shear connectors has become a key technological challenge that affects both the safety and economic efficiency of the structure [4,5].

Convenience during construction, great fatigue resistance, and enhanced structural rigidity are three major advantages of traditional PBL shear connectors, which utilize a perfobond steel plate configuration to provide the shear resistance mechanism of concrete

https://doi.org/10.3390/buildings15193567

shear dowel [6,7]. With the progressive development of modern bridge engineering technologies, the application scope of this connector system in composite bridges has expanded from conventional beam connectors to more complex load-bearing scenarios, such as hybrid structural joints and temporary anchoring systems in cantilever construction. However, engineering practices indicate that multi-row and multi-column arrangements of shear connectors can lead to significant shear stress concentration at the steel–concrete interface, resulting in interface damage accumulation that may compromise the structural durability and fatigue life [8–11]. To address this critical issue, recent research has focused on optimizing and innovating the load transfer mechanism of connectors. The latest experimental studies indicate that the incorporation of new structural solutions, such as foam-filled T-section structures and rubber vibration-damping sleeve composite studs, can significantly improve the uniformity of shear transfer in composite sections. Among these innovations, the rubber sleeve and PBL composite connector, through the stress buffering effect of elastic materials, has been proven to exhibit superior stress redistribution capabilities under cyclic loading [12–15]. The application of AI predictive technologies in the advanced modeling of structural connectors can provide novel insights for enhancing structural safety and predictive accuracy [16]. These technological advancements provide new solutions for enhancing the overall performance and service life of composite structures.

Research on PBL shear connectors has primarily focused on experimental investigations and finite element analysis (FEA) techniques [17–20]. Liu et al. [14,21] proposed the incorporation of rubber rings to alleviate the stress concentration issues in PBL shear connectors and validated their effectiveness in improving the initial stiffness and ductility of the connectors through push-out tests and finite element simulations. The finite element method has been demonstrated as an effective tool for simulating the entire testing process, significantly reducing the associated testing costs [14,16–18].

Although finite element analysis of single PBL rubber-ring shear connectors has been conducted in existing studies (such as Liu et al. [14,21]), the research on the refined finite element model of Twin-PBL rubber-ring shear connectors is still blank. This study established for the first time a three-dimensional finite element model of Twin-PBL rubber-ring connectors considering the superelasticity of rubber, the damage plasticity of concrete, and the complex interaction between reinforcing bars and concrete, systematically revealing its shear force transfer mechanism and failure mode under this more complex configuration (as shown in Figure 1).

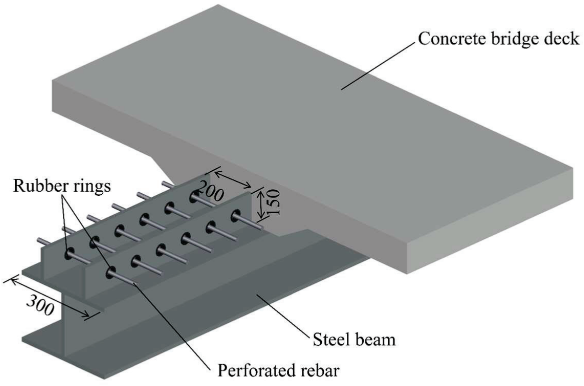

Figure 1. Twin-PBL rubber-ring shear connector.

This study established a total of 23 finite element models using solid finite element analysis to systematically investigate the mechanical behavior of Twin-PBL rubber-ring shear connectors. These models encompass a range of geometric dimensions and material strengths to comprehensively evaluate the connector’s performance under various operating conditions. Through comparative analysis, the significant influences of parameters such as rubber ring thickness, perforated rebar diameter, and material strength on the shear performance of the connector are revealed, providing essential theoretical foundations for optimized design. The objective is to deepen the understanding of their shear performance and to evaluate the effects of the rubber ring and other design parameters on the overall shear resistance of the connector.

By comparing with the most representative previous works, the innovations and contributions of this study are mainly reflected in the following three aspects. Firstly, this study systematically investigates the role of rubber rings under the double PBL configuration for the first time, which better aligns with the actual stress conditions of multi-row connectors in engineering. Secondly, the model can more accurately reflect the real mechanical behavior of multi-component collaborative work, especially the interaction between double concrete dowels and rubber rings. Thirdly, a more comprehensive understanding of the influence laws of design parameters has been obtained, and on this basis, the first shear capacity calculation formula specifically for Twin-PBL rubber ring connectors is proposed.

2. Design of Twin-PBL Rubber-Ring Shear Connector

Natural rubber was employed for the rubber rings, C60 concrete was applied for the concrete slabs, Q345 steel was used for the H-beam and perfobond plates, and HRB400-grade hot-rolled steel bars were selected for the rebars in the connectors. In particular, the structural rebar was 16 mm in diameter, the rubber ring was 4 mm thick, and the perforated rebar was 20 mm in diameter. To decrease the effect of end-bearing pressure from the concrete, foam blocks were positioned at the leading edge of the perfobond plate in the direction of its sliding. All dimensional parameters are illustrated in Figure 2.

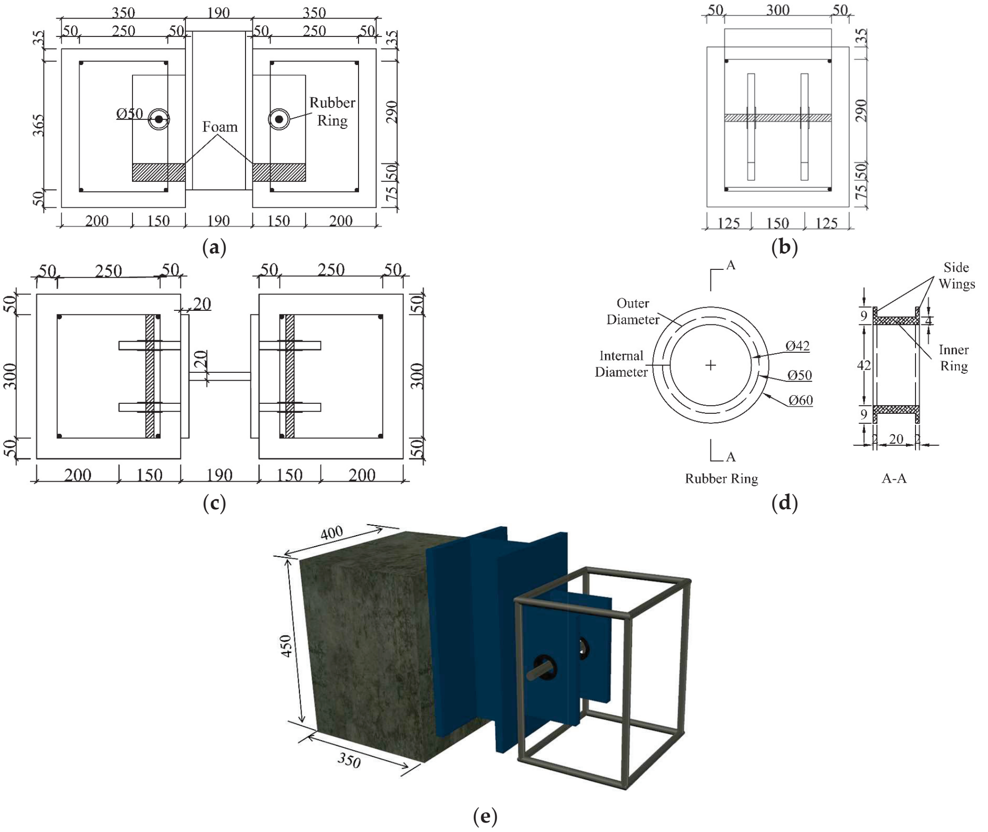

Figure 2. Specimen configuration of Twin-PBL rubber-ring shear connector/mm: (a) main view; (b) side view; (c) top view; (d) rubber ring; (e) 3D illustration.

3. Finite Element Analysis

3.1. Modeling Details and Element Selection

To thoroughly investigate the internal failure mechanism of Twin-PBL rubber-ring shear connectors, ABAQUS/Explicit was employed for comprehensive modeling and simulation analyses. Considering the biaxial symmetry of the model, a quarter model of the push-out test was developed, including a single perfobond plate connector. The detailed configuration of this model is illustrated in Figure 3. In the model, the total time for the analysis step is set to 0.1 s, with no mass scaling applied, ensuring that the ratio of kinetic energy to internal energy is less than 1%. Through this modeling and simulation methodology, the understanding of the mechanical behavior and failure mechanisms of the connector under loading conditions was significantly improved.

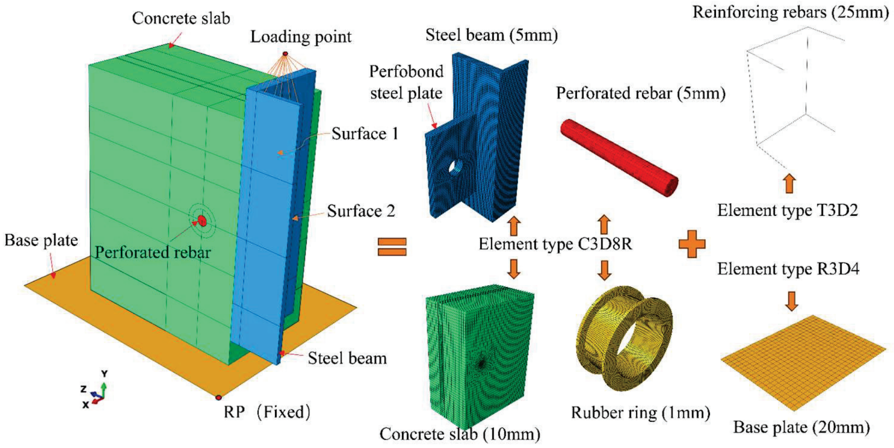

Figure 3. Finite element model.

In the finite element simulation of Twin-PBL rubber-ring shear connectors under pull-out loading, a combination of solid, truss, and rigid element types was utilized for meshing. Specifically, the concrete slab, perforated rebar, rubber ring, perfobond steel plate, and steel beam were discretized using C3D8R solid elements, while the other reinforcements were modeled using T3D2 truss elements. The base plate was defined as an R3D4 rigid element. In order to optimize the use of computational resources, the global mesh was set to a relatively coarse 10 mm, except for the concrete dowel, perforated rebar, perfobond steel plate and rubber ring, which require finer meshing. However, for more complex stress distribution regions, such as the concrete dowel, rubber ring, perfobond steel plate and perforated rebar, a refined mesh was applied to ensure the accuracy of the simulation results. This meshing strategy effectively balances computational efficiency with result precision, providing a reliable foundation for subsequent analysis.

3.2. Boundary Conditions and Constraints

Symmetric constraints are applied in the x-direction on Surface 1 and in the z-direction on Surface 2, as shown in Figure 3. Coupling constraints are implemented to link the loading surface of the steel beam with the loading point. The perforated rebar is connected to the concrete dowel using tie constraints, while surface-to-surface contact is defined between the remaining components. The coefficient of friction between the concrete slab and the base plate is assigned a value of 0.5 [6], while the friction coefficients for other contact pairs are set to zero. The normal behavior of the contact surfaces is defined as “hard” pressure-overclosure, indicating that the interface cannot be penetrated but may separate. Displacement-controlled loading is applied in the simulation to improve convergence, enable precise control over the deformation process, simplify the application of complex loading conditions, and facilitate the extraction of simulation results.

3.3. Material Modeling

3.3.1. Material Constitution of Concrete

Given that the primary failure modes of concrete observed in the experiments are tensile cracking and crushing, and referring to relevant literature [19,22,23], the Concrete Damaged Plasticity (CDP) model with the following calibrated parameters are adopted: Dilation angle: ψ = 30°; Eccentricity: ε = 0.1; Biaxial strength ratio: f_{b0}/f_{c0} = 1.16; Stress ratio: K = 0.6667; Viscosity parameter: μ = 0.0005. Where f_{b0}/f_{c0} denotes the ratio of the initial equibiaxial compressive yield stress to the initial uniaxial compressive yield stress. The parameter K represents the ratio of the second stress invariant on the tensile meridian to that on the compressive meridian. The dilation angle defines the volumetric expansion characteristics of concrete during plastic deformation, namely the extent of volume change in the material under shear loading. The eccentricity governs the hyperbolic shape of the flow potential function, specifically delineating the deviation of the flow potential asymptote relative to the hydrostatic pressure axis. The stress–strain relationship under compressive loading and the stress-crack width relationship under tensile loading are presented in Figure 4.

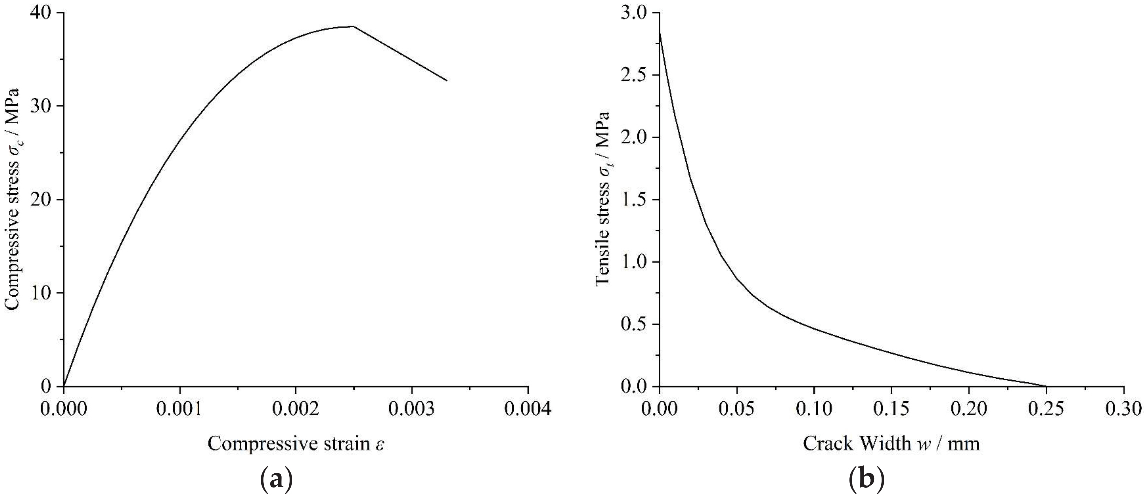

Figure 4. Material Constitution of Concrete: (**a**) compressive; (**b**) tensile.

This study adopts the stress–strain relationship for uniaxial concrete compression based on the nonlinear constitutive model proposed in CEB-FIP MC 2010 [24], due to the complexity of the concrete constitutive behavior. As shown in Figure 4, the stress–strain curve is divided into an ascending branch and a descending branch. The ascending branch is defined using Equations (1)–(3), while the descending branch is assumed to be linear and terminates when the stress reaches $0.85f_{ck}$. The ultimate strain ε_{cu} corresponding to $0.85f_{ck}$ is designated as 0.0033 [25], facilitating the calculation of the descending branch by Equation (4).

$$\sigma_c = \frac{(k \cdot \eta - \eta^2) f_{ck}}{1 + (k-2)\eta} \tag{1}$$

$$k = \frac{E_c \varepsilon_{cp}}{f_c} \tag{2}$$

$$\eta = \frac{\varepsilon_c}{\varepsilon_{cp}} \quad (3)$$

$$\sigma_c = \left(1 - 0.15\frac{\varepsilon_c - \varepsilon_{cp}}{\varepsilon_{cu} - \varepsilon_{cp}}\right) f_{ck} \quad (4)$$

The tensile strength of concrete is determined based on its splitting tensile strength obtained from material testing and Equation (5). Furthermore, considering the nonlinear constitutive relationship delineated by CEB-FIP MC 1990 [26], the stress-crack width relationship proposed by Hordijk et al. [27] is employed to characterize the post-cracking tensile behavior of concrete. The tensile softening curve is computed utilizing Equation (6).

$$f_t = 0.9 f_{ts} \quad (5)$$

$$\frac{\sigma_t}{f_t} = \left[1 + \left(c_1\frac{w}{w_c}\right)^3\right] exp\left(-c_2\frac{w}{w_c}\right) - \frac{w}{w_c}\left(1 + c_1^3\right) exp(-c_2) \quad (6)$$

where w denotes the crack width; w_c represents the crack width at zero tensile stress, expressed as $w_c = 5.14G_F/f_t$ (mm); G_F signifies the fracture energy necessary to generate a unit area of stress-free crack surface, defined by $G_F = 0.073{f_c}^{0.18}$ (N/mm); the constants c_1 and c_2 are assigned values of 3 and 6.93, respectively.

3.3.2. Steel Material Constitutive Properties

The steel plates and reinforcement bars are represented using a three-segment idealized elastoplastic hardening model with strain hardening behavior [14], as shown in Figure 5. This model consists of three distinct stages that describe the mechanical behavior of the steel components. Once the ultimate stress f_u and corresponding ultimate strain ε_u, are reached, ABAQUS automatically transitions to a horizontal branch in the stress–strain curve. The ultimate strain ε_u is defined as 0.2.

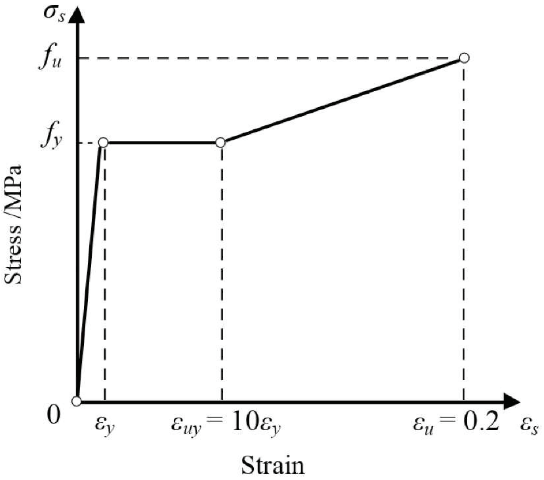

Figure 5. Steel material constitutive property.

3.3.3. Rubber Material Constitutive Properties

To accurately characterize the rubber ring as an isotropic hyperelastic material, the strain energy potential model from ABAQUS is employed. Given that the rubber ring is mechanically constrained by the concrete slab and the perfobond steel plate, a simplified polynomial form is selected for its constitutive description. The corresponding material parameters are obtained from the literature [14], including the coefficients C_{10} = 0.587 MPa, C_{20} = 0.0143 MPa, D_1 = 0.0866 MPa^{-1}, and D_2 = 0.

4. Shear Mechanism Analysis

This study employed solid finite element modeling and analytical methods to establish models of both the conventional Twin-PBL shear connector and the Twin-PBL rubber-ring shear connector. When the rubber ring thickness in the Twin-PBL rubber-ring shear connector is set to 4 mm, the load–slip curve shown in Figure 6 exhibits three distinct stages. The first stage is characterized by a steep elastic response, followed by a nonlinear plastic phase, and finally a quasi-linear phase, during which the slip increases significantly while the load remains almost constant. Throughout the loading process, the shear stress is gradually transferred from the perfobond steel plate to the rubber ring, concrete dowel, and perforated rebar. As long as the concrete dowel remains intact, the curve remains in the elastic phase. Once the concrete dowel begins to degrade and the primary load is transferred to the perforated rebar, the curve transitions into the plastic phase. Finally, when the concrete dowel is completely crushed and the majority of the load is carried by the perforated rebar, the curve approaches a nearly linear trajectory.

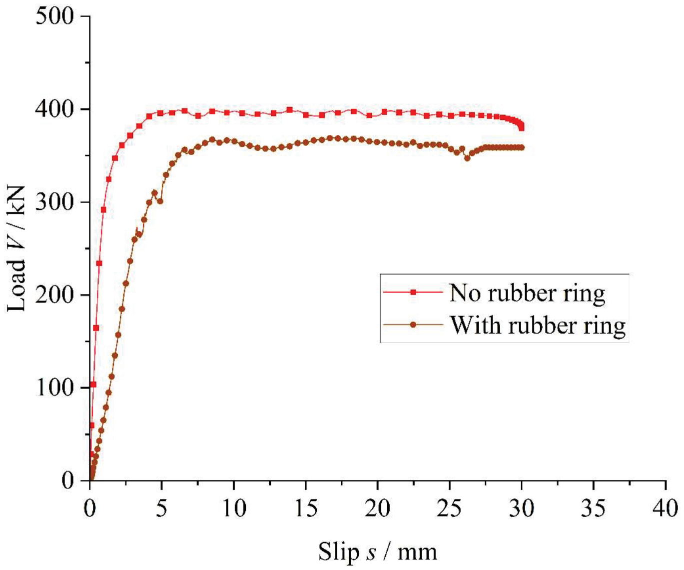

Figure 6. Load–slip curves.

The yield slip (S_y) is defined as the relative slip corresponding to the yield load (V_y), while the shear stiffness (K_s) is calculated as V_y/S_y. As shown in Figure 6, the conventional Twin-PBL shear connector exhibited a yield load (V_y) of 304.7 kN, an ultimate shear capacity (V_u) of 399.1 kN, and a shear stiffness (K_s) of 287.5 kN/mm. In contrast, the Twin-PBL rubber-ring shear connector exhibited corresponding values of 266.9 kN, 369.1 kN, and 84.4 kN/mm. In comparison to the conventional Twin-PBL shear connector, the yield load (V_y), ultimate shear capacity (V_u), and shear stiffness (K_s) of the Twin-PBL rubber-ring shear connector decreased by 16.9%, 7.5%, and 70.6%, respectively. These results indicate that the incorporation of the rubber ring significantly reduces the shear stiffness (K_s), while the reduction in ultimate shear capacity (V_u) is relatively minor. The primary reason for this situation is that the rubber ring possesses relatively low stiffness and contributes little to shear resistance, thereby reducing the overall stiffness of the connector. Additionally, with the diameter of the steel plate openings held constant, the presence of the rubber ring decreases the effective diameter of the concrete dowel, which in turn reduces its shear capacity. Furthermore, as rubber is an isotropic hyperelastic material with high deformability, the addition of the rubber ring significantly increases the yield displacement of the connector, thus improving its ductility.

5. Parametric Study

To thoroughly investigate the factors influencing the shear performance of Twin-PBL rubber-ring shear connectors, a total of 23 finite element models were developed in this study for systematic simulation and analysis. This study focused on five key parameters which are considered to significantly affect the shear performance of the connectors. These parameters include rubber ring thickness (t_r), perforated rebar diameter (d_r), concrete strength (f_{cu}), perforated rebar strength (f_{ry}), perfobond steel plate strength (f_{sy}). Through the analysis of these parameter variations, a more comprehensive understanding of their specific effects on the shear performance of the connectors can be obtained.

The specific results of the parametric analysis are summarized in Table 1, which provides detailed information on the shear performance of the connectors under different parameter combinations, including yield load, shear stiffness and other relevant indexes.

Table 1. Summary of parameter study results.

Model	t_r (mm)	d_r (mm)	f_{cu} (mm)	f_{ry} (mm)	f_{sy} (mm)	k_s (kN/mm)	V_y (kN)	V_u (kN)
TR-2	2	20	60	400	345	125.2	274.1	384.8
TR-4	4	20	60	400	345	84.4	253.3	369.1
TR-6	6	20	60	400	345	60.1	222.7	352.7
TR-8	8	20	60	400	345	45.1	217.1	336.7
DR-14	4	14	60	400	345	77.3	224.1	281.4
DR-16	4	16	60	400	345	79.3	225.9	317.2
DR-18	4	18	60	400	345	81.1	227.1	336.4
DR-20	4	20	60	400	345	84.4	253.3	369.1
DR-22	4	22	60	400	345	86.6	264.3	395.5
CU-40	4	20	40	400	345	75.8	197.2	277.8
CU-50	4	20	50	400	345	80.5	233.2	321.0
CU-60	4	20	60	400	345	84.4	253.3	369.1
CU-70	4	20	70	400	345	84.5	266.9	393.6
CU-80	4	20	80	400	345	89.5	273.3	437.1
RY-335	4	20	60	335	345	83.7	234.1	335.8
RY-400	4	20	60	400	345	84.4	253.3	369.1
RY-500	4	20	60	500	345	85.4	256.5	387.4
SY-235	4	20	60	400	235	83.0	224.1	325.6
SY-345	4	20	60	400	345	84.4	253.3	369.1
SY-390	4	20	60	400	390	84.3	257.5	363.7
SY-420	4	20	60	400	420	84.2	259.2	362.8
SY-460	4	20	60	400	460	83.9	269.4	372.2

5.1. Impact of Rubber Ring Thickness

The load–slip response and stress distribution characteristics of the Twin-PBL rubber-ring shear connector with varying rubber ring thicknesses are shown in Figure 7. With a fixed perfobond steel plate diameter, as the rubber ring thickness increases from 2 mm to 4 mm, 6 mm, and 8 mm—corresponding to a reduction in concrete dowel thickness from 26 mm to 22 mm, 18 mm, and 14 mm, respectively—the yield load (V_y) decreases by 7.6%, 18.8%, and 20.8%, while the shear stiffness (K_s) decreases by 32.6%, 52%, and 63.9%. These results demonstrate a consistent decline in both V_y and K_s with increasing rubber ring thickness. The reduction in ultimate shear capacity (V_u) by 4.1%, 8.4%, and 12.5% further confirms that the thickening of the rubber ring diminishes shear capacity by reducing the effective cross-sectional area of the concrete dowel.

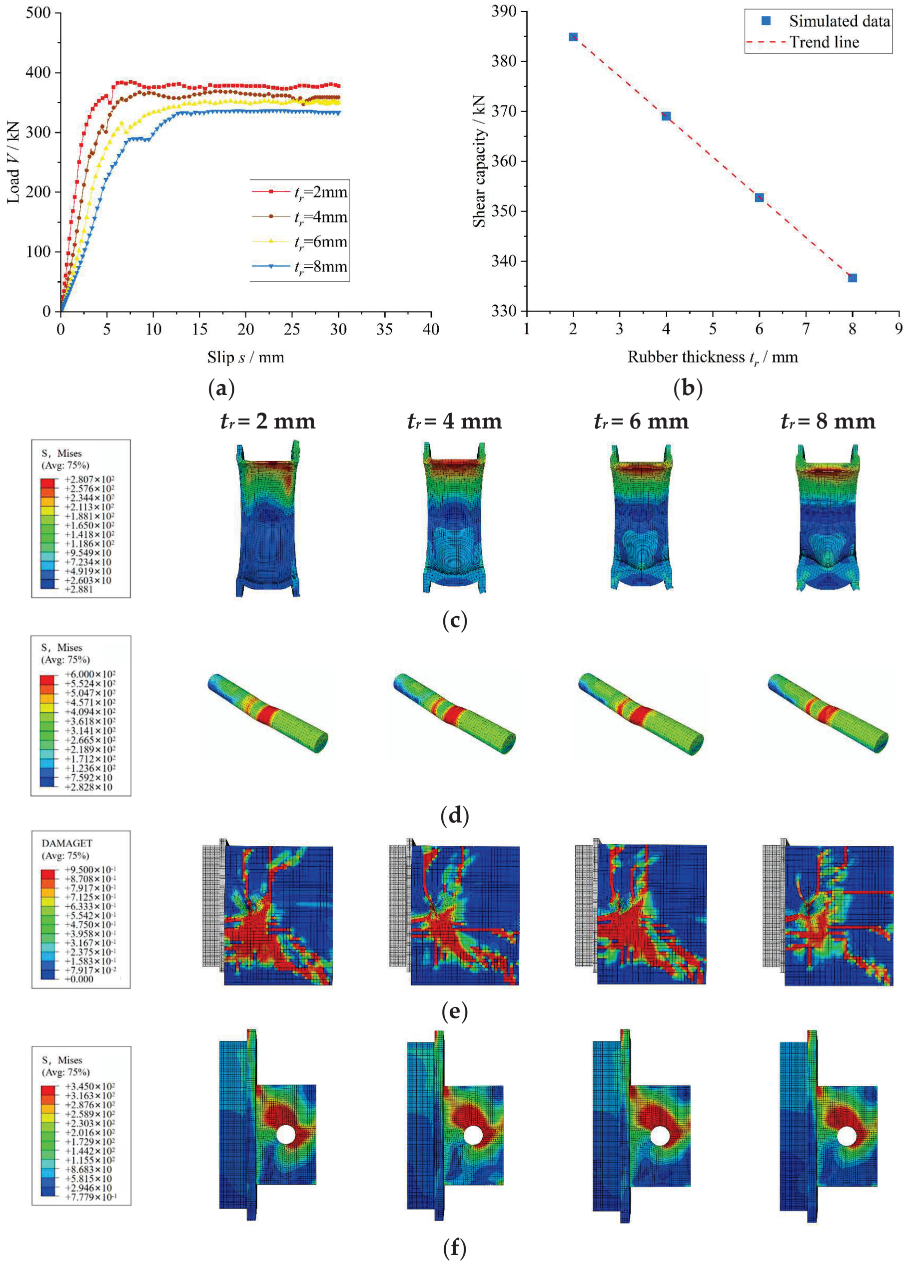

(**a**) (**b**)

(**c**)

(**d**)

(**e**)

(**f**)

Figure 7. Impact of rubber ring thickness: (**a**) load–slip curves; (**b**) impact analysis; (**c**) stress in rubber ring; (**d**) perforated rebar stress; (**e**) concrete tensile damage; (**f**) perfobond steel plate stress.

Notably, the stress distribution characteristics (Figure 7c–f) reveal that the stress concentration in the rubber ring is alleviated as its thickness increases. Meanwhile, the stress levels in the perforated rebar and perfobond steel plate do not change significantly, and the tensile damage of the concrete slab is reduced. This phenomenon arises from the fact that, with a constant perfobond steel plate diameter, the increase in rubber ring thickness reduces the concrete dowel thickness and weakens the shear capacity. However, through material stiffness reconstruction, the stress concentration at the interface between the rubber ring and the perfobond steel plate is effectively dispersed, and the load transfer path is optimized, thereby improving the stress state of the concrete slab.

5.2. Impact of Perforated Rebar Diameter

Figure 8 presents the load–slip response and stress distribution characteristics of the Twin-PBL rubber-ring shear connector with identical rubber ring thicknesses. Under a fixed perfobond steel plate diameter, when the perforated rebar diameter increases from 14 mm to 16 mm, 18 mm, 20 mm, and 22 mm, the shear capacity (V_u) increases by 12.8%, 19.6%, 31.2%, and 40.6%, respectively. The yield load (V_y) increases by 0.8%, 1.3%, 13.0%, and 17.9%, while the shear stiffness (K_s) increases by 2.6%, 4.9%, 9.2%, and 12.0%, correspondingly. These results indicate that an increase in the perforated rebar diameter leads to a consistent upward trend in all three performance parameters, highlighting that the rebar diameter is a key factor influencing the shear performance of the connector.

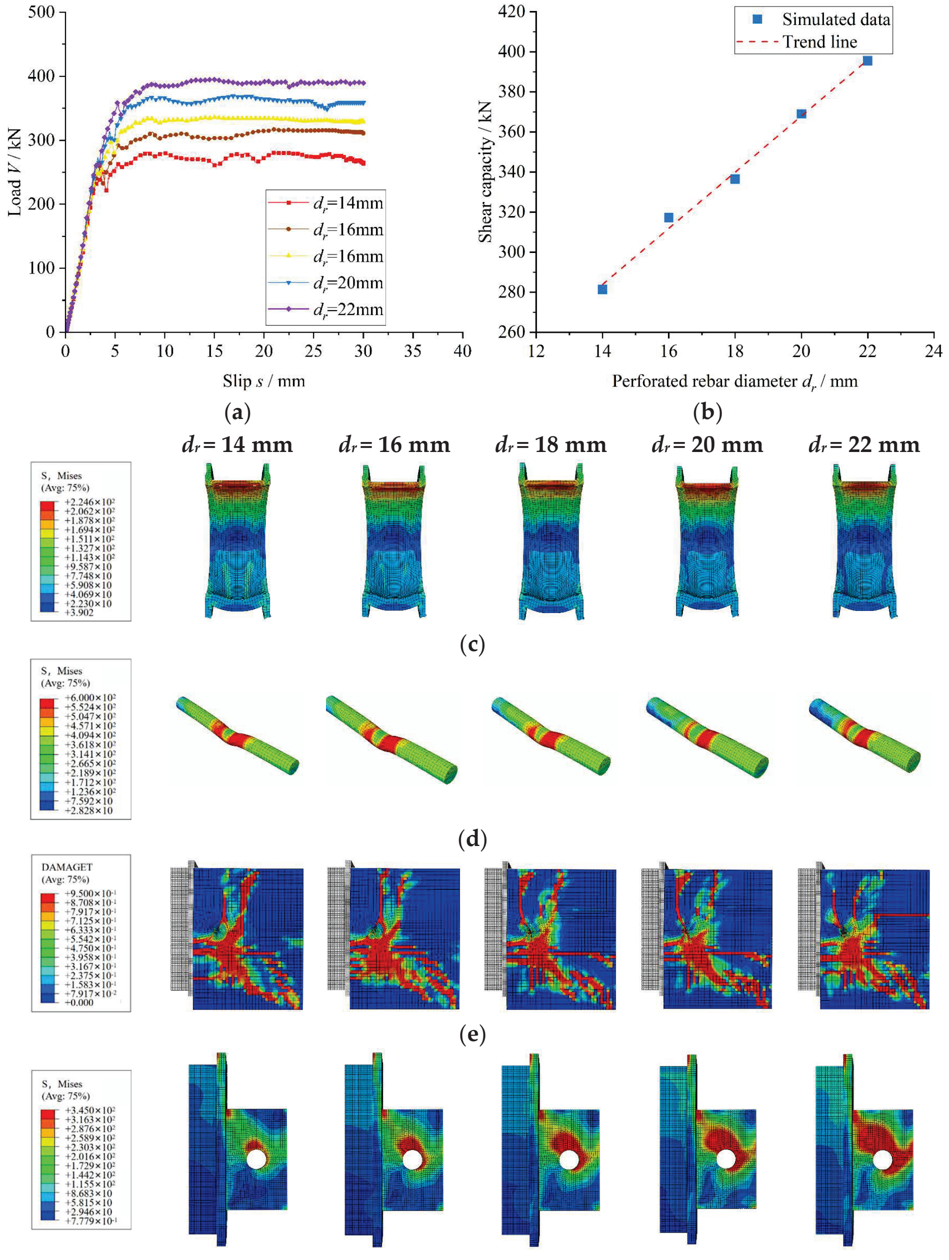

(**a**) (**b**)

(**c**)

(**d**)

(**e**)

(**f**)

Figure 8. Impact of reinforcement diameter: (**a**) load–slip curves; (**b**) impact analysis; (**c**) stress in rubber ring; (**d**) perforated rebar stress; (**e**) concrete tensile damage; (**f**) perfobond steel plate stress.

The stress distribution features (Figure 8c–f) indicate that the stress concentration in the rubber ring intensifies as its diameter increases. Meanwhile, the stress levels in the perforated rebar and perfobond steel plate remain relatively stable, while tensile damage to the concrete slab increases. This phenomenon arises because, with a fixed hole diameter in the perfobond steel plate, an increase in the perforated rebar diameter leads to a greater volume of shear force transmitted through the rebar, thereby enhancing the shear capacity of the connector. Keeping the steel plate opening diameter and rubber ring thickness constant, an increase in the perforated rebar diameter enlarges the volume of the rebar subjected to shear, thus increasing the shear force it endures. However, this also reduces the shear deformation capacity of the perforated rebar, resulting in greater damage to the concrete dowel. Conversely, such an increase reduces the thickness of the concrete dowel, diminishing the volume subjected to shear and, consequently, decreasing the shear force it bears. As shown in Figure 8a, the improvement in shear capacity due to the enhanced performance of the perforated rebar significantly surpasses the reduction in shear capacity caused by the weakened concrete dowel.

5.3. Impact of Concrete Strength

Figure 9 illustrates the load–slip curves and stress distribution characteristics of the Twin-PBL rubber-ring shear connector under varying concrete strengths. With all other model dimensions held constant, the compressive strength of the concrete slab increases from 40 MPa to 50 MPa, 60 MPa, 70 MPa, and 80 MPa. Consequently, the yield load (V_y) increases by 18.3%, 28.5%, 35.3%, and 38.6%, respectively. The shear stiffness (K_s) increases by 6.2%, 11.3%, 11.5%, and 18.1%, while the shear capacity (V_u) improves by 15.3%, 32.8%, 41.7%, and 57.3%. These findings demonstrate that increasing the concrete strength significantly enhances the shear performance of the Twin-PBL rubber-ring shear connector.

It is noteworthy that the stress distribution characteristics (Figure 9c–f) reveal a significant intensification of stress concentration within the rubber ring as the concrete strength increases. Simultaneously, stress concentration in the perforated rebar and perfobond steel plate also increases, while the tensile damage area in the concrete slab diminishes. The increase in concrete strength enhances the shear bearing capacity of the concrete dowel, enabling it to withstand greater loads before failure, thereby improving the overall shear capacity of the connector. The increased strength of the concrete surrounding the perfobond steel plate allows the slab to endure larger stresses transmitted by the plate, hence reducing its likelihood of failure. Moreover, the stress distribution in the perforated rebar and perfobond steel plate exhibits a pronounced concentration effect. This phenomenon can be attributed to the improved strength of the concrete dowel, which facilitates greater load-sharing between the dowel and the perforated rebar at higher load levels and also necessitates that the perfobond steel plate transfer greater shear forces.

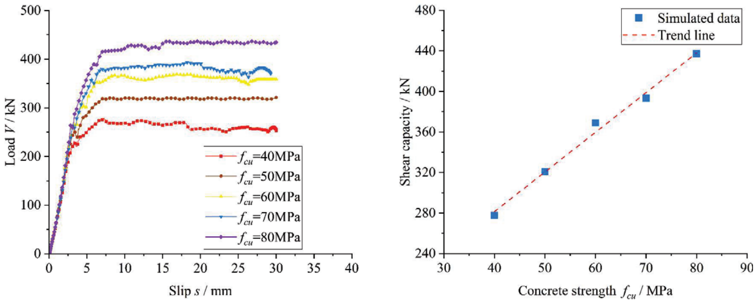

(**a**) (**b**)

Figure 9. *Cont.*

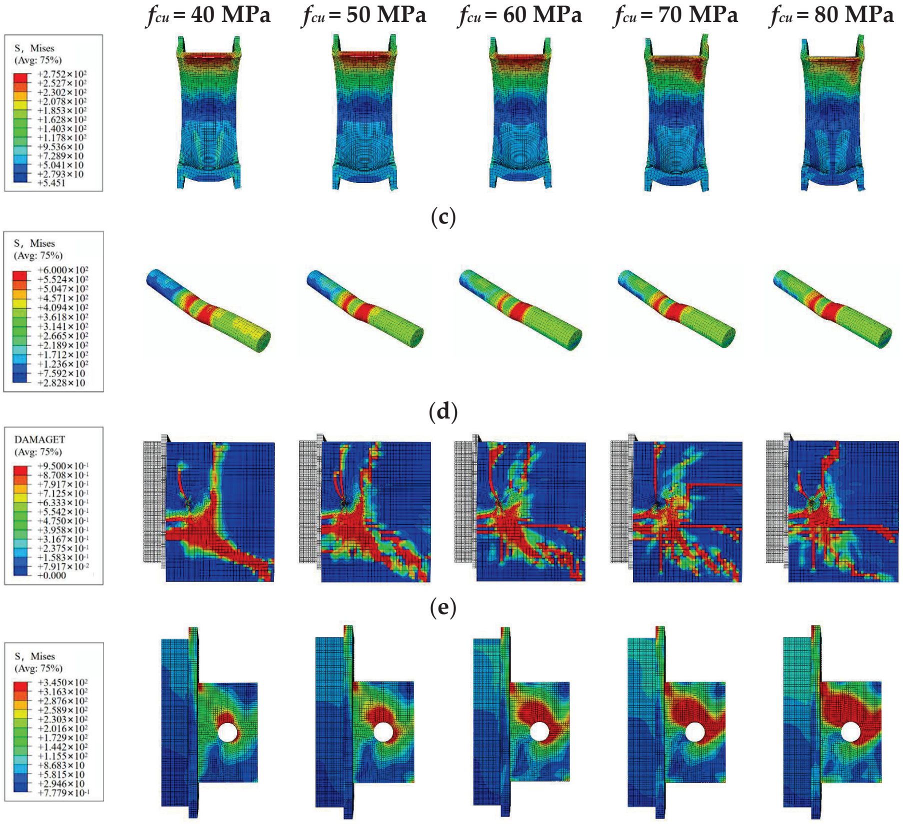

(**c**)

(**d**)

(**e**)

(**f**)

Figure 9. Impact of concrete strength: (**a**) load–slip curves; (**b**) impact analysis; (**c**) stress in rubber ring; (**d**) perforated rebar stress; (**e**) concrete tensile damage; (**f**) perfobond steel plate stress.

5.4. Impact of Perforated Rebar Strength

Figure 10 shows the load–slip curves and stress distribution characteristics of the Twin-PBL rubber-ring shear connector under varying strengths of perforated rebar. When the strength of the perforated rebar increases from 335 MPa to 400 MPa and 500 MPa, the yield load, shear stiffness, and shear capacity of the connector all improve, showing a positive correlation with the rebar strength. Specifically, the yield load (V_y) increases by 8.2% and 9.6%, respectively. The shear stiffness (K_s) increases by 0.8% and 2.0%, while the shear capacity (V_u) increases by 9.9% and 15.37%. These results confirm that enhancing the strength of the perforated rebar significantly improves the shear performance of the Twin-PBL rubber-ring shear connector.

The stress distribution characteristics (Figure 10c–f) demonstrate that increasing the strength of the perforated rebar intensifies stress concentration within the rubber ring. At the same time, stress becomes increasingly localized in both the perforated rebar and the perfobond steel plate, leading to an expansion of the tensile damage zone within the concrete slab. This behavior arises because the enhanced strength of the perforated rebar improves its load-bearing capacity while concurrently reducing its shear deformation capability, thereby delaying structural failure to higher load levels. However, the reduced shear deformation capacity causes the concrete dowel to fail at lower load thresholds, which in turn increases the compressive stress exerted on the concrete slab by the perforated rebar, resulting in significant tensile damage. As the load transfer through the perfobond steel plate intensifies, stress concentration progressively develops.

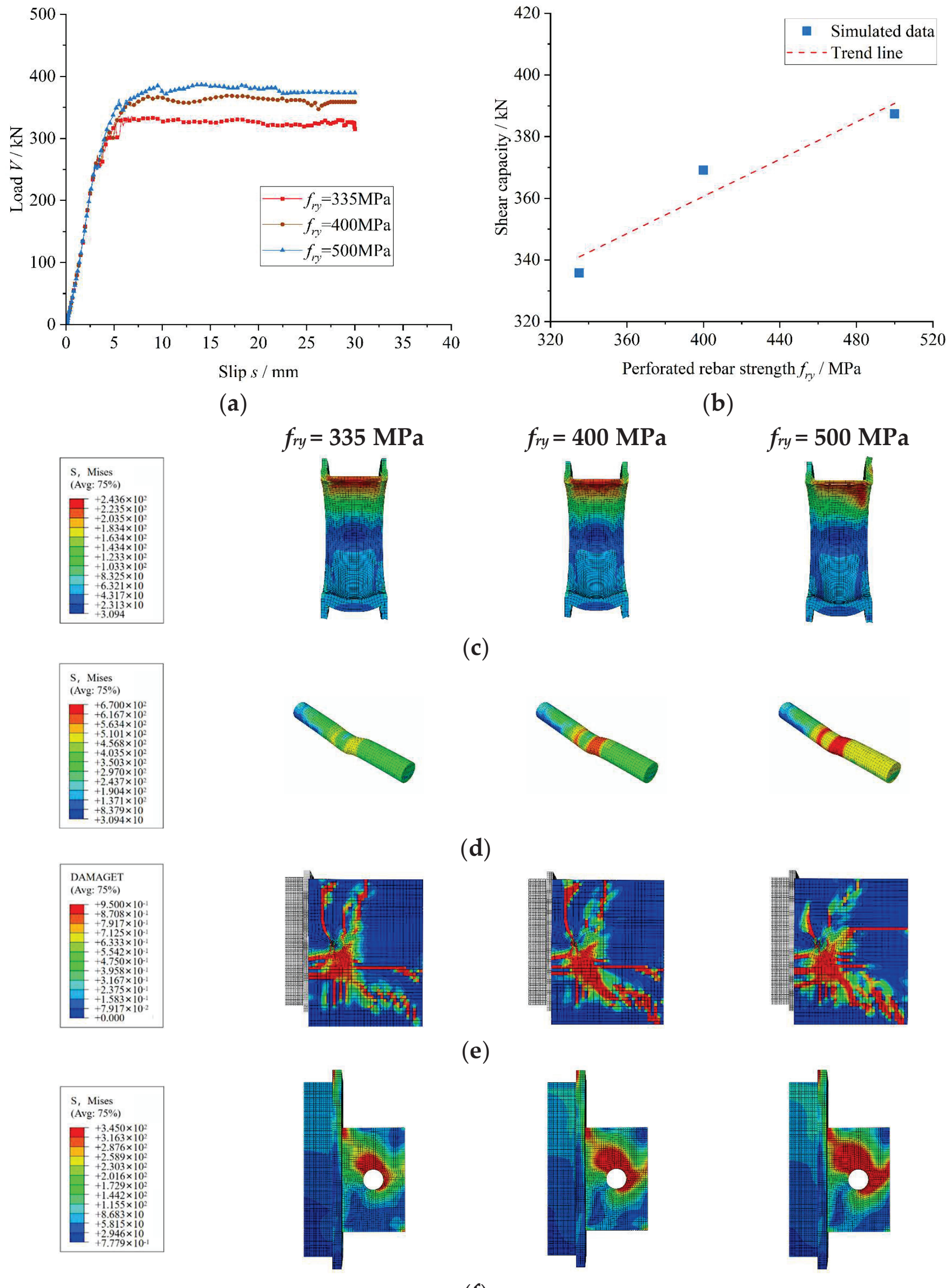

(**a**) (**b**)

(**c**)

(**d**)

(**e**)

(**f**)

Figure 10. Impact of reinforcement strength: (**a**) load–slip curves; (**b**) impact analysis; (**c**) stress in rubber ring; (**d**) perforated rebar stress; (**e**) concrete tensile damage; (**f**) perfobond steel plate stress.

5.5. Impact of Perfobond Steel Plate Strength

Figure 11 presents the load–slip curves and stress distribution characteristics of Twin-PBL rubber-ring shear connectors with varying perfobond steel plate strengths. The yield load (V_y) increases by 13.0%, 14.9%, 15.6%, and 20.2% for connectors incorporating perfobond steel plates with strengths of 345 MPa, 390 MPa, 420 MPa, and 460 MPa, respectively, as the strength of the perfobond steel plate is varied while the dimensions of all model components remain unchanged. The shear stiffness (K_s) increases by 1.7%, 1.6%, 1.5%, and 1.1%, while the shear capacity (V_u) increases by 13.36%, 11.7%, 11.4%, and 14.3%, respectively. These findings suggest that the influence of perfobond steel plate strength on the shear performance of the Twin-PBL rubber-ring shear connectors is subject to certain limitations.

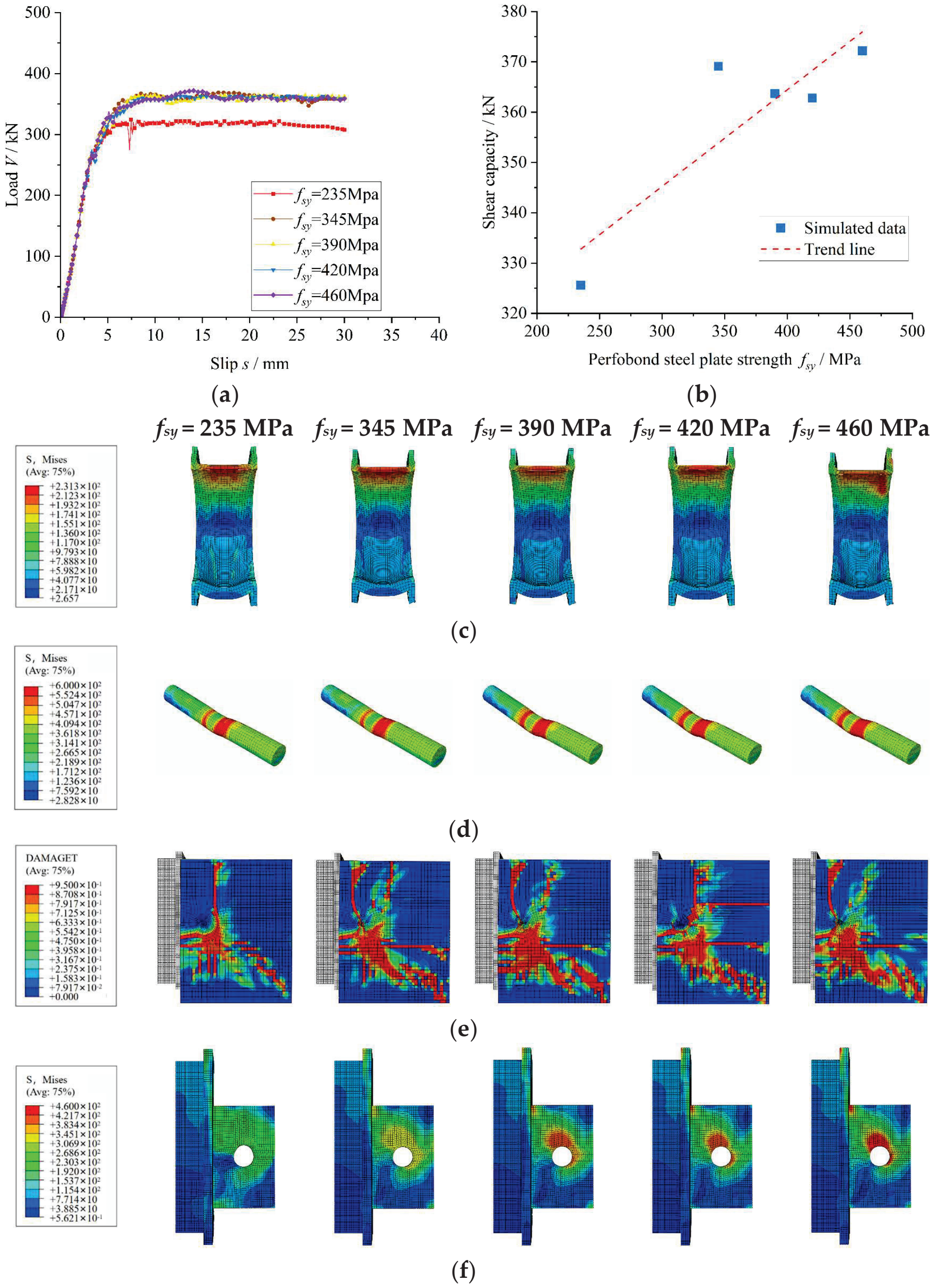

Figure 11. Impact of plate strength: (**a**) load–slip curves; (**b**) impact analysis; (**c**) stress in rubber ring; (**d**) perforated rebar stress; (**e**) concrete tensile damage; (**f**) perfobond steel plate stress.

The stress distribution characteristics (Figure 11c–f) indicate that the stresses in the rubber ring and perforated rebar remain relatively stable with increasing steel plate strength. Similarly, the tensile damage distribution on the concrete slab remains largely unchanged, except in the case of the 235 MPa steel plate. The stress in the steel plate is primarily concentrated above the openings and away from the steel beams, with this concentration becoming more pronounced as the strength increases. Notably, the high-strength steel plate does not fully yield, and yielding occurs only at the openings. The deformation levels of the steel plate and perforated rebar indicate that the deformation capacity of the steel plate decreases with increasing strength, leading to connector failure mostly due to shear in the perforated rebar.

6. Prediction Formula

6.1. Previous Expressions

To mitigate the influence of end-bearing pressure on the shear performance of the Twin-PBL rubber-ring shear connector, a 50 mm gap was introduced in the slip direction of the perfobond steel plate in parametric study. Assuming that only the friction between the concrete slab and the rigid base exists, all other contact surfaces of the model are frictionless. The following section reviews some important previous studies and associated equations.

Hosaka et al. conducted a classification analysis of connectors by evaluating the presence or absence of perforated rebar in the holes of the perfobond steel plate. Equation (7) was proposed to estimate the shear capacity of connectors without perforated rebar in the holes, while Equation (8) was developed for connectors that include perforated rebar in the holes [28].

$$V_u = 3.38\sqrt{t_p/d_p}d_p^2 f_c - 39.0\ \times\ 10^3 \tag{7}$$

$$V_u = 1.45\left[\left(d_p^2 - d_r^2\right)f_c + d_r^2 f_{ru}\right] - 26.1\ \times\ 10^3 \tag{8}$$

The parameters considered include the thickness of the perfobond steel plate (t_p), the concrete compressive strength (f_c), the rebar hole diameter (d_r), and the ultimate tensile strength (f_{ru}).

Zheng et al. investigated connectors composed of perfobond steel plates with notches and proposed Equation (9) to evaluate their shear capacity. A parametric analysis was performed on the notched perfobond steel plate connectors to examine the restraining effect of the perforated rebar on concrete, incorporating both pull-out tests and numerical simulations [29].

$$V_u =\ \gamma_n\gamma_e\left[0.42\left(d_p^2 - d_r^2\right)f_c + 1.15d_r^2 f_{ry} + 0.45d_p t_p f_{sy}\right] \tag{9}$$

In this context, V_u denotes the shear load capacity of a single perfobond steel plate. f_{ry} and f_{sy} represent the yield strengths of the perforated rebar and the steel plate, respectively, both expressed in MPa. The parameters f_c and d_r denote the concrete compressive strength and the diameter of the perforated rebar, respectively. Specifically, γ_n is a coefficient that accounts for the effect of the number of holes in the steel plate, defined as $\gamma_n = {n_p}^{-0.22}$, where n_p is the number of holes. γ_e is a coefficient that considers the influence of hole spacing on the steel plate, defined as $\gamma_e = 1 + 0.002\cdot(e_p - 200) \leq 1$, where e_p denotes the hole spacing.

6.2. Proposed Formula for Shear Capacity

Previous studies indicate that the shear capacity of the conventional Twin-PBL shear connectors is primarily contributed by the perforated rebars, concrete dowels, rubber rings, and perfobond steel plates. Given that the rubber ring is a low-stiffness material with limited load-bearing capacity, the shear capacity of the Twin-PBL rubber-ring shear connector is expressed as shown in Formula (10).

$$V_u = V_{ts} + V_{ct} + V_{ps} \tag{10}$$

V_{ts} denotes the shear capacity provided by the perforated rebar (in N); V_{ct} denotes the shear capacity provided by the concrete dowel (in N); V_{ps} denotes the shear capacity provided by the perfobond steel plate (in N).

Therefore, Equations (11) and (12) can be used to determine the shear capacity of the Twin-PBL rubber-ring shear connector.

$$V_u = D_1 A_{ts} f_{ry} + D_2 A_{ct} f_c + D_3 A_{ps} f_{sy} \tag{11}$$

$$V_u = D_1 d_r^2 f_{ry} + D_2 \left[d_p^2 - (d_r + 2t_r)^2 \right] f_c + D_3 d_p t_p f_{sy} \tag{12}$$

V_u denotes the shear capacity of an individual perfobond steel plate (in N); A_{ts} denotes the cross-sectional area of the perforated rebar, whereas A_{ct} represents the cross-sectional area of the concrete dowel. A_{ps} denotes the contact area between the perfobond steel plate and the dowel; d_p refers to the diameter of the perforation in the perfobond steel plate; f_c denotes the compressive strength of concrete; f_{ry} represents the yield strength of the perforated rebar; t_p denotes the thickness of the perfobond steel plate; f_{sy} indicates the yield strength of the perfobond steel plate; d_r signifies the diameter of the perforated rebar; t_r denotes the thickness of the rubber ring; and D_1, D_2, and D_3 are the three constant coefficients.

Nonlinear regression analysis of the findings from the finite element parameter analysis indicates that the best fitting performance of Equation (12) is achieved when the coefficients are set to $D_1 = 1.16$, $D_2 = 1.71$, and $D_3 = 0.18$. Equation (13) is derived to evaluate the shear capacity of an individual perfobond steel plate in the Twin-PBL rubber-ring shear connector.

$$V_u = 1.16 d_r^2 f_{ry} + 1.71 \left[d_p^2 - (d_r + 2t_r)^2 \right] f_c + 0.18 d_p t_p f_{sy} \tag{13}$$

Figure 12 presents a comparative analysis and validation of the shear capacity predicted by Equation (13) against the results obtained from finite element simulations. The mean and standard deviation of the ratio of predicted values to simulated values are 1.01 and 0.0556, respectively, demonstrating a strong agreement between theoretical predictions and numerical modeling outcomes.

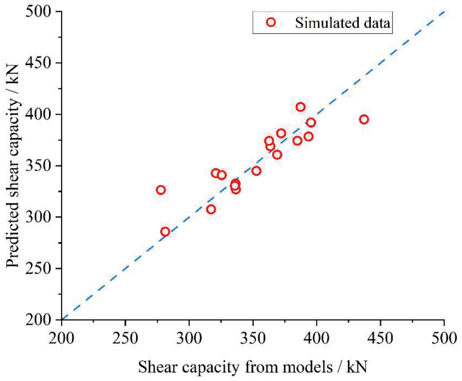

Figure 12. Comparative verification of shear capacity equations.

As shown in Figure 12, the predicted results exhibit excellent consistency with the finite element simulation outcomes, which provides a reliable reference for subsequent experimental validation and the broader application of the Twin-PBL rubber-ring shear connector.

7. Conclusions

This study investigates Twin-PBL rubber-ring shear connectors through a series of numerical simulations. First, the connector was designed. Subsequently, 23 different finite element models were established for comparative analysis based on the finite element simulation and analysis methodology described in reference [14]. Further, the shear performance of Twin-PBL rubber-ring shear connector as well as the factors affecting this performance were simulated and analyzed in detail. Finally, new equations for calculating the performance of the Twin-PBL rubber-ring shear connector were deduced. The following conclusions were drawn:

A comparative evaluation of the mechanical performance between the Twin-PBL rubber-ring shear connector and its conventional counterpart reveals that the inclusion of a 4 mm-thick rubber ring results in a slight 7.5% reduction in shear capacity, while simultaneously causing a significant 71% decrease in shear stiffness. This suggests that the incorporation of a low-stiffness rubber component primarily governs the reduction in structural stiffness, whereas its influence on the ultimate shear resistance is relatively minor.

A comparison of the mechanical performance between the Twin-PBL rubber-ring shear connector and the conventional connector demonstrates that the use of a 4 mm-thick rubber ring increases the yield slip of the former to 183.0% of that of the latter. This finding highlights the critical role of the rubber component in improving the deformation capacity of the shear connector system while maintaining structural integrity, as it significantly enhances ductility through its integration.

Finite element parametric studies on rubber rings with varying thicknesses indicate that the strategic integration of elastomeric components effectively mitigates stress concentrations at the perforation regions of the connectors. The enhanced deformability and optimized shear stress redistribution patterns observed in the numerical simulations show that rubber interlayers not only improve structural flexibility but also promote more uniform load transfer mechanisms, thereby fundamentally modifying the mechanical response characteristics of the connector system.

The analytical results demonstrate that parameters such as the diameter and tensile strength of the perforated rebars, the thickness of the rubber rings, and the compressive strength of the concrete have a significant impact on the shear load capacity and shear strength of the Twin-PBL rubber-ring shear connectors. Variations in these parameters can directly influence the performance of the connectors under shear loading, thereby affecting the overall safety and stability of the structural system. An increase in the diameter and tensile strength of the perforated rebars generally enhances the shear capacity of the connectors, whereas the thickness of the rubber rings primarily affects their deformation characteristics. Moreover, as a key structural material, higher concrete strength can considerably improve the shear performance of the connectors. However, the research results suggest that the strength of the perfobond steel plates exerts a relatively minor influence.

A shear capacity prediction formula specifically designed for the Twin-PBL rubber-ring shear connector is developed through a comprehensive review of existing shear capacity calculation methods and their derivation processes, combined with finite element parametric analysis results and the observed failure mechanisms of the connectors. The computed results exhibit a high degree of consistency with the finite element simulations, offering a dependable reference for further study and practical engineering applications.

In conclusion, this research employs the finite element method to investigate the shear performance of the Twin-PBL rubber-ring shear connector. Extensive simulations and analyses suggest that the Twin-PBL rubber-ring shear connector exhibits relatively low initial stiffness. This study identifies key factors influencing the shear performance of the connector, enabling the determination of an optimal combination of connector properties. The proposed method for predicting the shear bearing capacity of the Twin-PBL rubber-ring shear connector may provide valuable insights and reliable estimations for its anticipated performance in practical engineering applications.

Author Contributions: J.W. proposed the research project, designed the shear connector, and wrote the initial manuscript; P.C. established finite element models, performed numerical simulations and data analyses; Q.H. carried out text proofreading and project administration. All authors have read and agreed to the published version of the manuscript.

Funding: The study was sponsored by Project of General Scientific Research Program of Department of Education, Zhejiang Province (Y202250206).

Data Availability Statement: The data used to support the results of this study are available from the corresponding author upon request.

Acknowledgments: The authors would like to acknowledge Zhejiang Department of Education for the funding support.

Conflicts of Interest: The authors declare that they have no conflicts of interest.

References

1. He, J.; Liu, Y.; Pei, B. Experimental Study of the Steel-Concrete Connection in Hybrid Cable-Stayed Bridges. *J. Perform. Constr. Facil.* **2014**, *28*, 559–570. [CrossRef]
2. Zhang, Q.; Jia, D.; Bao, Y.; Cheng, Z.; Xiao, L.; Bu, Y. Internal Force Transfer Effect-Based Fatigue Damage Evaluation for PBL Shear Connector Groups. *J. Constr. Steel Res.* **2018**, *148*, 469–478. [CrossRef]
3. Zheng, S.; Zhao, C.; Liu, Y. Analytical Model for Load–Slip Relationship of Perfobond Shear Connector Based on Push-Out Test. *Materials* **2018**, *12*, 29. [CrossRef] [PubMed]
4. Kim, Y.-H.; Kang, J.-Y.; Kim, S.-H.; Kim, D.-J. Structural Performance of Steel Pile Caps Strengthened with Perfobond Shear Connectors under Lateral Loading. *Appl. Sci.* **2016**, *6*, 317. [CrossRef]
5. Xue, D.; Liu, Y.; He, J.; Ma, B. Experimental Study and Numerical Analysis of a Composite Truss Joint. *J. Constr. Steel Res.* **2011**, *67*, 957–964. [CrossRef]
6. Zheng, S.; Liu, Y.; Yoda, T.; Lin, W. Parametric Study on Shear Capacity of Circular-Hole and Long-Hole Perfobond Shear Connector. *J. Constr. Steel Res.* **2016**, *117*, 64–80. [CrossRef]
7. Gu, J.-C.; Liu, D.; Deng, W.-Q.; Zhang, J.-D. Experimental Study on the Shear Resistance of a Comb-Type Perfobond Rib Shear Connector. *J. Constr. Steel Res.* **2019**, *158*, 279–289. [CrossRef]
8. Zhang, Q.; Pei, S.; Cheng, Z.; Bao, Y.; Li, Q. Theoretical and Experimental Studies of the Internal Force Transfer Mechanism of Perfobond Rib Shear Connector Group. *J. Bridge Eng.* **2017**, *22*, 04016112. [CrossRef]
9. Liu, Y.; Xin, H.; Liu, Y. Load Transfer Mechanism and Fatigue Performance Evaluation of Suspender-Girder Composite Anchorage Joints at Serviceability Stage. *J. Constr. Steel Res.* **2018**, *145*, 82–96. [CrossRef]
10. Fang, Z.; Wu, J.; Xu, X.; Ma, Y.; Fang, S.; Zhao, G.; Jiang, H. Grouped Rubber-Sleeved Studs–UHPC Pocket Connections in Prefabricated Steel–UHPC Composite Beams: Shear Performance under Monotonic and Cyclic Loadings. *Eng. Struct.* **2024**, *305*, 117781. [CrossRef]
11. Zhang, Y.; Zhu, J.; Wu, L.; Lin, H.; Fang, Z.; Cen, Z.; Yang, Y.; Fang, S. Experimental and Numerical Analyses on the Shear Behavior of Grouped Single-Embedded-Nut High-Strength Bolts in Steel–Ultra-High-Performance Concrete Composite Slabs. *J. Build. Eng.* **2024**, *86*, 108829. [CrossRef]
12. Nie, J.-G.; Li, Y.-X.; Tao, M.-X.; Nie, X. Uplift-Restricted and Slip-Permitted T-Shape Connectors. *J. Bridge Eng.* **2015**, *20*, 04014073. [CrossRef]
13. Xu, X.; Liu, Y.; He, J. Study on Mechanical Behavior of Rubber-Sleeved Studs for Steel and Concrete Composite Structures. *Constr. Build. Mater.* **2014**, *53*, 533–546. [CrossRef]
14. Liu, Y.; Xin, H.; Liu, Y. Experimental and Analytical Study on Shear Mechanism of Rubber-Ring Perfobond Connector. *Eng. Struct.* **2019**, *197*, 109382. [CrossRef]
15. Xu, Y.; He, S.; Guan, P.; Mosallam, A.S.; Zeng, J.; Wan, Z. Shear Behavior of Flexible-Sleeve Perfobond Strip Connectors: Experimental and Analytical Studies. *Eng. Struct.* **2022**, *264*, 114380. [CrossRef]
16. Khatir, A.; Capozucca, R.; Khatir, S.; Magagnini, E.; Le Thanh, C.; Riahi, M.K. Advancements and Emerging Trends in Integrating Machine Learning and Deep Learning for SHM in Mechanical and Civil Engineering: A Comprehensive Review. *J. Braz. Soc. Mech. Sci. Eng.* **2025**, *47*, 419. [CrossRef]

17. Appavuravther, E.; Vandoren, B.; Henriques, J. Analytical and Numerical Investigation of Adhesively Bonded Perfobond Shear Connectors for Timber-Concrete Composite Floors. *Structures* **2024**, *70*, 107582. [CrossRef]
18. Asgari, A.; Ranjbar, F.; Bagheri, M. Seismic Resilience of Pile Groups to Lateral Spreading in Liquefiable Soils: 3D Parallel Finite Element Modeling. *Structures* **2025**, *74*, 108578. [CrossRef]
19. Bagheri, M. Seismic Resilience Assessment of RC Superstructures on Long–Short Combined Piled Raft Foundations: 3D SSI Modeling with Pounding Effects. *Structures* **2025**, *81*, 110176. [CrossRef]
20. Liu, Y.; Yang, H.; Luan, L.; Xu, X.; Liu, Y.; Du, X. Three Failure Modes of High-Strength Steel (HSS) Perfobond Connector Embedded in UHPC. *Eng. Struct.* **2023**, *286*, 116147. [CrossRef]
21. Liu, Y.; Liu, Y.; Xin, H.; Tian, H.; Wei, J. Numerical Study on Shear Performance of a New Perfobond Connector with Controllable Stiffness. *Adv. Mater. Sci. Eng.* **2020**, *2020*, 5384701. [CrossRef]
22. Sun, L.; Liu, Y.; Wang, H.; Shi, F.; Liu, J.; Jiang, L. Tensile Stiffness of Perfobond Rib Connectors in Steel–Concrete Composite Pylon of Bridges. *Eng. Struct.* **2023**, *284*, 115931. [CrossRef]
23. Sun, L.; Liu, Y.; Shi, F.; Wang, H. Pull-out Performance of Perfobond Rib Connectors in Steel High-Strength Concrete Composite Bridge Pylons. *Constr. Build. Mater.* **2023**, *366*, 130205. [CrossRef]
24. Walraven, J.C. *Model Code 2010-Final Draft: Volume 1*; Fib Fédération Internationale Du Béton: Lausanne, Switzerland, 2012; Volume 65.
25. Nguyen, H.T.; Kim, S.E. Finite Element Modeling of Push-out Tests for Large Stud Shear Connectors. *J. Constr. Steel Res.* **2009**, *65*, 1909–1920. [CrossRef]
26. Comité Euro-International du Béton. *CEB-FIP Model Code 1990: Design Code*; Thomas Telford Publishing: London, UK, 1993.
27. Hordijk, D.A. Tensile and Tensile Fatigue Behaviour of Concrete; Experiments, Model-Ling and Analyses. *Heron* **1992**, *37*, 3–79.
28. Hosaka, T.; Mitsuki, K.; Hiragi, H.; Ushijima, Y.; Tachibana, Y.; Watanabe, H. An Experimental Study on Shear Characteristics Ofperfobond Strip and Its Rational Strength Equations. *J. Struct. Eng. JSCE* **2000**, *46*, 1593–1604.
29. Zheng, S.; Liu, Y.; Liu, Y.; Zhao, C. Experimental and Numerical Study on Shear Resistance of Notched Perfobond Shear Connector. *Materials* **2019**, *12*, 341. [CrossRef]

buildings

Article

Stress Measurement and Analysis of Structural Parameters of Flat Arm Tower Crane Under Different Working Conditions

Qinghua Zhang [1,*], Bohao Mei [1], Hui Yang [2], Xin Hu [3], Wei An [4], Yanpeng Yue [1], Yanwei Xu [1] and Zhihao Wang [1,*]

[1] School of Civil Engineering and Communication, North China University of Water Resources and Electric Power, Zhengzhou 450045, China; meibohao@stu.ncwu.edu.cn (B.M.); yueyanpeng@ncwu.edu.cn (Y.Y.); xuyanwei@ncwu.edu.cn (Y.X.)

[2] China Construction Third Engineering Bureau Group Co., Ltd., Wuhan 430064, China; yanghui_cscec3b@163.com

[3] State Grid Henan Economic Research Institute, Zhengzhou 450000, China; hnhuxin@163.com

[4] POWER CHINA Henan Electric Power Engineering Co., Ltd., Zhengzhou 450007, China; anwei-heny@powerchina.cn

* Correspondence: zqh@ncwu.edu.cn (Q.Z.); wangzhihao@ncwu.edu.cn (Z.W.)

Abstract: With the expansion of high-rise building construction in China, tower cranes have become indispensable key equipment in the construction industry. To ensure the safety and structural reliability of tower cranes under complex working conditions, this paper takes a typical 40 m-high flat-arm tower crane as the research object. For the first time, the orthogonal test method was used to monitor the stress of key components (the root of the tower body and the root of the boom). The stress distribution characteristics of the tower crane structure under different working conditions were systematically analyzed. Then, based on the power spectral density analysis method, the natural frequency of the tower crane structure was identified. The influence of key structural parameters, such as lifting position, rope length, and lifting weight, on the stress of the tower crane was quantitatively studied through orthogonal experiments, revealing the multi-parameter coupling effect. The results show that the stress at the measuring point at the root of the tower body is significantly higher than that at the root of the boom. This indicates that the root of the tower body is the primary stress-bearing part of the tower crane structure, highlighting the need to focus on its fatigue performance and safety assessment. Based on the power spectral density analysis of the root stress of the tower crane, the natural frequencies of the tower crane structure were accurately identified. The first-order frequency was 0.10 Hz, and the second-order frequency was 0.20 Hz, providing data support for the study of the tower crane's dynamic characteristics. The orthogonal test analysis shows that the influences of lifting position, rope length, and lifting weight on the stress of the tower crane are consistent, with no significant differences. The effects of lifting position and rope length on stress are dominant, while the influence of lifting weight is relatively small. These research findings provide an important basis for the lightweight design and safety assessment of tower cranes.

Keywords: flat arm tower crane; stress measurement; structural parameters; orthogonal experiment

1. Introduction

Tower cranes [1] offer advantages such as high lifting heights, large turning radii, fast working speeds, and suitability for use with multiple nearby cranes. As a result, they have been widely employed in modern engineering construction [2]. However, during actual operation, tower cranes operate in harsh environments, enduring high-intensity loads and strong impacts over extended periods. Additionally, their working conditions are complex and constantly changing. This complex stress state can easily cause stress concentration in key structural components, which may subsequently lead to crack propagation and even structural failure. The weld areas of the tower crane are particularly susceptible to cracking due to stress concentration and manufacturing defects. However, local thin-walled components may buckle under external forces such as overload or strong winds, leading to fatigue damage and even structural failure. In severe cases, this may result in major safety incidents, including crane arm fractures and tower crane overturning [3]. Not only can it cause significant economic losses, but it may also pose a serious threat to the lives of construction workers [4–6]. Traditional design methods primarily rely on theoretical calculations, static analysis, and dynamic analysis. However, due to the difficulty of fully accounting for complex loads, boundary conditions, and structural nonlinear effects, these methods often fail to accurately capture the actual stress distribution under real working conditions. Obtaining stress data from key components of the tower crane through on-site measurements has become a crucial approach for evaluating its structural performance and safety status. Therefore, conducting stress measurements under various working conditions, analyzing the stress distribution characteristics in depth, and systematically assessing the influence of structural parameters on key components can provide a solid foundation for optimal design, safety assessment, and accident prevention. This research holds significant theoretical and engineering value in ensuring the safe and stable operation of tower cranes.

With the rapid development of industrialization and urbanization, concerns regarding structural safety and reliability have become increasingly prominent. Structural Health Monitoring (SHM) technology [7], as an advanced approach, provides a robust safeguard for structural safety and reliability by continuously monitoring and evaluating the condition of structures in real time. Traditional manual visual inspections rely on portable equipment, which is not only costly and inefficient but also ineffective in detecting hidden structural damage. In contrast, modern SHM technology enables real-time monitoring of strain, deflection, vibration, and other key parameters by installing sensors at critical structural locations [8]. This significantly reduces manpower and resource consumption while improving the accuracy and efficiency of inspections.

In recent years, significant progress has been made in the research on the mechanical properties, dynamic characteristics, and safety assessment of tower cranes. Scholars, both domestically and internationally, have conducted systematic and detailed studies through numerical simulations and field measurements, accumulating extensive theoretical and experimental findings.

In numerical simulation research, this method allows for flexible adjustment of various parameter settings and enables an in-depth analysis of the stress state of structural components under different loads, thanks to its advantages of low cost, convenience, and rapid operation. Jiang and Jiang [9] established a finite element model of a tower crane and conducted a transient dynamic analysis to reveal its vibration characteristics under different working conditions. They further performed a fatigue damage assessment and estimated the service life based on the stress time-history data of key nodes in the crane boom. Yang et al. [10] developed a fatigue damage and service life prediction model for the overhead crane girder by constructing a virtual prototype of the crane, obtaining the impact load spectrum, and incorporating the material S-N curve. Lehner et al. [11] employed numerical simulation to obtain the load spectrum of the crane-supporting structure, which was converted into a peak stress spectrum using the rain-flow counting method. The

Ansys software was then utilized to identify fatigue damage and predict service life for the crane-supporting structure. Li et al. [12] innovatively developed a three-parameter Weibull distribution model for stress spectrum acquisition and employed the Latin hypercube sampling technique to generate a random sample set of characteristic parameters, thereby obtaining the stress time-history of critical structural points. Dong et al. [13] applied an improved support vector regression algorithm to derive the equivalent fatigue load spectra, established a first principal stress time-history model for key components and obtained two-dimensional stress spectra using rain-flow counting statistics. Han and Lee [14] obtained the torque curve of the tower crane slewing reducer through an inertial endurance test. Combined with finite element analysis, they clarified the stress distribution pattern of critical areas in the tower crane slewing carrier. Hectors et al. [15] established a finite element model of the overhead crane runway girder structure based on measured data and evaluated the fatigue performance of key nodes using the hot spot stress method and fracture mechanics approach. Moskvichev and Chaban [16] investigated the evolution of fatigue crack length and crack tip stress intensity in crane girders under varying load cycles through numerical analysis. He et al. [17] used numerical simulation to calculate the response of the tower crane under working conditions and tornado loads, effectively assessing its safety under tornado impact. Lu et al. [18] analyzed the dynamic response of the tower crane through numerical simulation and investigated the effects of wind load and lifting load on its wind-induced vibration response at different construction stages. Chen et al. [19] analyzed the dynamic response of the tower crane and proposed a comprehensive safety assessment scheme for the tower crane under fluctuating wind loads. The numerical simulation method is useful for analyzing the mechanical properties of each component of the tower crane under different load conditions. However, its accuracy remains limited by the simplified assumptions of the finite element model and the uncertainty of various parameter settings. For example, factors such as boundary condition settings, the actual force states of connected components, and variations in material parameters can all affect the simulation results. Consequently, a certain deviation exists between the simulation and actual working conditions. Therefore, how to improve the numerical model, optimize the boundary condition setting, and improve the modeling accuracy of the connection parts. The establishment of more reliable simulation analysis methods is still the focus of current research.

Field measurement is the most intuitive and fundamental method for studying structural conditions and serves as a crucial basis for verifying the reliability of theoretical models and numerical simulations. Pástor et al. [20] utilized strain gauges to measure the stress distribution of the overhead crane's main girder under working conditions and obtained stress values at key locations. Xi et al. [21] collected in situ strain data of the suspension tower using a dynamic response monitoring system, analyzed the load characteristics and extrapolated the ultimate load. Park et al. [22] validated the model through static load experiments and assessed the fatigue life of the tower crane slewing carrier based on the stress at the bearing body, using the verified tower crane slewing reducer model. Liu et al. [23] validated the crane's vibration model through field experiments and investigated the effects of parameters such as payload mass, boom length, and mast height on its vibration response. Xu and Wu [24] used acoustic emission technology and the two-parameter basis function method to monitor and analyze the crack propagation state in steel structures and obtain the critical value of crack propagation. Li et al. [25] developed a real-time monitoring system for tower cranes based on Internet of Things technology and established two tower response prediction models using machine learning algorithms, enabling intelligent monitoring and prediction of the entire tower crane operation process. Wei et al. [26] combined field tests and theoretical analysis to investigate the local cracking failure mechanism of the crane and estimated the fatigue life of the crack zone based on the stress spectrum under working conditions. On-site measurements have inherent limitations, such as high cost, complex implementation, and susceptibility to environmental factors (e.g., temperature, humidity, wind speed). However, as a crucial method for directly obtaining the actual structural response, it accurately reflects the characteristics of the tower crane under real working conditions.

Stress analysis is the core of structural safety assessment, as it intuitively reflects the mechanical properties of a structure under load, identifies its weak points, and provides a basis for optimal structural design. Field stress measurements play a key role in numerical modeling. They not only compensate for the shortcomings of finite element models but also serve for model verification and calibration, thereby enhancing the reliability and accuracy of simulations. Numerical simulations are often constrained by the setting of boundary conditions, the stress state of connected components, and assumptions about material parameters. Field measurement data provide a practical basis for these key parameters, helping to optimize models, correct errors, and improve the consistency of simulation results with real-world conditions. By incorporating field stress measurements, numerical simulations can compensate for shortcomings in boundary conditions and actual force states, providing reliable support for a more accurate evaluation of the structural behavior of tower cranes.

In this study, a 40 m-high flat-arm tower crane was selected as the research object, and real-time stress data of key components under typical working conditions were obtained through on-site stress monitoring. The actual stress state of the tower crane was accurately determined, and the natural frequency of the structure was identified through power spectral density analysis. Using an orthogonal experimental design, the effects of structural parameters such as lifting position, rope length, and lifting weight on the tower crane's stress were systematically analyzed. In this study, the orthogonal test and stress spectrum analysis were innovatively combined for the first time to reveal the mechanism of the multi-parameter coupling effect's influence on the stress of the tower crane. This approach fills the gap in the stress analysis of flat-arm tower cranes under the interaction of multiple parameters. The findings provide a theoretical basis for the structural design and safety assessment of flat-arm tower cranes, offering significant guidance for engineering practice and contributing to improved operational safety and structural reliability.

2. Research Methodology

2.1. Project Overview and Test Arrangement

The object of the measurement is a flat-top tower crane in operation during the development of the Central Plains Digital Industrial Park (West Park) project. The project is located in the industrial park area of Zhongmu County, Zhengzhou City, between the southern auxiliary road of Jinshui Avenue and the northern side of Fugui Third Road. A tower crane located at the edge of the site, which is convenient for measurement operations, was selected as the test object for this experiment. The tower crane being tested is shown in Figure 1, and Table 1 presents the main performance parameters of the crane.

Due to the complex structure of the tower crane and the harsh working environment, there are many factors affecting its structural stress. In order to systematically study the stress distribution law of tower cranes, three key structural parameters of lifting position (A), rope length (B), and lifting weight (C) are selected as the analysis objects. Among these factors, the lifting position has a significant impact on the bending moment distribution and stress concentration of the tower crane. Different lifting positions alter the structural force distribution, thereby affecting the overall stability and safety of the tower crane. The rope length is a key factor in determining the dynamic response and stress distribution of the tower crane. Particularly during the lifting process, it directly influences the load swing characteristics and system stability, thereby altering the stress state of the tower crane. As the primary external load of the tower crane structure, lifting weight is a key factor influencing stress distribution. Different load levels can cause significant variations in internal forces, thereby profoundly affecting the safety and durability of the tower crane.

Figure 1. The tower crane of the test site.

Table 1. Main performance parameters of tower crane.

Parameter	Value	Parameter	Value
Operating range (m)	2.5~65	Independent working height (m)	46
Maximum lifting weight (kg)	1.00×10^4	Measured tower crane height (m)	40
Balance weight (kg)	1.86×10^4	Rated lifting moment (kN·m)	1600
Lift arm length (m)	66.8	Maximum lifting moment (kN·m)	1920
Balance arm length (m)	15.5	Lifting speed ($\text{m}\cdot\text{min}^{-1}$)	0~95

Each factor is set at three levels to comprehensively cover typical operating conditions in real-world engineering. The lifting position is set at 63 m (far from the tower), 36 m (mid-range), and 2 m (near the tower), representing the tower crane's maximum, medium, and minimum working radii. These positions reflect the structural response under extreme, typical, and light load conditions. The rope length is set at 29 m, 20 m, and 10 m, representing the tower crane's maximum, medium, and short rope lengths, respectively. This setup is used to study the effects of different swing amplitudes and dynamic responses on structural stresses. The lifting weights are set at 520 kg, 750 kg, and 1300 kg, representing light, medium, and near-rated load conditions, respectively, to analyze the structural response under different stress states. Table 2 lists the specific impact factors and their levels. The selection of these parameters is based on the typical working conditions of the tower crane in actual construction. It covers a range of scenarios, from light to heavy loads, short to long lifting ropes, and positions close to or far from the tower body. This ensures that the test results comprehensively reflect the structural response characteristics of the tower crane under different conditions, providing a reliable basis for its optimal design and safety evaluation.

Table 2. The factors and levels based on orthogonal design.

Level	Factors		
	Lifting Position (m)	Rope Length (m)	Lifting Weight (kg)
1	63	29	520
2	36	20	750
3	2	10	1300

An orthogonal experimental method [27] was employed for the on-site measurements. Following the principle of orthogonality, nine representative working conditions were selected from all possible combinations using the L9(3^4) orthogonal table. Here, '9' represents the number of trials, '3' denotes the three levels for each factor, and '4' signifies the maximum number of factors that can be examined. This design minimizes factor interactions, enabling a clear analysis of each factor's individual effect on the structural response. By using the orthogonal table, the number of test conditions was reduced from 27 to 9, allowing for a comprehensive investigation of the influence of various factors and their interactions on tower crane structural stress with significantly improved test efficiency. The details of each condition are shown in Table 3. The specific position diagram of the working conditions is shown in Figure 2. The orthogonal experimental method achieved an efficient, rapid, and cost-effective experimental design. This approach ensures a balanced combination of all test factors while significantly reducing the number of tests, yielding the most representative experimental results.

Table 3. Measured working conditions table.

No.	Lifting Position (m)	Rope Length (m)	Lifting Weight (kg)
C1	63	29	520
C2	36	20	520
C3	2	10	520
C4	2	20	750
C5	36	29	750
C6	63	10	750
C7	63	20	1300
C8	36	10	1300
C9	2	29	1300

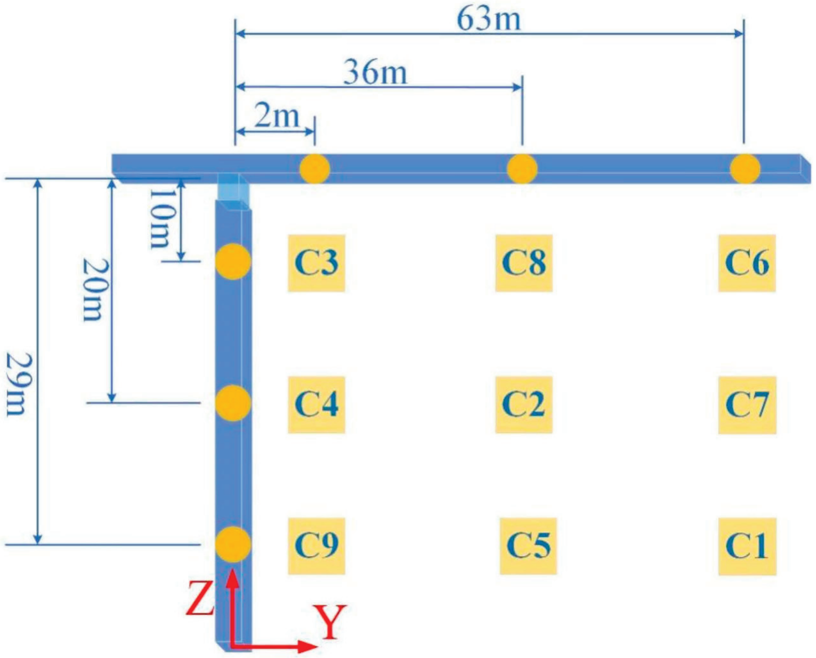

Figure 2. The specific position diagram of the working conditions.

2.2. Testing Instruments and Measurement Point Arrangements

This study employed a passive monitoring method, where strain measurements of the tower crane under actual working conditions were recorded using the DH5902N (Donghua

Testing Technology Co., Ltd., Taizhou, China) data acquisition and analysis system. No external excitations, such as impact hammers or vibrators, were applied. This method effectively captures the stress response under various working conditions and provides reliable data support for evaluating the performance of tower crane structures. The field test instrument mainly includes strain gauges, dynamic signal test and analysis systems, etc., and the signal acquisition instrument is the DH5902N rugged data acquisition and analysis system (see Figure 3). This device supports intelligent wire recognition and can connect to various sensors, enabling the testing and analysis of multiple physical parameters. It is capable of real-time data collection, transmission, storage, display, and analysis in harsh environments with strong vibrations and extreme temperatures, allowing it to perform long-term monitoring tasks. The resistance strain gauge adopts a foil-type uniaxial strain gauge, which has the characteristics of good flexibility, easy pasting, and stable performance. Its substrate material type is phenolic-acetal, and the substrate size is 10.1 mm × 4.0 mm in length × width. The dimensions of the sensitive grid are 5.0 mm × 2.0 mm in length × width. The lead material is PVC lead; the exposed diameter of the inner core is 0.09 mm, and the outer diameter of the lead is 0.9 mm. The resistance value of the strain gauge is 119.8 ± 0.1 Ω, the sensitivity coefficient is 2.20 ± 1%, and the operating temperature range is −30~80 °C.

Figure 3. Field test instrument.

Based on the actual on-site conditions, considering the structural characteristics of the flat-top tower crane and the experiment's operational difficulties, the root of the tower body and the root of the jib were selected as the stress measurement locations. The specific arrangement of the measurement points is as follows: (1) Four strain gauges were attached around the cross-section at the root of the tower body, with the measurement points numbered A-1 to A-4. (2) One strain gauge was attached along the axial direction of the primary material at the root of the jib, with the measurement point numbered B-1. Figure 4 shows the schematic diagram of the measurement point layout for the on-site tower crane. During the on-site testing, the X-axis was set perpendicular to the jib direction, the Y-axis was aligned along the jib direction, and the Z-axis was oriented vertically. The experiment's field sampling is shown in Figure 5.

During the on-site measurements, the weather conditions were clear, with temperatures ranging from 26 °C to 35 °C and an average of approximately 30 °C. The wind, predominantly from the southeast at level 2, persisted throughout the day and night, with a relative humidity of 66%. Wind speed data were recorded in real-time using the anemometer mounted on the control panel inside the operator's cabin. Under various working conditions, the measured wind speed at the top of the tower crane ranged from a minimum of 0.3 m/s to a maximum of 2.4 m/s.

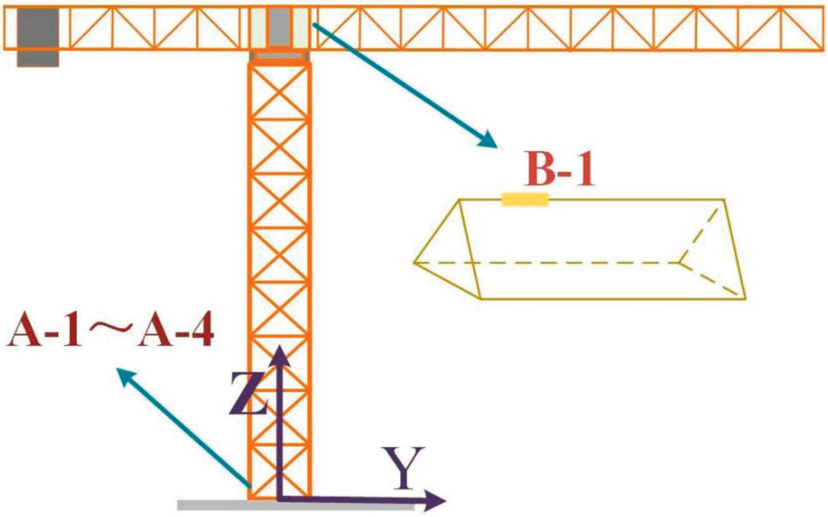

Figure 4. Layout of the measurement point at the site.

(**a**) Sampling at the root of the jib.

(**b**) Sampling at the base of the tower body.

Figure 5. Diagram of sampling at the experimental site.

3. Results

During the on-site testing, strain gauges were attached at the root of the tower body and the root of the jib. The sampling frequency for the measurement points was set to 50 Hz, and typical working conditions were selected for preliminary testing and analysis. Several short segments of signals were collected, and it was observed that all channels could effectively capture the measured signals. The selected range was appropriate, and the data were complete and reliable. During the formal testing, when the tower crane was in different working states, data collection of strain signals at each measurement point began when the crane reached the predetermined position and was stable.

During field sampling, to ensure data adequacy and representativeness, each sampling session was set to 600 s (10 min). Strain signals at various measurement points were recorded under different working conditions according to the on-site measurement layout. In total, 45 sets of strain data were collected during the field test. Figure 6 presents the strain history at A-1 and A-2, located at the root of the tower, under working condition C2. Due to the impact of the construction environment, the measured strain signals contained noise and irrelevant signals. Therefore, low-pass filtering was applied to the measured signals in MATLAB R2021b (Version 9.11) to improve the data's signal-to-noise ratio.

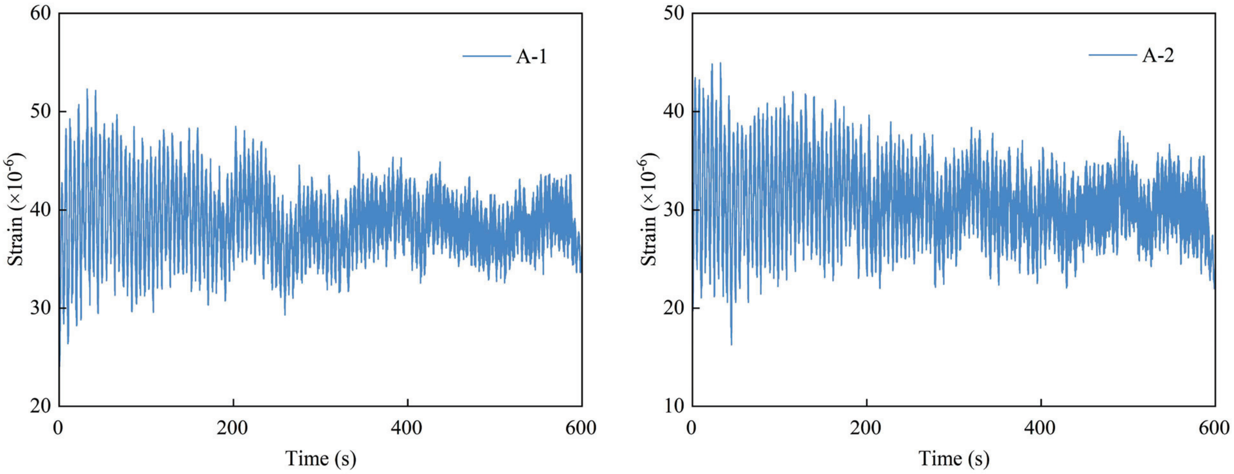

(**a**) A-1 position.

(**b**) A-2 position.

Figure 6. Strains at A-1 and A-2 under case C2.

3.1. Stress Measurement Results

During the on-site measurements, strain gauges were attached when the tower crane was unloaded (with no lifting load). The measured stress represents the additional stress relative to the initial balanced state of the tower crane. While the tower crane was in operation, all parts underwent elastic deformation. Based on Hooke's Law, the filtered strain time history was converted into a stress time-history, resulting in the stress values at each measurement point under different working conditions. Due to the large number of measurement points, only the stress identification results for a subset of the measurement points are provided in the paper. Table 4 presents the measured results of the stress mean (μ) and stress standard deviation (σ) for selected measurement points at the root of the tower body and the root of the jib.

Table 4. Stress identification results of measuring points under different working conditions.

No.	The Root of the Tower Body (MPa)						The Root of the Jib (MPa)	
	A-1		A-2		A-3		B-1	
	μ	σ	μ	σ	μ	σ	μ	σ
C1	−8.284	0.714	−7.807	0.713	6.885	0.784	−0.260	0.367
C2	8.106	0.658	6.427	0.614	−9.935	0.781	−3.123	0.331
C3	11.446	0.751	9.898	0.677	29.385	11.804	−1.901	0.225
C4	0.722	0.414	−1.183	0.491	1.427	0.510	−0.269	0.589
C5	3.347	0.587	2.459	0.639	−3.303	0.744	0.492	0.638
C6	23.384	1.465	−1.537	0.602	−3.733	0.754	0.387	0.366
C7	−2.909	1.298	−2.283	1.205	3.821	1.656	0.635	0.589
C8	25.988	1.566	22.065	1.358	−34.335	2.083	−5.656	0.455
C9	7.077	0.614	−2.907	0.734	3.427	0.637	0.255	0.664

Figure 7 shows the stress mean values at the measurement points under different working conditions. The maximum stress mean value under different working conditions occurs at various measurement points. Under C3 and C6, the stress values at the root of the tower body are significantly different, while the stress values under other working conditions show only minor differences. The stress mean values at the measurement points at the root of the tower body (A-1 to A-3) are all greater than the stress mean value at the measurement point at the root of the jib (B-1). The stress at the root of the jib is mainly caused by bending moments, while the stress at the root of the tower body is due to both bending moments and the additional stress caused by gravity. Under working condition C8, the maximum stress values at both the root of the tower body and the root of the jib occur. This is likely because, in condition C8, the lifting weight is the largest, and the rope length is the shortest. A longer rope can dampen the tower crane, reducing vibrations and stress. The nine working conditions were divided into three groups for comparison, each with consistent lifting weight. The working conditions with the shortest rope length in each group were C3, C6, and C8. The stress values under these conditions were higher than those in the other conditions within their respective groups.

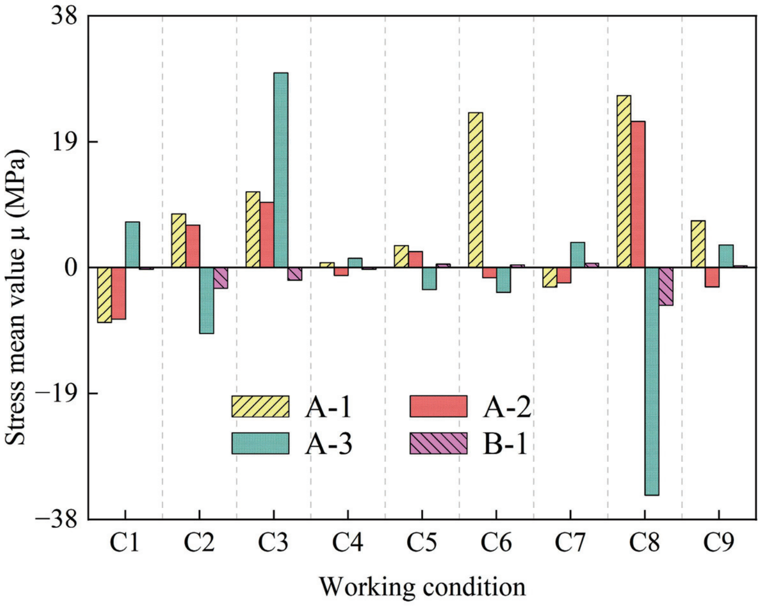

Figure 7. The mean stress μ at each measurement point under different working conditions.

3.2. Stress Response Spectrum

By conducting a power spectral density (PSD) analysis on the measured stress time-history signal, its frequency domain representation is obtained. The natural frequencies are identified from the prominent peaks in the PSD curve, which correspond to the primary vibration frequencies of the structure. Figure 8 shows the stress–power spectral density curves of the A-1 position under different working conditions, and the following conclusions can be drawn by combining the identification results of the first two natural frequencies of the tower crane in Table 5: Under working condition C5, the first-order frequency characteristics of the structure are not pronounced, but a significant peak is observed at 0.204 Hz. Under working conditions, C3, the first-order and second-order frequencies of the structure are 0.108 Hz and 0.148 Hz, respectively. In most cases (C1, C2, C4, C6, C7, C8, C9), the first- and second-order frequencies of the structure are stable at about 0.10 Hz and 0.20 Hz, respectively.

By comparing and analyzing the natural frequency results of tower cranes based on dynamic response recognition in the literature 28 (see Table 5), it is found that there is a large deviation in the first-order frequency recognition results under working conditions C1 and C2, but the error of the second-order frequency recognition results is controlled within 0.5%. Under other working conditions, the error of the natural frequency recognition result does not exceed 5%. (error calculation formula: error = (recognition result of this paper − recognition result of the literature 28)/recognition result of the literature 28 × 100%).

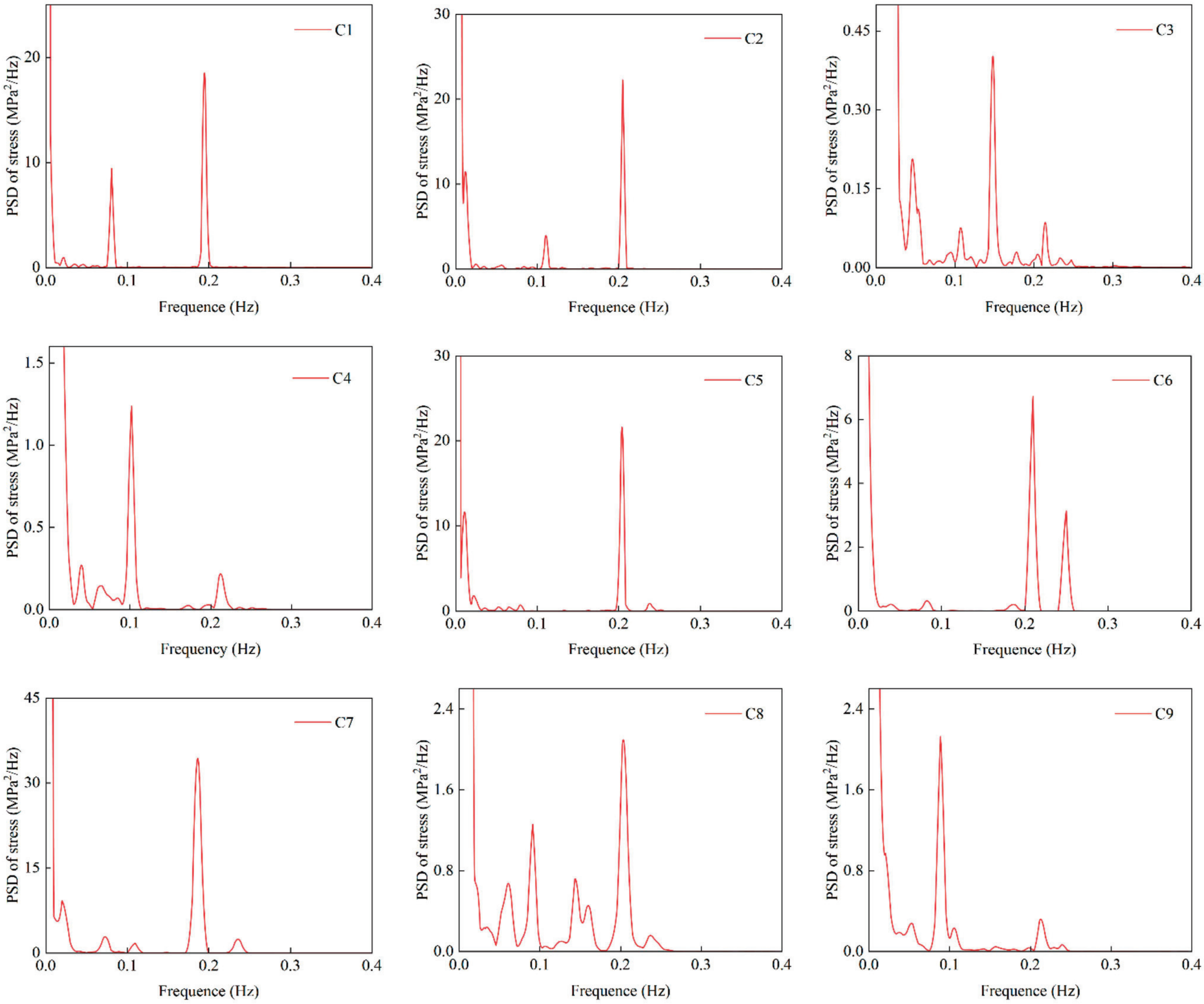

Figure 8. PSD of stress response at A-1 under different working conditions.

Table 5. Comparison of natural frequency identification results of tower cranes under different working conditions.

No.	Natural Frequency Results in This Document/Hz		Natural Frequency Results/Hz [28]		Error/%	
	First Order	Second Order	First Order	Second Order	First Order	Second Order
C1	0.081	0.194	0.114	0.195	−28.95	−0.51
C2	0.110	0.205	0.124	0.205	−11.29	0
C3	0.108	0.148	0.107	0.147	0.93	0.68
C4	0.102	0.214	0.107	0.206	−4.67	3.88
C5	/	0.204	0.110	0.204	/	0
C6	0.083	0.210	0.085	0.209	−2.35	0.48
C7	0.073	0.187	0.073	0.186	0	0.54
C8	0.091	0.202	0.091	0.205	0	−1.46
C9	0.089	0.213	0.088	0.212	1.14	0.47

In summary, the natural frequency recognition results based on velocity response in [28] are in good agreement with the research in this paper. It is further confirmed that under suitable working conditions, the natural frequency of the tower crane can be accurately identified through the power spectral density analysis of the stress response of the tower crane root. This discovery provides a new technical approach for the field test of the structural dynamic characteristics of tower cranes and has important engineering application value for the safety assessment and health monitoring of tower cranes.

3.3. Orthogonal Experimental Analysis of Stress

The orthogonal test method is an efficient and scientific multi-factor test design method that can comprehensively analyze the influence of various factors and their interactions in a small number of experiments through the rational arrangement of the orthogonal table. Its core advantages lie in efficiency, comprehensiveness, and scientificity. This method is widely used in engineering optimization and other fields [29–31] and is a powerful tool to solve multi-factor optimization problems. The orthogonal test method has significant advantages in identifying key parameters and optimizing structural design. However, it is based on the assumption that interactions between factors are negligible, which may not hold true under complex or wide-ranging load conditions. Orthogonal test methods struggle to effectively capture such complex behaviors. Therefore, caution should be exercised when applying orthogonal test methods in scenarios involving highly nonlinear loading conditions.

Considering the numerous measurement points on the tower crane, this paper selects the measurement points at the root of the tower (A-1, A-2) and the upper chord of the jib root (B-1) as representatives. The study focuses on the effects of lifting position (A), rope length (B), and lifting weight (C) on the structural stress of the tower crane. The measured stress mean values were used as the analysis indicators for the orthogonal experiment. By conducting range analysis and variance analysis on the experimental results, each factor's influence on the tower crane's structural stress and the significance level of each factor were determined, providing a reference for the following research phase.

3.3.1. Range Analysis

Table 6 shows the arrangement of the orthogonal experiment. Table 7 presents the results of the range analysis for the orthogonal experiment, where K_{i} (i = 1, 2, 3) represents the sum of the experimental results for the level of a given factor, with the mean value indicated, representing the range, reflecting each factor's influence on the response variable. Based on the range R, the influencing factors can be ranked. A larger R indicates that the variation of that factor has a more significant impact on the response variable, making the factor more critical [32]. In the analysis, only the main effects on the structural stress mean values were considered, while the interaction effects between the factors were ignored. As shown in Table 6, by comparing the corresponding mean values and ranges of each experimental factor, the influence of each factor on the structural stress can be determined. At point A-1, with $\mathrm{R_B} > \mathrm{R_A} > \mathrm{R_C}$, the primary order of impact on the stress mean values is as follows: rope length > lifting position > lifting weight. This indicates that rope length is the most crucial factor affecting the stress mean values. At points A-2 and B-1, with $\mathrm{R_A} > \mathrm{R_B} > \mathrm{R_C}$, the order of importance for the factors affecting the stress mean values is as follows: lifting position > rope length > lifting weight. This indicates that lifting position is the most critical factor influencing the stress mean values. Lifting weight has the least influence on the stress mean values at both the root of the tower body and the root of the jib.

Table 6. Orthogonal test analysis table.

No.	Lifting Position A	Rope Length B	Lifting Weight C	Mean Value of Stress (MPa)		
				A-1	A-2	B-1
C1	1	1	1	−8.284	−7.807	−0.260
C2	2	2	1	8.106	6.427	−3.123
C3	3	3	1	11.446	9.898	−1.901
C4	3	2	2	0.722	−1.183	−0.269
C5	2	1	2	3.347	2.459	0.492
C6	1	3	2	23.384	−1.537	0.387
C7	1	2	3	−2.909	−2.283	0.635
C8	2	3	3	25.988	22.065	−5.656
C9	3	1	3	7.077	−2.907	0.255

Table 7. Range analysis table.

Position	Parameter	Lifting Position A	Rope Length B	Lifting Weight C	Order of Importance
A-1	K_1	4.06	0.71	3.76	
	K_2	12.48	1.97	9.15	
	K_3	6.41	20.27	10.05	
	R	8.42	19.56	6.30	B > A > C
A-2	K_1	−3.88	−2.75	2.84	
	K_2	10.32	0.99	−0.09	
	K_3	1.94	10.14	5.63	
	R	14.19	12.89	5.71	A > B > C
B-1	K_1	0.25	0.16	−1.76	
	K_2	−2.76	−0.92	0.20	
	K_3	−0.64	−2.39	−1.59	
	R	3.02	2.55	1.96	A > B > C

3.3.2. Variance Analysis

Range analysis does not distinguish between experimental error effects and factor effects; it only reflects the relative importance of the factors influencing the experimental response. In contrast, variance analysis decomposes the sum of squares of deviations in the experimental data into the sum of squares for each factor's deviation and the sum of squares for experimental errors. By comparing the sum of squares of deviations for each factor with the sum of squares for experimental errors, the extent of each factor's influence on the response variable can be explained, and the significance of each factor's effect can be verified.

The results of the variance analysis for the factors affecting the structural stress of the tower crane are shown in Table 8. The F-value is used to measure the significance of the influence of the factor level change on the experimental index, and the larger the F-value, the more significant the influence of the factor on the experimental index. According to the F distribution table, $F_{0.10}(2,2) = 9.00$ and $F_{0.05}(2,2) = 19.00$. At A-1, $F_C < F_A < F_B < F_{0.05}(2,2) = 19.00$, and the influence of each factor on the structural stress is as follows: rope length > lifting position > lifting weight. At A-2 and B-1, $F_C < F_B < F_A < F_{0.05}(2,2) = 19.00$, and the influence of each factor on the structural stress is as follows: lifting position > length of lifting rope > lifting weight. This is consistent with the conclusion of the range analysis, which further verifies the reliability of the analysis. In addition, the influence of the lifting position, rope length, and lifting weight on the stress of the tower crane did not reach a significant level ($p > 0.05$), and there was no statistically significant difference.

Table 8. Results of Variance Analysis.

Position	Source	The Sum of Squared Deviations	Degrees of Freedom	F	*p*
A-1	A	113.157	2	0.878	0.533
	B	719.032	2	5.577	0.152
	C	69.557	2	0.539	0.650
	Error	128.938	2		
	R^2	0.875			
A-2	A	305.448	2	13.919	0.067
	B	264.038	2	12.032	0.077
	C	48.950	2	2.231	0.310
	Error	21.945	2		
	R^2	0.966			
B-1	A	14.406	2	2.824	0.262
	B	9.848	2	1.930	0.341
	C	7.101	2	1.392	0.418
	Error	5.101	2		
	R^2	0.860			

Analyze the proportion of the F-value of each measurement point: for the measurement point at the root of the tower, at A-1, the F-value of the length of the lifting rope accounts for the largest proportion, reaching 79.7%, indicating that it has the most significant influence on the structural stress. At A-2, the influence of the lifting position predominates, with an F-number of 49.4%. Lifting weight has the least effect on the root stress of the tower, and the F-value accounts for only 7.8%. For the measuring point B-1 at the root of the boom, the F-value of the lifting position accounted for the largest proportion, which was 46.0%; The impact of lifting weight was the smallest, and the F-number accounted for 22.7%.

In summary, the length of the lifting rope and the lifting position are the main factors affecting the structural stress of the flat arm tower crane, while the influence of the lifting weight is relatively weak. The results of this analysis provide an important theoretical basis for the optimization of structural lightweight and the selection of working conditions.

4. Conclusions

In this paper, a 40 m-high flat-arm tower crane is taken as the research object, and the real-time working stress of the crane under various typical working conditions is obtained through on-site stress measurements. Compared with theoretical analysis methods and numerical simulations, on-site measurements can directly reflect the mechanical characteristics of tower cranes in real operating environments. This approach avoids errors caused by model simplifications and parametric assumptions. Through actual measurements, we have clarified the stress state of key components of the flat-arm tower crane and accurately identified its natural frequencies. The effects of lifting position, rope length, and lifting weight on structural stress were systematically analyzed. The research results provide a reliable reference and basis for the health monitoring and safety assessment of tower crane structures. They have practical engineering value for ensuring the safety and durability of tower crane operations. The main conclusions of this study are as follows:

(1) Through real-time working stress tests, the stress distribution characteristics of key components of the flat-arm tower crane have been determined. It was found that the average stress at each measuring point at the root of the tower body is generally

higher than that at the root of the boom. Notably, the maximum stress value under different working conditions is not fixed at a specific measurement point but varies with the working conditions.

(2) The natural frequency of a structure is independent of the applied load. Based on the power spectral density analysis method, the natural frequency of the tower crane structure was successfully identified. The results show that the first-order natural frequency of the tower crane structure is approximately 0.10 Hz, while the second-order natural frequency is around 0.20 Hz under different working conditions. By analyzing the power spectral density curve of the stress response at the root of the tower crane, the natural frequency of the structure can be accurately determined. This not only verifies the feasibility of identifying the natural frequency of the structure through stress monitoring but also provides a reliable technical approach for the dynamic characteristics analysis and health monitoring of flat-arm tower cranes, offering significant engineering application value.

(3) Using the orthogonal test method, the influence of three key structural parameters—lifting position, rope length, and lifting weight—on the structural stress of the tower crane was systematically studied. The results indicate that the effects of these three factors on the structural stress of the tower crane are consistent, with no significant differences ($p > 0.05$). Through the analysis of F-value weights, it was found that the lifting position and the length of the lifting rope are the primary factors affecting the stress at the root of the tower crane and the root of the boom, while the influence of the lifting weight is relatively small. This conclusion provides an important basis for the optimization and safety assessment of tower cranes. In practical applications, it is essential to comprehensively consider the coupling effects of multiple parameters to achieve the efficient and safe operation of the tower crane structure.

This study was conducted on a specific tower crane. Due to differences in material properties, geometric configuration, boundary conditions, and working environments, the research findings are primarily applicable to the analyzed tower crane structure. However, the methods and findings presented in this paper provide a valuable reference for understanding the stress distribution and fatigue behavior of this type of tower crane. Caution should be exercised when generalizing these conclusions to tower cranes with different designs or operating conditions. For other types of tower cranes, further research is required to account for variations in structural characteristics, load scenarios, and environmental factors.

This study establishes a robust experimental foundation for the optimal design and safety evaluation of tower cranes. Future research should be extended to a broader range of tower crane types, systematically investigating their stability, modal characteristics, and dynamic response under complex working conditions through an integrated approach combining on-site measurements, theoretical analysis, and numerical simulation. By leveraging a multi-method collaborative analysis, the mechanical behavior of tower cranes can be assessed with greater accuracy, enabling the development of a more generalized theoretical framework and providing a solid foundation for engineering applications. Furthermore, future studies should emphasize the long-term structural health monitoring of tower cranes, systematically evaluating their fatigue performance and damage evolution. This would offer scientific guidance for ensuring their safe operation and extending their service life while enhancing their stability and reliability under complex environmental conditions.

Author Contributions: Conceptualization, H.Y., X.H. and W.A.; methodology, Q.Z. and Z.W.; investigation, Y.Y., Q.Z. and Y.X.; writing—original draft preparation, B.M., Q.Z. and H.Y.; writing—review and editing, B.M. and Q.Z. All authors have read and agreed to the published version of the manuscript.

Funding: Henan Province Science and Technology Research and Development Program Joint Fund (Applied Research Category) Project (242103810102); The Key Research Programs of Higher Education Institutions in Henan Province (24B560012); The Henan Province Science and Technology Research Projects (242102320046); China State Construction Engineering Corporation Scientific Research Project (CSCEC-2021-Q-63).

Data Availability Statement: The data presented in this study are available on request from the corresponding author.

Conflicts of Interest: Hui Yang was employed by the China Construction Third Engineering Bureau Group Co., Ltd. Wei An was employed by the POWER CHINA Henan Electric Power Engineering Co., Ltd. The remaining authors declare that the research was conducted in the absence of any commercial or financial relationships that could be construed as a potential conflict of interest.

References

1. Sadeghi, S.; Soltanmohammadlou, N.; Rahnamayiezekavat, P. A systematic review of scholarly works addressing crane safety requirements. *Saf. Sci.* **2021**, *133*, 105002. [CrossRef]
2. Jeong, I.; Hwang, J.; Kim, J.; Chi, S.; Hwang, B.; Kim, J. Vision-based productivity monitoring of tower crane operations during curtain wall installation using a database-free approach. *J. Comput. Civ. Eng.* **2023**, *37*, 04023015. [CrossRef]
3. Hu, S.; Fang, Y.; Moehler, R. Estimating and visualizing the exposure to tower crane operation hazards on construction sites. *Saf. Sci.* **2023**, *160*, 106044. [CrossRef]
4. Jiang, W.; Ding, L. Unsafe hoisting behavior recognition for tower crane based on transfer learning. *Autom. Constr.* **2024**, *160*, 105299. [CrossRef]
5. Chen, Y.; Zeng, Q.; Zheng, X.; Shao, B.; Jin, L. Safety supervision of tower crane operation on construction sites: An evolutionary game analysis. *Saf. Sci.* **2022**, *152*, 105578. [CrossRef]
6. Ali, A.; Zayed, T.; Wang, R.; Kit, M. Tower crane safety technologies: A synthesis of academic research and industry insights. *Autom. Constr.* **2024**, *163*, 105429. [CrossRef]
7. Zhang, J.; Huang, M.; Wan, N.; Deng, Z.; He, Z.; Luo, J. Missing measurement data recovery methods in structural health monitoring: The state, challenges and case study. *Measurement* **2024**, *231*, 114528. [CrossRef]
8. Deng, Z.; Huang, M.; Wan, N.; Zhang, J. The current development of structural health monitoring for bridges: A review. *Buildings* **2023**, *13*, 1360. [CrossRef]
9. Jiang, H.; Jiang, X. Fatigue life prediction for tower cranes under moving load. *J. Mech. Sci. Technol.* **2023**, *37*, 6461–6466. [CrossRef]
10. Yang, M.; Chang, Z.; Xu, G.; Wang, C.; Wang, P. Analysis on fatigue life of overhead travelling crane girder under impact load for sustainable transport system. *IET Intell. Transp. Syst.* **2020**, *14*, 1426–1432. [CrossRef]
11. Lehner, P.; Krejsa, M.; Parenica, P.; Krivy, V.; Brozovsky, J. Fatigue damage analysis of a riveted steel overhead crane support truss. *Int. J. Fatigue* **2019**, *128*, 105190. [CrossRef]
12. Li, Y.; Jin, A.; Dai, Y.; Yang, D.; Zheng, B.; Correia, J. Prediction of remaining fatigue life of in-service bridge cranes. *Appl. Sci.* **2023**, *13*, 12250. [CrossRef]
13. Dong, Q.; Yu, Y.; Xu, G. Fatigue residual life estimation of jib structure based on improved v-SVR algorithm obtaining equivalent load spectrum. *Fatigue Fract. Eng. Mater. Struct.* **2020**, *43*, 1083–1099. [CrossRef]
14. Jeongwoo, H.; Geun-Ho, L. Fatigue life prediction of the carrier of slewing reducer for tower crane. *J. Korean Soc. Manuf. Process Eng.* **2015**, *14*, 131–140. [CrossRef]
15. Hectors, K.; Chaudhuri, S.; De Waele, W. Fracture mechanics and hot spot stress-based fatigue life calculation: Case study for a crane runway girder. *Fatigue Fract. Eng. Mater. Struct.* **2022**, *45*, 2662–2675. [CrossRef]
16. Moskvichev, V.; Chaban, E. Analysis of propagation of fatigue cracks in crane girders. *Inorg. Mater.* **2019**, *55*, 1496–1502. [CrossRef]
17. He, Z.; Gao, M.; Liang, T.; Lu, Y.; Lai, X.; Pan, F. Tornado-affected safety assessment of tower cranes outer-attached to super high-rise buildings in construction. *J. Build. Eng.* **2022**, *51*, 104320. [CrossRef]
18. Lu, Y.; Gao, M.; Liang, T.; He, Z.; Feng, F.; Pan, F. Wind-induced vibration assessment of tower cranes attached to high-rise buildings under construction. *Autom. Constr.* **2022**, *135*, 104132. [CrossRef]
19. Chen, W.; Qin, X.; Yang, Z.; Zhang, P. Wind-induced tower crane vibration and safety evaluation. *J. Low Freq. Noise Vib. Act. Control.* **2020**, *39*, 297–312. [CrossRef]
20. Pástor, M.; Lengvarsky, P.; Hagara, M.; Kulka, J. Experimental investigation of the fatigue life of a bridge crane girder using S-N method. *Appl. Sci.* **2022**, *12*, 10319. [CrossRef]

21. Xi, Y.; Li, H.; Sun, L.; Wang, Z. Extreme load extrapolation and long-term fatigue assessment of offshore wind turbine tower based on monitoring data. *Ocean Eng.* **2024**, *300*, 117180. [CrossRef]
22. Park, Y.; Cho, S.; Han, J.; Shim, S. Fatigue life prediction of planet carrier in slewing reducer for tower crane based on model validation and field test. *Int. J. Precis. Eng. Manuf.* **2017**, *18*, 435–444. [CrossRef]
23. Liu, F.; Yang, J.; Wang, J.; Liu, P. Tower Crane Effect on the Vibration Response of Elastic Foundation. *Iran. J. Sci. Technol. Trans. Civ. Eng.* **2023**, *47*, 3839–3850. [CrossRef]
24. Xu, B.; Wu, Q. Stress fatigue crack propagation analysis of crane structure based on acoustic emission. *Eng. Fail. Anal.* **2020**, *109*, 104206. [CrossRef]
25. Li, Q.; Fan, W.; Huang, M.; Jin, H.; Zhang, H.; Ma, J. Machine learning-based prediction of dynamic responses of a tower crane under strong coastal winds. *J. Mar. Sci. Eng.* **2023**, *11*, 803. [CrossRef]
26. Wei, G.Q.; Yin, Q.Z.; Zhao, Y.; Dang, Z.; Lu, Z.W. Fatigue failure analysis and life prediction of wheel load local area of ladle crane. *Meas. Sci. Technol.* **2024**, *35*, 126120. [CrossRef]
27. Dai, S.; Wang, H.; An, S.; Yuan, L. Mechanical properties and microstructural characterization of metakaolin geopolymers based on orthogonal tests. *Materials* **2022**, *15*, 2957. [CrossRef]
28. Zhang, Q.; Wang, Z.; Yang, H.; Zhao, J.; Xu, Y. Field Test and Analysis of Influence Factors on the Dynamic Characteristics of Self-Supporting Flat Arm Tower Crane Under Multiple Working Conditions. *J. Vib. Eng.* **2024**, 1–9. Available online: http://kns.cnki.net/kcms/detail/32.1349.TB.20240829.1811.006.html (accessed on 20 February 2025). (In Chinese).
29. Chen, M.; Zhang, Z.; Deng, Q.; Feng, Y.; Wang, X. Optimization of underfloor air distribution systems for data centers based on orthogonal test method: A case study. *Build. Environ.* **2023**, *232*, 110071. [CrossRef]
30. Li, Y.; She, L.; Wen, L.; Zhang, Q. Sensitivity analysis of drilling parameters in rock rotary drilling process based on orthogonal test method. *Eng. Geol.* **2020**, *270*, 105576. [CrossRef]
31. Li, X.; Hao, J. Orthogonal test design for optimization of synthesis of super early strength anchoring material. *Constr. Build. Mater.* **2018**, *181*, 42–48. [CrossRef]
32. Xu, L.; Zhang, Y.; Zhang, Z.; Taylor, S.; Chen, M.; Wang, X. Experimental investigation on thermal performance of self-service cold storage cabinet based on the orthogonal test. *Appl. Therm. Eng.* **2024**, *242*, 122315. [CrossRef]

buildings

Article

Vehicle–Bridge Coupling of Road–Rail Dual-Use Network Arch Bridge Based on a Noniterative Approach: Parametric Analysis and Case Study

Haocheng Chang [1], Rujin Ma [1,*], Baixue Ge [2] and Qiuying Zhu [3]

[1] College of Civil Engineering, Tongji University, Shanghai 200092, China; changhc16@tongji.edu.cn
[2] College of Engineering, Sanda University, Shanghai 201209, China; baixuege@sandau.edu.cn
[3] Department of Logistics Management, Soochow University, Suzhou 215031, China; qying97@163.com
* Correspondence: rjma@tongji.edu.cn

Abstract: In the realm of road–rail dual-use bridges, conducting accurate vehicle–bridge coupling analysis is crucial, as the combined effects of road traffic and rail transit induce complex dynamic challenges. This study investigates a road–rail dual-use network arch bridge, highlighting the dynamic effects induced by light rail loadings. By employing a noniterative vehicle–bridge coupling analysis method, the dynamic responses of hangers caused by vehicular and light rail loads are effectively captured. Additionally, this study explores the influence of various parameters, including vehicle types, driving lanes, and road surface roughness on the responses of hangers positioned at different locations along the bridge. The findings reveal that light rail induces significantly larger dynamic effects compared to motor vehicles. When the light rail operates closer to the hanger, the responses of hangers are more pronounced. Furthermore, different road surface roughness level notably affects the amplitude of axial stress and bending moment fluctuations. Poorer road conditions amplify these dynamic effects, leading to increased stress variations. These insights underscore the necessity of integrating considerations for both road and rail traffic in the structural analysis and design of network arch bridges to ensure their reliability and serviceability.

Keywords: vehicle–bridge coupling; light rail; vehicles; hangers; parametric analysis

1. Introduction

Road–rail dual-use bridges [1,2], which accommodate both vehicular and rail traffic, are increasingly important in regions with high-density transportation networks. These bridges not only optimize space and reduce construction costs but also enhance connectivity in urban and intercity transit systems. However, the coexistence of road and rail traffic creates significant structural challenges, as these dual-use bridges must withstand the dynamic loads from both vehicle and train movements. This interaction, referred to as Vehicle–Bridge Coupling (VBC), is crucial for the design, analysis, and maintenance of road–rail dual-use bridges [3–5]. The complexity of VBC necessitates precise and comprehensive studies to ensure the safety, durability, and performance of such infrastructure throughout its service life [6,7].

VBC refers to the dynamic interaction between moving loads (vehicles and trains) and the structural response of the bridge [8,9]. The complexity of this interaction in road–rail dual-use bridges arises from the differing dynamic characteristics of road vehicles and rail systems. Road vehicles, particularly heavy trucks, induce significant vertical

https://doi.org/10.3390/buildings15050801

displacements and stresses on bridge components [10], while light rail or trains generate additional longitudinal forces, vibrations, and bending moments [11–13]. These dynamic effects can lead to fatigue damage, increased maintenance needs, and, in extreme cases, structural failure if not adequately addressed in the design and analysis stages.

The study of train-bridge coupling vibrations began in 1849 after the vehicle-induced vibration incident on the Chester railway bridge. Frýba, based on a unified system model of vehicles and bridges, derived the analytical solution for bridges with different vehicle models passing over a simply supported beam [14], and conducted a parametric analysis of the impact of vehicle and bridge parameters, track irregularities, and other factors on the vehicle–bridge system [15]. Wang et al. [16,17] proposed a 19-degree-of-freedom and a 23-degree-of-freedom train model considering nonlinear coupling and studied the impact of trains on bridges at different speeds. Diana and Cheli [18] systematically studied the dynamic characteristics of trains traveling on large-span deformable bridges.

Compared to railway loads, the load from road vehicles is smaller, and early vehicle–bridge coupling vibrations were not significant. However, with the construction of large-span bridges, the main spans of newly built bridges have become more flexible, and the issue of vehicle–bridge coupling vibrations has gradually gained attention. Azimi et al. [19] proposed a method using a Vehicle–bridge Interaction (VBI) element to simulate the contact between the vehicle and the bridge. Ju et al. [20] used moving wheel elements, spring-damping elements, concentrated masses, and rigid connections to simulate complex vehicle models. Many scholars have conducted extensive parametric analyses of the vehicle–bridge system [21,22]. Studies [23,24] also provide valuable insights into the coupling mechanisms between road and rail traffic and offer novel perspectives on bridge safety and longevity.

Recent studies [25,26] have shown that the interaction between these two types of traffic can lead to complex dynamic effects, particularly in critical components such as hangers in network arch bridges [27]. The dynamic forces caused by light rail vehicles, for example, tend to be more severe than those generated by motor vehicles, especially when the rail operates close to structural components such as hangers. These forces, when coupled with uneven road surfaces [19,28,29], further complicate the bridge's response, resulting in increased axial stresses and bending moments in main elements.

The study of vehicle–bridge coupling analysis has garnered considerable attentions, particularly with the increasing demand for resilient and multi-functional infrastructure [30,31]. Various methods have been employed to model and analyze the dynamic effects of mixed traffic on bridges. Traditional VBC analyses often rely on iterative methods, which, though accurate, are computationally expensive and time-consuming, especially for large structures like road–rail dual-use network arch bridges [32,33]. While finite element analysis (FEA) has been used to model vehicle–bridge interaction [34], earlier models were often limited in their ability to simultaneously account for the coupled dynamic effects of both road and rail traffic. Recent approaches [35–37] have leveraged sophisticated computational tools, such as ANSYS (v2021) and MATLAB (v2017), to better simulate real-world conditions, including varying vehicle speeds, road roughness, and dynamic forces from light rail.

Building upon these developments, this study focuses on a non-iterative approach to VBC, offering a more efficient alternative to traditional methods. The study uses the Qilu Yellow River Bridge, one of the world's longest network arch bridges, as a case study. It explores how various factors, such as vehicle types, lane positions, and road surface roughness, influence the dynamic responses of critical bridge components, particularly hangers. This approach incorporates both road and rail traffic, which adds a unique dynamic component to the system, highlighting the complexity of the interaction between these two traffic modes and its impact on the bridge's structural performance.

The main contributions of this study are as follows:

- A detailed case study of the Qilu Yellow River Bridge, one of the world's longest network arch bridges, providing valuable insights into the dynamic behavior of such structures.
- A comprehensive investigation of how different vehicle types (including heavy vehicles and light rail) and lane positions influence the dynamic response of critical bridge components, especially hangers.
- An evaluation of the impact of road surface roughness on the axial stresses and bending moments in the hangers under real traffic conditions.
- A deeper understanding of the combined dynamic effects of road traffic and light rail transit on the structural performance of the bridge.

2. Noniterative Method for Vehicle–Bridge Coupling

The simplified noniterative method for vehicle–bridge coupling proposed in the former work [27] is used here, in which the velocity terms in both the vehicle model and surface model are omitted.

The general dynamic equilibrium equation (vibration equation) for a vehicle or bridge [38,39] is:

$$\boldsymbol{M}\ddot{\boldsymbol{z}} + \boldsymbol{C}\dot{\boldsymbol{z}} + \boldsymbol{K}\boldsymbol{z} = \boldsymbol{F}, \tag{1}$$

where $\boldsymbol{M}$ is the mass of the vehicle. $\boldsymbol{C}$ is the damping. $\boldsymbol{K}$ stands for the stiffness matrices. $\ddot{\boldsymbol{z}}$, $\dot{\boldsymbol{z}}$, $\boldsymbol{z}$ and are the acceleration, velocity and displacement, respectively. $\boldsymbol{F}$ is the external force vector.

For a two-axle vehicle model of seven degrees of freedom without considering the velocity terms, the force $\boldsymbol{F_v}$ can be written as:

$$\boldsymbol{F_v} = \{0, 0, 0, k_{w1}z_{g1}, k_{w2}z_{g2}, k_{w3}z_{g3}, k_{w4}z_{g4}\}, \tag{2}$$

where k_{wi} is the stiffness coefficient of wheel i (i = 1, 2, 3, 4). The forced displacement exerted on wheel i, due to the road's influence, is denoted as z_{gi}.

In this work, a two-axle multi-degree-of-freedom light-rail-vehicle model to simulate the train. The model is more representative of real vehicles. In the multi-degree-of-freedom vehicle model, the vehicle body is not treated as a mass unit but as a rigid body unit. A pair of wheels is treated as a mass unit, connected by springs and dampers. The bogie is modeled as a rigid unit, connected to the vehicle body and wheelsets by springs and dampers. By considering the effect of the bogie, this model is closer to the actual light-rail vehicle. The train prototype is an A-type vehicle with a 6-carriage configuration.

For a two-axle multi-degree-of-freedom light-rail-vehicle model (see Figure 1) without considering the velocity terms, the force $\boldsymbol{F_{vt}}$ can be written as:

$$\boldsymbol{F_{vt}} = \{0, 0, 0, k_{w1}z_{g1}, k_{w2}z_{g2}, k_{w3}z_{g3}, k_{w4}z_{g4}, k_{w5}z_{g5}, k_{w6}z_{g6}\}, \tag{3}$$

where k_{wi} is the stiffness coefficient of wheel i (i = 1, 2, 3, 4, 5, 6). The forced displacement exerted on wheel i, due to the road's influence, is denoted as z_{gi}, which can be computed as the sum of road roughness or track irregularity $r(x_i)$ and the instantaneous displacement z_{xi} of the bridge at the wheel i:

$$z_{gi} = r(x_i) + z_{xi}. \tag{4}$$

It should be noted that the load from the light-rail vehicle includes multiple types, such as vertical load, lateral load, and hunting load. Vertical load refers to the load in the vertical direction generated by the vehicle's weight and the interaction between the vehicle and the bridge, typically related to the vehicle's gravity. Lateral load refers to the lateral forces generated by a vehicle during motion, typically caused by its sideway movement or contact with the track. This load affects the bridge's lateral stability. Hunting load refers to the dynamic loads generated by the vehicle's oscillatory movement or "hunting" phenomenon. The hunting effect usually occurs when the track is uneven or when the vehicle speed is high, causing the vehicle to oscillate laterally, resulting in additional lateral dynamic loads. In this study, only the vertical load of the train is considered in its impact on the bridge.

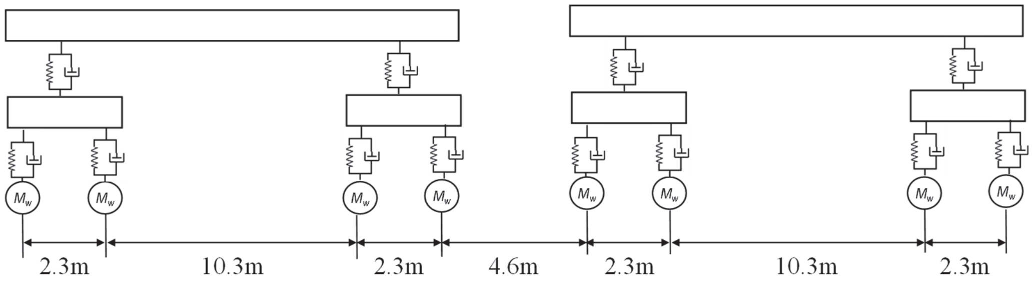

Figure 1. Illustration of the light-rail-vehicle model.

For a bridge, the damping matrix $\boldsymbol{C_b}$ is typically computed using Rayleigh damping theory. This model characterizes the damping properties of a system in structural dynamics. According to Rayleigh damping theory, $\boldsymbol{C_b}$ is computed as [40]:

$$\boldsymbol{C_b} = \boldsymbol{\alpha M_b} + \boldsymbol{\beta K_b}, \tag{5}$$

where $\boldsymbol{\alpha}$ and $\boldsymbol{\beta}$ are the Rayleigh damping coefficients. These coefficients are derived from experimental data or the system's physical properties. They are calculated using the mode-damping ratio:

$$\boldsymbol{\alpha} = \frac{2\omega_i\omega_j(\zeta_i\omega_j - \zeta_j\omega_i)}{\omega_j^2 - \omega_i^2}, \tag{6}$$

$$\boldsymbol{\beta} = \frac{2(\zeta_j\omega_j - \zeta_i\omega_i)}{\omega_j^2 - \omega_i^2}, \tag{7}$$

where ω_i and ω_j are the natural frequencies of vibration for the ith and jth modes, respectively. The damping ratios ζ_i and ζ_j correspond to these modes, based on empirical data.

The surface model is primarily composed of the road surface roughness model and the track irregularity model. Road surface roughness is typically modeled as a zero-mean stationary Gaussian random process. The distribution function corresponding to road surface roughness is formulated as:

$$S(\omega_k) = \begin{cases} \overline{\alpha} \cdot {\omega_k}^{\beta},\ \omega_l < \omega_k < \omega_u \\ 0,\ \text{others} \end{cases}, \tag{8}$$

where $S(\omega_k)$ represents the power spectral density function of road surface roughness, while β denotes the frequency index, typically set to 1.94. Here, ω_k refers to the spatial frequency, with ω_l and ω_u being the lower and upper spatial frequency limits, respectively. The coefficient $\overline{\alpha}$ characterizes the road surface roughness and can be categorized into five levels, ranging from excellent (A) to very poor (E). Further details regarding these classifications are provided in ref. [27].

Inverse Fourier transform can be used to obtain the road surface roughness as:

$$r(x) = \sum_{k=1}^{N} 2\sqrt{S(\omega_k)\Delta\omega}\cdot\cos(2\pi\omega_k x + \phi_k), \tag{9}$$

$$\omega_k = \omega_l + (k - 1/2)\,\Delta\omega, \tag{10}$$

$$\Delta\omega = (\omega_u - \omega_l)/N, \tag{11}$$

where ϕ_k represents the random phase angle within the interval $[0, 2\pi]$; x is the longitudinal coordinate; N corresponds to the number of terms in the trigonometric series.

The track irregularity is quantified as:

$$S_v(\Omega) = \frac{A_v \times \Omega_c^2}{(\Omega^2 + \Omega_r^2)(\Omega^2 + \Omega_c^2)}, \tag{12}$$

in which Ω is the spatial frequency of track irregularities. Detailed descriptions of Ω_c, Ω_r and A_v can be found in ref. [27]. The validation of the noniterative method is provided in ref. [27], where it was demonstrated that the results from this method align well with those obtained using traditional iterative methods and experimental data. The noniterative method has no restrictions on the FEM, making it applicable to a wide variety of bridge types. Additionally, it improves efficiency by eliminating the need for iterative processes, although it tends to be slightly conservative. In summary, the noniterative method offers high transferability, enhanced efficiency, and accuracy, making it well-suited for analyzing the impact of various parameters, including vehicle types, driving lanes, and road surface roughness, on the responses of hangers at different locations along the Qilu Yellow River Bridge in this study.

3. Application to a Road–Rail Dual-Use Network Arch Bridge

The present study focuses on the Qilu Yellow River Bridge, a major infrastructure located in Jinan City, Shandong Province, extending a total length of 6742 m. Figure 2 shows the elevation layout of the Qilu Yellow River Bridge. This bridge is an exemplary network-tied arch design, featuring a main span of 420 m, positioning it among the longest of its kind globally. Notably, the bridge is engineered as a dual-purpose road–rail structure, accommodating both vehicular traffic and urban rail transit, configured with two-way, eight-lane provisions. The network arch design is supported by 88 hangers, critical components for maintaining structural integrity under dynamic loads. The main beam is made of Q345qE steel. The arches are made of Q420qE steel, and the hangers consist of high-stress epoxy-coated steel strands. The main properties of the steel materials are shown In Table 1. In the subsequent analysis, the steel material remains in an elastic state.

Table 1. Properties of steel.

Part	Main Beam	Arch	Hangers
Steel type	Q345qE	Q420qE	Steel strand
Elastic modulus (Mpa)	206,000	20,6000	200,000
Shear modulus (Mpa)	79,000	79,000	--
Poisson’s ratio	0.31	0.31	--
Design value of tensile/compressive/bending strength (Mpa)	275	335	1005
Standard value of tensile strength (Mpa)	--	--	1860
Design value of shear strength (Mpa)	160	160	--
Coefficient of thermal expansion (°C)	0.000012	0.000012	0.000012

To facilitate a comprehensive vehicle–bridge coupling analysis, three strategically located hangers—designated as A, B, and C (see Figure 2)—have been selected. These hangers are positioned at key points along the bridge: near the support, at the quarter, and at the midspan, respectively. Given the dual-use nature of this bridge, detailed vehicle–bridge coupling analysis is imperative for understanding the coupled dynamic behavior and ensuring the bridge's long-term serviceability under mixed traffic conditions.

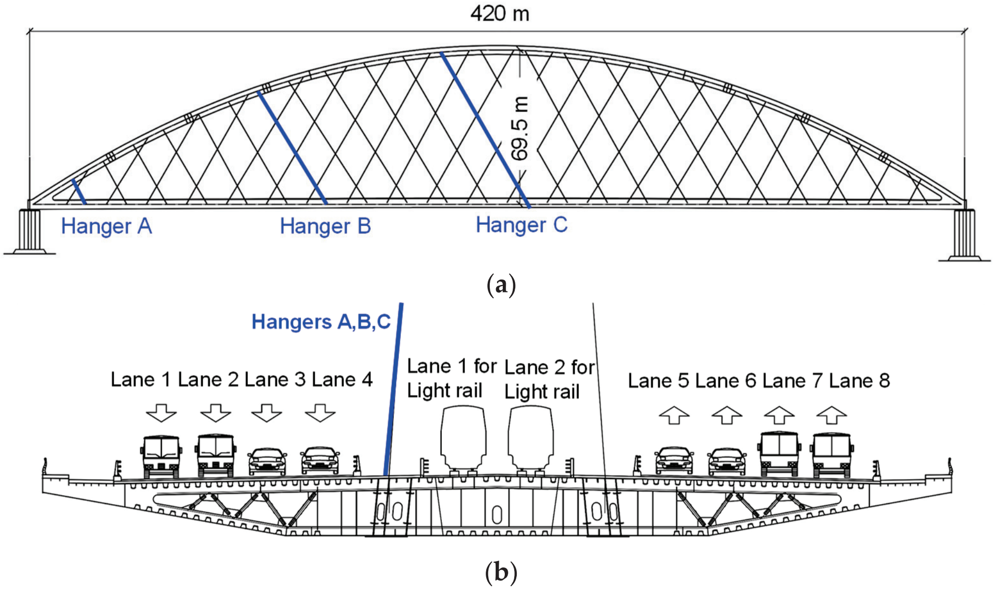

Figure 2. (**a**) Elevation layout of the Qilu Yellow River Bridge; (**b**) lane layout of the main span. Note: Reprinted with permission from ref. [27], 2024, Elsevier.

The finite element model (FEM) of the bridge was constructed using ANSYS (v19.0) software. The primary components, including the main arch, girder, and hangers, were modeled using Beam4 elements. For the girder, a fishbone beam method was employed, where rigid elements represented the two inner lanes, with nodes precisely located at the lane centers to apply vehicle loads. To account for the mass and rotational inertia of the bridge deck, mass21 elements were utilized, concentrating these properties along the bridge's centerline. According to the design schematics, constraints were enforced at the base of the arch ribs. Figure 3 illustrates the FEM and the corresponding boundary conditions in detail. In addition to self-weight, the dead load includes pavement, railings, pipelines, and other components, totaling 223 kN/m. Under the basic combination of loads shortly after the completion of the bridge, the steel structure of the 420m-span main girder is primarily subjected to tension. The maximum tensile stress at the bottom edge is 232.6 MPa, while the maximum tensile stress at the top edge is 173.9 Mpa.

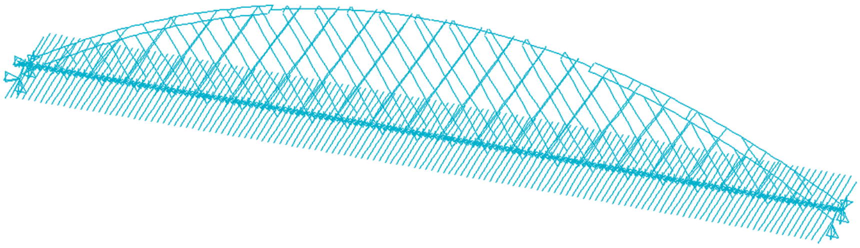

Figure 3. Finite element model and boundary conditions of the Qilu Yellow River Bridge.

The process for applying the prestressing force to the hangers is as follows. First, we create an initial model of the bridge and perform a static analysis to obtain the bridge profile. If the profile differs from the actual/design profile, we adjust the stresses in the hangers and rerun the static analysis. This procedure is repeated until the obtained bridge profile matches the actual profile and the final stresses in the hangers correspond to the initial locked-in stresses. The axial forces in the hanger rods under dead load are shown in Figure 4. The distribution of dead load axial forces in the hanger rods is relatively uniform, with the maximum axial force in the hanger rods of the 420 m-span tied-arch bridge reaching 3548.1 kN. Furthermore, it should be noted that the initial axial stresses of hangers A, B, and C are 515.73 Mpa, 378.24 Mpa, and 394.49 Mpa, respectively.

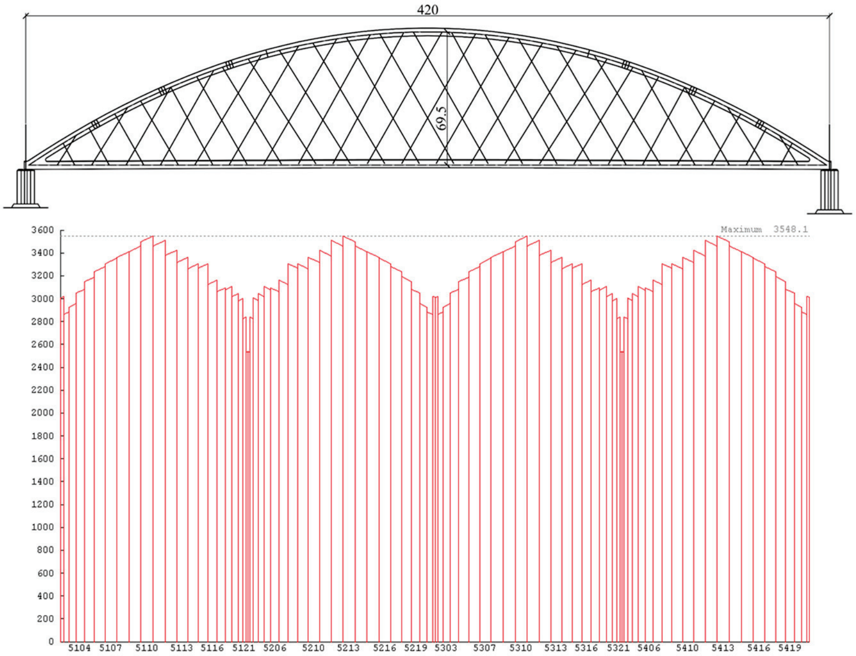

Figure 4. The axial forces in the hanger rods under dead load.

The main parameters of the four motor vehicle types can be found in ref. [41]. The parameters of train prototype (an A-type vehicle with a 6-carriage configuration in Figure 1) are shown in Table 2.

Table 2. Parameters of train.

Parameter	Value
Car body mass (ton)	39.5
Bogie mass (ton)	2.2
Wheelset mass (ton)	1.9
Primary Suspension Vertical Stiffness (kN/m)	1746
Secondary Suspension Vertical Stiffness (kN/m)	820
Primary Suspension Vertical Damping (kN·s/m)	60
Secondary Suspension Vertical Damping (kN·s/m)	217.4
Wheel Radius (m)	0.42

The flowchart of the noniterative method for vehicle–bridge coupling is depicted in Figure 5. The methodology proceeds as follows. (1) Generate road surface roughness samples using MATLAB (v2020), and combine them with the longitudinal slope of the bridge to obtain the variations in the bridge deck profile along the vehicle's travel path. The longitudinal slope of the bridge is an important factor because it affects how the vehicle interacts with the bridge deck, influencing the dynamic loading conditions. By incorporating the longitudinal slope with the surface roughness, we can more accurately simulate the real-world driving conditions, where vehicles experience both surface irregularities and slope variations, which can impact the vehicle's stability and response, especially when traveling uphill or downhill. (2) Use the APDL command script to establish the mass-spring-damper model of the vehicle. (3) Treat the bridge as a rigid body and apply the longitudinal slope of the bridge and road surface roughness generated by MATLAB (v2020) as forced displacements to the wheel supports along the vehicle's travel distance, in order to obtain the wheel support reaction forces as a function of distance. (4) Use ANSYS (v19.0) software to establish a spatial finite element model of the bridge, applying the wheel support reaction forces as external loads. After amplifying the loads using the impact coefficient calculated, apply the amplified loads to the bridge model to obtain the bridge's response. This method significantly improves both computational efficiency and convergence by eliminating the iterative process. Moreover, the approach accounts for the effects of longitudinal gradients of the bridge deck and road surface roughness on the bridge's dynamic response.

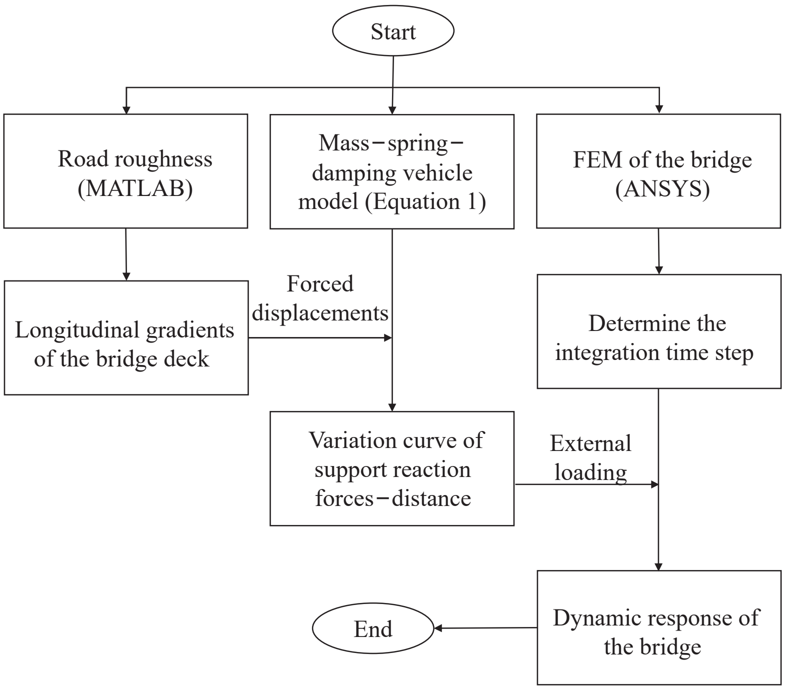

Figure 5. Flowchart of the noniterative method for vehicle–bridge coupling analysis.

The reliability and accuracy of the noniterative vehicle–bridge coupling method have been thoroughly validated in ref. [27]. Furthermore, the motor vehicle and light rail models, road surface profiles, and traffic distribution models employed in the subsequent parameter analysis are based on the frameworks established in ref. [27]. A detailed description of these models and their implementation can be found in ref. [27], where the methodology and underlying assumptions are meticulously documented. This foundational work underpins the current study's analysis and ensures the robustness of the vehicle–bridge coupling approach applied here.

4. Parametric Analysis of Hanger Responses for the Applied Bridge

4.1. Effect of Vehicle Types

4.1.1. Motor Vehicles

In this section, we consider scenarios where trailers with weights of 1.5 t, 10 t, 30 t, and 50 t run at a constant speed in lane 1. Moreover, the road surface roughness level of C is considered. Figure 6 shows the time-dependent axial stress of hangers A, B, and C. It is evident that as vehicles pass through the hangers, the axial stresses of the hangers reach peak values. Notably, the 50 t trailer induces the most significant increase in axial stress, with 7.7 Mpa, 8.3 Mpa, and 9.8 Mpa stress improvement for hangers A, B, and C, respectively. It is worth noting that as vehicles gradually move away from the hangers, the stress of hangers B and C does not reach the axial stress under self-weight. Instead, it initially drops to a value lower than the self-weight stress before gradually rising back up to the stress caused by self-weight. The reason is the asynchronous displacements of the upper and lower vertices of hangers under vertical vehicle loads. For example, when a 50 t trailer runs through the bridge, the vertical displacement and displacement difference in the upper and lower vertices of hanger C are plotted in Figure 7a,b, respectively. The figures clearly illustrate the asynchronous behavior of the upper and lower vertices, where their vertical displacements exhibit distinct trends. Specifically, the vertical displacement difference in hanger C is observed to be less than the difference induced by the hanger's self-weight at certain time intervals. This reduction in the displacement difference between the upper and lower vertices is a critical factor contributing to the unloading phenomenon observed in the hanger. The proximity of hanger A to the bridge support results in a less pronounced unloading effect, indicating that the stress range of most hangers in network arch bridges tends to increase as vehicles move away from the hangers compared to when they are approaching. This behavior underscores the dynamic response of the hangers and highlights the importance of considering such asynchronous displacements in vehicle–bridge coupling analyses.

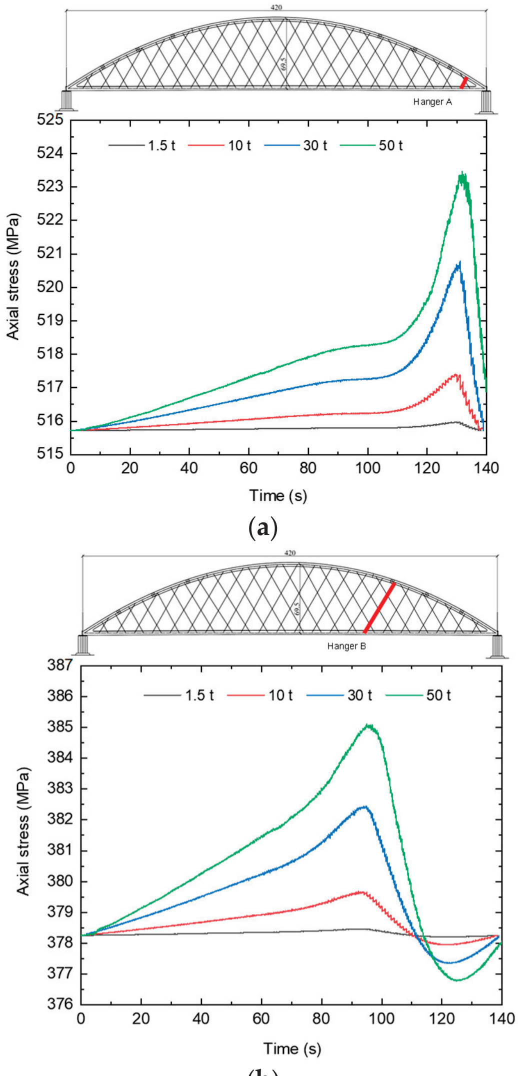

(**a**)

(**b**)

Figure 6. *Cont.*

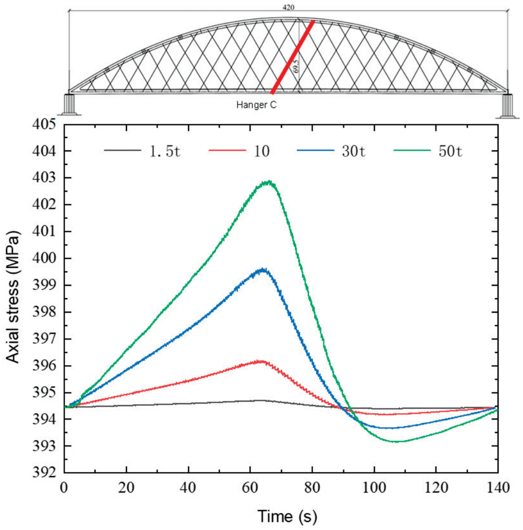

(**c**)

Figure 6. Time-dependent axial stress of hangers considering different vehicle types: (**a**): hanger A; (**b**) hanger B; (**c**): hanger C.

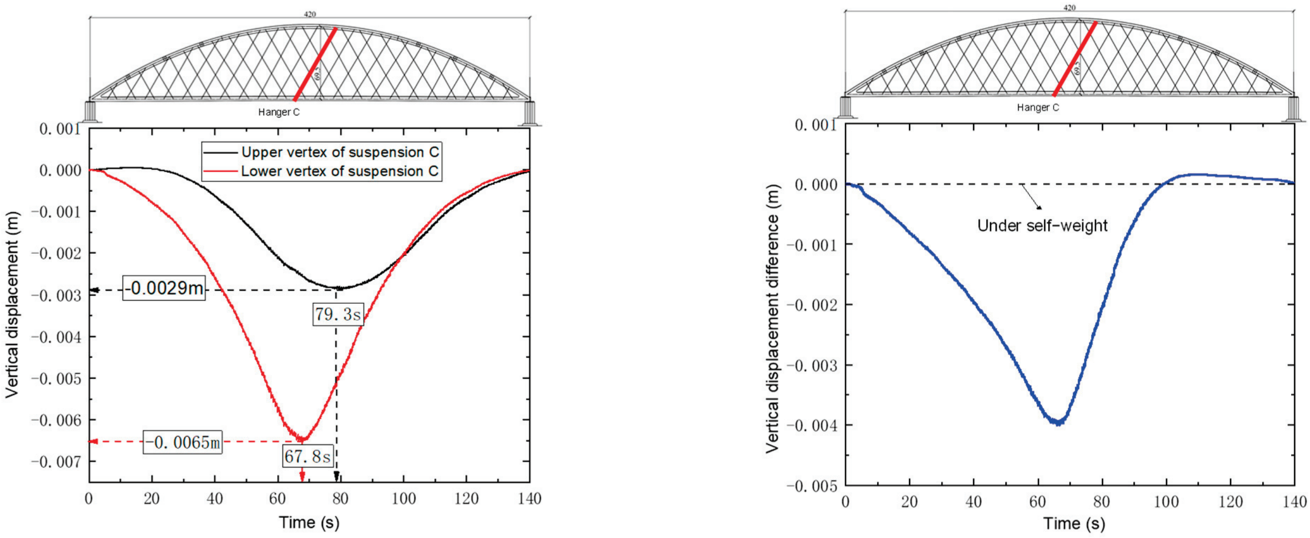

(**a**) (**b**)

Figure 7. (**a**) Vertical displacement of the upper and lower vertices of hanger C; (**b**) vertical displacement difference between upper and lower vertices of hanger C.

4.1.2. Light Rail Vehicles

The light rail operates in its designated lane (i.e., lane 1 for light rail). Figure 8 illustrates the time-dependent axial stress of the hangers under light rail loading. Specifically, Figure 8a shows the stress variation for hanger A, Figure 8b depicts the stress response of hanger B, and Figure 8c describes the stress fluctuations for hanger C. These figures clearly indicate the trend and characteristics of the stress variations experienced by each hanger when the light rail travels over the bridge. A detailed analysis of the data in Figure 8 reveals that hanger A undergoes the stress fluctuation of 12.9 Mpa. Hanger B and hanger C experience stress fluctuations of 25.2 Mpa and 35.4 Mpa, respectively. These observations indicate that despite the relatively lower frequency of light rail passages compared to conventional motor vehicles, the resultant stress impact on the hangers is notably more significant. This highlights that the dynamic loads exerted by light rail vehicles induce substantial stress variations, which can have a considerable impact on the structural integrity of the bridge.

For hanger A, the stress fluctuations are most significant when the light rail passes near the hanger. For hangers B and C, the stress fluctuations are more pronounced when the light rail initially enters the bridge. The fluctuations (as observed in Figure 8) may be induced by the track irregularity and hangers B and C are particularly sensitive to the dynamic effects associated with light rail loading, as evidenced by the more pronounced stress fluctuations observed. These findings underscore the importance of recognizing the heightened dynamic effects introduced by light rail vehicles, which appear to impose significant challenges to the structural performance of the hangers, particularly in localized regions. The observed stress responses of hangers B and C suggest a greater sensitivity to these dynamic loads, underscoring the need for careful consideration in the design, monitoring, and maintenance of the bridge to ensure its long-term structural integrity.

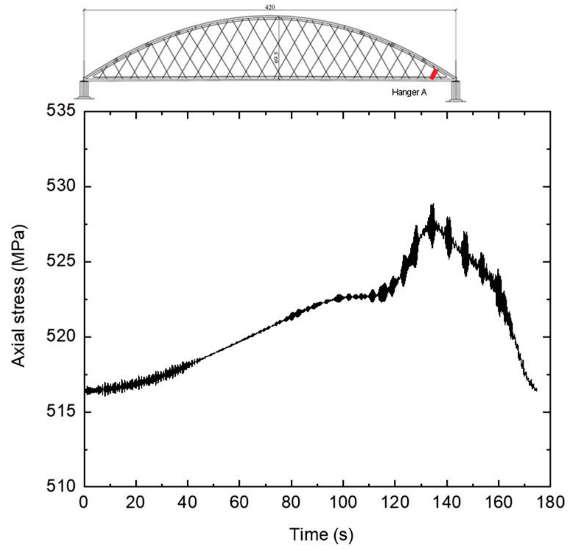

(**a**)

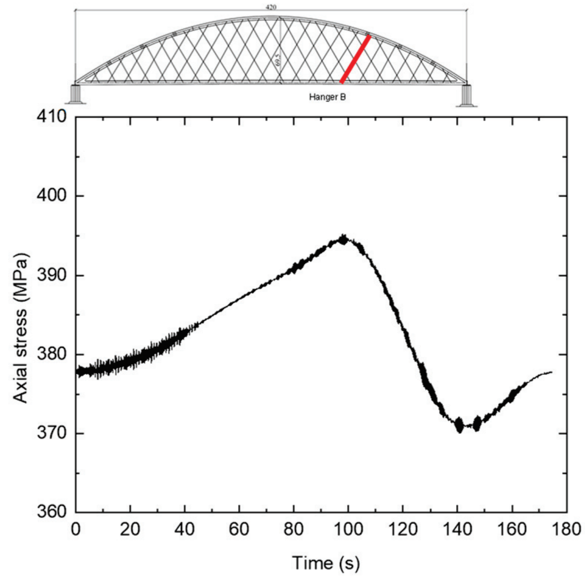

(**b**)

Figure 8. *Cont.*

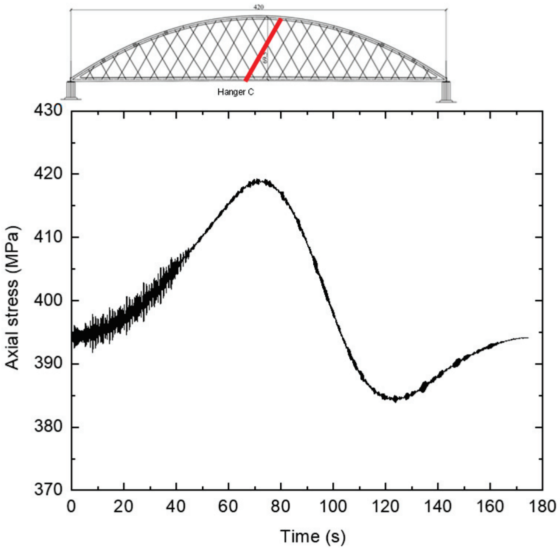

(c)

Figure 8. Time-dependent axial stress of the hangers under the light rail loading: (**a**): hanger A; (**b**) hanger B; (**c**) hanger C.

Due to the large dynamic amplification factor and significant stress variations observed in hanger C under vehicle loadings, it is identified as the most critical hanger for detailed examination. Figures 9 and 10 present the time-dependent bending moments of hanger C under the loads imposed by motor vehicles and light rails, respectively. The overall pattern closely follows that of the axial stress in the hanger (see Figures 6 and 8), with bending moments reaching their peak values as vehicles pass over the hangers and subsequently diminishing as the vehicles move away. Specifically, under light rail loading conditions, hanger C experiences longitudinal and transverse bending moment variations of 231.5 N·m and 115.3 N·m, respectively. These variations lead to maximum stress changes of 4.6 Mpa and 2.4 Mpa among the different steel wires within the hanger, which, when superimposed, makes the steel wires on the side with higher stress more susceptible to damage compared to those on the side with lower stress. This affects the fatigue life of both the steel wires and the hanger. The bending moment analysis of the hanger here can provide a basis for the analysis of the uneven fatigue life distribution of the steel wires inside the hanger. The pronounced stress variation also highlights the critical nature of hanger C and underscores the importance of accurately assessing its performance under such dynamic loading conditions. Moreover, the distinct differences in the bending moment profiles for vehicle and light rail loads reveal the varying impact of different types of loading on the structural integrity of the hanger. The bending moments not only peak as vehicles traverse the hangers but also display a notable reduction pattern during vehicle departure, indicating the dynamic nature of the load transfer process. This behavior emphasizes the need for a comprehensive understanding of both longitudinal and transverse bending moments to accurately predict the structural response and ensure the durability and safety of the hanger under diverse operational scenarios.

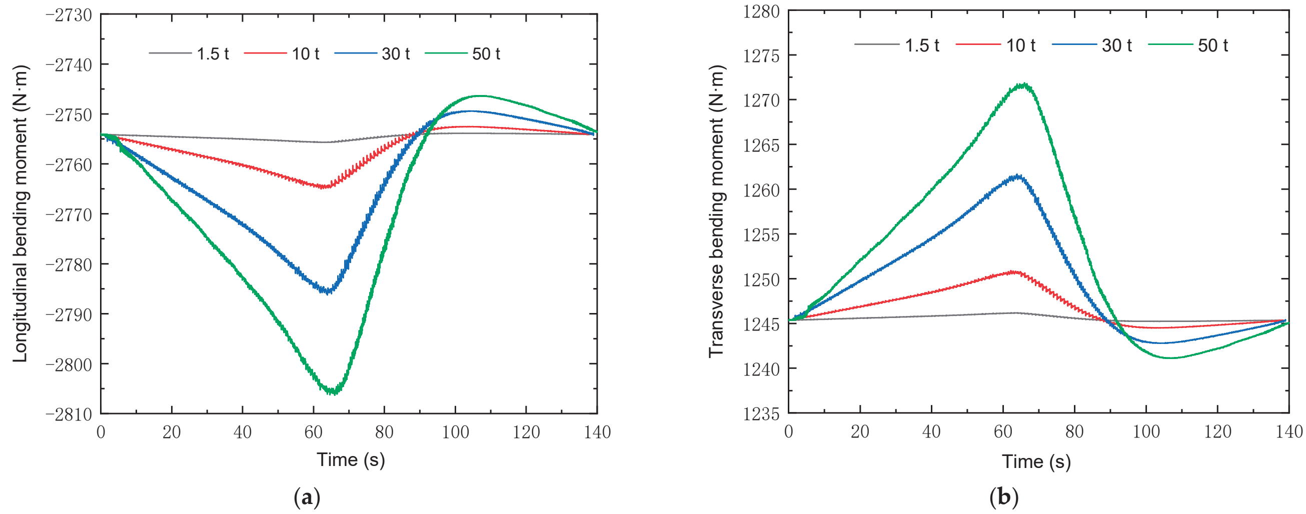

(a)

(b)

Figure 9. Time-dependent bending moment of hanger C, considering different vehicle types: (**a**) longitudinal bending moment; (**b**) transverse bending moment.

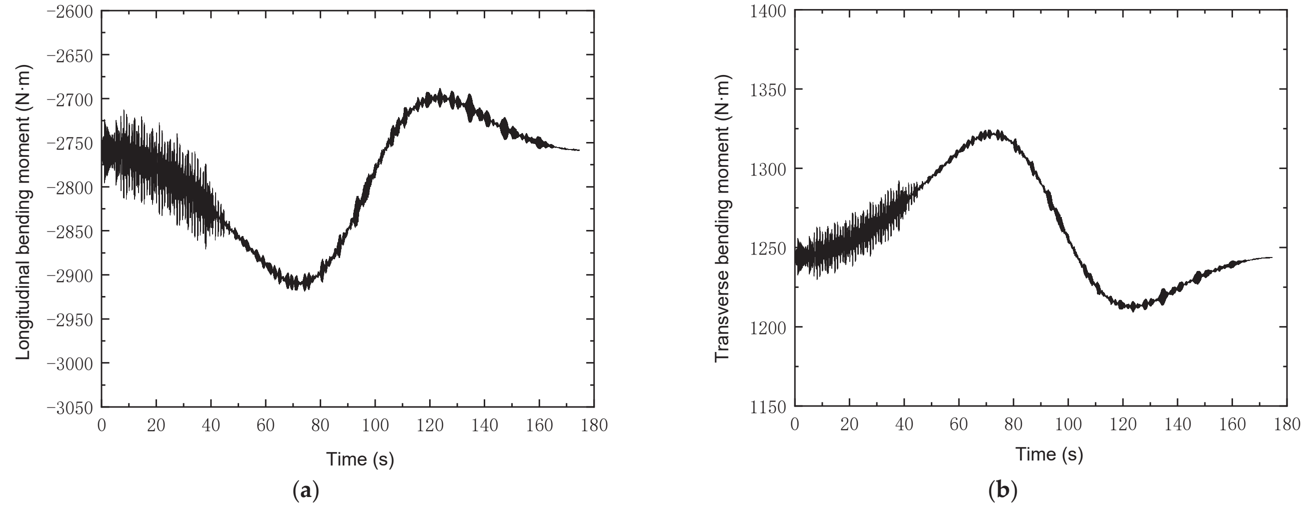

(a)

(b)

Figure 10. Time-dependent bending moment of hanger C under the light rail loading: (**a**) longitudinal bending moment; (**b**) transverse bending moment.

4.2. Effect of Motor Vehicles Lanes

The bridge has a total width of 60.7 m, incorporating eight lanes for vehicles and two lanes designated for light rail, as illustrated in Figure 2. In this section, it is assumed that eight six-axle trucks, each weighing 50 t, travel simultaneously at the same speed on Lanes 1 through 8, with a road surface roughness level of C. The axial stress, longitudinal bending moments, and transverse bending moments of hanger C are depicted in Figures 11a, 11b and 11c, respectively. Due to the opposite direction of traffic flow between Lanes 5 to 8 and Lanes 1 to 4, the results associated with Lanes 5 to 8 are displayed in reverse order of time. It is observed that vehicles driving on the outermost lanes on the same side of the hanger C (Lane 1) have the most substantial impact on its response, resulting in the largest stress variations. The influence gradually decreases for Lanes 2 to 4. Conversely, lanes on the opposite side (Lanes 5 to 8) exhibit a significantly reduced impact when compared to the lanes on the same side (Lanes 1 to 4). Among these, Lane 8 predominantly contributes to the unloading of hanger C after the vehicles have passed. From these observations, it is clear that in practical engineering scenarios, heavy trucks often travel in the outer lanes, leading to more pronounced effects on the structural responses of hangers.

Therefore, it is essential to take into account the lane distribution characteristics of different vehicle types when analyzing and designing for load impacts on bridge components.

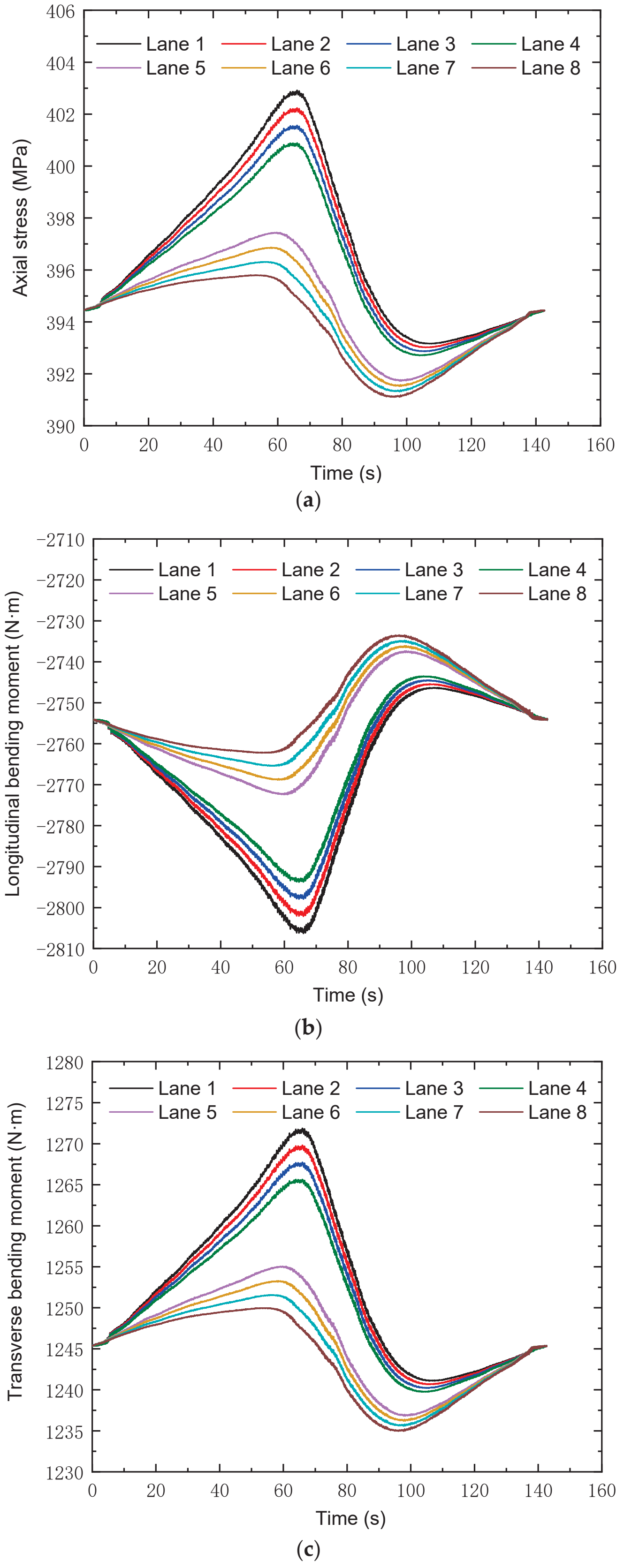

Figure 11. Time-dependent responses of hanger C, considering different lanes: (**a**) axial stress; (**b**) longitudinal bending moment; (**c**) transverse bending moment.

4.3. Effect of Light Rail Lanes

Figure 12 details the time-dependent responses of hanger C, considering light rail traveling in different lanes, which include the following points.

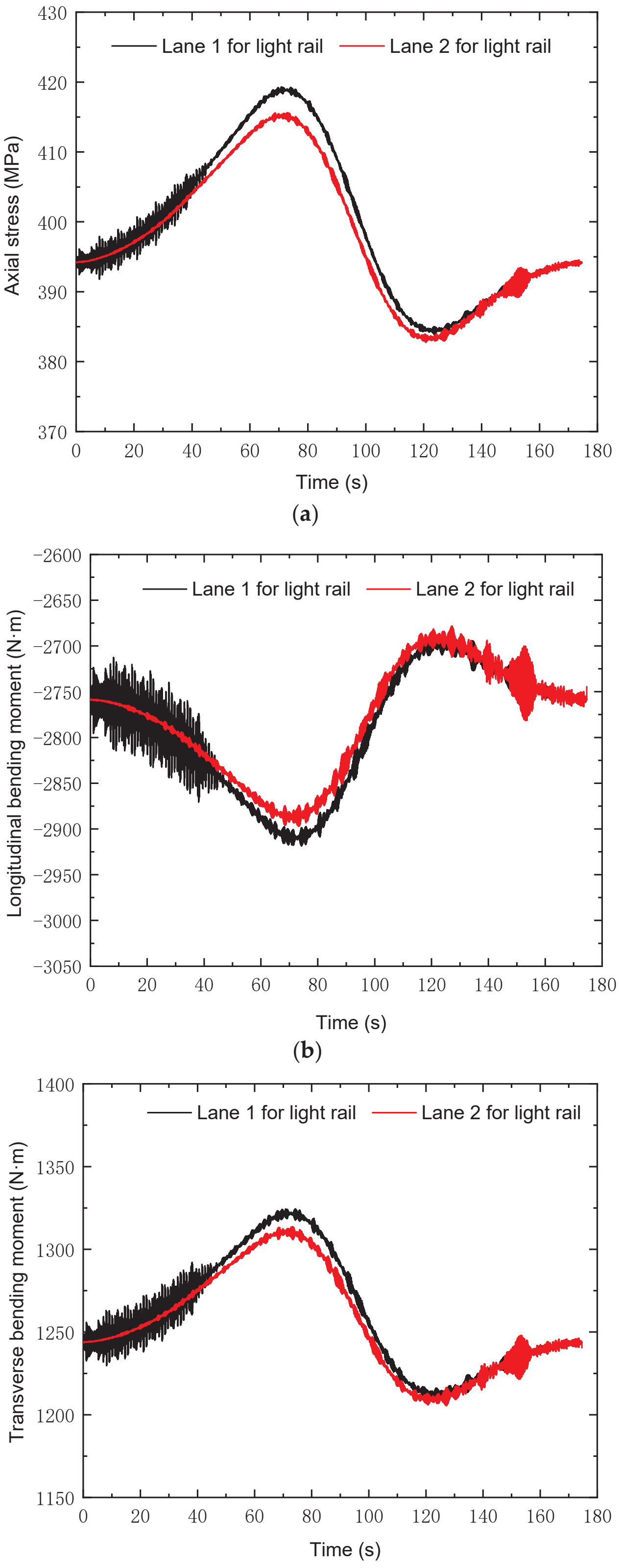

(**a**)

(**b**)

(**c**)

Figure 12. Time−dependent responses of hanger C, considering light rail traveling in different lanes: (**a**) axial stress; (**b**) longitudinal bending moment; (**c**) transverse bending moment.

(a) Axial stress: The axial stress variations are more significant when the light rail is in Lane 1, showing higher peaks and more pronounced fluctuations compared to those in Lane 2. This indicates that the proximity of the light rail lane to the hanger significantly influences the axial stress experienced by the hanger.

(b) Longitudinal bending moment: The longitudinal bending moments also exhibit higher peaks when the light rail is in Lane 1. The bending moment decreases gradually as the light rail moves across the bridge, with the largest variations occurring at the entry point of the light rail.

(c) Transverse bending moment: Similarly to the longitudinal bending moment, the transverse bending moments are higher when the light rail is closer to the hanger (Lane 1). This further emphasizes the critical impact of lane positioning on the stress distribution within the hangers.

The fluctuation in the response of hanger C is notably larger when the light rail operates in Lane 1 compared to Lane 2. This suggests a more significant influence of the light rail lane that is closer to the hangers. Additionally, it is observed that, regardless of whether the light rail operates in Lane 1 or Lane 2, the responses of hanger C exhibit the greatest fluctuations when the light rail initially enters the bridge. This phenomenon is more pronounced when the light rail is operating in Lane 1, highlighting the importance of initial load impact on hanger performance. To ensure the bridge's stability and minimize the lane effect of light rails, it is recommended that the light rail lanes be placed closer to the central line of the bridge deck. This strategic placement helps distribute the loads more evenly and reduces the potential for excessive stress concentrations on the hangers. Moreover, it enhances the overall structural integrity of the bridge. In conclusion, the analysis of the time-dependent responses of hanger C under light rail loading underscores the necessity of considering lane positioning and its effects on bridge stability. The findings suggest that proper lane placement can significantly reduce the stress variations and bending moments experienced by the hangers, thereby enhancing the overall durability and safety of the bridge structure.

4.4. Effect of Road Surface Roughness

Figure 13 illustrates the time-dependent axial stress, as well as longitudinal and transverse bending moments of hanger C, under road surface roughness grades C (general) and E (very poor). It can be observed that variations in road surface roughness have a relatively minor impact on the hanger's overall response. However, the road surface roughness significantly influences the amplitude of fluctuations in axial stress and bending moments. The poorer the road surface condition, the greater the fluctuation in both axial stress and longitudinal and transverse bending moments, especially when vehicles pass through the hanger. For example, the response of hanger C associated with road surface roughness level E exhibits more pronounced fluctuations compared to those associated with road surface roughness level C, particularly during vehicle passages near the hanger. This observation indicates that poor road surface conditions amplify the dynamic effects on hanger C, resulting in increased stress variations.

The increased fluctuation amplitude under worse road conditions is crucial because stress amplitude is a primary factor affecting the fatigue performance of hangers. Elevated stress fluctuations can accelerate the initiation and propagation of fatigue cracks, ultimately reducing the lifespan of the hangers. Therefore, in the context of bridge design and maintenance, it is essential to consider the impact of road surface roughness on hangers' responses to ensure long-term durability and safety. Regular monitoring and maintenance of the road surface can help mitigate these adverse effects, thereby enhancing the structural integrity and service life of the bridge. Moreover, considering different road surface roughness levels in the analysis provides a more comprehensive understanding of the bridge's performance under various operating conditions. This approach helps in designing more robust bridges that can withstand a wide range of real-world scenarios, ultimately contributing to improved reliability of bridge structures.

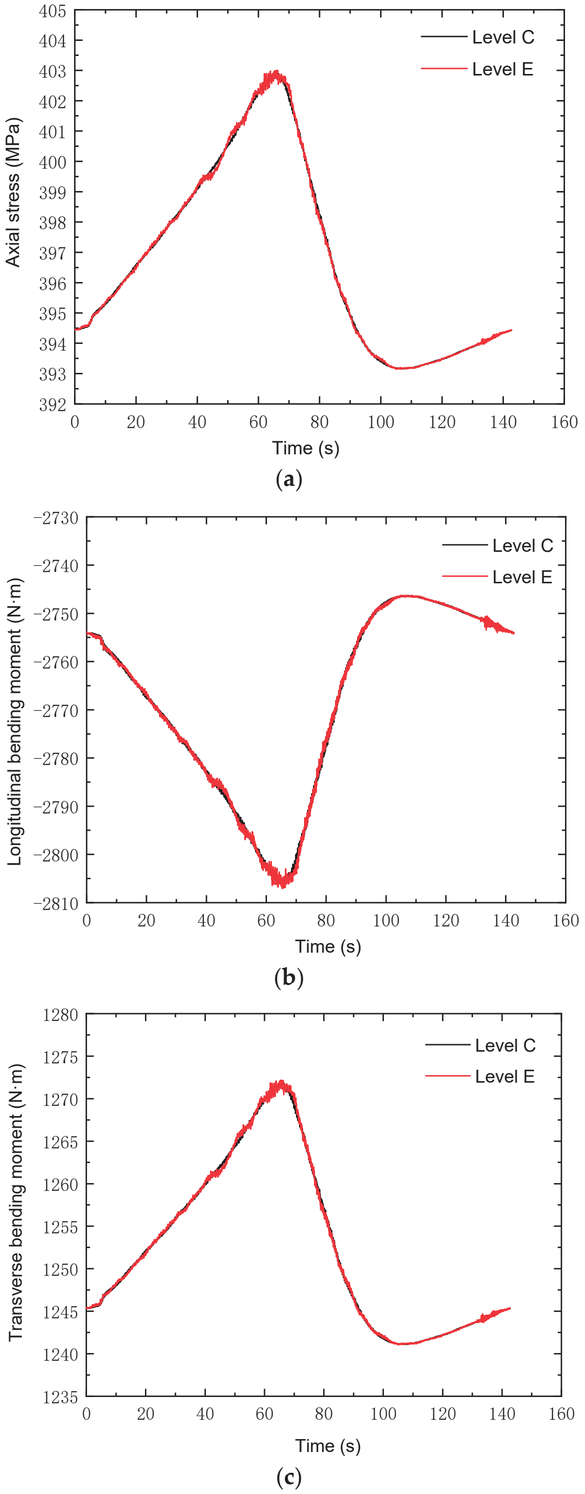

Figure 13. Time-dependent responses of hanger C, considering different road surface roughness levels: (**a**) axial stress; (**b**) longitudinal bending moment; (**c**) transverse bending moment.

5. Conclusions

In this study, the responses of hangers in a network arch bridge designed for both highway and light rail traffic under real traffic conditions were investigated using a non-iterative vehicle–bridge coupling method. The effects of vehicle types, driving lanes, and road surface roughness were considered in the analysis. The key findings are summarized as follows.

- Heavy vehicle loads, especially from 50 t trailers, significantly increase hanger axial stress. Hanger C, in particular, experiences the highest stress increment, with a peak increase of 9.8 MPa. This demonstrates the substantial impact of heavy vehicles on hanger stress. However, light rail vehicles induce even greater stress fluctuations. For instance, hanger A exhibits a maximum stress increase of 12.9 MPa, while hangers B and C show fluctuations of 25.2 MPa and 35.4 MPa, respectively. This underscores the dynamic loading effects of light rail traffic and its potential to affect the structural integrity of the hangers more severely than highway vehicles.
- The influence of vehicle lanes on hanger responses is notable, particularly for outermost lanes. Vehicles on Lane 1 induce the largest stress variations, suggesting that lane positioning should be considered in bridge design to mitigate stress concentrations. Additionally, the placement of light rail tracks closer to the hangers, as seen in Lane 1, intensifies the stress variations in hanger C. This highlights the importance of optimizing the positioning of light rail lanes to improve load distribution and reduce localized stress concentrations.
- Road surface roughness amplifies dynamic loading effects. Poor road conditions, particularly grade E surfaces, exacerbate stress and bending moment fluctuations, underlining the need to account for road surface quality in the design and maintenance of the bridge.
- Hanger C, located at midspan, exhibits the most significant stress fluctuations across all loading conditions. This indicates that midspan hangers are critical to the overall structural performance, with both axial stress and bending moments peaking as vehicles pass.

In conclusion, the study emphasizes the importance of accounting for vehicle types, lane positioning, light rail track placement, and road surface conditions in bridge design. Addressing these factors will help engineers enhance the structural performance, durability, and safety of hangers in network arch bridges under various traffic conditions.

Due to limitations in computational capabilities, the finite element model of the network arch bridge with wire mesh hangers used in this study primarily employed beam elements. The components are connected at common nodes. In future studies, solid elements should be used to model the connection between the hangers and the main beam to improve the accuracy of the calculations, while also better reflecting the local force characteristics at the connection points.

Author Contributions: Methodology, H.C., R.M., B.G. and Q.Z.; Software, B.G. and Q.Z.; Validation, H.C., B.G. and Q.Z.; Formal analysis, B.G. and Q.Z.; Investigation, H.C.; Writing—original draft, H.C.; Writing—review & editing, R.M. and B.G.; Supervision, R.M.; Project administration, Q.Z.; Funding acquisition, Q.Z. All authors have read and agreed to the published version of the manuscript.

Funding: This work was supported by the National Natural Science Foundation of China [grant number 52178153], the National Natural Science Foundations of China [grant number 52238005], Shanghai Pujiang Program [grant number 22PJD079], Shanghai Pujiang Program [grant number 21PJD077] and China Postdoctoral Science Foundation [grant number 2022M722426]. The opinions presented in this paper are those of the authors and do not necessarily reflect the views of the sponsoring organizations.

Data Availability Statement: The data presented in this study are available on request from the corresponding author. The data are not publicly available due to privacy or ethical restrictions.

Conflicts of Interest: The authors declare no conflicts of interest.

References

1. Zou, Y.; Yue, P.; Shi, K.; Xue, F.; He, X.; Liu, Q. Effects of High-Speed Trains on Trucks Running on a Road–Rail Dual-Use Bridge under Crosswind. *Int. J. Struct. Stab. Dyn.* **2022**, *22*, 2250122. [CrossRef]
2. Chen, D.H.; Li, Z.; Chen, H.; Guo, W.H. Vehicle-bridge coupling vibration reduction analysis for long span highway and railway bi-purpose cable-stayed bridge. *Appl. Mech. Mater.* **2013**, *361*, 1223–1227. [CrossRef]
3. Li, H.; Wang, T.; Wu, G. *Dynamic Response Prediction of Vehicle-Bridge Interaction System Using Feedforward Neural Network and Deep Long Short-Term Memory Network, Structures*; Elsevier: Amsterdam, The Netherlands, 2021; pp. 2415–2431.
4. Aloisio, A.; Contento, A.; Alaggio, R.; Quaranta, G. Physics-based models, surrogate models and experimental assessment of the vehicle–bridge interaction in braking conditions. *Mech. Syst. Signal Process.* **2023**, *194*, 110276. [CrossRef]
5. Aloisio, A.; Alaggio, R. Probabilistic Comparative Analysis of Vehicle–Bridge Interaction Models for Predicting Bridge Response under Moving Vehicles. *J. Eng. Mech.* **2024**, *150*, 04023121. [CrossRef]
6. Zhang, N.; Zhou, Z.; Wu, Z. Safety evaluation of a vehicle–bridge interaction system using the pseudo-excitation method. *Railw. Eng. Sci.* **2022**, *30*, 41–56. [CrossRef]
7. Devendiran, D.K.; Banerjee, S. Influence of Combined Corrosion–Fatigue Deterioration on Life-Cycle Resilience of RC Bridges. *J. Bridge Eng.* **2023**, *28*, 04023014. [CrossRef]
8. Xu, S.; Zhou, S.; Zeng, Z.; Ma, R. The vehicle-bridge interaction influence on suspender of arch bridge under various driving parameters. In Proceedings of the 2022 International Conference on Intelligent Transportation, Big Data & Smart City (ICITBS), Hengyang, China, 26–27 March 2022; IEEE: Piscataway, NJ, USA, 2022; pp. 1457–1461.
9. Li, J.; Feng, D. Fatigue life evaluation of bridge stay cables subject to monitoring traffic and considering road roughness. *Eng. Struct.* **2023**, *293*, 116572. [CrossRef]
10. Yang, Y.; Yau, J. Vehicle-bridge interaction element for dynamic analysis. *J. Struct. Eng.* **1997**, *123*, 1512–1518. [CrossRef]
11. Inglis, C.E. *A Mathematical Treatise on Vibrations in Railway Bridges*; Cambridge University Press: Cambridge, UK, 2015.
12. Yau, J.D.; Frýba, L. A Quasi-Vehicle/Bridge Interaction Model for High Speed Railways. *J. Mech.* **2015**, *31*, 217–225. [CrossRef]
13. Dimitrakopoulos, E.G.; Zeng, Q. A three-dimensional dynamic analysis scheme for the interaction between trains and curved railway bridges. *Comput. Struct.* **2015**, *149*, 43–60. [CrossRef]
14. Frýba, L. *Vibration of Solids and Structures Under Moving Loads*; Springer Science & Business Media: Berlin/Heidelberg, Germany, 2013.
15. Frýba, L. *Dynamics of Railway Bridges*; Thomas Telford Publishing: London, UK, 1996.
16. Wang, T.; Garg, V.K.; Chu, K. Railway bridge/vehicle interaction studies with new vehicle model. *J. Struct. Eng.* **1991**, *117*, 2099–2116. [CrossRef]
17. Wang, T.L. Impact in a railway truss bridge. *Comput. Struct.* **1993**, *49*, 1045–1054. [CrossRef]
18. Diana, G.; Cheli, F. Dynamic interaction of railway systems with large bridges. *Veh. Syst. Dyn.* **1989**, *18*, 71–106. [CrossRef]
19. Azimi, H.; Galal, K.; Pekau, O.A. A modified numerical VBI element for vehicles with constant velocity including road irregularities. *Eng. Struct.* **2011**, *33*, 2212–2220. [CrossRef]
20. Ju, S.H.; Lin, H.T.; Hsueh, C.C.; Wang, S.L. A simple finite element model for vibration analyses induced by moving vehicles. *Int. J. Numer. Methods Eng.* **2006**, *68*, 1232–1256. [CrossRef]
21. Brady, S.P.; O'Brien, E.J.; Žnidarič, A. Effect of vehicle velocity on the dynamic amplification of a vehicle crossing a simply supported bridge. *J. Bridge Eng.* **2006**, *11*, 241–249. [CrossRef]
22. Kim, C.W.; Kawatani, M.; Kim, K.B. Three-dimensional dynamic analysis for bridge–vehicle interaction with roadway roughness. *Comput. Struct.* **2005**, *83*, 1627–1645. [CrossRef]
23. Carbonari, S.; Nicoletti, V.; Martini, R.; Gara, F. Dynamics of bridges during proof load tests and determination of mass-normalized mode shapes from OMA. *Eng. Struct.* **2024**, *310*, 118111. [CrossRef]
24. Sheibani, M.; Ghorbani-Tanha, A.K. *Obtaining Mass Normalized Mode Shapes of Motorway Bridges Based on the Effect of Traffic Movement, Structures*; Elsevier: Amsterdam, The Netherlands, 2021; pp. 2253–2263.
25. Guo, S.; Jiang, Y.; Zhang, W.; Zeng, Y. Study on Dynamic Characteristics of Long-Span Highway-Rail Double-Tower Cable-Stayed Bridge. *Buildings* **2024**, *14*, 1733. [CrossRef]
26. Zhao, R.; Zheng, K.; Wei, X.; Jia, H.; Liao, H.; Li, X.; Wei, K.; Zhan, Y.; Zhang, Q.; Xiao, L. State-of-the-art and annual progress of bridge engineering in 2020. *Adv. Bridge Eng.* **2021**, *2*, 29. [CrossRef]

27. Ge, B.; Ma, R.; Zhu, Q.; Chen, A.; Chang, H. Fatigue life prediction of corroded hangers with parallel steel wire in a network arch bridge under vehicle-bridge interaction based on a novel noniterative simplified method. *Int. J. Fatigue* **2024**, *187*, 108457. [CrossRef]
28. Abuodeh, O.; Locke, W.; Redmond, L.; Sreenivasulu, R.V.; Schmid, M. *Examining Methods for Modeling Road Surface Roughness Effects in Vehicle–Bridge Interaction Models via Physical Testing, Society for Experimental Mechanics Annual Conference and Exposition*; Springer: Berlin/Heidelberg, Germany, 2023; pp. 33–47.
29. Camara, A.; Kavrakov, I.; Nguyen, K.; Morgenthal, G. Complete framework of wind-vehicle-bridge interaction with random road surfaces. *J. Sound Vib.* **2019**, *458*, 197–217. [CrossRef]
30. Xu, Y.; He, J. *Smart Civil Structures*; CRC Press: Boca Raton, FL, USA, 2017.
31. Esen, A.F.; Laghrouche, O.; Woodward, P.K.; Medina-Pineda, D.; Corbisez, Q.; Shih, J.Y.; Connolly, D.P. Numerical analysis of high-speed railway slab tracks using calibrated and validated 3D time-domain modelling. *Railw. Eng. Sci.* **2024**, *32*, 36–58. [CrossRef]
32. Kwasniewski, L.; Li, H.; Wekezer, J.; Malachowski, J. Finite element analysis of vehicle–bridge interaction. *Finite Elem. Anal. Des.* **2006**, *42*, 950–959. [CrossRef]
33. Lu, X.; Kim, C.; Chang, K. Finite element analysis framework for dynamic vehicle-bridge interaction system based on ABAQUS. *Int. J. Struct. Stab. Dyn.* **2020**, *20*, 2050034. [CrossRef]
34. Yang, Y.B.; Lin, C.W. Vehicle–bridge interaction dynamics and potential applications. *J. Sound Vib.* **2005**, *284*, 205–226. [CrossRef]
35. Li, Y.; Xu, X.; Zhou, Y.; Cai, C.S.; Qin, J. An interactive method for the analysis of the simulation of vehicle–bridge coupling vibration using ANSYS and SIMPACK. *Proc. Inst. Mech. Eng. Part F J. Rail Rapid Transit* **2018**, *232*, 663–679. [CrossRef]
36. Zhou, J.; Huang, C.; Deng, J.; Zhang, J.; Zhang, L. A co-simulation approach for straddle monorail vehicle–bridge interaction subjected to nonlinear excitation. *Adv. Eng. Softw.* **2023**, *180*, 103458. [CrossRef]
37. Cui, C.; Chen, A.; Ma, R. An improved continuum damage mechanics model for evaluating corrosion–fatigue life of high-strength steel wires in the real service environment. *Int. J. Fatigue* **2020**, *135*, 105540. [CrossRef]
38. Stoura, C.D.; Paraskevopoulos, E.; Dimitrakopoulos, E.G.; Natsiavas, S. A Dynamic Partitioning Method to solve the vehicle-bridge interaction problem. *Comput. Struct.* **2021**, *251*, 106547. [CrossRef]
39. González, A.; Feng, K.; Casero, M. Detection, localisation and quantification of stiffness loss in a bridge using indirect drive-by measurements. *Struct. Infrastruct. Eng.* **2023**, 1–19. [CrossRef]
40. Chowdhury, I.; Dasgupta, S.P. Computation of Rayleigh damping coefficients for large systems. *Electron. J. Geotech. Eng.* **2003**, *8*, 1–11.
41. Cui, C.; Chen, A.; Ma, R.; Wang, B.; Xu, S. Fatigue life estimation for suspenders of a three-pylon suspension bridge based on vehicle–bridge-interaction analysis. *Materials* **2019**, *12*, 2617. [CrossRef] [PubMed]

buildings

MDPI

Article

Behavior of Concrete-Filled Steel Tube Columns with Multiple Chambers and Round-Ended Cross-Sections under Axial Loading

Jing Liu [1,2], Tao Zhang [3], Zhicheng Pan [4,5,*] and Fanjun Ma [4]

1 Key Laboratory of Green Building and Intelligent Construction in Higher Educational Institutions of Hunan Province, Hunan City University, Yiyang 413000, China; liujing@hncu.edu.cn
2 A Dual Innovation Platform Combining Production, Education and Research with Science and Technology of the Construction Industry of Hunan Province, Hunan City University, Yiyang 413000, China
3 School of Civil Architecture, Zhengzhou University of Aeronautics, Zhengzhou 450000, China; zhangtao0226@zua.edu.cn
4 Sinohydro Engineering Bureau 8 Co., Ltd., Changsha 410004, China; mafanjun@126.com
5 Power China Chizhou Changzhi Prefabricated Construction Co., Ltd., Chizhou 247100, China
* Correspondence: panzhichengcsu@163.com

Abstract: Concrete-filled round-ended steel tubes (CFRTs) are a unique type of composite stub columns, which have the advantage of aesthetics and a well-distributed major–minor axis. Thus, the structure has been widely employed as piers and columns in bridges. To improve the mechanical performance of CFRTs with a large length–width ratio and to enhance the restraint effect of steel tubes on concrete, this study investigates the compressive property of multi-chamber, concrete-filled, round-ended steel tubular (M-CFRT) stub columns using a combination of experimental and numerical analyses. A detailed compression test on eight specimens is conducted to examine the compressive property of M-CFRT stub columns. The study focuses on understanding the influence of some key parameters on ultimate bearing capacity, failure stage, damage modes, and ductility. Additionally, the accuracy of the finite element modeling method in simulating the ultimate bearing capacity of the structure is verified. Finally, the calculating formula for the ultimate bearing capacity of M-CFRT stub columns is proposed on the basis of the experimental and numerical findings. Results of the formula calculation are consistent with the experimental data. These research findings serve as a valuable reference for designing similar structures in engineering practice.

Keywords: concrete-filled round-ended steel tubular stub column; multi-chamber steel tube; ultimate bearing capacity

1. Introduction

Round-ended reinforced concrete columns have a suitable major–minor axis distribution, a low flow resistance coefficient, and an attractive appearance; thus, this structure has been employed extensively as piers and columns in bridge engineering over the past decades [1–3]. However, building it is a highly difficult procedure that requires substantial formwork, particularly at the beam–column joints. Furthermore, as heavy haul railroads and tall bridges grow in popularity, the need for piers to have a certain bearing capacity, ductility, and anti-seismic property increases. Concrete-filled steel tubes are a good choice, due to their excellent mechanical properties and convenient construction characteristics [4–6].

A novel type of composite stub column, known as concrete-filled, round-ended steel tube (CFRT) stub columns, was proposed against this background. Given their rounded edges, CFRT members have high architectural aesthetic and may successfully lessen the influence of fluid load on the pier. In addition, CFRT stub columns can offer the benefit of not requiring a reinforced cage or formwork. In this construction method, permanent and integral formworks can be achieved by using external steel tubes, which can function as permanent and integral formworks, resulting in decreased labor costs, materials, and construction time. As a result of these advantages, CFRT stub columns have recently garnered increasing interest from domestic and foreign researchers and engineers and have been used in bridge construction, as demonstrated by the Weihe Bridge in Baoji City, China, the Houhu Cable-stayed Bridge in Wuhan, China, and the Platform of the Xinglin Gulf in Xiamen City, China (illustrated in Figure 1) [7,8].

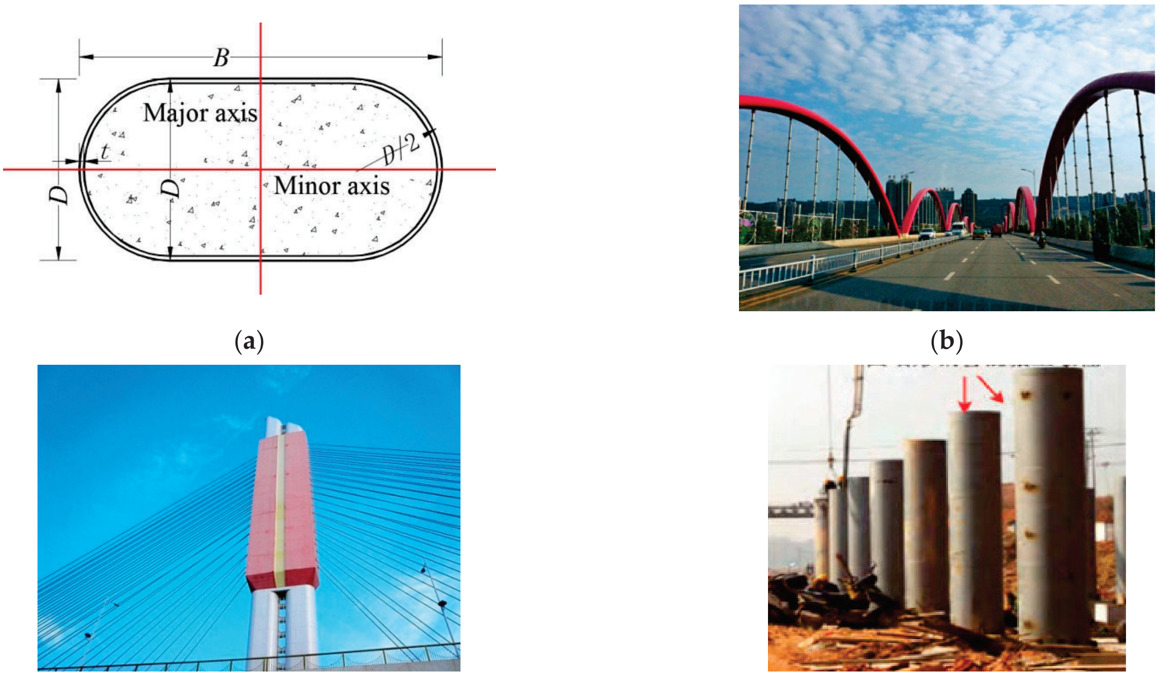

(**a**) (**b**) (**c**) (**d**)

Figure 1. Illustrations and typical applications of CFET members. (**a**) Cross-section of CFRTs. (**b**) Weihe bridge in Baoji City. (**c**) Cable-stayed bridge in Wuhan city. (**d**) Xinglin Gulf in Xiamen City.

In actual engineering, the axial compression performance is a key property for structures. To date, numerous experimental and finite element analysis (FEA) research have been conducted on the property of CFT stub columns or other structures under axial compression, and the research provided ideas for this study [9–17].

However, to the author's best knowledge, not many studies have been published on CFRT stub columns. Xie et al. [7,8] investigated the behavior of paired RECFST columns during the time of the construction of the Houhu Cable-stayed Bridge. Zhou et al. [18] conducted experimental studies on the compressive behavior of concrete-filled single-skin and double-skin steel tubular stub columns, and they also explored the effects of concrete strength and geometric dimension. Ding et al. [3] studied the behavior of CFRT stub columns under axial compression through experimental and numerical investigations and also suggested a simplified streamline for determining the ultimate carrying capacity. Han et al. [19] tested round-ended concrete, stainless steel, carbon steel, and multi-skin stub columns. They discovered that the composite stub columns exhibited strong bearing capacity and good ductility. In addition, Wang et al. [20] and Ding et al. [21] conducted a numerical investigation on the compressive properties of CFRT stub columns and proposed a novel method, which involves the welding of bidirectional stirrups to the inner surface of the round-ended steel tube, resulting in track-shaped, rebar-stiffened, concrete-filled, round-ended steel tubular stub columns. The analysis results demonstrated that the novel approach can successfully avert local buckling and enhance the overall ultimate carrying capacity.

Previous studies have found that welding work between the steel tubes and stirrups is a challenging task in practical engineering [20]. Additionally, as the aspect ratio (B/D) increases, the function of restraint of the steel tube on the core concrete decreases, and when the section aspect ratio of a round-ended CFST column is greater than 5.0, the constraints to the core concrete by a single-cavity steel tube becomes negligible, leading to an increased severity of the local buckling of the steel tube [3,21]. This issue makes it difficult to use the columns in engineering applications. To address these issues, this study proposes a new method to enhance the compressive property of composite stub columns, hereafter called multi-chamber, concrete-filled, round-ended steel tubular (M-CFRT) stub columns, as shown in Figure 2. However, the compressive behavior of these columns is currently unknown, and the effect of vertical diaphragms must also be investigated.

Through these research activities, the study aims to fill the research gaps and provide valuable insights into the design and utilization of M-CFRT stub columns in practical engineering. Specifically, on the basis of the experimental and numerical data results from our research group [3,21], the major objectives of this study are as follows: (1) explore the mechanical performances of the composite columns by conducting axial compression tests on eight specimens with different preformed chambers, (2) investigate the axial loading behavior by developing FE models based on the experimental results, and (3) derive a simplified formula for predicting the ultimate carrying capacity by applying ratio simplification in accordance with the superposition principle and on the basis of the tested and numerical consequences [3,17].

2. Experimental Investigation

2.1. Test Specimen

This study involved the design and testing of a total of eight specimens to examine the axial compressive properties of the M-CFRT stub columns. The effects of chamber construction and aspect ratio (B/D) were considered. Figure 2 shows the cross-section dimensions of the M-CFRT stub columns, and Table 1 provides the detailed information for each specimen. In the table, B represents the out-to-out dimension in the minor axis direction, while D represents the out-to-out dimension in the major axis direction and the diameter of the two semicircles of the cross-section. t denotes the parameter indicating the thickness of the steel tube and the vertical diaphragm, whereas L signifies the height of the specimen in millimeters. f_y stands for the yield strength of the steel, and f_{cu} represents the cube strength of the concrete. Expressed as the quotient of the steel tube area divided by the total cross-sectional area, the steel ratio is denoted as p_s. The ultimate bearing capacity of the specimens subjected to testing is represented by N_u.

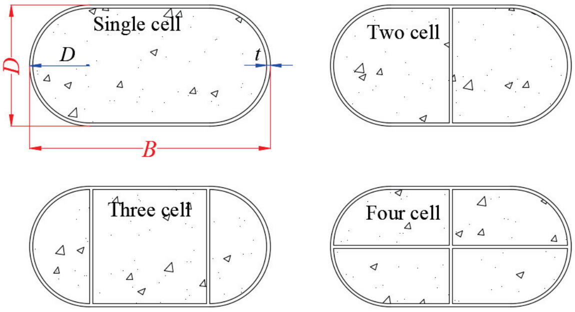

Figure 2. Cross-section of M-CFRT stub columns.

The fabrication of multi-chamber round-ended steel tubes consisted of two steps. Initially, U-shaped cross-sections were formed from the flat steel plates. Subsequently, two U-shaped cross-sections and several vertical diaphragms were joined together using single-bevel butt welds. The choice to use butt welds followed the guidelines specified in the standard GB 50017-2003 [22].

Table 1. Geometric properties and characteristics.

No.	Specimen ID	$B \times D \times t \times H$/mm	B/D	Chamber	f_s	f_{cu}	ρ_s	$N_{u,e}$/kN
1	CFST-A1	228 × 114 × 4 × 500	2	1	334	37	10.1	1420
2	CFST-A2	228 × 114 × 4 × 500	2	2	334	37	12.1	1740
3	CFST-A3	228 × 114 × 4 × 500	2	3	334	37	14.0	1800
4	CFST-A4	228 × 114 × 4 × 500	2	4	334	37	16.0	1930
5	CFST- A5	342 × 114 × 4 × 500	3	1	334	37	9.0	1830
6	CFST- A6	342 × 114 × 4 × 500	3	2	334	37	10.3	2400
7	CFST- A7	342 × 114 × 4 × 500	3	3	334	37	11.5	2510
8	CFST- A8	342 × 114 × 4 × 500	3	4	334	37	14.0	2715

2.2. Material Properties

Before the trial, the mechanical properties of the materials, including steel plate and concrete, were determined through material testing using standard methods. Mild steel was the type of steel used in this study, and three tensile coupons were cut to obtain the material properties of the steel tube used in the specimens. Additionally, the cubic compressive strength (f_{cu}) of concrete was obtained by testing concrete cubes. Further details regarding the material properties are summarized in Table 1.

2.3. Experimental Instrumentation

Axial compression experiments were conducted on eight specimens utilizing a universal pressure testing machine with a 500-ton capacity in the National Demonstration Center for Experimental Civil Engineering Education at Hunan City University. For the precise deformation measurement of the specimens, six strain rosettes (S) were affixed to the mid-height of the columns, and two LVDTs were affixed at an identical position, as illustrated in Figure 3. Meanwhile, the DH3818 static strain measurement system was used to obtain axial load vs. strain curves, while electronic transducers and a data acquisition system were used to collect axial load vs. deformation curves.

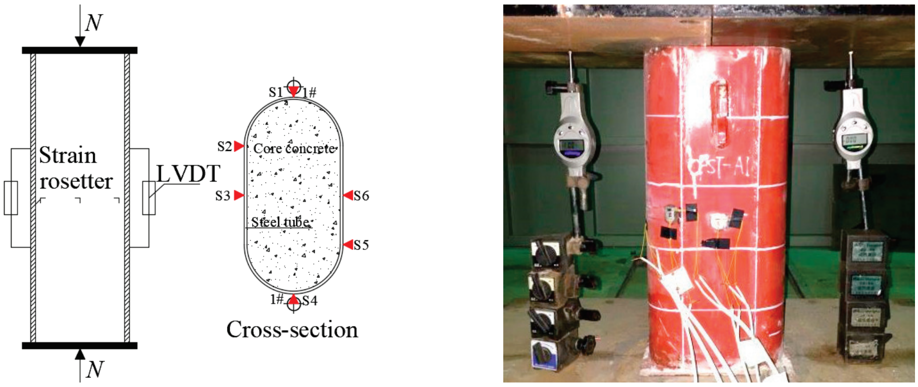

(**a**) (**b**)

Figure 3. Experimental instrumentation for all specimens. (**a**) Schematic view. (**b**) Experimental setup.

All specimens were tested under monotonic static loading, and the compressive load was applied to the top of the specimens through a load control mode. First, the load increased by a step of 1/20 of the expected ultimate load in the elastic stage. Second, the load was applied to the specimens via displacement control, with an increment of 0.2 mm after reaching approximately 60% of the expected ultimate bearing capacity. Each loading step lasted 3–5 min. When the load was up to the ultimate bearing load, the specimen was loaded slowly and continuously at a step of 0.5 mm, and data were recorded continuously for 5 min. Finally, the tests were stopped when the axial strain reached 0.04, which was the maximum strain of the specimens. The entire loading time for each specimen was approximately 1.5 h, utilizing the experimental configuration adopted from Ding et al. [3].

3. Experimental Results Analysis

3.1. Failure Stages

Figure 4 shows the axial load–strain curves of the specimens, where the compression of composite stub columns exhibited a consistent pattern. Consequently, it was segmented into three distinct stages: the elastic stage, the elastic–plastic stage, and the failure stage.

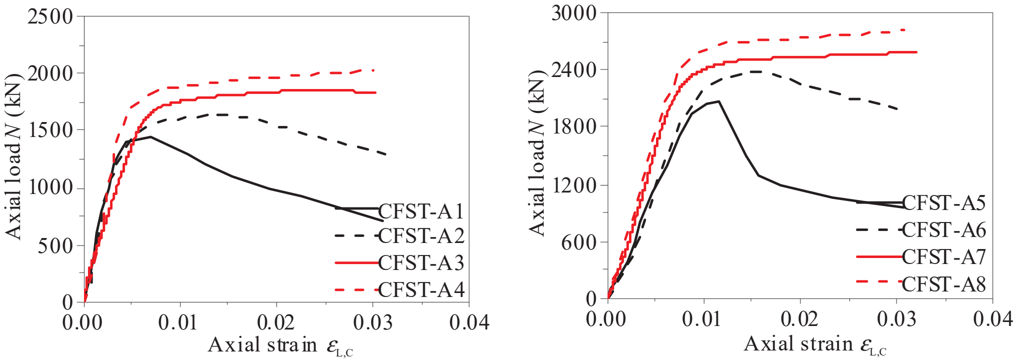

(**a**) (**b**)

Figure 4. Axial load–strain curves of specimens. (**a**) CFST-A1~CFST-A4 specimens. (**b**) CFST-A5~CFST-A8 specimens.

Stage I: During the elastic phase, the elastic modulus of all specimens remained constant. The imposed load increased quickly, whereas the elastic displacement was close to zero.

Stage II: In the elastic–plastic phase, as the applied load approached approximately 60–70% of the peak value, the steel tube initiated yielding. Subsequently, the axial load–strain curves manifested an elastic–plastic behavior.

Stage III: When the peak value was reached, the applied load decreased sharply as the displacement continued to increase. This phenomenon primarily resulted from the core concrete failure, coupled with the steel tube buckling.

3.2. Damage Modes

Figure 5 illustrates the characteristic failure modes observed in all examined specimens. As depicted, the failure modes among CFRT stub columns (such as specimens CFST-A1 and CFST-A5) and M-CFRT stub columns (such as specimens CFST-A2–CFST-A4 and CFST-A6–CFST-A8) were virtually indistinguishable overall. All the specimens showed remarkable axial compression deformation, and the outer steel tube exhibited local buckling.

After the compression test was stopped, the outer steel tube was cut off, and then the condition of the core concrete was observed, as shown in Figure 6. At first, the CFST-A1 specimen had an inclined shear rupture zone and/or even crushes in the core concrete, and the composite stub column could no longer withstand the axial load, as shown in Figure 6a. The analytical results demonstrated that the steel tube with a single cell cannot provide a sufficient confinement effect on the core concrete and therefore cannot effectively prevent the formation of the shear sliding crack in the core concrete. In addition, for the CFST-A2, CFST-A3, and CFST-A4 specimens, the core concrete was crushed only at the area of local buckling, as shown in Figure 6b–d, yet the core concrete remained intact due to the confinement effect of the steel tube. Therefore, the multicell steel tube helps enhance the confinement effect on the core concrete, fundamentally preventing the shear cracks in the core concrete from expanding rapidly and changing the failure mode of the composite stub columns.

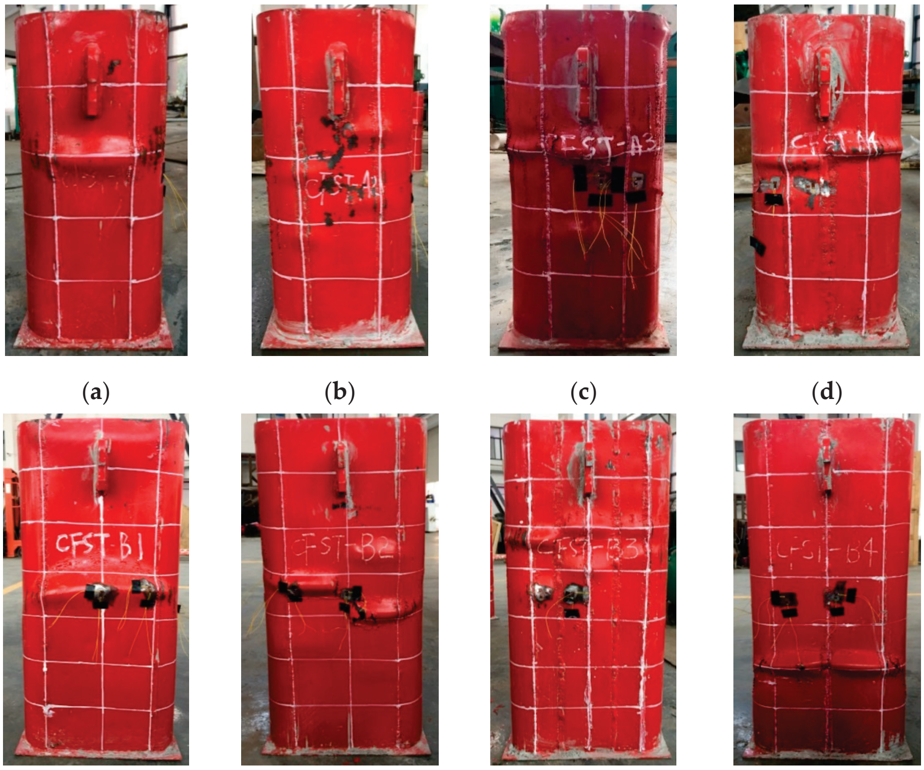
(**a**) (**b**) (**c**) (**d**)

(**e**) (**f**) (**g**) (**h**)

Figure 5. Typical failure modes for tested specimens. (**a**) CFST-A1. (**b**) CFST-A2. (**c**) CFST-A3. (**d**) CFST-A4. (**e**) CFST-A5. (**f**) CFST-A6. (**g**) CFST-A7. (**h**) CFST-A8.

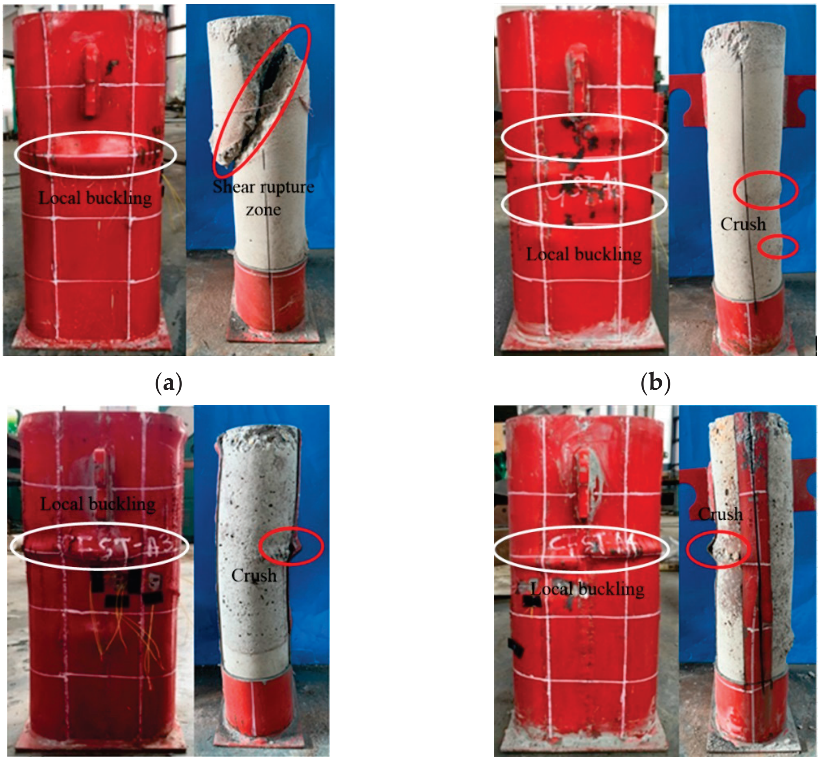
(**a**) (**b**)

(**c**) (**d**)

Figure 6. Typical failure modes for core concrete. (**a**) CFST-A1. (**b**) CFST-A2. (**c**) CFST-A3. (**d**) CFST-A4.

3.3. Ultimate Carrying Capacity

The presence of the multi-chamber steel tube stands out as a distinctive feature in M-CFRT stub columns, considerably setting them apart from conventional CFRT stub columns. Therefore, the multi-chamber steel tube, which affects the compressive behavior of M-CFRT stub columns, is discussed in detail in this section. Figure 7 shows the effects of chamber numbers and aspect ratio on the ultimate carrying capacity.

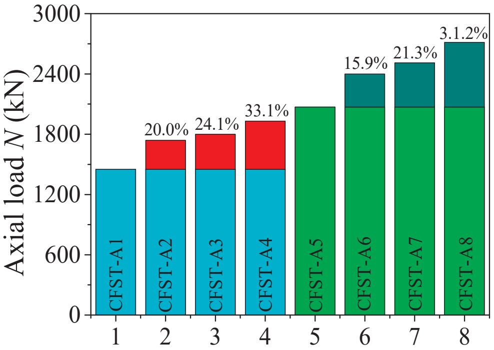

Figure 7. Comparison of ultimate carrying capacity for all specimens.

The number of chambers within the steel tube was considered while maintaining consistency with the aforementioned parameters. Compared with the ultimate carrying capacity of CFST-A1, those of CFST-A2, CFST-A3, and CFST-A4 were improved by 20.0%, 24.1%, and 33.1%, respectively, with the chamber number of the steel tube increasing from 1 to 2, 3, and 4. In addition, compared with the peak capacity of CFST-A5, those of CFST-A6, CFST-A7, and CFST-A8 were improved by 15.9%, 21.3%, and 31.2%, respectively, as the chamber number of the steel tube increased from 1 to 2, 3, and 4. Therefore, the above comparisons clearly demonstrated that the adopted multi-chamber steel tube can aid in enhancing the ultimate carrying capacity of composite columns.

The aspect ratio is another critical parameter that affects the property of M-CFRT stub columns; thus, it was scrutinized. The aspect ratios (B/D) were 2 and 3, and other parameters remained the same as above. Compared with the ultimate bearing capacity of CFST-A1–CFST-A4, that of CFST-A5–CFST-A8 remarkably improved by 33.4%, 37.9%, 39.4%, and 40.8%, respectively, with the aspect ratio increasing from 2 to 3. In summary, the ultimate carrying capacity is considerably affected by the aspect ratio.

3.4. Ductility

In this section, we select the ductility index (*DI*) [23] as a vital indicator for the compressive performance of M-CFRT stub columns. It is employed to analyze the effect of different factors on the ductility of composite columns. *DI* is defined as

$$DI = \frac{\varepsilon_{0.85}}{\varepsilon_{\mathrm{b}}} \tag{1}$$

where $\varepsilon_{0.85}$ is the axial strain when the load is reduced to 85% of the ultimate load, ε_{b} is equal to $\varepsilon_{0.75}/0.75$, and $\varepsilon_{0.75}$ is the axial strain when the load reaches 75% of the ultimate load in the pre-peak stage. $\varepsilon_{0.85}$ and ε_{b} were derived from Zhang et al. [23]. Figure 8 illustrates a comparison of the *DI* for all examined columns, calculated using Equation (1). A higher *DI* indicates a more gradual descent of the curve.

At first, Figure 8 reveals that compared with the *DI* value of CFST-A1, those of CFST-A2, CFST-A3, and CFST-A4 remarkably improved by 44.1%, 72.9%, and 91.5%, respectively, after welding multiple chambers into the steel tube. Additionally, compared with the *DI* value of CFST-A5, those of CFST-A6, CFST-A7, and CFST-A8 remarkably improved by 100.4%, 173.9%, and 239.1%, respectively.

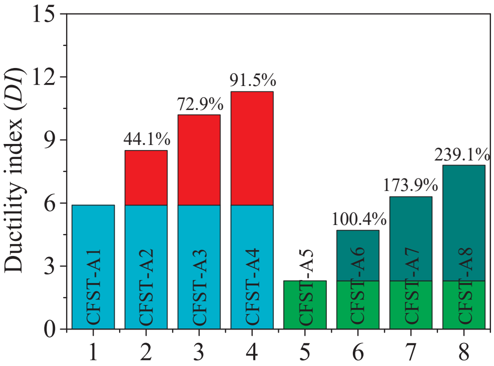

Figure 8. Comparison of ductility index *DI* for all specimens.

Therefore, the ductility of the composite stub column was improved by the multi-chamber steel tube. In particular, the higher the chamber number in the steel tube is, the better the ductility is. Moreover, in consideration of ductility, the use of M-CFRT stub columns with a multi-chamber steel tube and high-grade concrete is recommended in engineering practices.

4. FEA

4.1. FE Models

Several numerical studies have validated that the compressive performance of CFST columns with various cross-sections can be well and reasonably predicted through refined FE modeling with proper settings.

The FE models were created by ABAQUS/Standard 6.9 software [24], a widely employed tool for investigating the compressive behavior of CFST columns. The C3D8R solid element was used for all components of the composite columns. The mesh size in this study was 10 mm. The loading plate and the model were rigid bodies.

The interfacial behavior between the steel tube and core concrete, where the sliding formulation is finite sliding, was simulated using a surface-based interaction with hard contact in the normal direction and the Coulomb friction coefficient of 0.5 in the tangential direction to the interface. Two distinct surfaces may be coupled by a tie constraint so that no relative motion occurs between them. The interface interaction between different materials was derived from Zhang et al. [23].

The load was imposed by applying a specified displacement. Additionally, all degrees of freedom at the bottom and top ends of the M-CFRT stub columns had constraint. Figure 9 shows the FE models.

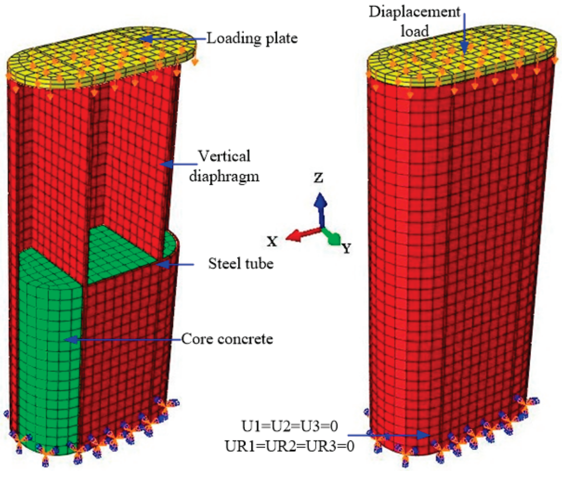

(**a**) (**b**)

Figure 9. The meshed FE model. (**a**) Different components element. (**b**) FE model.

4.2. Material Constitutive Models

In this study, ABAQUS/Standard FE software 6.9 [24] was employed for comprehensive FE modeling. The following stress–strain relationship for concrete under uniaxial compression, presented by Ding et al. [25], was used in the model:

$$y = \begin{cases} \frac{Ax+(B-1)x^2}{1+(A-2)x+Bx^2} & x \leq 1 \\ \frac{x}{\alpha(x-1)^2+x} & x > 1 \end{cases} \tag{2}$$

where the stress and strain ratios of the core concrete to the uniaxial compressive concrete are $y = \sigma/f_c$ and $x = \varepsilon/\varepsilon_c$, respectively. The core concrete's tension and strain are represented by σ and ε. The uniaxial compressive strength of concrete is expressed as $f_c = 0.4{f_{cu}}^{7/6}$, where f_{cu} is the compressive cubic strength of concrete. The strain associated with the peak compressive stress of concrete is denoted by ε_c, where ε_c is equal to $383\,{f_{cu}}^{7/18} \times 10^{-6}$. The parameter A is equal to $9.1{f_{cu}}^{-4/9}$, which is the ratio of the initial tangent modulus to the secant modulus at peak stress. $B = 1.6(A - 1)^2$ is a parameter that controls the decrease in the elastic modulus along the ascending branch of the axial stress–strain relationship. Parameter α can be assumed to be 0.15 for a steel tubular stub column filled with concrete.

Many experimental studies on the material properties of steel indicate that the constitutive behavior of steel can be described by an elasto-plastic model that takes into account the von Mises yield criteria, the Prandtl–Reuss flow rule, and isotropic strain hardening. This model has been validated in previous studies and is described below:

$$\sigma_i = \begin{cases} E_s\varepsilon_i & \varepsilon_i \leq \varepsilon_y \\ f_y & \varepsilon_y < \varepsilon_i \leq \varepsilon_{st} \\ f_y + \zeta E_s(\varepsilon_i - \varepsilon_{st}) & \varepsilon_{st} < \varepsilon_i \leq \varepsilon_u \\ f_u & \varepsilon_i > \varepsilon_u \end{cases} \tag{3}$$

where σ_i and ε_i are the equivalent stress and strain of the steel. f_y, and f_u(=1.5 f_y) are the yield strength and ultimate strength, respectively. E_s (=2.06 × 105 MPa) and E_{st} ($E_{st} = \zeta E_s$) are the elastic modulus and strengthening modulus. ε_y, ε_{st}, and ε_u are the yield strain, hardening strain, and ultimate strain of steel, which are described by $\varepsilon_u = \varepsilon_{st} + 0.5 f_s/(\zeta E_s)$, $\varepsilon_{st} = 12\varepsilon_b$, $\varepsilon_u = 120\varepsilon_b$, and $\zeta = 1/216$.

4.3. Experimental Verification

Based on the above settings, the validation of the FE modeling method involved a comparison between experimental and numerical results, focusing on axial load–strain curves and ultimate bearing capacity. This process assessed the practicality and precision of the modeling approach.

Figure 10 reflects the deformation process of specimens at various stages through axial load–strain curves. Table 1 compares the ultimate bearing capacity values obtained from the experiment ($N_{u,Exp}$) and the corresponding numerical results ($N_{u,FE}$). As shown in Figure 10, almost no differences between measured curves and predicted curves are observed at the initial stage. Moreover, a slight difference is observed between them at other stages, especially for the elastic–plastic stage. This difference exists because although FE models were generated under ideal conditions, preserving the accuracy of measured curves was impossible once concrete crushing and steel tube yielding started. In addition, a reasonable agreement is found, and the average ratio of $N_{u,FE}/N_{u,e}$ is 0.99, with a coefficient of variation of 0.084. Hence, above comparisons show that the FE-simulated curves can show satisfactory and reasonable agreement with the measured curves.

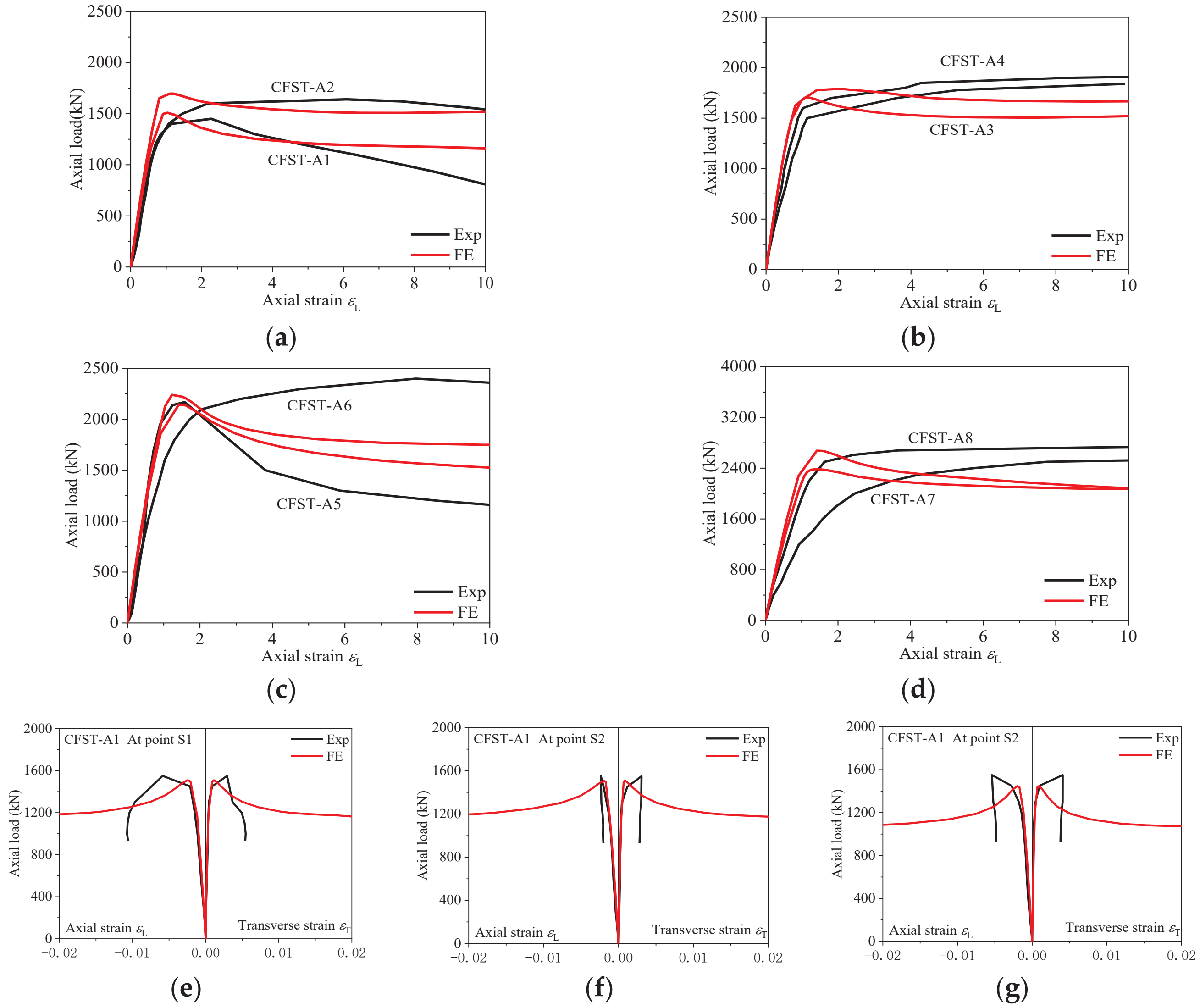

(a) (b) (c) (d) (e) (f) (g)

Figure 10. Comparisons of axial load vs. strain curves of specimens between experimental and FE results. (**a**) CFST-A1 and CFST-A2. (**b**) CFST-A3 and CFST-A4. (**c**) CFST-A5 and CFST-A6. (**d**) CFST-A7 and CFST-A8. (**e**) CFST-A1 at point S1. (**f**) CFST-A1 at point S2. (**g**) CFST-A1 at point S3.

Figure 11 shows the comparison of the stress contour of the core concrete at the ultimate loading state; the blue region represents the unconstrained region of the core concrete. (1) As the chamber in the steel tube is increased, the unconstrained area of the core concrete evidently decreases. (2) Additionally, almost no difference is found in the constrained area of the core concrete on the semicircle cross-section, owing to the strong confinement effect of the circular steel tube on the core concrete. It does not matter how many chambers there are. (3) Most notably, the unconstrained areas of the core concrete between two chambers and four chambers are almost the same, indicating that the steel tube with four chambers cannot remarkably improve the effect of restraint, and the effect of the vertical diaphragm on semicircles on the confinement effect is limited and even neglected.

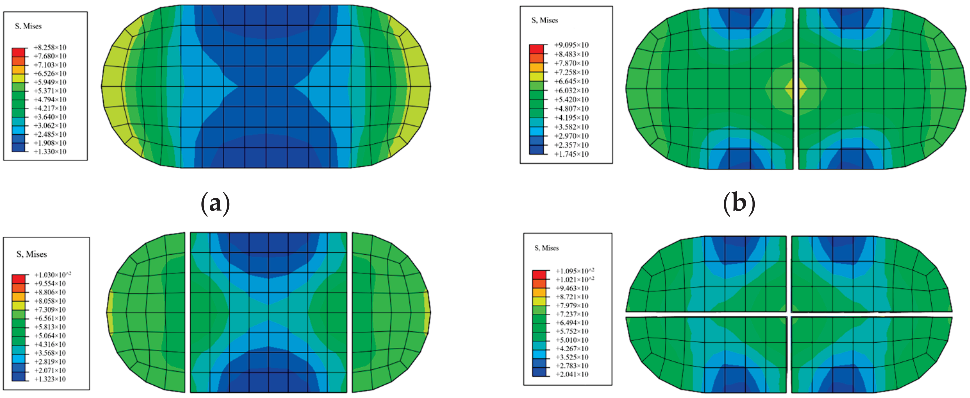

(**a**) (**b**)

(**c**) (**d**)

Figure 11. Comparisons of stress contours of the core concrete at the ultimate state. (**a**) single chambers. (**b**) two chambers. (**c**) three chambers. (**d**) four chambers.

5. Design Approach

Currently, various design formulas are used to determine the ultimate carrying capacity of composite columns, e.g., CFT stub columns with rectangular, square, circular, polygonal, and round-end cross-sections. Nevertheless, M-CFRT stub columns are not covered by the existing design approaches; rather, they are only appropriate for conventional CFT stub columns. In light of the foregoing research, this study aims to provide a novel formula for M-CFRT stub columns.

5.1. Parametric Study

A total of 96 FE models were established in consideration of the following key parameters: concrete strength ranging from C40 to C100, steel strength values of 235, 345, and 420 MPa, aspect ratio ranging from 2 to 4, steel ratio ranging from 0.02 to 0.08, and cell number ranging from 1 to 4. Table 2 lists the detailed parameters of FE models used in the calculation, with the columns with D = 1200 taken as examples.

Table 2. Geometric sizes of specimens for parametric study.

D/mm	*B*/mm	*B*/*D*	ρ_s	*Cell Number*	*L*/mm
1200	2400	2	0.02~0.08	1~4	5500
	3600	3			5500
	4800	4			7000

Noted: Q235 paired with C40 and C60, Q345 paired with C60 and C80, and Q420 paired with C80 and C100.

5.2. Model Simplification

On the basis of the aforementioned study, the M-CFRT stub columns with three chambers are inferred to have exhibited the optimal compressive performance, followed by the four-, two-, and single-chamber arrangements. In addition, M-CFRT stub columns can be considered a combination of rectangular/square and circular CFT stub columns. Hence, the empirical formula for calculating the ultimate bearing capacity of composite stub columns can be established through the application of the limit equilibrium approach, as outlined in references [3,21].

Numerical results are used to extract the stress distribution at the peak condition of M-CFRT stub columns. The stress envelope of the M-CFRT stub columns can be computed more simply, as illustrated in Figure 12.

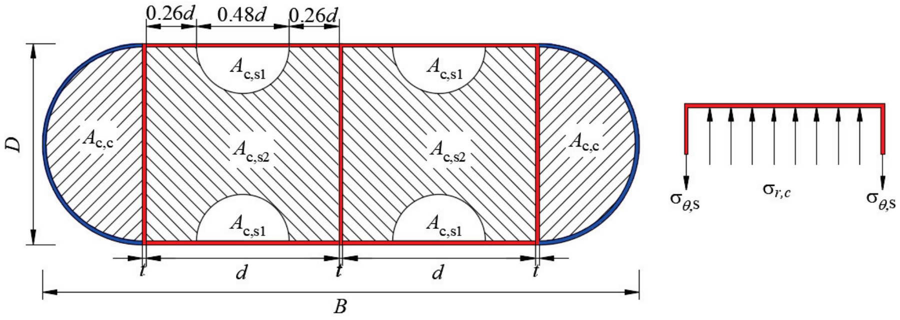

Figure 12. Simplified stress envelope with the mid-section of the M-CFRT stub column.

The reliance on the stress distribution and the unequivocal application of the superposition principle for the concrete cross-section at its peak state are imperative. In this context, A_c represents the overall cross-sectional area of the core concrete, while $A_{c,s2}$ and $A_{c,c}$ denote the areas of the core concrete constrained by square steel tubes and circular steel tubes, respectively. Additionally, $A_{c,s1}$ signifies the unconstrained region of the core concrete. Furthermore, as illustrated in Figure 11, d is the width of the square concrete ($d = D - 2t$). The relationships listed below can be stated in this manner:

$$\begin{cases} A_{c,c}+(n-1)A_{c,s} = A_c \\ A_{c,s1} = 0.18A_{c,s} \\ A_{c,s2} = 0.82A_{c,s} \end{cases} \tag{4}$$

5.3. Formulation

On the basis of the verified FE models, a parametric study on 96 FE full-scale models were further performed to examine the performance of M-CFRT stub columns subjected to axial loading: aspect ratio, which ranges from 1 to 4; steel ration, which ranges from 0.05 to 0.2; concrete strength, which ranges from C40 to C100; and steel yield strength, which ranges from Q235 to Q420.

The longitudinal stress of the square/rectangular steel tube was extracted as soon as the numerical results of the axial load–strain response attained its peak state. Moreover, Figure 13 illustrates the correlation between the ultimate strength ($f_{sc} = N_u/A_{sc}$) and ratio value of axial stress to yield strength for CFT stub columns with square/rectangular cross-sections, where the axial stress of the steel tube is denoted as $\sigma_{L,s}$.

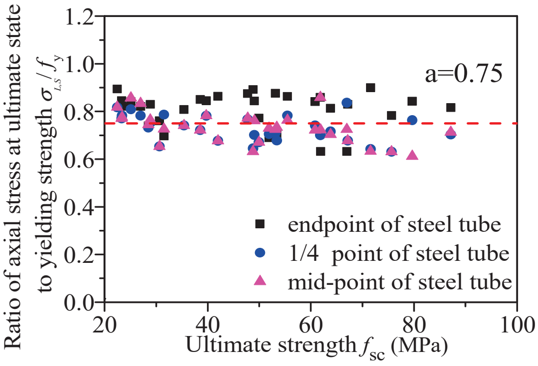

Figure 13. Average ratio of axial compressive stress to yield stress of the steel tube.

As shown in Figure 11, when M-CFRT columns reach their maximum strength, the ratio value of the axial compressive stress to the yield stress is as follows:

$$\sigma_{L,s} = 0.75f_y \tag{5}$$

The tensile transverse stress ($\sigma_{\theta,\mathrm{s}}$) of the steel tube can be determined by applying the von Mises yield criterion for steel, as follows:

$$\sigma_{\theta,\mathrm{s}} = 0.36 f_{\mathrm{y}} \tag{6}$$

As shown in Figure 11, the relationship between the transversal stress ($\sigma_{\theta,\mathrm{s}}$) of the steel tube and the radial concrete stress ($\sigma_{r,\mathrm{c}}$) of the core concrete at the ultimate state can be expressed as follows:

$$\sigma_{r,\mathrm{c}} = \frac{2t\sigma_{\theta,\mathrm{s}}}{d} \tag{7}$$

In consideration of the confining stress, the axial compressive stress ($\sigma_{L,\mathrm{c}}$) of the core concrete can be expressed as follows:

$$\sigma_{L,\mathrm{c}} = f_{\mathrm{c}} + p\sigma_{r,\mathrm{c}} \tag{8}$$

where p is the coefficient of lateral pressure ($p = 3.4$) [26].

On the basis of the static equilibrium criterion, the ultimate carrying capacity (N_{u}) of M-CFRT columns in the mid-height region is categorized into two parts, attributable to the distinct confinement effects of square/rectangular and circular steel tubes on the core concrete: the circular CFT stub column ($N_{\mathrm{u,c}}$) and the square/rectangular CFT column ($N_{\mathrm{u,s}}$); therefore, this formula can be expressed as

$$N_{\mathrm{u}} = N_{\mathrm{u,c}} + N_{\mathrm{u,s}} \tag{9}$$

$$N_{\mathrm{u}} = (A_{\mathrm{c.c}} f_{\mathrm{c}} + 1.7A_{\mathrm{s.c}} f_{\mathrm{y}}) + ((n-1)\sigma_{L,\mathrm{c}} A_{\mathrm{c,s2}} + f_{\mathrm{c}} A_{\mathrm{c,s1}} + \sigma_{L,\mathrm{s}} A_{\mathrm{s,s}}) \tag{10}$$

The cross-sectional area of the circular steel tube is denoted as $A_{\mathrm{s,c}}$, while the cross-sectional area of the square steel tube is represented as $A_{\mathrm{s,s}}$; A_{s} represents the total cross-sectional area of the steel tube, $A_{\mathrm{s}} = A_{\mathrm{s,c}} + A_{\mathrm{s,s}}$; and n is the aspect ratio (B/D).

Subsequently, substituting Equations (4)–(8) into Equation (10), the resulting ultimate carrying capacity of the columns (N_{u}) can be defined as

$$N_{\mathrm{u}} = (A_{\mathrm{c.c}} f_{\mathrm{c}} + 1.7A_{\mathrm{s.c}} f_{\mathrm{y}}) + ((n-1)\ A_{\mathrm{c,s}} f_{\mathrm{c}} + 1.25A_{\mathrm{s.s}} f_{\mathrm{y}}) \tag{11}$$

$$N_{\mathrm{u}} = A_{\mathrm{c}} f_{\mathrm{c}} + (1.7\ A_{\mathrm{s.c}} + 1.25A_{\mathrm{s.s}}) f_{\mathrm{y}} \tag{12}$$

Herein, when the aspect ratio ($n = B/D$) is taken as 1, Equation (9) can be expressed as follows:

$$N_{\mathrm{u}} = A_{\mathrm{c}} f_{\mathrm{c}} + 1.7A_{\mathrm{s.c}} f_{\mathrm{y}} \tag{13}$$

The equation denoted by Equation (11), incorporating the confinement effect exerted by a multi-chamber steel tube on the core concrete, is utilized to estimate the ultimate bearing capacity of M-CFRT stub columns. Moreover, it is applicable for predicting the ultimate carrying capacity of circular CFT stub columns, as expressed in Equation (10), namely, M-CFRT stub columns with $B/D = 1$.

5.4. Formula Validation

To confirm the overall applicability and to assess the precision of the proposed formula (Equation (11)), Figure 14 illustrates the comparison of the ultimate carrying capacity between the predicted and FEA results. The comparison involves Eurocode 4 design formulas, comprising 96 FE full-scale models; the ratios represent the values of the predicted outcomes divided by the tested/FE results. The accuracy of the predicted results increases when the average ratio approaches 1.

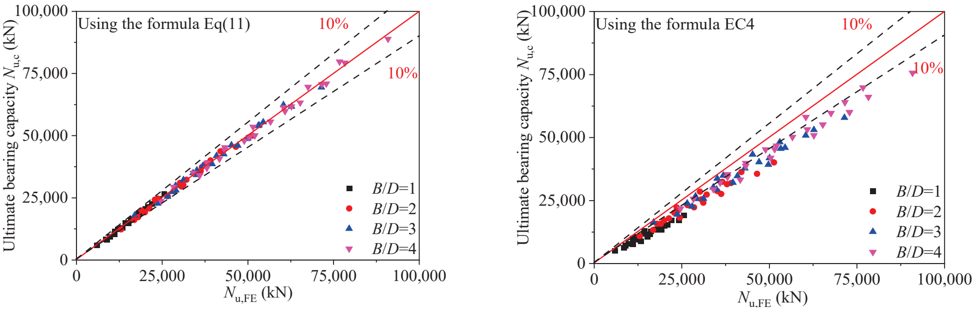

(**a**) (**b**)

Figure 14. Comparison of the ultimate bearing capacity between FE and predicted results. (**a**) Formula Equation (11). (**b**) Eurocode 4.

As depicted in Figure 14a, the average ratio of $N_{\mathrm{u,FE}}/N_{\mathrm{u,Eq}}$ is 1.00, with a coefficient of variation of 0.032; the absolute average error is 0.026. In this study, the comparisons clearly demonstrate that reasonable agreement is obtained between the numerical results and the corresponding predicted values, suggesting that Equation (11) can be a reasonable estimate for the ultimate carrying capacity.

Meanwhile, Figure 14b shows that the average ratio of $N_{\mathrm{u,FE}}/N_{\mathrm{u,EC}}$ is 1.20, with a coefficient of variation of 0.080; the absolute average error is 0.143. Evidently, the FE results considerably surpass the corresponding predicted values specified in the standard Eurocode 4 [26], while the predicted strength is relatively conservative. This is because the confinement effects of the semicircle and rectangular steel tube on the core concrete are different in degrees, and both the confinement effects in standard Eurocode 4 are not considered and also overlooked. To sum up, the suggested formula Equation (11) is a reasonable and feasible calculation method.

6. Conclusions

The primary aim of this research is to investigate the compressive behavior of M-CFRT stub columns using a combination of experimental and numerical investigations. The following conclusions can be drawn:

(1) On the basis of the test results, all the specimens under axial loading are thought to undergo three stages before failing: elastic stage, elastic–plastic stage, and failure stage. Additionally, the vertical diaphragm (chamber number), which can effectively prevent and/or delay the core concrete crushing, essentially changes the failure modes of M-CFRT stub columns. Furthermore, M-CFRT stub columns exhibit greater ductility compared with CFRT stub columns.

(2) The ultimate carrying capacity and ductility of M-CFRT stub columns remarkably increase with the increase in the chamber number in the steel tube. That is, the axial behavior of M-CFRT stub columns is improved by the multi-chamber steel tube, namely, the vertical diaphragm.

(3) The observed strong concordance between tested and FE results suggests a favorable agreement. On the basis of these observations, a simplified formula for calculating the ultimate bearing capacity of M-CFRT stub columns is introduced, employing the limit equilibrium method. The predicted results from this formula align well with FE and experimental ones. Consequently, this formula is a reasonable and feasible calculation method for M-CFRT stub columns.

Author Contributions: Software, investigation, data curation, writing—original draft, and funding acquisition, J.L.; methodology, validation, formal analysis, resources, and funding acquisition, T.Z.; conceptualization, writing—review and editing, visualization, supervision, and Funding acquisition, Z.P.; conceptualization, methodology, investigation, resources, and project administration, F.M. All authors have read and agreed to the published version of the manuscript.

Funding: This research is financially supported by the National Natural Science Foundation of China (Nos. 52008159 and 52208220), Hunan Education Department Foundation Funded Project (No. 21A0504), Natural Science Foundation of Hunan Province (No. 2022JJ30112), Aid program for Science and Technology Innovative Research Team in Higher Educational Institutions of Hunan Province, Science and Technology Project of Henan Province (No. 222102320014), Education Reform Research and Practice Project (No. zhjy23-78), Graduate Quality Curriculum Project (No. 2023YJSKC05), Key Research and Development Project of Anhui Province (No. 2022o07020003), Scientific and Technological Project for Housing and Urban–Rural Development in Anhui Province (No. 2023-YF-112), Science and Technology Planning Project of Guichi District, Chizhou City (No. GCKJ202210), and Scientific Research Team Plan of Zhengzhou University of Aeronautics (No. 23ZHTD01009). Their support is gratefully acknowledged.

Data Availability Statement: The data presented in this study are available upon request from the corresponding author. The data are not publicly available due to privacy.

Conflicts of Interest: Authors Zhicheng Pan and Fanjun Ma were employed by the company Sinohydro Engineering Bureau 8 Co., Ltd. Author Zhicheng Pan was employed by the company Power China Chizhou Changzhi Prefabricated Construction Co., Ltd. The remaining authors declare that the research was conducted in the absence of any commercial or financial relationships that could be construed as a potential conflict of interest.

References

1. Shen, Q.H.; Wang, J.H.; Wang, W.Q.; Wang, Z.B. Performance and design of eccentrically-loaded concrete-filled round-ended elliptical hollow section stub columns. *J. Constr. Steel Res.* **2018**, *150*, 99–114. [CrossRef]
2. Singh, H.; Tiwary, A.K.; Eldin, S.M.; Ilyas, R.A. Behavior of stiffened concrete-filled steel tube columns infilled with nanomaterial-based concrete subjected to axial compression. *J. Mater. Res. Technol.* **2023**, *24*, 9580–9593. [CrossRef]
3. Ding, F.X.; Fu, L.; Yu, Z.W.; Li, G. Mechanical performances of concrete-filled steel tubular stub columns with round ends under axial loading. *Thin-Walled Struct.* **2015**, *97*, 22–34.
4. Liao, J.; Zeng, J.J.; Quach, W.M.; Zhou, J.K. Axial compressive behavior and model assessment of FRP-confined seawater sea-sand concrete-filled stainless steel tubular stub columns. *Compos. Struct.* **2023**, *311*, 116782. [CrossRef]
5. Liao, J.; Li, Y.L.; Ouyang, Y.; Zeng, J.J. Axial compression tests on elliptical high strength steel tubes filled with self-compacting concrete of different mix proportions. *J. Build. Eng.* **2021**, *40*, 102678. [CrossRef]
6. Al-Nini, A.; Nikbakht, E.; Syamsir, A.; Shafiq, N.; Mohammed, B.S.; Al-Fakih, A.; Al-Nini, W.; Amran, Y.M. Flexural behavior of double-skin steel tube beams filled with fiber-reinforced cementitious composite and strengthened with CFRP sheets. *Materials* **2020**, *13*, 3064. [CrossRef]
7. Xie, J.X.; Lu, Z.A.; Tang, P.; Liu, D. Modal analysis and experimental study on round-ended CFST coupled column cable stayed bridge. In Proceedings of the 2nd International Conference on Mechanic Automation and Control Engineering (MACE), Inner Mongolia, China, 15–17 July 2011; Volume 8, pp. 2302–2304.
8. Xie, J.X.; Lu, Z.A. Numerical simulation and test study on non-uniform areas of round-ended CFST tubular tower. In Proceedings of the Third International Conference on Information and Computing (ICIC2010), Wuxi, China, 4–6 June 2010; Volume 4, pp. 19–22.
9. Al-Fakih, A.; Al-Osta, M.A. Finite element analysis of rubberized concrete interlocking masonry under vertical loading. *Materials* **2022**, *15*, 2858. [CrossRef] [PubMed]
10. Gong, F.; Maekawa, K. Multi-scale simulation of freeze-thaw damage to RC column and its restoring force characteristics. *Eng. Struct.* **2018**, *156*, 522–536. [CrossRef]
11. Zhu, X.; Abe, H.; Hayashi, D.; Tanaka, H. Behavioral characteristics of RC beams with non-uniform corrosion along the reinforcement. *J. Intell. Constr.* **2023**, *1*, 9180019. [CrossRef]
12. Li, P.; Wang, H.; Nie, D.; Wang, D.; Wang, C. A method to analyze the long-term durability performance of underground reinforced concrete culvert structures under coupled mechanical and environmental loads. *J. Intell. Constr.* **2023**, *1*, 9180011. [CrossRef]
13. Wan, C.Y.; Zha, X.X. Nonlinear analysis and design of concrete-filled dual steel tubular columns under axial loading. *Steel Compos. Struct.* **2016**, *20*, 571–597. [CrossRef]
14. Zhu, A.Z.; Zhang, X.W.; Zhu, H.P.; Zhu, J.H.; Lu, Y. Experimental study of concrete filled cold-formed steel tubular stub columns. *J. Constr. Steel Res.* **2017**, *134*, 17–27. [CrossRef]
15. Wang, J.F.; Shen, Q.H.; Jiang, H.; Pan, X.B. Analysis and design of elliptical concrete filled thin-walled steel stub columns under axial compression. *Int. J. Steel Struct.* **2018**, *18*, 365–380. [CrossRef]
16. Zhao, Y.G.; Yan, X.F.; Lin, S.Q. Compressive strength of axially loaded circular hollow centrifugal concrete-filled steel tubular short columns. *Eng. Struct.* **2019**, *201*, 109828. [CrossRef]
17. Pi, T.; Chen, Y.; He, K.; Han, S.H.; Wan, J. Study on circular CFST stub columns with double inner square steel tubes. *Thin-Walled Struct.* **2019**, *140*, 195–208. [CrossRef]

18. Zhou, F.; Young, B. Experimental investigation of concrete-filled single-skin and double-skin steel oval hollow section stub columns. *Thin-Walled Struct.* **2019**, *140*, 157–167. [CrossRef]
19. Han, L.H.; Ren, Q.X.; Li, W. Tests on stub stainless steel-concrete-carbon steel double-skin tubular (DST) columns. *J. Constr. Steel Res.* **2011**, *67*, 437–452. [CrossRef]
20. Wang, J.F.; Shen, Q.H. Numerical analysis and design of thin-walled RECFST stub columns under axial compression. *Thin-Walled Struct.* **2018**, *129*, 166–182. [CrossRef]
21. Ding, F.X.; Fu, L.; Liu, X.M.; Liu, J. Mechanical performances of track-shaped rebar stiffened concrete-filled steel tubular (SCFRT) stub columns under axial compression. *Thin-Walled Struct.* **2016**, *99*, 168–181. [CrossRef]
22. *GB 50017-2003*; Code for Design of Steel Structures. China Planning Press: Beijing, China, 2003.
23. Zhang, T.; Ding, F.X.; Wang, L.P.; Liu, X.M.; Jiang, G.S. Behavior of polygonal concrete-filled steel tubular stub columns under axial loading. *Steel Compos. Struct.* **2018**, *28*, 573–588.
24. Smith, M. *ABAQUS/Standard User's Manual, Version 6.9*; Dassault Systèmes Simulia Corp.: Providence, RI, USA, 2009.
25. Ding, F.X.; Ying, X.Y.; Zhou, L.C.; Yu, Z.W. Unified calculation method and its application in determining the uniaxial mechanical properties of concrete. *Front Struct. Civ. Eng.* **2011**, *5*, 381–393. [CrossRef]
26. *EN 1994-1-1:2004*; Design of Composite Steel and Concrete Structures Part1-1: General Rules-Structural Rules for Buildings. European Committee for Standardization: Brussels, Belgium, 2004.

buildings

MDPI

Article

Study on Structural Parameter Sensitivity and the Force Transmission Mechanism of Steel–Concrete Joints in Hybrid Beam Bridges

Lijun Jia [1], Shanshan Yuan [1], Jiawei Li [1], Tingying Wu [2], Gangyi Zhan [3] and Huiteng Pei [1,2,*]

[1] Department of Bridge Engineering, College of Civil Engineering, Tongji University, No. 1239 Siping Road, Shanghai 200092, China; jialj@tongji.edu.cn (L.J.); 2232315@tongji.edu.cn (S.Y.); 2132367@tongji.edu.cn (J.L.)
[2] Jiangxi Communications Design and Research Institute Co., Ltd., Nanchang 330052, China; lufh2009@163.com
[3] China Railway Shanghai Design Institute Group Co., Ltd., Shanghai 200070, China; civil_zgy@vip.163.com
* Correspondence: 2180098@tongji.edu.cn

Abstract: In this study, a refined model of the Shanghai Damaogang Bridge's (hybrid beam type) box deck joints is established. The correctness of the model is verified by construction monitoring. For the front and back bearing plates, the force performance of the joint members under the most unfavorable loads is investigated, and the force transmission mechanism is analyzed. The influence of the bearing plate thickness and the joints' stiffness on the stress distribution of the joint members, the internal force of the joints, and the force-transfer efficiency is investigated by the method of controlling variables, and the optimal structural parameters of the nodes are also studied. The results show that, within the proximity of the back bearing plate, the thickness of the back bearing plate affects stress distribution in the joint. The increased stiffness of the welding studs makes the range of shear force along the bridge direction of the top and bottom welding studs larger, and the longitudinal distribution of welding stud shear force is more uneven. The concrete structure bears a higher proportion of the internal force in the joint compared to the steel structure.

Keywords: hybrid beam bridge; steel–concrete joint; bearing plate; welding studs; force transmission mechanism

1. Introduction

Hybrid beam bridges employ steel beams instead of concrete beams in the mid-span to reduce the self-weight of the main beam, therefore improving its span capacity and fully leveraging the material properties of both steel and concrete. Unlike composite beam bridges that utilize multiple materials on the same section [1–3], hybrid beam bridges utilize different materials along the span direction. Therefore, steel–concrete joints are key structures within hybrid beam bridges, and the rationality of these joints directly impacts the safety of the bridge. With the widespread adoption of the hybrid beam bridge, such as the Xupu Bridge in Shanghai, Yongjiang Railway Bridge in Ningbo, Mawei Bridge in Fuzhou, and so on, scholars are increasingly focusing on the mechanical properties of steel–concrete joints.

The overall mechanical performance and force transfer mechanism of the joint are crucial aspects in the research on the hybrid beam joints [4]. Tang et al. [5] conducted a finite element analysis to study the force characteristics and structural parameters of the cellular steel–concrete joint in the back bearing plate of a hybrid girder cable-stayed bridge. Zhang et al. [6] performed model tests and finite element analyses on the steel–concrete joints in the Wusu Bridge, examining the force transmission mechanism of the joints in a hybrid beam cable-stayed bridge. Xing et al. [7] conducted model tests on the steel–concrete joints in a cable-stayed bridge, establishing a finite element analysis model using ANSYS to discuss the simulation analysis method used for the steel–concrete joints in a hybrid beam cable-stayed bridge. Zhang et al. [8], based on the elastic continuous medium layer method and considering the slip between the steel structure and the concrete and the local pressure of the concrete, proposed a theoretical calculation method for the cellular steel–concrete joints within a back bearing plate in a hybrid beam, and analyzed the factors affecting the force transmission mechanism of the joint using the finite element method. He et al. [9] studied the mechanical properties of steel–concrete joints using UHPC grouting in single cable-plane hybrid beam cable-stayed bridges through model tests and numerical analyses. Yang et al. [10] conducted model tests on the joints in a high-speed railway hybrid beam cable-stayed bridge, proposed simplified calculation formulas for deflection and rotation, and analyzed the thickness of the bearing plate at the joint based on the finite element method. Pu et al. [11] investigated the fatigue performance of the joints in a new type of long-span railway cable-stayed bridge based on model tests and numerical analyses. The results show that the thickness of the end bearing plate significantly influences the fatigue performance of the joint, and a recommended thickness range of the end bearing plate is provided. Gu et al. [12] studied the structural performance of the steel–concrete joints in a hybrid beam cable-stayed bridge through model tests and the finite element method, analyzing the force transmission mechanism of the joints. Yao et al. [13] proposed a new type of steel–concrete joint for long-span railway hybrid beam cable-stayed bridges, conducting model tests and studying the influence of different structural parameters on the mechanical properties of the joint using the finite element method. Xu et al. [14] established a full-scale model of a new type of joint, performed static bending tests, and analyzed the influence of material damage plasticity on the mechanical properties of the new joint based on the finite element method. Zhou et al. [15] conducted model tests and a finite element analysis on the joints in a railway bridge, studying the force transmission mechanism and the influence of structural design parameters on the mechanical properties of the joint. Liang et al. [16] conducted half-scale model tests on the joint between a steel–concrete composite beam and concrete beam in a large-span cable-stayed bridge. They established a finite element model to study the crack development law of the joint and proposed a new type of joint with an improved crack resistance performance. However, most of these studies are centered on the joints in cable-stayed bridges, and the construction methods and stress characteristics of hybrid continuous beam bridges differ from those of cable-stayed bridges. Further investigations are required to study the structural parameter sensitivity and force transmission mechanism of steel–concrete joints in hybrid beam bridges.

The design and mechanical properties of the internal structure of the joint are also important aspects in the studying joints. He et al. [17] introduced a new type of steel–concrete joint for hybrid beam cable-stayed bridges using perfo-bond connectors and analyzed its mechanical properties by carrying out push-out tests on perfo-bond connectors and 1:2 model tests on the joint. He et al. [18] investigated the failure mode, ductility, and other mechanical properties of perfo-bond connectors in hybrid beam cable-stayed bridge joints. They proposed a method for predicting the ultimate resistance of perfo-bond connectors using the shear failure of the dowel. Jin et al. [19] designed 39 push-out specimens to study the influence of various parameters such as hole size and hole shape on the mechanical properties of large perfo-bond connectors in the steel–concrete joints in hybrid bridges. They proposed a formula for calculating the shear capacity of the encased perfo-bond connector. Zou et al. [20] developed a finite element model for push-out tests on perfo-bond connectors in the steel–concrete joints in hybrid bridges and studied the shear performance and force transmission mechanism of perfo-bond connectors. Based on numerical simulation and theoretical methods, Zou et al. [21] further delved into the mechanical behavior of perfo-bond connectors at the joint and gave a simplified calculation method for determining the maximum slip, effective utilization rate, and load ratio. Zhou et al. [22] designed a full-scale model of a joint from a hybrid beam cable-stayed bridge and conducted fatigue tests based on this model to study the fatigue performance of the joint's steel structure, concrete structure, and connectors.

In addition to the aforementioned considerations, scholars have also studied the influence of the joint's position on the bridge structure. Zhao et al. [23] examined the influence of joint positioning on the nonlinear stability of the construction process in large-span hybrid beam cable-stayed bridges. He et al. [24] proposed a method for determining the optimal joint location based on the concept of system equivalence, and the effectiveness of the method was verified by some case studies.

Hybrid beams find application in cable-stayed bridges, suspension bridges, and beam bridges [25]. In different bridge types, the force characteristics of the joints in the hybrid beams are different. In cable-stayed bridges, the axial force generated by cable action in the main beam is conducive to the connection between the steel structure and the concrete in the joint. While in continuous beam bridges, the main beam primarily experiences shear force and a bending moment. To ensure joint reliability, multiple longitudinal prestressed tendons need to be placed in this section. At present, steel–concrete hybrid structures are mostly employed in cable-stayed bridges and relatively less in beam bridges. Existing studies have primarily focused on the hybrid beam joints in cable-stayed bridges. However, because of the excellent spanning capacity and economic performance of hybrid beam bridges, more and more hybrid beam bridges have been built, but as mentioned above, the joint structure used in beam bridges is complex, and the internal force transmission and distribution are not clear yet. Moreover, most of the above studies are based on finite element models, while this study establishes a finite element model of the joints based on the engineering background of the Damaogang Bridge in Shanghai, and verifies the correctness of the model through construction monitoring. Combining this model with on-site construction monitoring, our study investigates the impact of bearing plate thickness on the joint stress distribution. Additionally, it explores the influence of welding stud stiffness on the shear force in the top and bottom welding studs, and analyzes the force transmission mechanism in the joint.

2. Engineering Background

Damaogang Bridge in Shanghai is a three-span steel–concrete hybrid continuous-girder bridge with a span arrangement of (65 + 135 + 65) m. The mid-span of this bridge consists of a 40 m long concrete beam, a 55 m long steel beam, and a 40 m long concrete beam. The steel box girder's ends are connected to the concrete sections through the steel–concrete joints featuring the front and back bearing plates with cells. In order to ensure the shear force transfer between the concrete beam and steel beam, and to prevent stripping between the steel structure and the concrete structure, welding studs are arranged on the top and bottom plates and bearing plates. Additionally, the perfo-bond connectors embedded in the concrete are employed on the top and bottom plates of the steel box girder. At the same time, steel tendons are connected in the hole, subjecting the concrete within to a three-dimensional compression state, thereby enhancing the shear bearing capacity. The longitudinal internal prestressed steel strand is anchored at one end to the end bearing plate, while the other end is anchored within the concrete. The externally prestressed steel strand passes through the joints and the steel beam, with both ends anchored in the concrete to make the connection between the concrete beam and the steel beam firm. Figure 1 shows the joint structure.

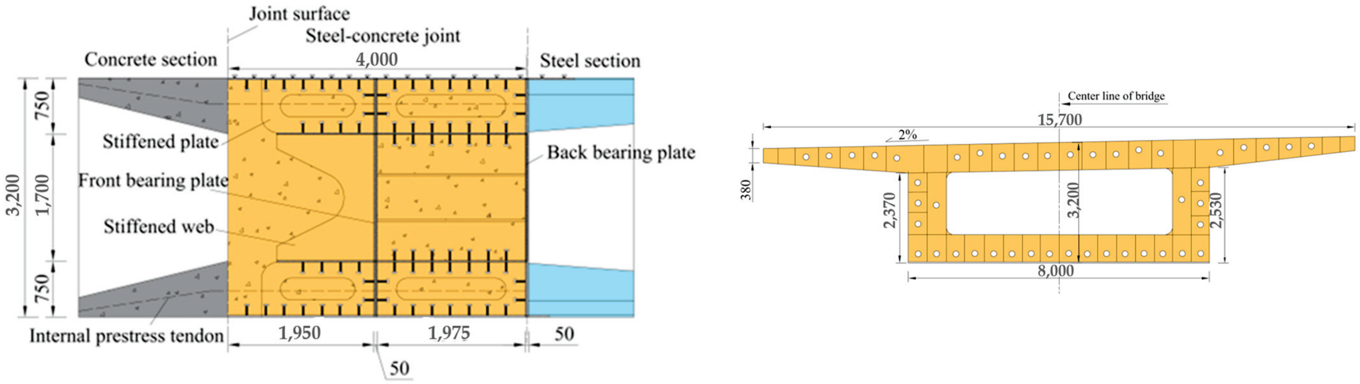

(**a**) (**b**)

Figure 1. (**a**) Longitudinal section of joint (unit: mm); (**b**) cross section of joint (unit: mm).

3. Finite Element Model

3.1. Establishment of Finite Element Model

To study the reasonable structural parameters and force transmission mechanism of the steel–concrete joint, this paper establishes a refined finite element model of the bridge joint using the ANSYS version 18.2 mechanical software, and verifies the correctness of the model with on-site monitoring data.

The joint of the bridge is located at about one-third of the main span, with relatively small structural internal forces. At the same time, the joint uses thicker steel plates and concrete, and a concrete beam transition section and a steel beam transition section are set at both ends of the joint, resulting in lower stress levels for each component of the joint. Without considering the local stress concentration, it can be considered that the components of the joint have always been in the linear elastic range under load. Therefore, this paper only establishes the linear constitutive relationship of the material during simulation, and the material properties are shown in Table 1. In the model, the tension force of the finely rolled threaded tendon is 568.2 kN, and the controlled tension stress of the longitudinal steel strand is 1395 MPa, taking into account a 20% prestress loss.

Table 1. Material/component properties.

Material/Component	Elastic Modulus (10^4 MPa)	Poisson's Ratio	Volume Weight (kN/m^3)
concrete	3.55	0.2	26
steel	20.6	0.3	78.5
vertical prestressed tendon	20.0	/	78.5
longitudinal prestressed steel strand	19.5	/	78.5

In the finite element model, the steel plate is simulated by shell181 elements; the concrete in the joint cell is simulated by solid65 elements; the prestressed tendon is simulated by link8 elements; and the tensioning process of the prestressed tendon is simulated by giving the initial strain to the link8 elements. The linear axial spring element Combin14 is employed to simulate the studs and perfo-bond connectors at the joint. The steel plate element is discretized into quadrilateral grids, while the concrete element is discretized into tetrahedral grids. The structural influence of prestressed tendons is primarily concentrated at the anchorage points, and each prestressed tendon is represented by a single element. The finite element model of the joint is shown in Figure 2.

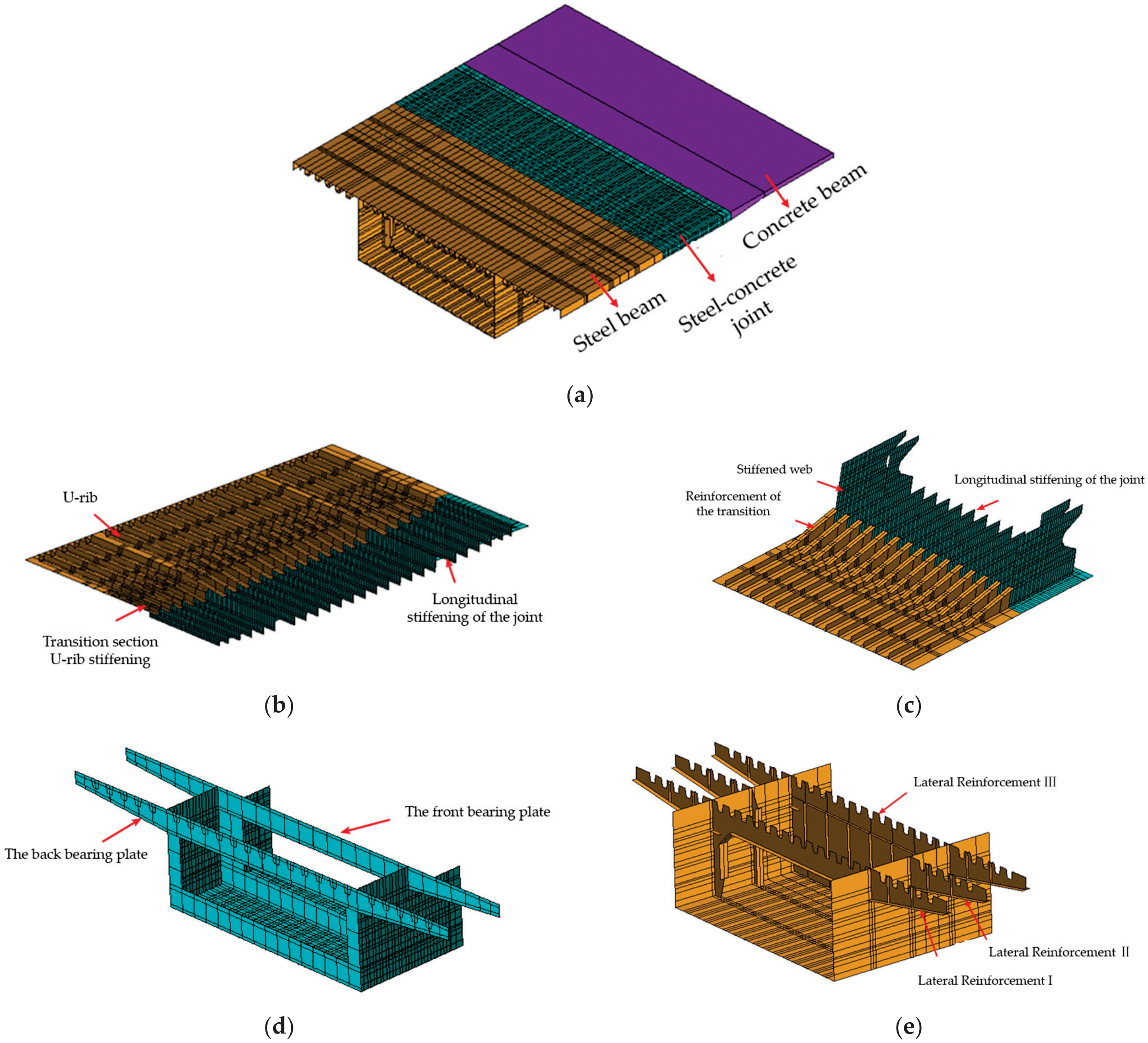

(**a**)

(**b**) (**c**)

(**d**) (**e**)

Figure 2. The finite element model of a joint. (**a**) The fine finite element model of the joint; (**b**) top plate stiffened longitudinally; (**c**) bottom plate lengthwise stiffened and stiffened web; (**d**) joint bearing plate; (**e**) steel beam section transverse partition.

In the finite element model, the frictional force transmission between the steel structure and the concrete at the joint is ignored. Only the influence of the bearing plates and connecting parts is considered, which provides a certain safety reserve for the calculation results. To account for the high stiffness and small deformation in the concrete section during simulation, the model structure is formed into a single cantilever system by constraining the six-direction freedoms of the nodes at the end section of the concrete beam. A main node is established at the centroid position of the steel beam's end section, and a constraint equation is employed to connect the main node with other nodes in the section, forming a rigid domain. Based on Midas Civil version 2020, a finite element model of the superstructure of the bridge is established, and the influence line of the positive bending moment of the joint section is calculated and analyzed. Considering the most unfavorable load combination, the influence line of the positive bending moment of the joint section is calculated and analyzed, and the most unfavorable layout of the vehicle load and the internal force of the section are extracted. These internal force values are then applied to the main node as the internal force boundary condition of the refined model, as outlined in

Table 2. Under working condition 1, the maximum positive bending moment appears at the B-B section of the joint (at the back bearing plate). Meanwhile, under working condition 2, the maximum positive bending moment appears at the A-A section (at the section where the joint welding studs are located), as shown in Figure 3. The vehicle load and bridge deck pavement load in the finite model are simulated according to the surface uniform load form of 10.5 kN/m and 105 kN/m, respectively.

Table 2. Internal force boundary conditions.

Loading Case	Bending Moment (kN·m)	Axial Force (kN)	Shearing Force (kN)
working condition 1	75,162.6	−8930.8	−2890.1
working condition 2	72,647.8	−8921.5	−2763.2

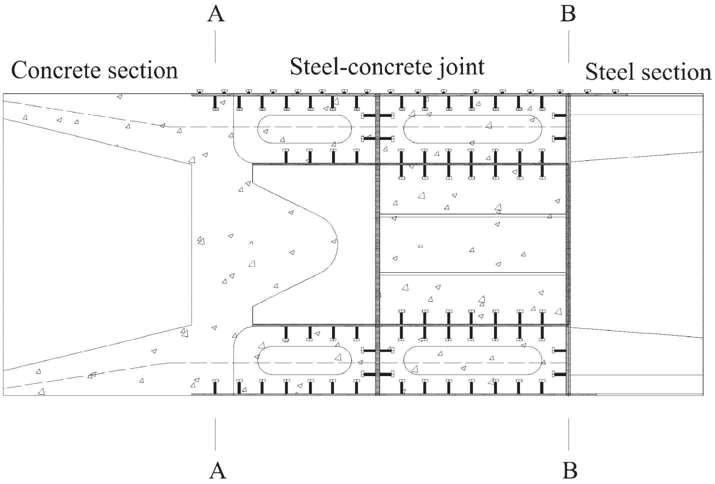

Figure 3. The most unfavorable sections of positive bending moment under two working conditions.

To mitigate the impact of boundary conditions at both ends of the local model on the stress analysis of the joint, the main concrete beam and main steel beam on both sides are taken as 6 m each, with a joint length of 4 m. The longitudinal extent of the entire local model is 16 m. Figure 4 shows the finite element model of the joint.

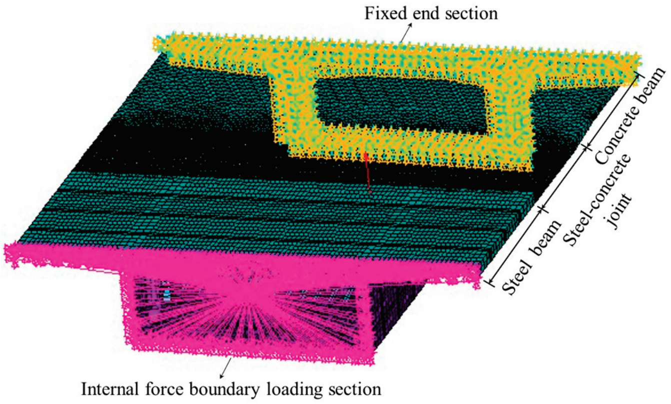

Figure 4. The finite element model's boundary conditions.

3.2. *Verification of Finite Element Model*

In order to verify the correctness of the finite element model, the longitudinal stress of the joint under the working condition of prestressed tendon tension at the joint during on-site construction is monitored with a fiber Bragg grating strain sensor. Figure 5 shows the layout of the measurement points. The concrete stress monitoring section adopts embedded strain gauges and is bound to the stressed steel bar. The stress monitoring section of the steel structure is affixed to the top and bottom plates of the steel box and the surface of longitudinal stiffener using surface-mount strain gauges. TS1~TS3 represent the measuring points of the steel structure top plate; BS1~BS3 represent the measuring points in the steel structure bottom plate; TC1~TC3 represent the measuring points in the concrete top plate; BC1~BC3 represent the measuring points in the concrete bottom plate.

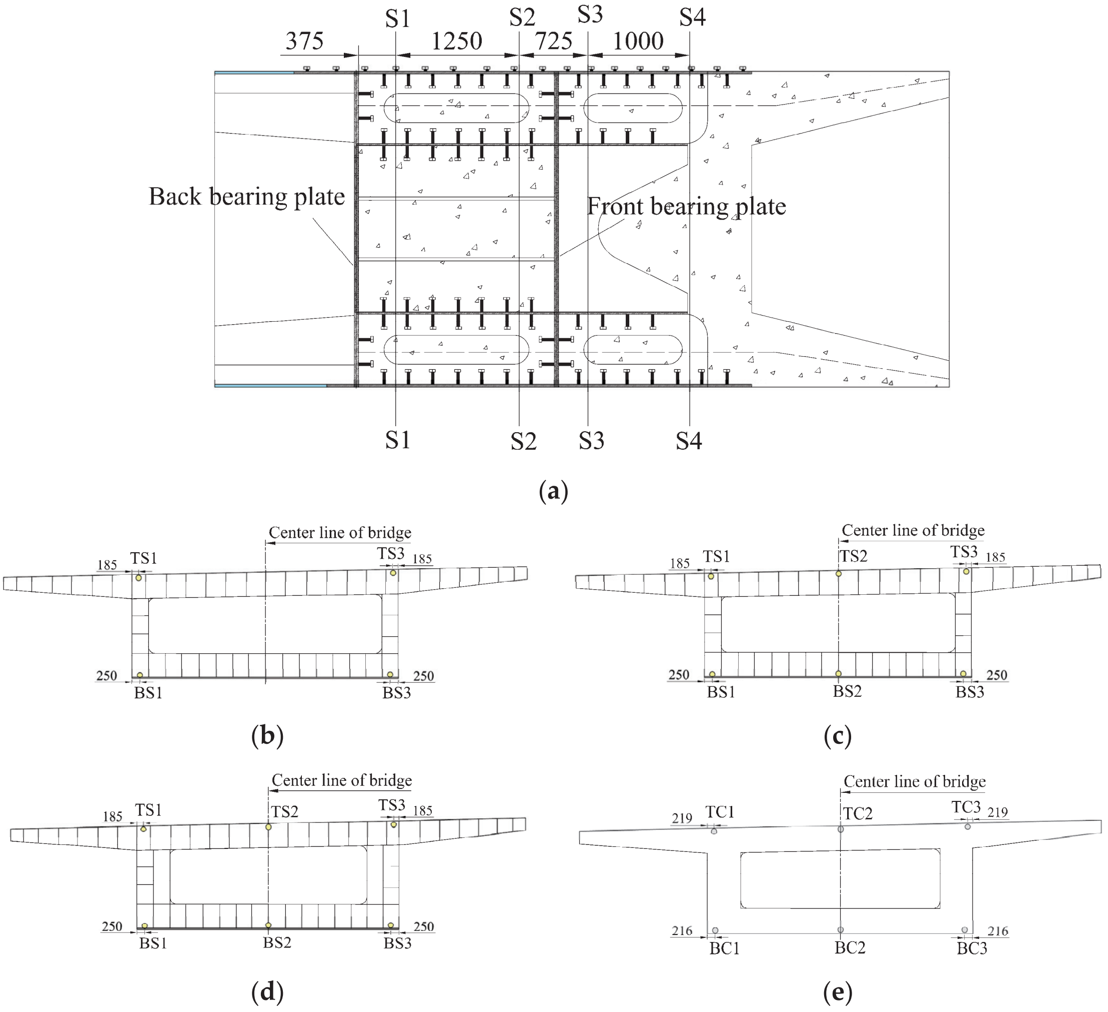

Figure 5. (**a**) Stress monitoring sections (unit: mm); (**b**) steel structure measuring point arrangement of S1–S1 section (unit: mm); (**c**) steel structure measuring point arrangement of S2–S2 section (unit: mm); (**d**) steel structure measuring point arrangements of S3–S3 and S4–S4 sections (unit: mm); (**e**) concrete structure measuring point arrangements of S3–S3 and S4–S4 sections (unit: mm). Under the working condition of prestressed tendon tension at the joint, the longitudinal stress values were measured and calculated at each designated point, as presented in Tables 3 and 4. The calculated stress values at the joint are in good agreement with the measured stress values. The maximum error between the calculated stress values of the steel structure and the measured stress values of the steel structure does not exceed 20%, and the maximum error between the calculated stress values of the concrete structure and the measured stress values of the concrete structure does not exceed 15%. This oversight results in a certain safety margin in the calculation results. The reason for the error between the calculated and measured values may be that the model only considers the action of the bearing plates and the connectors, while ignoring the friction transmission between the steel and concrete structures at the joint. This omission leads to a certain safety margin in the calculated results. The above results show that the finite element model is consistent with the actual situation, thereby verifying the model's accuracy.

Table 3. Monitoring point longitudinal stress in steel structure top and bottom plates (MPa).

Section	Point	Measured Value	Calculated Value
S1–S1	TS1	−7.65	−8.60
	TS3	−7.81	−8.03
	BS1	−5.13	−4.22
	BS3	−4.82	−4.16
S2–S2	TS1	−14.01	−13.12
	TS2	−17.24	−18.09
	TS3	−11.31	−12.79
	BS1	−12.98	−13.74
	BS2	−17.35	−17.83
	BS3	−13.89	−13.50
S3–S3	TS1	−10.21	−9.61
	TS2	−12.54	−11.78
	TS3	−8.54	−9.37
	BS1	−12.32	−11.41
	BS2	−11.85	−12.16
	BS3	−11.84	−11.15
S4–S4	TS1	−4.54	−5.01
	TS2	−4.24	−4.80
	TS3	−5.33	−4.96
	BS1	−5.88	−5.48
	BS2	−5.23	−5.54
	BS3	−5.56	−5.38

Table 4. Monitoring point longitudinal stress in concrete structure top and bottom plates (MPa).

Section	Point	Measured Value	Calculated Value
S3–S3	TC1	−2.18	−2.42
	TC2	−2.68	−2.94
	TC3	−2.54	−2.38
	BC1	−3.25	−3.39
	BC2	−2.98	−2.86
	BC3	−3.41	−3.32
S4–S4	TC1	−2.87	−3.13
	TC2	−3.35	−3.13
	TC3	−2.84	−3.03
	BC1	−3.84	−3.98
	BC2	−3.75	−3.65
	BC3	−3.79	−3.92

4. Structural Parameter Sensitivity

4.1. Thickness of the Back Bearing Plate

To satisfy the stiffness requirements, a larger thickness of the bearing plate is generally selected during design. In the background bridge, the thickness of the bearing plate is 50 mm. In this paper, 30 mm, 50 mm, and 70 mm back bearing plates are selected to establish finite element models and analyze the structural stress characteristics under working condition 1.

The Von Mises stress distributions in the back bearing plates with different thicknesses under working condition 1 are shown in Figure 6. At the welding positions between the back bearing plate and the stiffeners, as well as the anchoring positions of the prestressed tendons, there will be a significant stress concentration. The maximum concentrated stress values of the back bearing plates with different thicknesses are 153.71 MPa, 112.5 MPa, and 83.29 MPa. When the thickness of the back bearing plate increases, the overall level of

Mises stress decreases which alleviates the phenomenon of stress concentration, making the stress distribution more uniform.

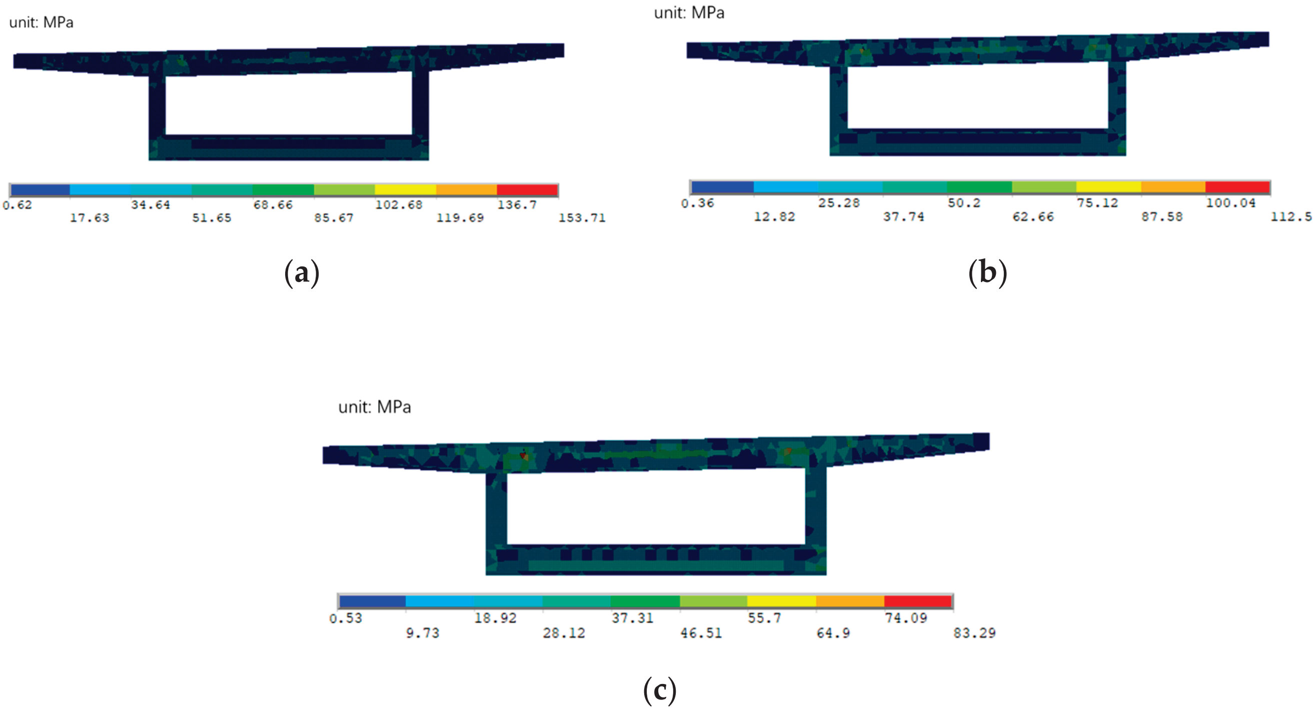

(**a**) (**b**) (**c**)

Figure 6. (**a**) The Mises stress in the back bearing plate when t = 30 mm (unit: MPa); (**b**) the Mises stress in the back bearing plate when t = 50 mm (unit: MPa); (**c**) the Mises stress in the back bearing plate when t = 70 mm (unit: MPa).

In the joint, two points at the beam centerline position and web position in the top plate are selected, marked as top_m and top_w, respectively; two points at the beam centerline position and web position in the bottom plate are selected, marked as bot_m and bot_w, respectively, for the joint stress analysis.

Figures 7 and 8 show the longitudinal stress at each point of the steel structures in the joints with different thicknesses of the back bearing plates under working condition 1. Near the back bearing plate, the compressive stress in the steel top plate experiences a slight reduction with increasing thickness of the back bearing plate, but the effect is not significant, while the tensile stress in the steel bottom plate increases with the increase in the back bearing plate thickness. When the back bearing plate thickness changes, the stress in the top and bottom plates only changes near the back bearing plate, and there is almost no change in other positions. The impact range of the back bearing plate thickness on the stress in the steel structure is mainly between 0 mm and 200 mm. This indicates that the influence of the back bearing plate thickness on the steel structure is mainly in the vicinity of the bearing plate, and the thickness of the back bearing plate significantly affects the stress in the steel structure's bottom plate.

Figures 9 and 10 show the longitudinal stress at each point in the concrete structures within the joints with different thicknesses of the back bearing plates under working condition 1. The results show that the influence range of the back bearing plate thickness on concrete stress is mainly between 0 mm and 400 mm. Within this range, the compressive in of the concrete top plate demonstrates an increase with the augmentation of the back bearing plate thickness, while the tensile stress in the concrete bottom plate decreases with the increase in the back bearing plate thickness. When the back bearing plate thickness increases, the pressure transmitted from the back bearing plate to the concrete structure will increase, and the stress distribution within the concrete structure will be more uniform.

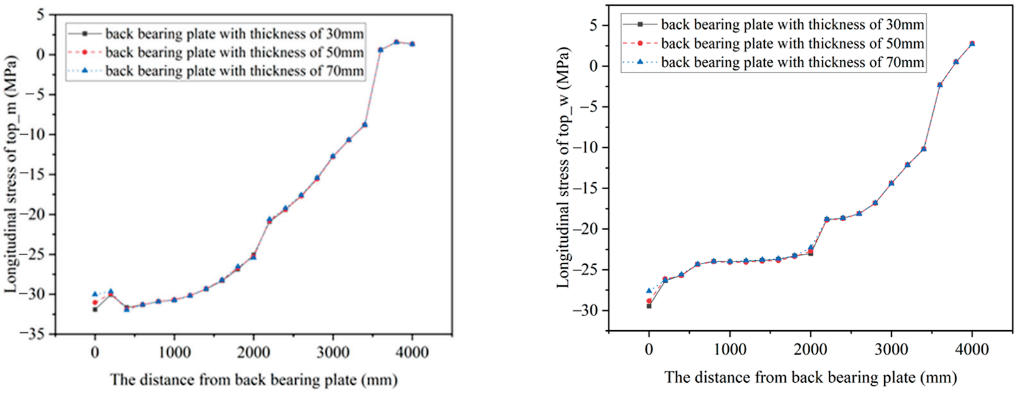

(**a**) (**b**)

Figure 7. The longitudinal stress in a steel top plate. (**a**) The longitudinal stress at top_m; (**b**) The longitudinal stress at top_w.

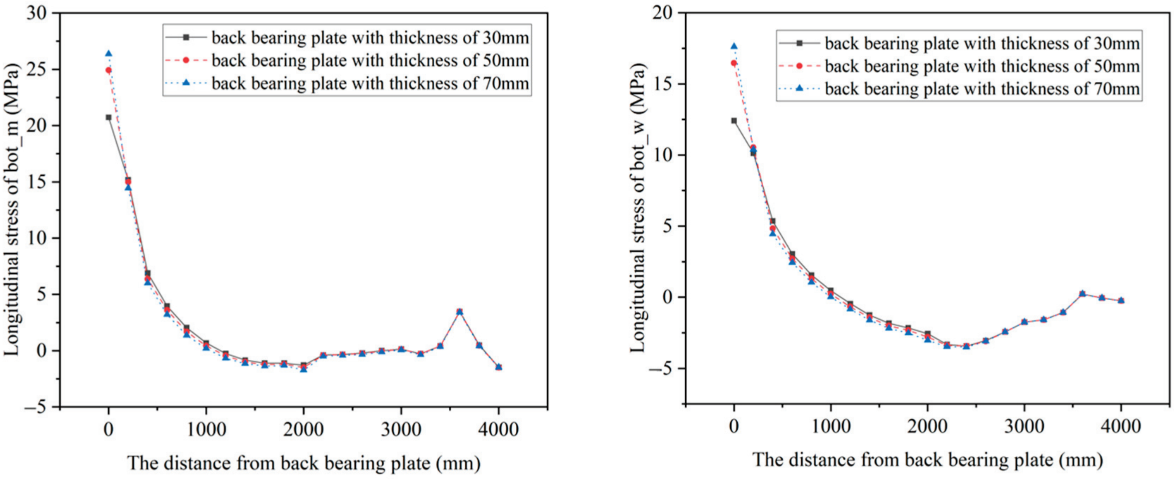

(**a**) (**b**)

Figure 8. The longitudinal stress in steel bottom plate. (**a**) The longitudinal stress at bot_m; (**b**) The longitudinal stress at bot_w.

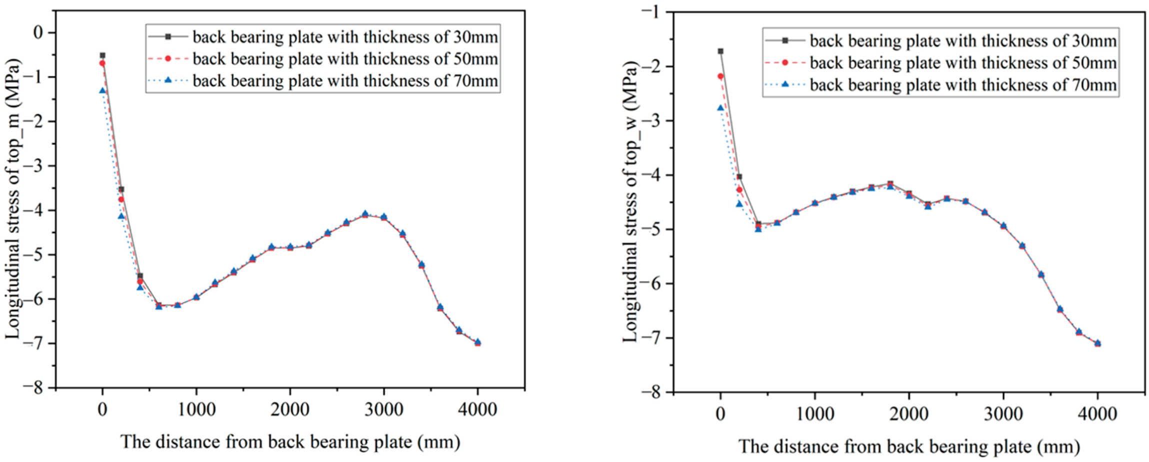

(**a**) (**b**)

Figure 9. The longitudinal stress in concrete top plate. (**a**) The longitudinal stress at top_m; (**b**) The longitudinal stress at top_w.

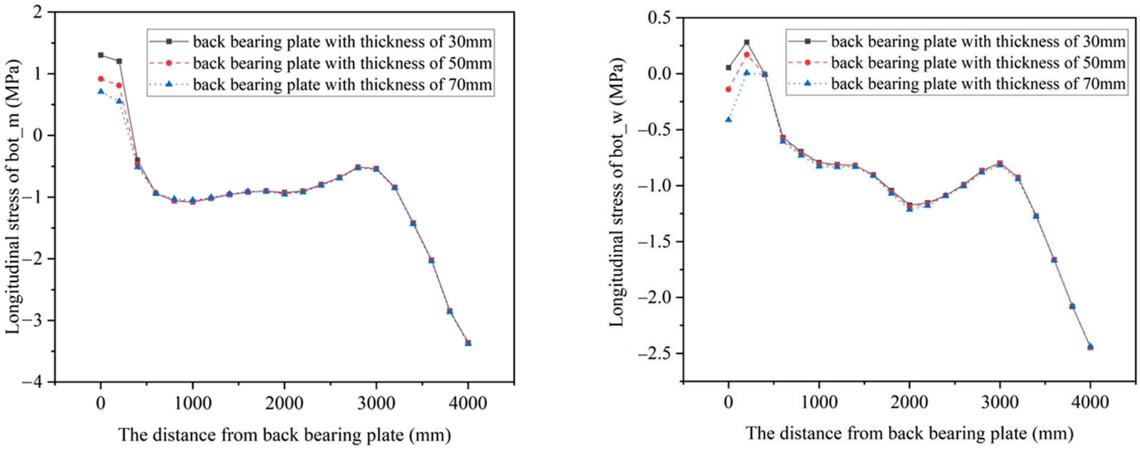

(**a**) (**b**)

Figure 10. The longitudinal stress in concrete bottom plate. (**a**) The longitudinal stress at bot_m; (**b**) The longitudinal stress at bot_w.

The change in the thickness of the back bearing plate can affect the stress distribution near the back bearing plate of the joint. For the steel structure, the stress levels and changes in stress caused by the change in the thickness of the back bearing plate are relatively small compared to the allowable stress of the steel structure, but a thicker back bearing plate can alleviate the stress concentration phenomenon, making the Mises stress distribution more uniform and the overall stress level in the back bearing plate decrease; for the concrete structure, the increase in the back bearing plate thickness can reduce the tensile stress near the back bearing plate. Therefore, a range of 50 mm~70 mm is suggested for the thickness of the back bearing plate.

4.2. Stiffness of the Welding Studs

Based on the stiffness of the welding studs in the background bridge, the stiffness is reduced by 0.5 times, kept constant, and increased by 0.5 times. The welding studs with different stiffnesses are represented by 0.5 Ks, 1.0 Ks, and 1.5 Ks, as shown in Table 5. The influence of the stiffness of the welding studs on the shear force of the top and bottom plate welding studs is studied.

Table 5. Stiffness of the welding studs.

Welding Stud Number	Shear Stiffness (kN/mm)	Tensile Stiffness (kN/mm)
0.5 Ks	180	122.5
1.0 Ks	360	245
1.5 Ks	540	367.5

Along the longitudinal direction of the bridge, fourteen rows of welding studs are arranged on the top and bottom plates of the steel structure, extending from the section of the back bearing plate to the steel–concrete joint surface. The welding studs near the centerline of the bridge and web were selected to investigate the impact of the welding studs' stiffness on the shear force along the bridge direction of the top and bottom studs under working condition 2.

Under working condition 2, the distribution of shear forces along the bridge direction of the top and bottom plate welding studs in the joints with different stiffness welding studs is shown in Figures 11 and 12, where a positive shear force represents the relative displacement of concrete and steel units in opposite directions, and a negative shear force represents the relative displacement of the two in backward directions.

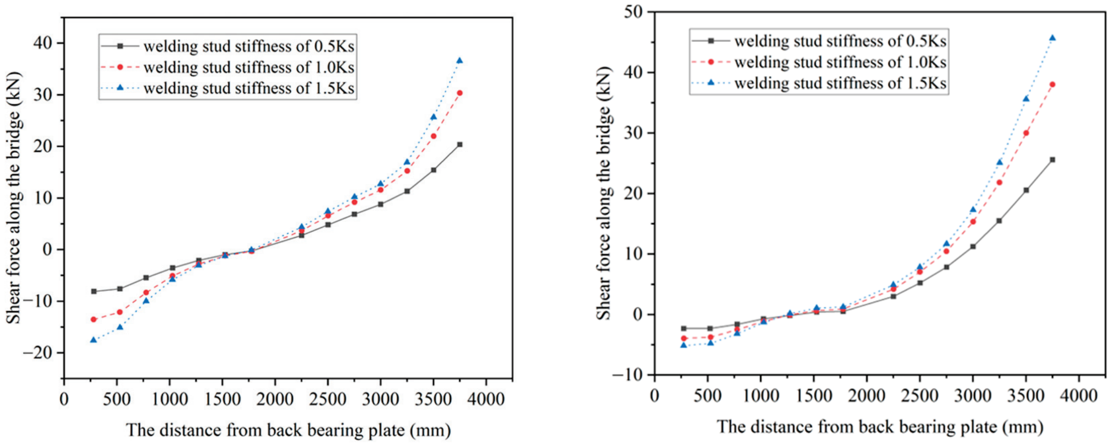

(**a**) (**b**)

Figure 11. The shear force along the bridge of the top plate welding studs. (**a**) The shear force of welding studs near the centerline of the bridge; (**b**) the shear force of welding studs near the web.

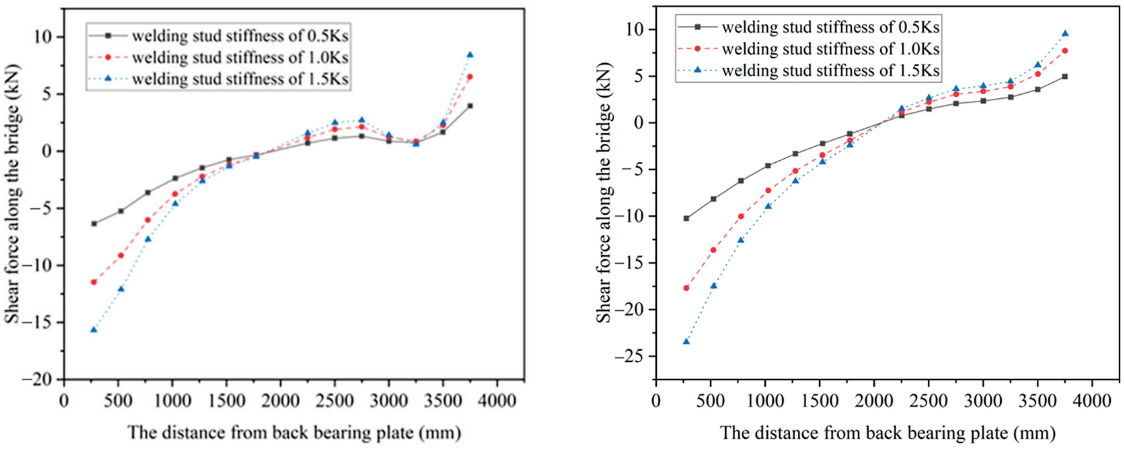

(**a**) (**b**)

Figure 12. The shear force along the bridge of the bottom plate welding studs. (**a**) The shear force of welding studs near the centerline of the bridge; (**b**) the shear force of welding studs near the web.

For the top plate, the distribution of stud shear forces near the web and the centerline of the bridge is consistent, as is shown in Figure 11. On the whole, with the increase in the welding studs' stiffness, the shear forces along the bridge direction of the welding studs in the same position increase. The closer the position is to the back bearing plate or the steel–concrete joint surface, the more clearly the shear force increases. In addition, with the increase in the welding studs' stiffness, the change rate of the shear force along the bridge direction of the top plate welding studs also increases. The results indicate that the increase in the stiffness of the welding studs leads to a larger range of shear forces along the bridge direction of the top plate welding studs, and the longitudinal distribution of shear forces along the bridge direction of the top plate welding studs also becomes more uneven.

For the bottom plate, there is a peak shear force in the stud near the centerline of the bridge between the front bearing plate and the steel–concrete joint surface. In contrast, the longitudinal distribution of the studs' shear forces near the web does not show this characteristic; but on the whole, there is consistency in the stud shear forces near the web and the centerline of the bridge, as is shown in Figure 12. With the increase in the studs' stiffness, the shear forces of the studs in the same position increase, which is most significant near the back bearing plate and the steel–concrete joint surface. In addition, with the increase in the studs' stiffness, the change rate of shear force along the bridge direction of the top plate welding studs also increases. The results indicate that the increase in the stiffness of the welding studs leads to a larger range of shear forces along the bridge direction of the bottom plate welding studs, and the longitudinal distribution of shear forces along the bridge direction of the top plate welding studs also becomes more uneven.

The influence of changes in welding stud stiffness on the shear force of the top and bottom plate welding studs is mainly manifested in the change in the shear force values and the change in the shear force distribution. With the increase in the welding studs' stiffness, the maximum shear force of the top and bottom plate welding studs increases, and the longitudinal distribution of the shear forces of the welding studs becomes more uneven. This non-uniform distribution can lead to an excessive localized force in the process of force transmission at the joint. To make the forces within the welding studs more uniform, enhance the overall utilization efficiency of the welding studs, and prevent damage caused by excessive forces within the welding studs, the stiffness of the welding studs should not be too large on the basis of ensuring the safety of the joint connection.

5. Force Transmission Mechanism

To investigate the force transmission mechanism of the joint, nine sections were strategically chosen, ranging from the back bearing plate section to the joint surface, with a consistent spacing of 0.5 m. Based on working condition 1, the internal force bearing ratios of both the steel and concrete structures in the joint of the background bridge are calculated, as shown in Figure 13.

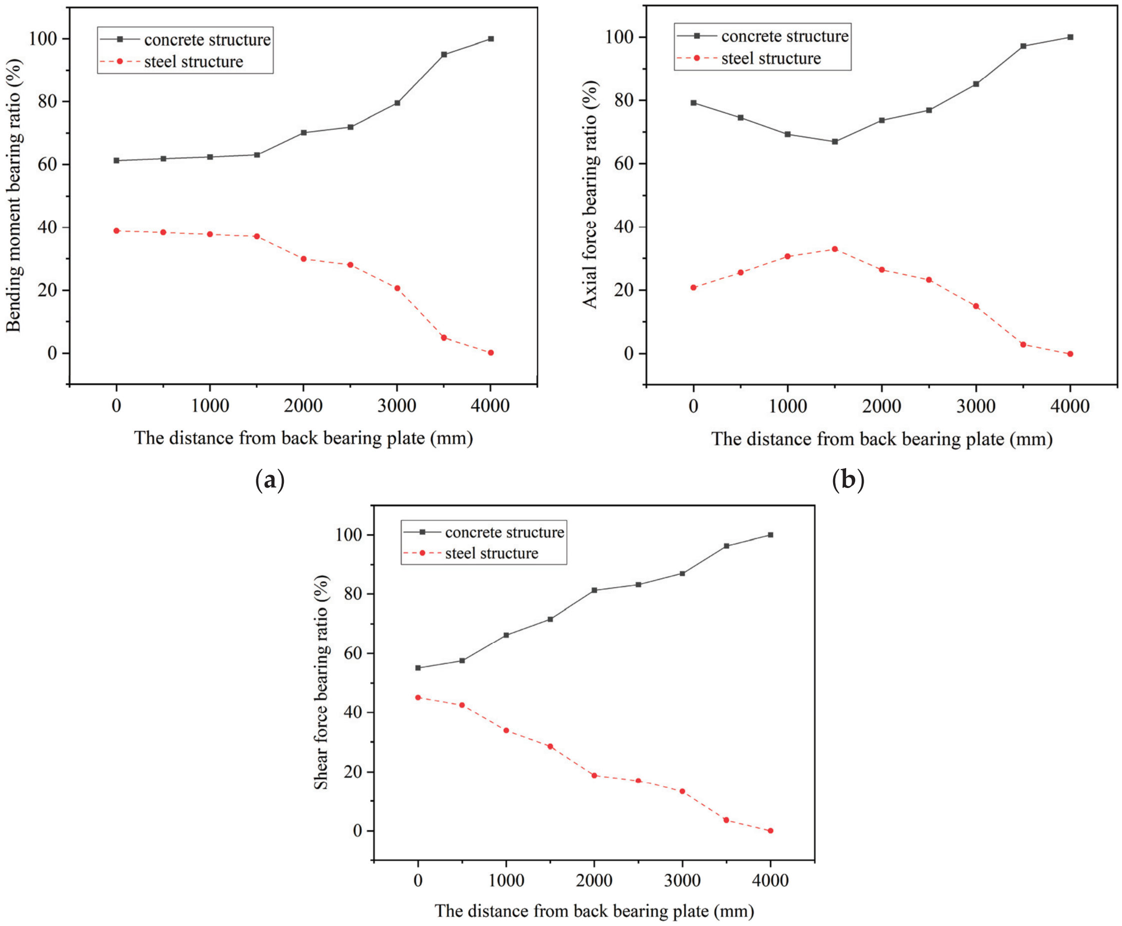

(**a**) (**b**)

(**c**)

Figure 13. The internal force bearing ratios of the steel structure and concrete structure. (**a**) The bending moment bearing ratio; (**b**) the axial force bearing ratio; (**c**) the shear force bearing ratio.

In the section proximate to the rear bearing plate, 61% of the bending moment, 79% of the axial force, and 55% of the shear force are borne by the concrete structure, while the remaining internal forces are borne by the steel structure. With the increase in section distance, the ratio of the bending moment borne by the concrete structure steadily rise; the ratio of axial force borne by the concrete structure exhibits an initial decrease followed by an increase; the ratio of shear force borne by the concrete structure increases uniformly. The results indicate that the internal force bearing ratio of the concrete structure is higher than that of the steel structure in the joint, and the concrete near the joint surface will bear all the internal forces.

The steel beam section first disperses stress to components such as the top and bottom plates, web plates, and stiffeners through the transition section of the steel beam, resulting in stress reduction. The normal stress generated by axial force and bending moment is transferred from the steel structure to the concrete structure through the contact-bearing way of the rear bearing plate, which is the main way of transferring the normal stress in the joint with a short force path and high efficiency. The remaining normal stress is transmitted to the concrete structure by shearing through the connectors on the top and bottom plates, web plates, and perforated plates, which is an indirect force transfer method, extending the force transfer path and increasing the force transfer area. The combination of bearing and shearing at the joint facilitates the transfer of normal stress from the steel beam section to the concrete beam section.

6. Conclusions

In this research, a finite element model of the joints in a bridge is established to investigate the influence of the bearing plate thickness and welding studs stiffness on the mechanical behavior of the joint and to analyze the force transmission mechanism of the joint. The main conclusions are as follows:

1. The stress values calculated at the joint are in good agreement with the measured stress values, in which the maximum error between the calculated and measured values of the steel structure does not exceed 20%; the maximum error between the calculated and measured values of the concrete structure does not exceed 15%. Neglecting the frictional force transmission between the steel structure and the concrete at the joint results in a certain safety reserve for the calculation results;
2. The use of a thicker back bearing plate can alleviate the stress concentration phenomenon at the welding positions between the back bearing plate and the stiffeners, as well as at the anchoring positions of the prestressed tendons, making the Mises stress distribution more uniform and the overall stress level decrease. The change in the bearing plate thickness has a large impact on the stresses within the steel structure and the concrete in the proximity of the bearing plate. For the steel structure near the back bearing plate, the compressive stress of the steel top plate decreases with an increase in the back bearing plate's thickness, while the tensile stress in the steel bottom plate escalates correspondingly, and the opposite is true for the concrete structures. The influence range of the back bearing plate thickness on concrete stress is mainly between 0 mm and 400 mm. It is recommended to maintain a back bearing plate thickness within the range of 50 mm~70 mm;
3. Reducing the stiffness of the welding studs by 0.5 times, keeping it the same, or increasing it by 0.5 times shows that an increase in the welding studs' stiffness makes the range of the shear force along the bridge direction of the top and bottom welding studs larger, and the longitudinal distribution of the welding studs' shear force is more uneven. To avoid the damage caused by the excessive forces of the welding studs, the stiffness of the welding studs should not be too large on the basis of ensuring the safety of the joint connection;
4. The internal force bearing ratio of the concrete structure is higher than that of the steel structure in the joint. The transmission of normal stress at the junction occurs from the steel beam section to the concrete beam section through two ways: bearing and

shearing. Notably, the primary mode of force transmission for normal stress involves contact bearing through the back bearing plate.

Author Contributions: Conceptualization, L.J.; methodology, L.J. and S.Y.; formal analysis, L.J., H.P., J.L., S.Y., T.W. and G.Z.; investigation, H.P. and J.L.; Data curation, J.L., S.Y., T.W. and G.Z.; writing—original draft preparation, S.Y. and L.J.; writing—review and editing, H.P., S.Y., T.W. and G.Z.; supervision, L.J. and H.P.; project administration, H.P. All authors have read and agreed to the published version of the manuscript.

Funding: This work was supported by the National Natural Science Foundation of China (51878488), Department of Transportation of Jiangxi Province (2022H0019) and Department of Transportation of Jiangxi Province (2023H0008).

Data Availability Statement: The data from this study are available from the corresponding author upon reasonable request.

Acknowledgments: The authors sincerely thank the people who provided assistance during the writing and publication process of the paper.

Conflicts of Interest: Authors Tingying Wu and Huiteng Pei were employed by Jiangxi Communications Design and Research Institute Limited Company. Author Gangyi Zhan was employed by China Railway Shanghai Design Institute Group Limited Company. The authors declare that the research was conducted in the absence of any commercial or financial relationships that could be construed as a potential conflict of interest.

References

1. Yepes, V.; Dasí-Gil, M.; Martínez-Muñoz, D.; López-Desfilis, V.J.; Martí, J.V. Heuristic Techniques for the Design of Steel-Concrete Composite Pedestrian Bridges. *Appl. Sci.* **2019**, *9*, 3253. [CrossRef]
2. Gara, F.; Carbonari, S.; Leoni, G.; Dezi, L. Finite Elements for Higher Order Steel–Concrete Composite Beams. *Appl. Sci.* **2021**, *11*, 568. [CrossRef]
3. Lei, Q.; Wang, P.; Nan, H. Study on Mechanical Properties of Simply-Supported Composite Beams Considering Creep and Slip. *Appl. Sci.* **2022**, *13*, 193. [CrossRef]
4. Brunesi, E.; Peloso, S.; Pinho, R.; Nascimbene, R. Cyclic testing and analysis of a full-scale cast-in-place reinforced concrete wall-slab-wall structure. *Bull. Earthq. Eng.* **2018**, *16*, 5309–5339. [CrossRef]
5. Tang, L.; Wu, W.; Liu, G.; Xu, G. Structural performance of rear bearing-plate connection with cells in steel-concrete hybrid girder. *Eng. Mech.* **2010**, *27*, 234–243.
6. Zhang, D.L.; Bao, Y.W.; Gao, J.H.; Xiao, L.; Li, X.Z. Research on load transfer mechanism of steel-concrete joint section of hybrid beam cable-stayed bridge. *Adv. Mater. Res.* **2013**, *639–640*, 216–219. [CrossRef]
7. Xing, B.; Li, X.Z. The numerical simulation analysis method of steel-concrete joint section in hybrid girder of cable-stayed bridge. *Adv. Mater. Res.* **2014**, *1049–1050*, 226–233. [CrossRef]
8. Zhang, G.; Chen, C.; Liu, Y. Load transfer mechanism between cells and bearing-plate in hybrid girder joint. *J. Tongji Univ. Nat. Sci.* **2017**, *45*, 658–663.
9. He, S.; Mosallam, A.S.; Fang, Z.; Liu, L. Structural evaluation of steel–concrete joint with uhpc grout in single cable–plane hybrid cable-stayed bridges. *J. Bridge Eng.* **2019**, *24*, 04019022. [CrossRef]
10. Yang, S.; Pu, Q.; Shi, Z.; Hong, Y. Mechanical behavior of steel–concrete composite joints in railway hybrid cable-stayed bridges. *J. Constr. Steel Res.* **2020**, *173*, 106242. [CrossRef]
11. Pu, Q.; Yang, S.; Shi, Z.; Hong, Y.; Zhou, Y. Fatigue performance of an innovative steel–concrete joint in long-span railway hybrid box girder cable-stayed bridges. *J. Bridge Eng.* **2021**, *26*, 04020129. [CrossRef]
12. Gu, Y.-W.; Nie, X.; Liu, Y.-F.; Duan, S.-K.; Fan, J.-S. Experimental and numerical study of steel-to-concrete joint section in hybrid cable-stayed bridges. *J. Constr. Steel Res.* **2021**, *187*, 106982. [CrossRef]
13. Yao, Y.; Yan, M.; Shi, Z.; Wang, Y.; Bao, Y. Mechanical behavior of an innovative steel–concrete joint for long-span railway hybrid box girder cable-stayed bridges. *Eng. Struct.* **2021**, *239*, 112358. [CrossRef]
14. Xu, C.; Zhang, L.; Su, Q.; Abbas, S. Mechanical behavior of a novel steel–concrete joint in concrete-composited hybrid continuous bridges. *Structures* **2022**, *36*, 291–302. [CrossRef]
15. Zhou, Y.; Pu, Q.; Shi, Z.; Gou, H.; Chen, X. Experimental and numerical parametric study of the mechanical properties in a steel–concrete joint section. *Int. J. Civ. Eng.* **2022**, *20*, 1431–1446. [CrossRef]
16. Liang, H.; Tan, K.; Deng, K.; Zhang, Y.; Zhao, C.; Yang, T. Crack resistance of steel–concrete hybrid joint between concrete girder and steel–concrete composite girder in long-span cable-stayed bridge under hogging moment. *J. Bridge Eng.* **2023**, *28*, 05022013. [CrossRef]

17. He, J.; Liu, Y.; Pei, B. Experimental study of the steel-concrete connection in hybrid cable-stayed bridges. *J. Perform. Constr. Facil.* **2014**, *28*, 559–570. [CrossRef]
18. He, S.; Fang, Z.; Fang, Y.; Liu, M.; Liu, L.; Mosallam, A.S. Experimental study on perfobond strip connector in steel–concrete joints of hybrid bridges. *J. Constr. Steel Res.* **2016**, *118*, 169–179. [CrossRef]
19. Di, J.; Zou, Y.; Zhou, X.; Qin, F.; Peng, X. Push-out test of large perfobond connectors in steel–concrete joints of hybrid bridges. *J. Constr. Steel Res.* **2018**, *150*, 415–429. [CrossRef]
20. Zou, Y.; Di, J.; Zhou, J.; Zhang, Z.; Li, X.; Zhang, H.; Qin, F. Shear behavior of perfobond connectors in the steel-concrete joints of hybrid bridges. *J. Constr. Steel Res.* **2020**, *172*, 106217. [CrossRef]
21. Zou, Y.; Zheng, K.; Zhou, J.; Zhang, Z.; Li, X. Mechanical behavior of perfobond connector group in steel–concrete joint of hybrid bridge. *Structures* **2021**, *30*, 925–936. [CrossRef]
22. Zhou, Y.; Pu, Q.-H.; Shi, Z.; Gou, H.-Y.; Yang, S.-L. Experimental study on fatigue performance of steel-concrete joint section of hybrid girder cable-stayed bridge. *Adv. Steel Constr.* **2022**, *18*, 536–543. [CrossRef]
23. Zhao, L.; Sun, C.; Yang, X. Stability analysis of edong yangtze river bridge during construction. *J. Southwest Jiaotong Univ.* **2012**, *47*, 741–747.
24. He, Z.-Q.; Chen, J.; Liu, Z.; Ma, Z.J. An explicit approach for determining the rational length of steel portion in steel–concrete hybrid girder bridges. *J. Bridge Eng.* **2023**, *28*, 05022011. [CrossRef]
25. Liu, M. Practices and prospects of steel-concrete composite technology in bridge engineering. *Bridge Constr.* **2022**, *52*, 18–25.

buildings

MDPI

Article

A Novel Dual Self-Centering Friction Damper for Seismic Responses Control of Steel Frame

Juntong Qu [†], Xinyue Liu [†], Yuxiang Bai *, Wenbin Wang, Yuheng Li, Junxiang Pu and Chunlei Zhou

School of Architecture and Planning, Yunnan University, Kunming 650504, China; 15808654138@163.com (J.Q.); 18487091835@163.com (X.L.)
* Correspondence: byx@mail.ynu.edu.cn
† These authors contributed equally to this work.

Abstract: Due to their weight, the seismic response control of buildings needs a large-scale damper. To reduce the consumption of shape memory alloys (SMAs), this study proposed a dual self-centering pattern accomplished by the coil springs and SMA, which could drive the energy dissipation device to recenter. Combined with the friction energy dissipation device (FD), the dual self-centering friction damper (D-SCFD) was designed, and the motivation and parameters were described. The mechanical properties of D-SCFD, including the simplified D-SCFD mechanical model, theoretical index calculations of recentering, and energy dissipation performance, were then investigated. The seismic response mitigation of the steel frame adopting the D-SCFDs under consecutive strong earthquakes was finally analyzed. The results showed that a decrease in the consumption of SMA by the dual self-centering pattern was feasible, especially in the case of low demand for the recentering performance. Reducing the D-SCFD's recentering performance hardly affected the steel frame's residual inter-story drift ratios when the residual deformation rate was less than 50%, which can help strengthen the controls on the steel frame's peak seismic responses. It is recommended to utilize the D-SCFD with not too high a recentering performance to mitigate the seismic response of the structure.

Keywords: dual self-centering; shape memory alloy; D-SCFD; seismic response mitigation

1. Introduction

Passive energy dissipation devices can provide additional stiffness and damping for buildings, which improves the safety of buildings by reducing earthquake responses [1,2]. Engineers choose displacement-dependent dampers because of their consistent mechanical performance and inexpensive production costs [3]. Therefore, displacement-dependent dampers have been widely used in the construction and seismic strengthening of buildings located in earthquake-prone areas, such as buckling restrained braces (BRBs), friction energy dissipation devices (FDs), metallic yielding dampers (MYDs), etc. [4–6]. Traditional displacement-dependent dampers, on the other hand, run the risk of causing higher post-earthquake residual deformations of buildings, which can easily raise the economic cost and technological problems of post-earthquake rehabilitation [7]. In this regard, many scholars have developed a series of self-centering dampers to improve the recentering performance of dampers and reduce the post-earthquake residual deformations of buildings [8].

In past research, a kind of self-centering damper simultaneously composed of prestressed tendons and energy dissipation devices has been designed. The prestressed tendons, which mainly include steel strands, basalt fiber tendons, aramid fiber bundles, etc. [9–16]. During the unloading process, the prestressed tendons drive energy dissipation devices to recenter. The self-centering dampers with prestressed tendons often have significant demands for prestressing force to obtain the appropriate recentering effect. However, the demands for high prestressing force will increase the difficulties of manufacturing the dampers and cause a series of problems, such as tension, anchorage, relaxation of the prestressed tendons, etc. In addition, it will lead to excessive elastic deformations of prestressed tendons, and the maximum deformations of dampers will be limited. Concurrently, there is significant worry over another type of self-centering damper. These dampers use mechanisms that compress disc springs or ring springs to drive them to recenter. Research about its mechanical behavior and the performance of shock absorption has been carried out. Xu and Fan et al. [17–19] combined the pre-pressed disc springs and FD into a self-centering energy dissipation brace, conducted the experiments, and established an axial force formula. Filiatrault et al. [20] proposed a self-centering friction energy dissipation device for reducing the earthquake responses of buildings based on the friction hysteresis of ring springs and conducted prototype tests of dampers to observe their practical mechanical behavior. Khoo et al. [21,22] used ring springs to reduce the residual deformations of sliding hinge joints and conducted prototype tests of self-centering joints.

A shape memory alloy (SMA) has the good performance of self-centering and energy dissipation simultaneously, and its plastic deformation caused by external loads will rapidly dissipate after unloading [23]. Under cyclic load, SMA can also disperse the input energy, which is suitable for the advancement of self-centering energy dissipation devices. Qian et al. [24] proposed a self-centering damper-based SMA wire and investigated how the pre-strain of SMA affects the hysteretic performance of the damper through tests. Shi et al. [25–28] developed a self-centering energy dissipation brace based on SMA cables and proved that its hysteretic performance and mitigation for structural seismic responses were, respectively, researched through mechanical experiments and finite element analysis. The FD can effectively dissipate the energy input from an earthquake and protect the components of buildings [29]. Thus, the means of developing self-centering dampers by combining SMA with FD has attracted much attention. Li et al. [30] proposed a self-centering FD by connecting the SMA rods in parallel with the FD, and then the corresponding mechanical tests and parameter analysis were conducted. Chen and Qiu et al. [31,32] developed a self-centering variable FD in which the SMA elements provided the pre-tightening force for variable FD and drove the damper to recenter simultaneously. Zheng et al. [33,34] proposed a self-centering isolator with SMA to mitigate the seismic response of bridges.

In February 2023, earthquakes with a magnitude of 7.8 and 7.6 occurred in southeast Turkey successively, just nine hours apart [35]. Multiple aftershocks are frequently felt in response to a mainshock, and mainshock–aftershock sequences (MS-AS) can cause structural damage to accumulate and quickly put the structure in a more risky state. For that reason, lots of scholars have considered MS-AS when investigating the seismic performance of structures. Lu et al. [36] proposed a method for the seismic damage prediction of regional buildings that took into account MS-AS. Raghunandan et al. [37] analyzed the aftershock vulnerability of reinforced concrete (RC) frames and found that the collapse resistance capacities of buildings would decrease with the strength of MS increasing. Wen et al. [38] proposed MS-AS damage spectra at soft soil sites. Yu et al. [39] found that the AS reduced the collapse resistance capacity through the MS-AS vulnerability analysis of inelastic single-degree-of-freedom systems. Zhou et al. [40] established a seismic demand model for RC structures and the corresponding formula for estimation of earthquake fragilities, which showed that the MS-AS would improve the exceedance probability of buildings.

To achieve the recentering effect, the traditional self-centering damper-based SMAs need a large consumption of SMA, which leads to a high cost. Thus, this study suggested using coil springs and SMA in a dual self-centering (D-SC) drive mode with a low cost. A novel dual self-centering friction damper (D-SCFD) design was put into practice. Through small-scale mechanical testing, the impacts of pre-tightening force and loading displacement amplitudes on D-SCFD's energy dissipation and recentering performance were examined. The parameter study was conducted using the simplified mechanical model of D-SCFD as well as existing index formulas for energy dissipation performance and recentering. Lastly, the seismic response control impacts of D-SCFD with variable recentering performance on SF under MS-AS were examined using a multi-story steel frame (SF) as the analytical object.

2. Design of D-SCFD

2.1. Configuration of D-SCFD

The main functional elements of D-SCFD are coil springs, SMA rods, and FD with two sliding surfaces. The D-SC was formed after the connection of coil springs in parallel with SMA rods. The components of the D-SCFD were as follows: an internal panel, asbestos friction sheets, external panels with coil spring anchor plates, high-strength bolts, high-strength nuts, SMA rods, coil springs, guide bars, and a connection block for connecting the two external panels. The configuration of the D-SCFD is shown in Figure 1.

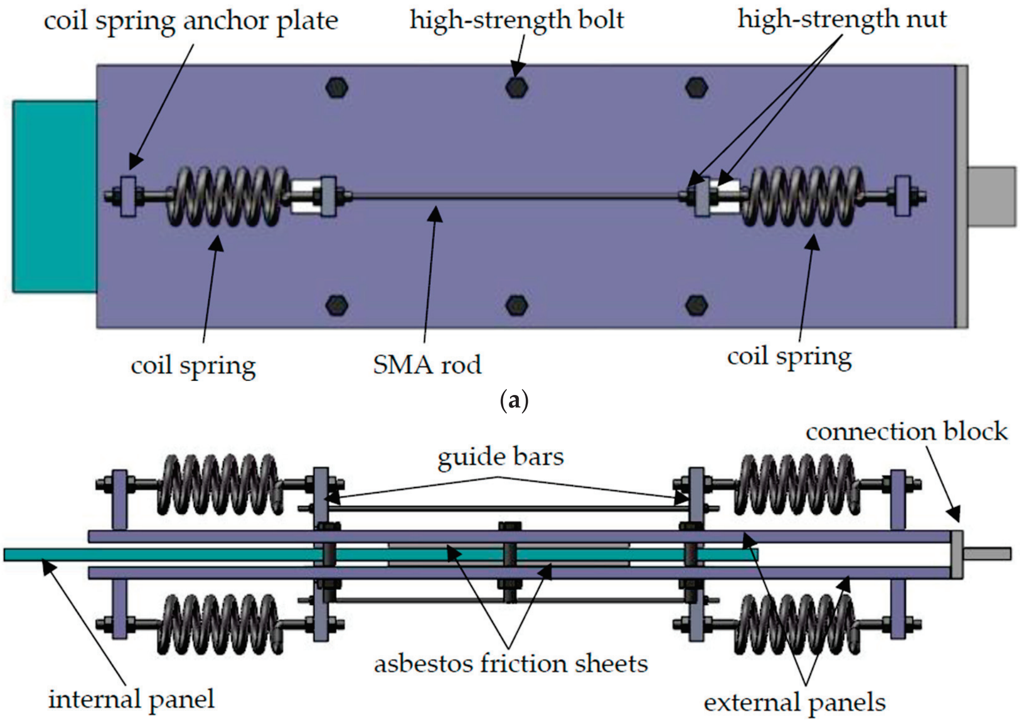

(**a**)

(**b**)

Figure 1. Configuration of D-SCFD: (**a**) planform and (**b**) side view.

During the assembly process of the FD, two asbestos friction sheets were, respectively, fixed on the upper and lower surfaces of the internal panel and kept sliding with the external panels. Screw holes were saved on both sides of the external panels, and the friction sheets were pre-tightened using high-strength bolts. For the D-SC, the two ends of the guide bars had reserved holes for the anchorages of the SMA rods and the coil springs. After the two guide bars, respectively, passed through the corresponding slots reserved at both ends of the three panels, the two guide bars were connected by SMA rods. The two ends of the SMA rods were anchored to the guide bars by high-strength nuts. Each guide bar was attached to the matching anchor plate on the external panels by two pairs of coil springs. High-strength nuts were also used to secure the ends of coil springs. Finally, the connection block was welded to one end of the external panels to complete the D-SCFD system.

2.2. Working Principle of D-SCFD

In the process of the reciprocating motion of the D-SCFD, the SMA rods were always alternately in two states of tension and recentering. Meanwhile, the coil springs on one side were alternately in two states of compression and recentering. The axial force response of D-SC inhibited the deformation of D-SCFD during loading. In the unloading process, the restoring force of D-SC was composed of the elastic force of coil springs and the transformation stress of SMA rods, which drove the D-SCFD to recenter by overcoming the frictional force generated by the FD.

The working principle of D-SCFD is shown in Figure 2. When the external excitation caused the tensile deformation of the damper, the relative displacement between the internal panel and the external panels occurred. It also caused sliding friction between the friction sheets and the external panels, dissipating the energy intake from seismic excitation. The internal panel simultaneously pushed the guide bar on one side while the guide bar on the other side was stationary relative to the external panels, stretching the SMA rods and compressing the coil springs on one side. When the D-SCFD was compressed, the guide bar on one side remained motionless in relation to the external panels, while that on the other was pushed by the internal panel. It compressed the coil springs on the other side while stretching the SMA rods. The force for the recentering of the damper was provided by coil springs and SMA rods, reducing the consumption of SMA rods.

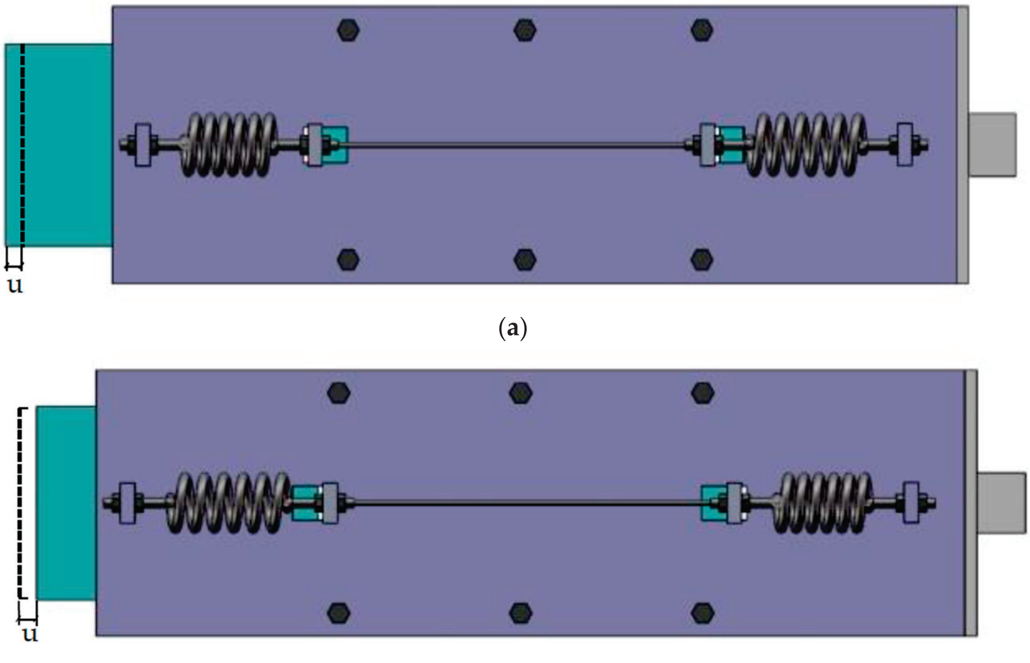

(**a**)

(**b**)

Figure 2. Working principle of D-SCFD: (**a**) tension state and (**b**) compression state, where *u* denotes the axial deformation.

3. Test

3.1. Tensile Test of SMA

According to the literature [32], the mechanical properties of SMA tend to be stable after cyclic tensile loading. Therefore, before the test of D-SCFD, the SMA rod with a diameter of 4 mm was trained 20 times under equal-amplitude cyclic tensile loading, which made the mechanical properties of the SMA rod stable. The contents of nickel and titanium in the SMA rod were 50.1% and 49.9%, respectively. Meanwhile, the transformation stress and strain of SMA rods were obtained by the cyclic tensile test under variable amplitude loading. The loading rate of the tensile tests was set to 5 mm/min, and the ambient temperature was 15 °C. The parameters of the tensile test conditions are shown in Table 1, and the corresponding loading equipment is shown in Figure 3.

Table 1. Tensile test conditions of the SMA rod.

No.	Section Area of SMA (mm^2)	Loading Rate (mm/min)	Number of Loading Cycles	Strain Amplitude (%)
1	12.57	5	20	5
2	12.57	5	1	3 5 7

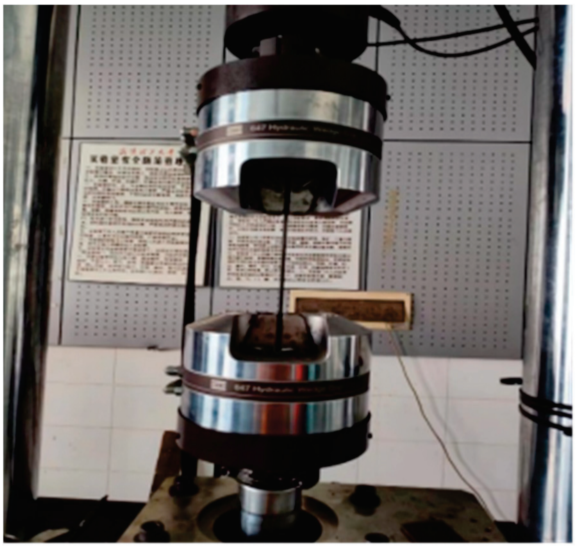

Figure 3. Loading equipment of the SMA rod.

As shown in Figure 4, the constitutive curves from the results of the tensile test revealed that the residual strain of the SMA rod reached 1.98% after the first tension. In the subsequent cyclic tensile test under equal amplitude loading, the residual strain became small, indicating that the SMA rod had a good capacity for self-centering. With the increase in the number of loading cycles, the SMA stress gradually decreased and tended to be stable. The maximum stresses of SMA rods in the 14th and 20th tensile tests were 452.38 MPa and 446.46 MPa, respectively. The relative difference between both was only 1.33%, and the amplitude of the fluctuations was small. The stress of the SMA rod increased linearly with the strain increases in the cyclic tensile test under varying amplitude loadings, and subsequently, the stress increased at a slower rate when the martensitic transformation occurred. In the unloading process, the SMA rod with a different initial strain had stress–strain curves with three different kinds of slopes, and the descent rate of stress was lowest during the reverse martensitic transformation of SMA. The stress–strain curves from the tensile tests showed that the SMA rod had good superelastic properties, and the mechanical properties after tensile training were less affected by the loading times. The transformation stress and strain of SMA with the maximum tensile strain of 7% are shown in Table 2.

Table 2. Transformation stress and strain of the SMA rod.

σ_{Ms} (MPa)	ε_{Ms} (%)	σ_{Mf} (MPa)	ε_{Mf} (%)	σ_{As} (MPa)	ε_{As} (%)	σ_{Af} (MPa)	ε_{Af} (%)
454.19	1.82	609.89	6.97	271.78	5.29	116.08	0.47

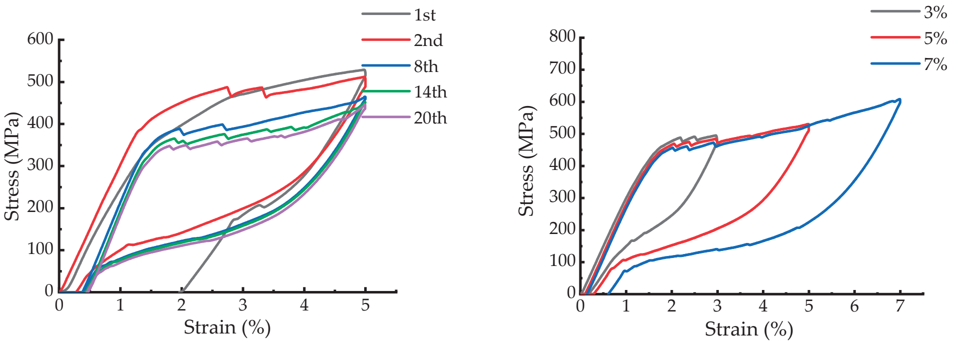

(**a**) (**b**)

Figure 4. Stress–strain curves from the tensile test of the SMA rod: (**a**) under equal amplitude loading and (**b**) under variable amplitude loading.

3.2. Mechanical Test of D-SCFD

To study the effects of the loading displacement amplitude and FD's pre-tightening force on the mechanical properties of D-SCFD, a small-scale specimen with the maximum permissible deformation of 21 mm was fabricated according to the configuration described earlier, and the mechanical tests of FD and D-SCFD were conducted under low-reversed cyclic loading. The material of the friction sheets was composed of asbestos and brass wires in FD. The SMA rods after tensile training were installed in D-SCFD, whose working length was 300 mm. For the coil springs, the diameter of the spring wire was 8 mm, the outer diameter was 50 mm, and the axial stiffness was 145 N/mm. The material of the coil springs was Mn-Cr Alloy (Mn 1.02%, Cr 0.29%). The tensile strength of the high-strength bolts and nuts was 1200 MPa, and the diameter of the screw was 10 mm. The rest of D-SCFD adopted the steel with a yield strength of 235 MPa. The specimen, test conditions, and test device are shown in Figure 5, Table 3, and Figure 6, respectively. The ambient temperature was 15 °C.

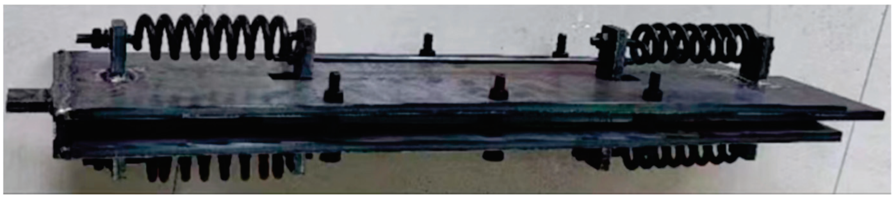

Figure 5. Specimen of D-SCFD.

Table 3. Test conditions of D-SCFD.

No.	ID of Specimen	Section Area of SMA (mm^2)	Loading Rate (mm/min)	Loading Displacement Amplitude (mm)	Pre-Tightening Force of FD (kN)
1	FD	0	5	9 15 21	7
2	D-SCFD	25.13	5	9 15 21	3 5 7

The hysteretic curves of FD with a pre-tightening force of 7 kN are shown in Figure 7. The axial force generated by FD was stable, and the hysteretic curves under different loading displacement amplitudes were rectangular in shape. The areas of hysteretic curves increased with the increase in the axial deformation of FD. According to the results from the tests of FD and the configuration with two sliding surfaces, the coefficient of sliding friction was 0.50, which was denoted by μ. As shown in Figure 8, the shapes of the hysteretic curves of D-SCFD were similar to those of the stress–strain curves of SMA, both of which are “flag-shape”. The axial force of D-SCFD fluctuated slightly at the start of the martensitic transformation of SMA rods during loading and became stable gradually with the increase in the axial deformation. The areas of the hysteretic curves of D-SCFD also increased while the pre-tightening force of FD increased, and they were positively correlated with the axial deformation. After the pre-tightening force of FD was magnified, the horizontal coordinates of hysteretic curves with an axial force of 0 kN increased during unloading, indicating that the residual deformation of D-SCFD increased. The hysteretic curves from the test of D-SCFD reflected that the performance of energy dissipation could be improved by magnifying the axial force responses of FD, but the performance of recentering would be adversely affected.


(**a**) (**b**)

Figure 6. Test devices of D-SCFD: (**a**) loading device and (**b**) data acquisition device.

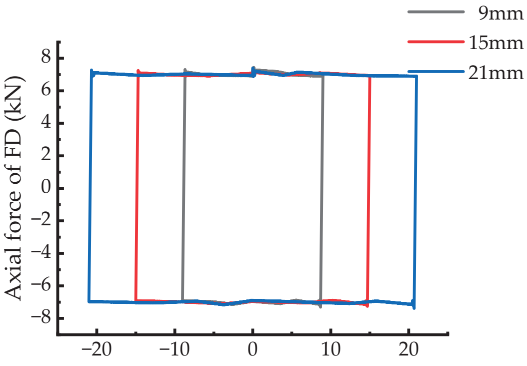

Figure 7. Hysteretic curves of FD.

The mechanical property parameters, such as dissipated energy, secant stiffness, equivalent viscous damping, and the rate of residual deformation, denoted by W, K, ξ_{eq}, and R_{dr}, respectively, were used to measure the performance of D-SCFD in this study. The mechanical property parameters of D-SCFD are shown in Figure 9. The ξ_{eq} of D-SCFD fluctuated with the increase in axial deformation, the maximum variation of which only reached 2.37%. Thus, the ξ_{eq} of D-SCFD was less affected by the loading displacement amplitude. The relative increment of W was close to that of the strain energy, which was caused by the increase in the axial deformation of D-SCFD. That was the main reason why the ξ_{eq} of D-SCFD was less affected by the loading displacement amplitude. Wherein, the strain energy of D-SCFD is $KD^2/2$, and D denotes the axial deformation of D-SCFD. The ξ_{eq} of D-SCFD increased with the magnification of the pre-tightening force of FD, indicating that the relative increment of *W* caused by magnifying the pre-tightening force of FD was greater than that of strain energy.

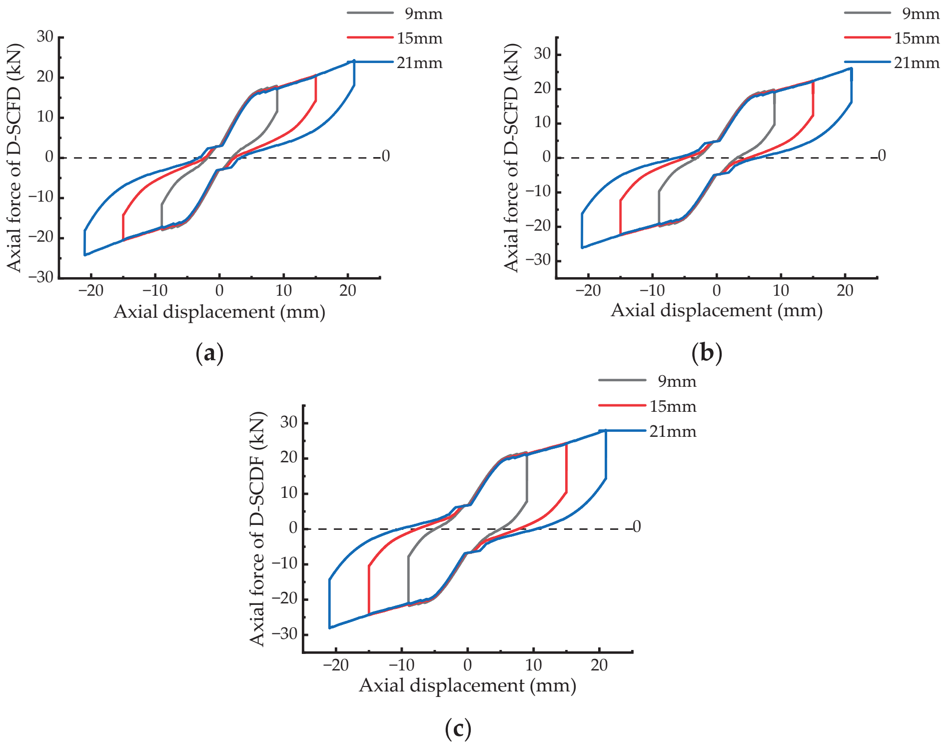

(**a**) (**b**) (**c**)

Figure 8. Hysteretic curves of D-SCFD: (**a**) pre-tightening force of FD is 3 kN, (**b**) pre-tightening force of FD is 5 kN, and (**c**) pre-tightening force of FD is 7 kN.

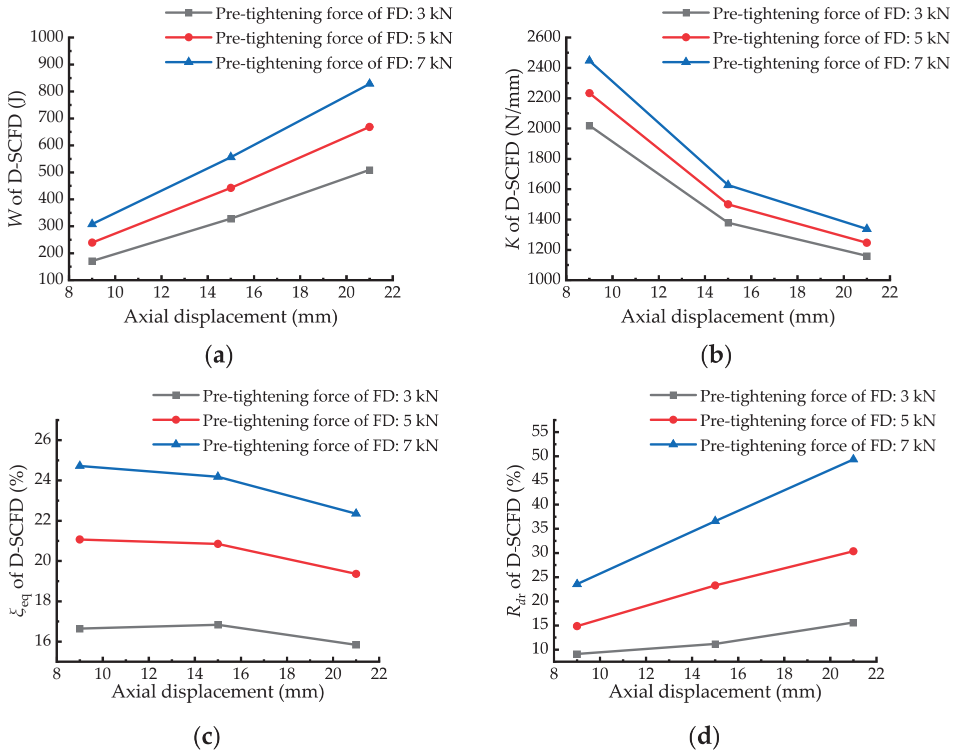

(**a**) (**b**) (**c**) (**d**)

Figure 9. Mechanical property parameters of D-SCFD: (**a**) dissipated energy, (**b**) secant stiffness, (**c**) equivalent viscous damping, and (**d**) rate of residual deformation.

The R_{dr} of D-SCFD increased after magnifying the pre-tightening force of FD, and the maximum value of R_{dr} reached 49.35%. The slope of each force–deformation curve of D-SCFD decreased with the increase in axial deformation when SMA underwent reverse martensitic transformation. This indicates that the amplification of R_{dr} was positively correlated with the axial deformation. The experimental results of D-SCFD showed that the performance of energy dissipation was less affected by the axial deformation after the martensitic transformation of SMA happened but more affected by the pre-tightening force of FD. Meanwhile, the recentering performance of D-SCFD was negatively correlated with the pre-tightening force of FD, whose reduction caused by magnifying the pre-tightening force of FD became more obvious with the increase in axial deformation.

4. Simplified Mechanical Model and Parameter Analysis

4.1. Verification of Simplified Mechanical Model

A simplified mechanical model of D-SCFD was established to analyze the influence of coil springs, SMA rods, and FD on the performance of recentering and energy dissipation. In the model, the relations of restoring force provided by those elements could be acquired, which meet the requirements related to different performance objectives of recentering. Meanwhile, the accuracy of the simplified mechanical model was verified according to the experimental results. The simplified analysis model is shown in Figure 10. D-SCFD was generated in parallel by coil springs, SMAs, and FD, and the axial force response was the sum of that provided by each element.

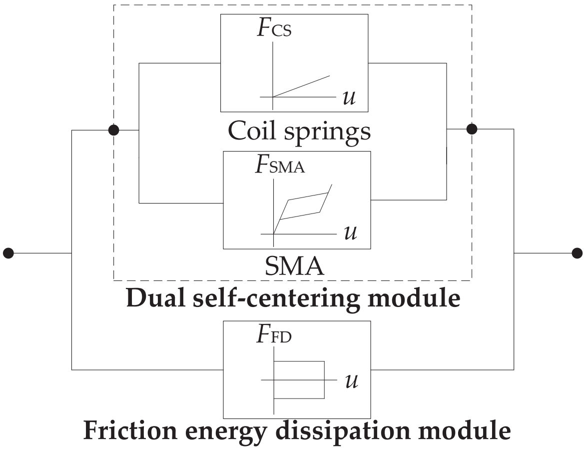

Figure 10. Schematic diagram of D-SCFD simplified analysis model.

Referring to the previous study [41], the axial force of SMA rods is calculated by a piecewise linear algorithm here. In addition, we ignored the difference in the elastic modulus between the austenitic and martensitic phases of SMA rods. Compared with the SMA mechanical model proposed by Brinson and Auricchio [42,43], the suggested model in this study needs a lower computational cost. The convenient calculations of R_{dr} and ξ_{eq} can be derived from this model, too. The axial force of D-SCFD can be calculated by the following:

$$F_{\text{D-SCFD}} = k_{\mathrm{CS}}u + P\mu \mathrm{sgn}(\frac{du}{dt}) + F_{\mathrm{SMA}} \tag{1}$$

where $F_{\text{D-SCFD}}$ is the axial force response of D-SCFD; k_{CS} denotes the total stiffness of the coil springs; u is the axial deformation of D-SCFD; t denotes the time; P and μ are the pre-tightening force and sliding friction coefficient of FD, respectively; sgn(x) is a symbolic function that returns either 1 or -1, depending on the positivity or negativity of x; F_{SMA} is the axial force of the SMA rods, and the value can be derived from the following:

$$F_{\mathrm{SMA}} = \varepsilon(u\frac{du}{dt})F_{\mathrm{SMA}}^{\mathrm{L}} + \varepsilon(-u\frac{du}{dt})F_{\mathrm{SMA}}^{\mathrm{U}} \tag{2}$$

where $\varepsilon(x)$ is a step function and returns 0, 1/2, or 1 according to the relationship between x and 0; $F_{\mathrm{SMA}}^{\mathrm{L}}$ and $F_{\mathrm{SMA}}^{\mathrm{U}}$ are the axial force responses of SMA rods during loading and unloading, respectively, which can be calculated by the following:

$$F_{\mathrm{SMA}}^{\mathrm{L}}=\begin{cases} k_{\mathrm{SMA},1}u, & |u|\leqslant u_{\mathrm{Ms}} \\ \mathrm{sgn}(u)[k_{\mathrm{SMA},2}(|u|-u_{\mathrm{Ms}})+F_{\mathrm{Ms}}], & u_{\mathrm{Ms}}<|u|\leqslant u_{\mathrm{Mf}} \end{cases} \tag{3}$$

$$F_{\mathrm{SMA}}^{\mathrm{U}}=\begin{cases} k_{\mathrm{SMA},1}u, & |u|\leqslant u_{\mathrm{Af}} \\ \mathrm{sgn}(u)[k_{\mathrm{SMA},2}(|u|-u_{\mathrm{Af}})+F_{\mathrm{Af}}], & u_{\mathrm{Af}}<|u|\leqslant u'_{\mathrm{AS}} \\ \mathrm{sgn}(u)[k_{\mathrm{SMA},1}(|u|-u_{\mathrm{UL}}^{\mathrm{S}})+F_{\mathrm{UL}}^{\mathrm{S}}], & u'_{\mathrm{AS}}<|u|\leqslant u_{\mathrm{UL}}^{\mathrm{S}} \end{cases} \tag{4}$$

where $k_{\mathrm{SMA},1}$ and $k_{\mathrm{SMA},2}$ denote the linear stiffness of SMA rods before and after martensitic transformation, respectively; u_{Ms} and F_{Ms} are the axial deformation and force of SMA rods at the start of martensitic transformation, respectively. u_{Mf} denotes the axial deformation of SMA rods at the end of martensitic transformation. u_{Af} and F_{Af} are the axial deformation and force at the end of the reverse martensitic transformation of SMA rods, respectively. $u_{\mathrm{UL}}^{\mathrm{S}}$ and $F_{\mathrm{UL}}^{\mathrm{S}}$ are the axial deformation and force of SMA rods at the beginning of unloading, respectively, which can be calculated by way of $F_{\mathrm{SMA}}^{\mathrm{L}}$. u'_{AS} represents the axial deformation of SMA rods at the point of where reverse martensitic transformation begins, whose calculation is given as below:

$$u'_{\mathrm{As}}=\frac{F_{\mathrm{Af}}-F_{\mathrm{UL}}^{\mathrm{S}}-k_{\mathrm{SMA},2}u_{\mathrm{Af}}+k_{\mathrm{SMA},1}u_{\mathrm{UL}}^{\mathrm{S}}}{k_{\mathrm{SMA},1}-k_{\mathrm{SMA},2}} \tag{5}$$

When the axial deformation of D-SCFD reaches the maximum permissible value, the rate of residual deformation and equivalent viscous damping derived from the simplified mechanical model are expressed as below:

$$R_{\mathrm{dr}}=\begin{cases} \dfrac{\beta}{\alpha+\frac{\sigma_{\mathrm{Ms}}\varepsilon_{\mathrm{Mf}}}{\sigma_{\mathrm{Mf}}\varepsilon_{\mathrm{Ms}}}}, & F_{\mathrm{FD}}\leqslant F_{\mathrm{CS}}\frac{\varepsilon_{\mathrm{Af}}}{\varepsilon_{\mathrm{Mf}}}+F_{\mathrm{Mf}}\frac{\sigma_{\mathrm{Af}}}{\sigma_{\mathrm{Mf}}} \\ \dfrac{\beta+\frac{(\sigma_{\mathrm{Mf}}-\sigma_{\mathrm{Ms}})\varepsilon_{\mathrm{Af}}}{\sigma_{\mathrm{Mf}}(\varepsilon_{\mathrm{Mf}}-\varepsilon_{\mathrm{Ms}})}-\frac{\sigma_{\mathrm{Af}}}{\sigma_{\mathrm{Mf}}}}{\alpha+\frac{(\sigma_{\mathrm{Mf}}-\sigma_{\mathrm{Ms}})\varepsilon_{\mathrm{Mf}}}{\sigma_{\mathrm{Mf}}(\varepsilon_{\mathrm{Mf}}-\varepsilon_{\mathrm{Ms}})}}, & \begin{array}{c} F_{\mathrm{CS}}\frac{\varepsilon_{\mathrm{Af}}}{\varepsilon_{\mathrm{Mf}}}+F_{\mathrm{Mf}}\frac{\sigma_{\mathrm{Af}}}{\sigma_{\mathrm{Mf}}}<F_{\mathrm{FD}}\ \& \\ F_{\mathrm{FD}}\leqslant F_{\mathrm{CS}}\frac{\varepsilon_{\mathrm{As}}}{\varepsilon_{\mathrm{Mf}}}+F_{\mathrm{Mf}}\frac{\sigma_{\mathrm{As}}}{\sigma_{\mathrm{Mf}}} \end{array} \\ \dfrac{\beta+\frac{\sigma_{\mathrm{Ms}}\varepsilon_{\mathrm{Mf}}}{\sigma_{\mathrm{Mf}}\varepsilon_{\mathrm{Ms}}}-1}{\alpha+\frac{\sigma_{\mathrm{Ms}}\varepsilon_{\mathrm{Mf}}}{\sigma_{\mathrm{Mf}}\varepsilon_{\mathrm{Ms}}}}, & F_{\mathrm{CS}}\frac{\varepsilon_{\mathrm{As}}}{\varepsilon_{\mathrm{Mf}}}+F_{\mathrm{Mf}}\frac{\sigma_{\mathrm{As}}}{\sigma_{\mathrm{Mf}}}<F_{\mathrm{FD}} \end{cases} \tag{6}$$

$$\xi_{\mathrm{eq}}=\frac{2(\frac{\varepsilon_{\mathrm{Mf}}-\varepsilon_{\mathrm{Ms}}}{\varepsilon_{\mathrm{Mf}}})[\frac{\sigma_{\mathrm{Ms}}-\sigma_{\mathrm{Af}}}{\sigma_{\mathrm{Mf}}}-\frac{(\sigma_{\mathrm{Mf}}-\sigma_{\mathrm{Ms}})(\varepsilon_{\mathrm{Ms}}-\varepsilon_{\mathrm{Af}})}{\sigma_{\mathrm{Mf}}(\varepsilon_{\mathrm{Mf}}-\varepsilon_{\mathrm{Ms}})}]+4\beta}{2\pi(1+\alpha+\beta)} \tag{7}$$

where α denotes the ratio of the axial force of the coil springs to that of SMA rods when the axial deformation of D-SCFD reaches the maximum permissible value; β is the ratio of the axial force of FD to that of SMA rods in the same situation. F_{CS} represents the maximum axial force of the coil springs.

Combined with the tensile test results of SMA, the hysteretic curves of D-SCFD were predicted using the simplified mechanical model outlined here. The comparison of hysteretic curves between the predicted and experimental results is shown in Figure 11. The main parameters of the simplified mechanical model are listed in Table 4. The axial force responses with the double lines computed by the simplified model during loading fit well with the test findings. In the unloading, there were small differences in $F_{\text{D-SCFD}}$ between the predicted and experimental values. The simplified model ignored the distinction of elastic modulus between the austenitic and martensitic phases of SMA and did not consider that the stress–strain curves had the characteristics of "smooth transition" at the start of reverse martensitic transformation. That was the main reason behind the prediction of $F_{\text{D-SCFD}}$ deviating from the experimental results during unloading.

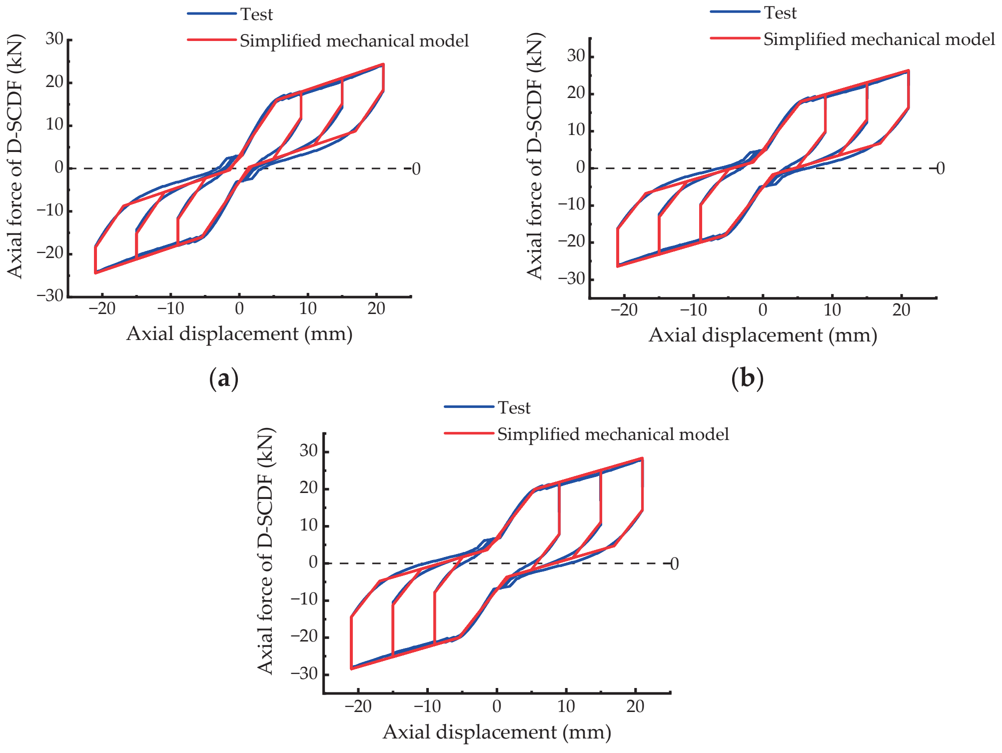

(**a**) (**b**)

(**c**)

Figure 11. Comparison of hysteretic curves between the predicted and experimental results: (**a**) pre-tightening force of FD is 3 kN, (**b**) pre-tightening force of FD is 5 kN, and (**c**) pre-tightening force of FD is 7 kN.

Table 4. Parameters of the mechanical model.

u_{Ms} (mm)	F_{Ms} (N)	u_{Mf} (mm)	F_{Mf} (N)	u_{Af} (mm)	F_{Af} (N)	$k_{\mathrm{SMA,1}}$(N/mm)	$k_{\mathrm{SMA,2}}$ (N/mm)
5.47	11,409.18	21.00	15,328.21	1.40	2915.95	2085.77	251.84

The maximum difference in $F_{\text{D-SCFD}}$ between the predicted and the experimental values was only 2.93 kN, which is acceptable. When the axial deformation of D-SCFD reached the maximum permissible value, a comparative analysis of the theoretical and experimental values of R_{dr} and ξ_{eq} was conducted, as presented in Table 5. The corresponding maximum absolute error was only 10.27% and 0.81%, respectively. Therefore, the calculation methods of R_{dr} and ξ_{eq} derived from the simplified mechanical model can describe the recentering and energy dissipation performance of D-SCFD.

Table 5. Comparison of theoretical and experimental values of R_{dr} and ξ_{eq}.

Pre-Tightening Force of FD (kN)	Theoretical R_{dr} (%)	Experimental R_{dr} (%)	Absolute Error of R_{dr} (%)	Theoretical ξ_{eq} (%)	Experimental ξ_{eq} (%)	Absolute Error of ξ_{eq} (%)
3	6.03	15.63	9.6	15.03	15.84	0.81
5	21.48	30.35	8.87	18.72	19.36	0.64
7	39.08	49.35	10.27	21.89	22.35	0.46

4.2. Parameter Analysis

The methods introduced earlier were used to calculate the R_{dr} and ξ_{eq} with different α and β. The α was used to describe the ratio of axial force provided by coil springs and

SMA rods. The β measured the ratio of axial force provided by the FD and SMA rods. While the total force of the damper is constant, the consumption of SMA can decrease with an increase in α and β. Based on that, the variation trends of recentering and energy dissipation performance of D-SCFD were further analyzed, which are shown in Figure 12. The value of α ranged from 0 to 100%. When the α was 0, the variation trend of R_{dr} had three different growth rates with the increase in β. This also indicated that continuing to magnify the F_{FD} would result in a significant increase in R_{dr} in the absence of coil springs, especially in the case where the F_{FD} exceeded F_{Af}. After increasing α, the growth rate of R_{dr} relative to β gradually decreased, which indicated that coil springs could improve the recentering performance of D-SCFD. ξ_{eq} rose with the increase in β, and the growth rate decreased gradually. However, magnifying α led to a decrease in ξ_{eq}, the amplitude of which decreased gradually. The variation trends of R_{dr} and ξ_{eq} appeared, suggesting that improving the recentering performance will bring about a decrease in the energy dissipation performance, both of which are contradictory. Therefore, the proportion of restoring forces provided by coil springs, SMA, and FD is critical, as it is a requirement for D-SCFD to work optimally in terms of both recentering and energy dissipation.

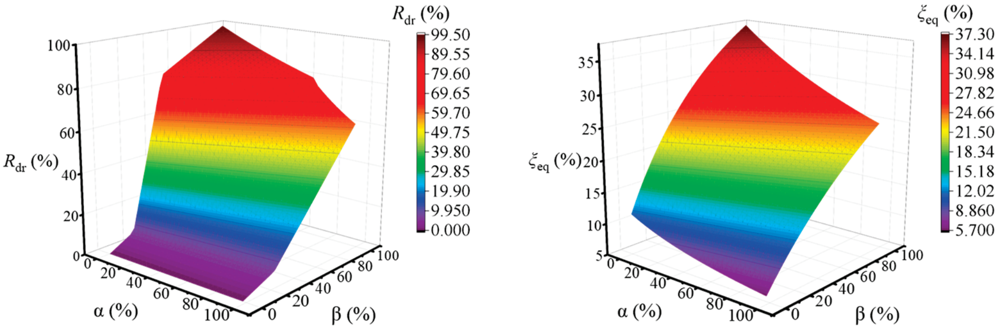

(**a**) (**b**)

Figure 12. Variation trends of recentering and energy dissipation performance: (**a**) R_{dr} and (**b**) ξ_{eq}.

Firstly, the relationship between α and β was determined by the calculation method of R_{dr}, which can achieve three different performance targets for recentering. Then, the influence of the corresponding α and β on the energy dissipation performance of D-SCFD was analyzed. When the R_{dr} was 10%, 30%, and 50%, the relationship between α and β satisfied the equation as below:

$$\beta = \begin{cases} \frac{\alpha}{10} + 0.2016, & R_{dr} = 10\% \\ \frac{3\alpha}{10} + 0.2707, & R_{dr} = 30\% \\ \frac{5\alpha}{10} + 0.3398, & R_{dr} = 50\% \end{cases} \tag{8}$$

Combining the relation equation and calculation method of ξ_{eq}, the curves of ξ_{eq} with different targets of recentering performance of D-SCFD are shown in Figure 13. The ξ_{eq} of D-SCFD decreased with the increase in α and a reduction in ξ_{eq} gradually rose with the decrease in R_{dr}. When R_{dr} was 10%, 30%, and 50%, respectively, the corresponding maximum reduction in ξ_{eq} was 6.87%, 3.97%, and 1.83%, respectively. Therefore, when the high recentering performance target is taken, it is inappropriate to choose a larger ratio of axial force of coil springs to that of SMA, which can avoid a sharp decline in the energy dissipation performance of the D-SCFD. As the recentering performance target decreases, that ratio can be magnified appropriately, reducing the consumption of SMAs.

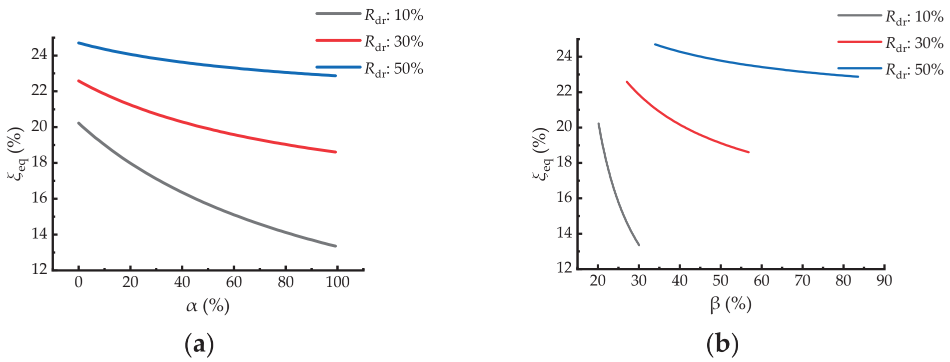

Figure 13. Variation trends of ξ_{eq} with different performance of recentering: (**a**) influence of α and (**b**) influence of β.

5. Seismic Response Mitigation of Multi-Story SF

5.1. Overview of Structure Case

A five-story steel frame (SF) is selected as the case, which is located in Jiangsu Province, China. The control effects of D-SCFD on the seismic responses of SF were obtained by nonlinear time history analysis, considering the different recentering performances of D-SCFD. The structural plane of SF is shown in Figure 14. The members of SF adopted steel with a yield strength of 355 MPa, the design of which considered earthquake action according to the Chinese code for seismic design of buildings (GB 50011-2010) [44]. Its beams and columns will not yield after experiencing frequently occurred earthquakes (FOE). According to the Chinese code for seismic design of buildings [44], the S_a(0.74 s, 4%) and S_a(0.74 s, 5%) of the SF under FOE and maximum considered earthquake (MCE) are 0.19 g and 0.91 g, respectively. Here, $S_a(T_1, \xi)$ denotes the spectral acceleration corresponding to the first translational period of SF, and the letter g denotes the gravitational acceleration.

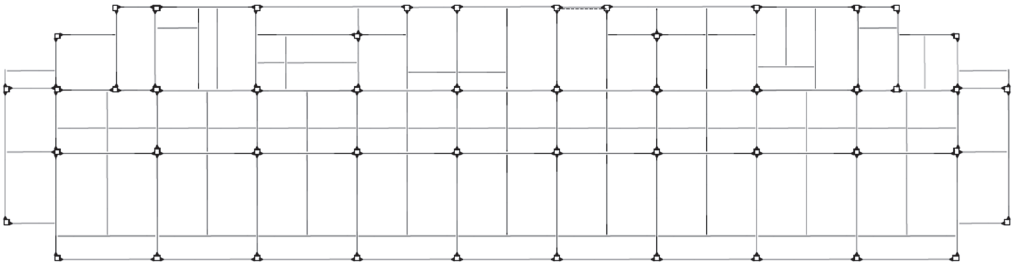

Figure 14. Structural plane of SF.

5.2. Ground Motion Inputs

The previous studies [36–40] reflected that the MS-AS would lead to the accumulation of structural damage and that the AS should be considered in the control of structural seismic responses. Therefore, seven groups of MS-AS records were selected as the excitation, and the directions of inputs were the same as those of the first translational vibration mode of SF. The information about each ground motion is listed in Table 6. When compared to $S_a(T_1, \xi)$, using the peak ground acceleration (PGA) to characterize the intensities of ground motions readily makes structure responses more distinct [45]. Based on the S_a(0.74 s, 5%) being 0.91 g when SF experiences MCE, the accelerations of all ground motions were adjusted accordingly. Meanwhile, time intervals of 20 s were added between the MS and AS, and durations of 10 s were added to the ends of the AS to analyze the residual deformations of the structure. The acceleration and response spectra curves are shown in Figure 15 and Figure 16, respectively.

Table 6. Information about ground motions.

No.	Event	MS		AS		Station
		Earthquake Magnitude (Mw)	**Date**	**Earthquake Magnitude (Mw)**	**Date**	
GM1	Chalfant Valley	5.77	20 July 1986	6.19	21 July 1986	Bishop, Paradise Lodge
GM2	Whittier Narrows	5.99	1 October 1987	5.27	4 October 1987	Bell Gardens, Jaboneria
GM3	Northridge	6.69	17 January 1994	5.28	20 March 1994	Arleta, Nordhoff Fire Sta
GM4	Chi-Chi, Taiwan	7.62	20 September 1999	6.20	20 September 1999	CHY024
GM5	L'Aquila, Italy	6.30	6 April 2009	5.60	7 April 2009	L'Aquila, Parking
GM6	Darfield, New Zealand	7.00	3 September 2010	6.20	21 February 2011	Canterbury Aero Club
GM7	Kahramanmaras, Turkey	7.70	6 February 2023	7.60	6 February 2023	6203

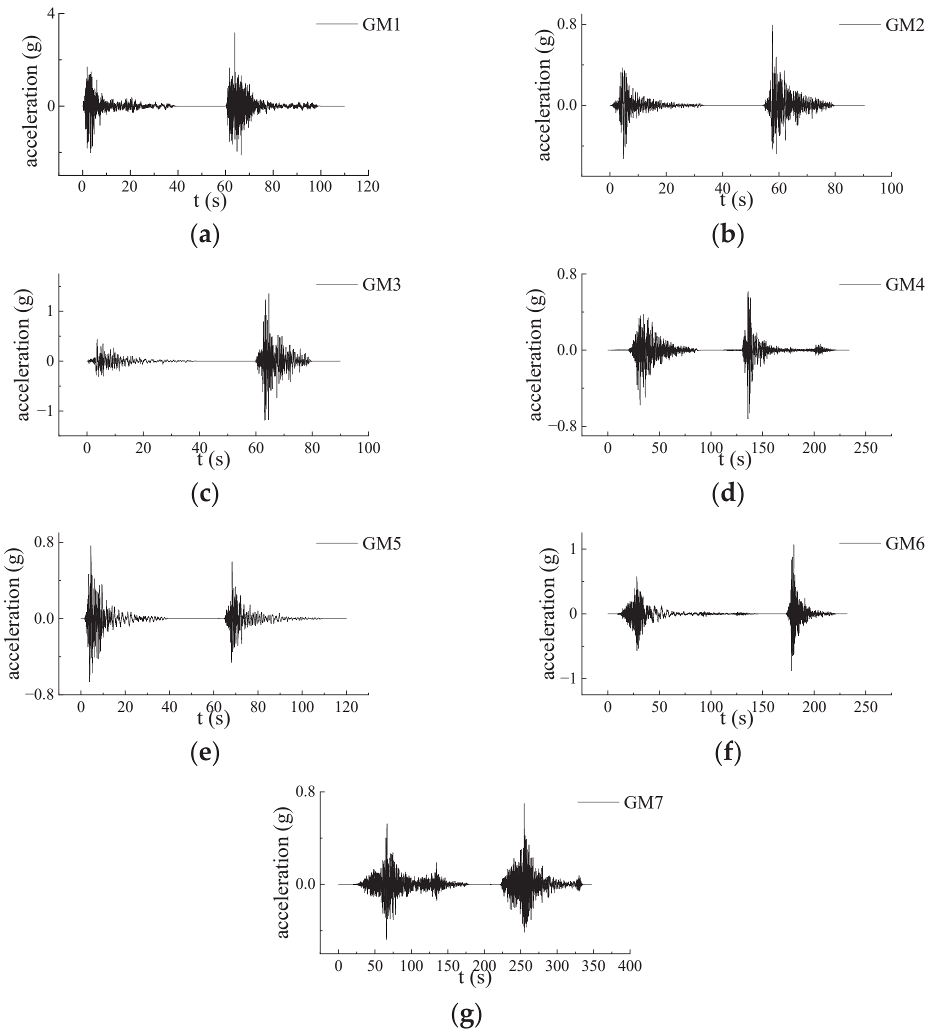

(**a**) (**b**) (**c**) (**d**) (**e**) (**f**) (**g**)

Figure 15. Acceleration of ground motions: (**a**) GM1, (**b**) GM2, (**c**) GM3, (**d**) GM4, (**e**) GM5, (**f**) GM6, and (**g**) GM7.

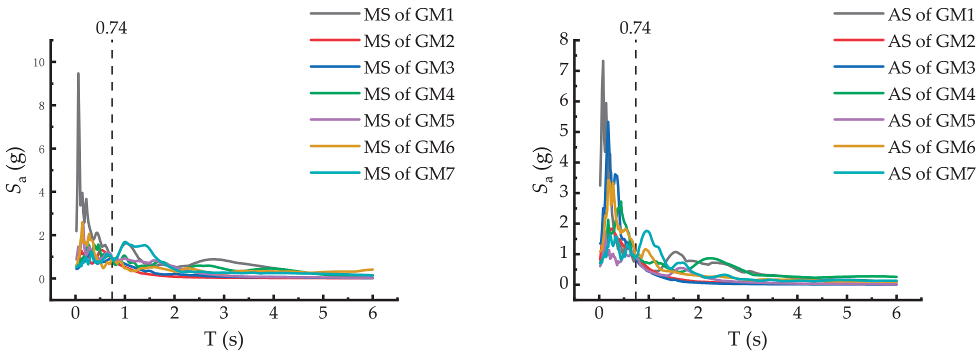

(**a**) (**b**)

Figure 16. Response spectra of ground motions: (**a**) MS and (**b**) AS.

5.3. D-SCFD

To analyze the seismic response control effects of D-SCFD with different recentering performances, D-SCFDs with R_{dr} values of 10%, 30%, and 50% were used to mitigate the seismic responses of SF, respectively. The layout of the D-SCFDs on each floor is shown in Figure 17.

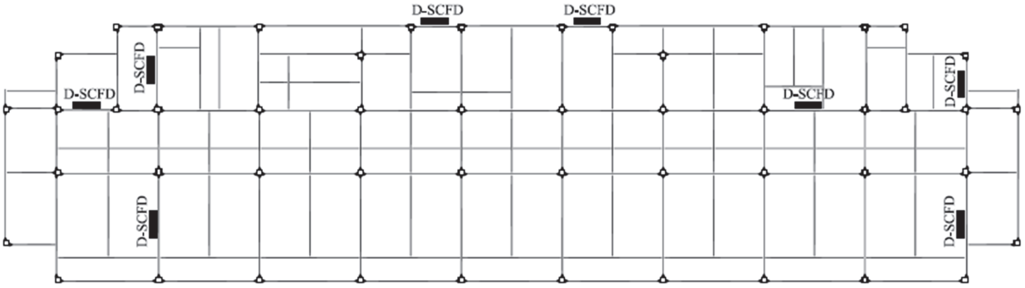

Figure 17. Plane layout of D-SCFDs.

In addition to one damper at each corresponding plane position of the top two floors, two dampers were set on each of the other floors. The α of D-SCFD was taken as 20%, and the β corresponding to the three different recentering performances was obtained earlier using the relation equation mentioned. The maximum axial forces of all D-SCFDs were 500 kN, whose limits of deformation were 60 mm based on the maximum inter-story drift responses of SF under the MCE. The main design parameters of D-SCFD are listed in Table 7.

Table 7. Design parameters of D-SCFD.

No.	ID of Damper	Maximum Axial Force (kN)	Limits of Deformations (mm)	α (%)	β (%)	Theoretical ξ_{eq} (%)	Theoretical R_{dr} (%)	Section Area of SMA (mm^2)	Stiffness of Coil Springs (kN/mm)	Pre-Tightening Force of FD (kN)
1	D-SCFD-1	500.00	60.00	20.00	22.16	17.99	10.00	576.69	1.17	77.95
2	D-SCFD-2	500.00	60.00	20.00	33.07	21.24	30.00	535.61	1.09	108.00
3	D-SCFD-3	500.00	60.00	20.00	43.98	24.07	50.00	499.95	1.02	134.10

To simulate the D-SCFD, the three elements of linear, multi-linear elastic, and plastic (wen) in SAP2000 were connected in parallel. The axial mechanical behavior of D-SCFD was described in the numerical model. The results from the mechanical test of D-SCFD were used to validate the method of simulation above. The parameters and hysteretic curves for validation are presented in Table 8 and Figure 18, respectively. The difference in hysteretic curves between the SAP2000 model and the test is small.

Table 8. Parameters for validation.

ID of Damper	Coil Springs	FD			SMA						
	Linear	Plastic (Wen)			Multi-Linear Elastic				Plastic (Wen)		
	k (kN/mm)	k_1 (kN/mm)	F_y (kN)	k_2/k_1 (%)	u_1 (mm)	F_1 (kN)	u_2 (mm)	F_2 (kN)	k_1 (kN/mm)	F_y (kN)	k_2/k_1 (%)
D-SCFD	0.29	7.00	7.00	0.00	5.46	7.77	21.00	11.68	3.64	3.64	0.00

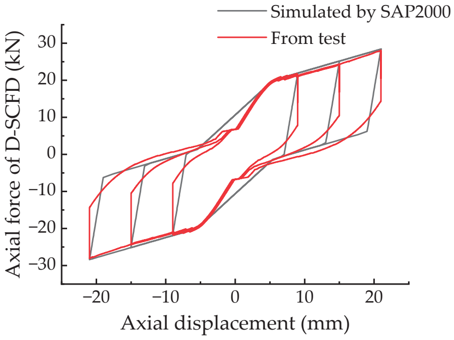

Figure 18. Comparison of hysteretic curves between the SAP2000 model and the test.

According to Table 7, the simulation parameters are presented in Table 9, which were derived from the SMA phase transition stress and strain from the test. The hysteretic curves simulated by SAP2000 are shown in Figure 19a. The simulation results of ξ_{eq} and R_{dr} had small deviations from the theoretical values, and the maximum absolute errors were only 12.14% and 1.20%, respectively. The connection between the D-SCFD and the SF is shown in Figure 19b. Compared with D-SCFD-1, the maximum SMAs' axial force of D-SCFD-2 and D-SCFD-3 decreased by 7.12% and 13.31%, respectively, which is advantageous to reduce the consumption of SMA.

Table 9. Simulation parameters of D-SCFD.

ID of Damper	Coil Springs	FD			SMA						
	Linear	Plastic (Wen)			Multi-Linear Elastic				Plastic (Wen)		
	k (kN/mm)	k_1 (kN/mm)	F_y (kN)	k_2/k_1 (%)	u_1 (mm)	F_1 (kN)	u_2 (mm)	F_2 (kN)	k_1 (kN/mm)	F_y (kN)	k_2/k_1 (%)
D-SCFD-1	1.17	77.95	77.95	0.00	15.67	176.19	60.00	265.98	5.47	85.72	0.00
D-SCFD-2	1.09	108.00	108.00	0.00	15.67	163.51	60.00	246.91	5.09	79.74	0.00
D-SCFD-3	1.02	134.10	134.10	0.00	15.67	152.75	60.00	230.59	4.74	74.31	0.00

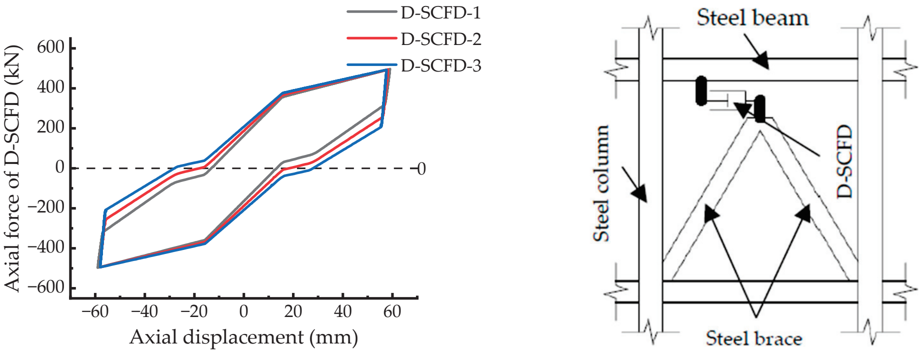

(**a**) (**b**)

Figure 19. (**a**) Simulated hysteretic curves of D-SCFDs and (**b**) connection between D-SCFD and SF.

5.4. Mitigation of Seismic Responses

After the nonlinear time history analysis utilizing SAP2000, the peak inter-story drift ratios (PIDRs) under each ground motion are shown in Figure 20. D-SCFDs reduced the PIDRs of SF under the earthquake, whose safety was effectively improved. With different D-SCFDs, the maximum inter-story drifts of SF were 43.60 mm, 51.69 mm, and 50.02 mm, respectively, less than the limit of deformations. The average peak inter-story drift ratios (APIDRs) and the control rates of those under seven ground motions are shown in Table 10. Wherein, the APIDRs of the second and third floors were larger than the others. For the control effects of APIDRs, the D-SCFD-3 was better than D-SCFD-2, and the D-SCFD-2 was better than D-SCFD-1. The control impacts of APIDRs revealed that lowering the recentering performance of D-SCFDs was advantageous for improving the control effect of the structure's maximum lateral deformations, while R_{dr} did not surpass 50%.

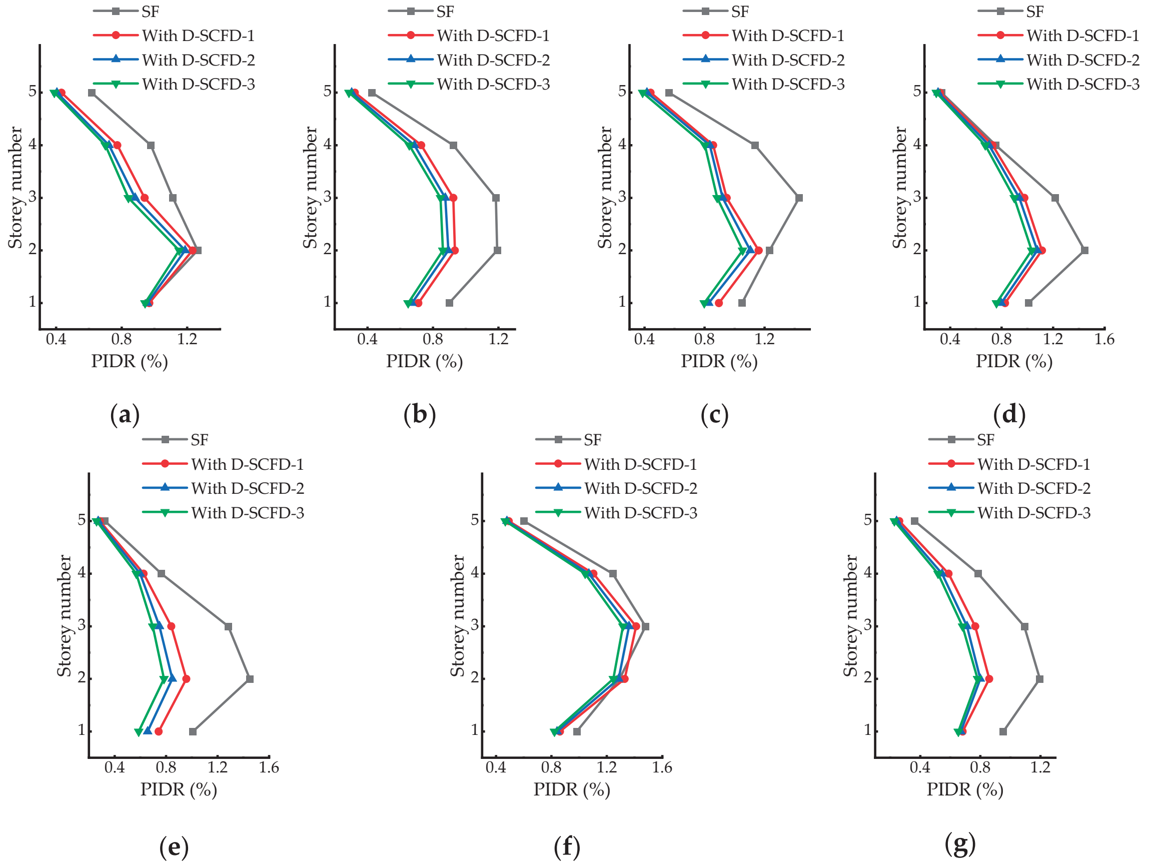

(**a**) (**b**) (**c**) (**d**)

(**e**) (**f**) (**g**)

Figure 20. PIDRs of structure under different ground motions: (**a**) GM1, (**b**) GM2, (**c**) GM3, (**d**) GM4, (**e**) GM5, (**f**) GM6, and (**g**) GM7.

Table 10. APIDRs and the corresponding control rates.

Number of Story	SF	SF with D-SCFD-1		SF with D-SCFD-2		SF with D-SCFD-3	
	APIDR (%)	APIDR (%)	Control Rate of APIDR (%)	APIDR (%)	Control Rate of APIDR (%)	APIDR (%)	Control Rate of APIDR (%)
1	0.980	0.813	17.04	0.775	20.92	0.774	21.02
2	1.296	1.084	16.36	1.028	20.68	0.987	23.84
3	1.257	0.973	22.59	0.919	26.89	0.881	29.91
4	0.941	0.773	17.85	0.737	21.68	0.709	24.65
5	0.461	0.365	20.82	0.347	24.73	0.330	28.42

The average residual inter-story drift ratios (ARIDRs) of the SF are shown in Table 11. D-SCFDs significantly reduced the ARIDRs of SF, which could reduce the post-seismic recovery costs of the structure. The differences in the control effects of ARIDRs were tiny, which were generated by the discrepancies in the recentering performances of D-SCFDs. The maximum difference was only 0.008%, and its level was micro. Therefore, when the R_{dr} was less than 50%, the objectives of recentering performances of D-SCFDs hardly had obvious effects on the residual deformations of the structure after an earthquake. The average peak floor accelerations (APFAs) under seven ground motions are shown in Table 12. D-SCFDs reduced the floor acceleration responses, thereby reducing the inertial forces caused by the earthquakes. Meanwhile, D-SCFD-3 had the best control effect on APFAs, followed by D-SCFD-2, and the control effect of D-SCFD-1 was relatively minimal. Differences in APFA mitigation resulted in previous variations in APIDR control rates, both of which were primarily caused by the different recentering performances of D-SCFDs. After minimizing the aims of recentering performances, the D-SCFDs had a larger value of ξ_{eq}, which had better energy consumption performance and resulted in better APIDR and APFA mitigation.

Table 11. ARIDRs and the corresponding control rates.

Number of Story	SF	SF with D-SCFD-1		SF with D-SCFD-2		SF with D-SCFD-3	
	ARIDR (%)	ARIDR (%)	Control Rate of ARIDR (%)	ARIDR (%)	Control Rate of ARIDR (%)	ARIDR (%)	Control Rate of ARIDR (%)
1	0.027	0.013	51.85	0.010	62.96	0.009	66.67
2	0.054	0.025	53.70	0.020	62.96	0.017	68.52
3	0.048	0.021	56.25	0.017	64.58	0.017	64.58
4	0.021	0.012	42.86	0.010	52.38	0.009	57.14
5	0.005	0.004	20.00	0.004	20.00	0.006	−20.00

Table 12. APFAs and corresponding control rates.

Number of Story	SF	SF with D-SCFD-1		SF with D-SCFD-2		SF with D-SCFD-3	
	APFA ($\mathrm{m/s^2}$)	APFA ($\mathrm{m/s^2}$)	Control Rates of APFA (%)	APFA ($\mathrm{m/s^2}$)	Control Rates of APFA (%)	APFA ($\mathrm{m/s^2}$)	Control Rates of APFA (%)
1	12.03	10.31	14.30	10.03	16.63	9.82	18.37
2	14.28	11.40	20.17	10.85	24.02	10.59	25.84
3	12.35	11.87	3.89	11.37	7.94	10.94	11.42
4	15.86	14.39	9.27	13.88	12.48	13.58	14.38
5	24.09	19.52	18.97	18.71	22.33	18.01	25.24

6. Conclusions

In this study, a new dual self-centering damper (D-SCFD) was proposed, which was generated by connecting coil springs, SMA rods, and a friction energy dissipation device (FD) in parallel. While carrying out the mechanical tests of small-scale specimens, a simplified mechanical model was established. The theoretical index calculations of the performance of recentering and energy dissipation were derived and used to analyze the influence of coil springs, SMA rods, and FD on the performance of D-SCFD. Eventually, the seismic response control effects of D-SCFD on multi-story steel frames (SFs) were analyzed, which experienced consecutive strong earthquakes. The main conclusions are as follows:

1. The recentering and energy dissipation performances of D-SCFD were contradictory. It is necessary to define the reasonable relationship between the axial force provided by coil springs, SMA, and FD, which can make the D-SCFD give play to the ideal performance of recentering and energy dissipation.

2. After magnifying the axial force response of FD, the energy dissipation performance of D-SCFD increased, but the recentering performance decreased. Meanwhile, a reduction in the recentering performance was positively correlated with the loading displacement amplitude. After the martensitic transformation of SMA, the loading displacement amplitude had little effect on the energy dissipation performance of D-SCFD.
3. The simplified mechanical model of D-SCFD, the theoretical index calculations of the performance of recentering, and energy dissipation could accurately describe the mechanical behaviors of D-SCFD. In the suggested model, the parameters are related to the mechanical properties of each component, which is beneficial to its serviceability. With the reduction in the recentering performance target and the increase in the axial force ratio of the coil springs, the decrease in the energy dissipation performance of D-SCFD would be slower.
4. When the recentering performance of D-SCFD is required to be high, it is not appropriate to excessively increase the axial force ratio of the coil springs to avoid a rapid decline in the performance of energy dissipation. With the decrease in the recentering performance target, the proportion of axial force provided by the coil springs can be appropriately increased, thereby reducing the consumption of SMA.
5. The simulations of D-SCFD utilizing SAP2000 were close to the test. Adjusting the R_{dr} to 50% from 10%, the section area of SMA decreased by 13.31% in D-SCFD with a α of 20%. Simultaneously, the control rate of the average peak inter-story drift ratio (APIDR) increased 7.48% in the story with the maximum APIDR. However, the maximum variation of average residual inter-story drift ratios (ARIDRs) only reached 0.008%. Therefore, when D-SCFD is used to mitigate seismic responses, the performance of recentering can be appropriately reduced.
6. Compared to the existing self-centering damper-based SMA, the consumption of SMA in D-SCFD was less, which avoided the expensive cost. In the future, the combination of a dual self-centering pattern (D-SC) and other kinds of passive energy dissipation devices could be promising.

Author Contributions: Conceptualization, J.Q., X.L. and Y.B.; methodology, X.L. and Y.B.; software, X.L. and Y.B.; validation, J.Q., X.L. and Y.B.; formal analysis, W.W., Y.L. and J.P.; investigation, J.Q. and W.W.; resources, J.Q.; data curation, W.W., Y.L. and J.P.; writing—original draft preparation, X.L. and Y.B.; writing—review and editing, J.Q., X.L. and Y.B.; visualization, J.Q., J.P. and C.Z.; supervision, J.Q. and J.P.; project administration, J.Q.; funding acquisition, J.Q. All authors have read and agreed to the published version of the manuscript.

Funding: This research was funded by the National Natural Science Foundation of China (No. 41867069) and the Yunnan Provincial Department of Education Program (No. 2023Y0260).

Data Availability Statement: The data presented in this study are available from the corresponding author upon reasonable request.

Acknowledgments: The authors extend their appreciation to the technological support from School of Architecture and Planning, Yunnan University.

Conflicts of Interest: The authors declare no conflicts of interest.

Nomenclature

SMA	Shape memory alloy
FD	Friction energy dissipation device
D-SCFD	Dual self-centering friction damper
BRB	Buckling restrained brace
MYD	Metallic yielding damper
MS-AS	Mainshock–aftershock sequence
RC	Reinforced concrete
D-SC	Dual self-centering
SF	Steel frame

W	Dissipated energy
K	Secant stiffness
ξ_eq	Equivalent viscous damping
R_dr	Rate of residual deformation
$F_\text{D-SCFD}$	Axial force response of D-SCFD
k_CS	Total stiffness of the coil springs
u	Axial deformation of D-SCFD
t	Time
P	Pre-tightening force of FD
μ	Sliding friction coefficient of FD
$\mathrm{sgn}(x)$	Symbolic function
F_SMA	Axial force of the SMA rods
$\varepsilon(x)$	Step function
F^L_{SMA}	Axial force responses of SMA rods during loading
F^U_{SMA}	Axial force responses of SMA rods during unloading
$k_\mathrm{SMA,1}$	Linear stiffness of SMA rods before martensitic transformation
$k_\mathrm{SMA,2}$	Linear stiffness of SMA rods after martensitic transformation
u_Ms	Axial deformation of SMA rods at the start of martensitic transformation
F_Ms	Axial force of SMA rods at the start of martensitic transformation
u_Mf	Axial deformation of SMA rods at the end of martensitic transformation
u_Af	Axial deformation of SMA rods at the end of the reverse martensitic transformation
F_Af	Axial force of SMA rods at the end of the reverse martensitic transformation
u^S_{UL}	Axial deformation of SMA rods at the beginning of unloading
F^S_{UL}	Axial force of SMA rods at the beginning of unloading
u'_{AS}	Axial deformation of SMA rods at the beginning of the reverse martensitic transformation
α	Ratio of the maximum axial force of the coil springs to that of SMA rods
β	Ratio of the maximum axial force of FD to that of SMA rods
$S_\mathrm{a}(T_1, \xi)$	Spectral acceleration corresponding to the first translational period of structure
PIDR	Peak inter-story drift ratio
APIDR	Average peak inter-story drift ratio
ARIDR	Average residual inter-story drift ratio
APFA	Average peak floor acceleration

References

1. Almajhali, K.Y.M. Review on passive energy dissipation devices and techniques of installation for high rise building structures. *Structures* **2023**, *51*, 1019–1029. [CrossRef]
2. Divyah, N.; Prakash, R.; Srividhya, S.; Ajay Prakash, K. Control of vibrations in high-rise structures using base isolation technology. *Mater. Today Proc.* 2023. [CrossRef]
3. Ilbeigi, S.; Jahanpour, J.; Farshidianfar, A. A novel scheme for nonlinear displacement-dependent dampers. *Nonlinear Dyn.* **2012**, *70*, 421–434. [CrossRef]
4. Hussain, H.; Kim, D.-K.; Zhao, W. Advancements and Future Prospects of Buckling Restrained Braces for Corrosive-Environments: A Comprehensive Literature Review. *Buildings* **2023**, *13*, 2156. [CrossRef]
5. Amiri, J.V.; Navayinia, B.; Navaei, S. Evaluation of performance of eccentric braced frame with friction damper. *Struct. Eng. Mech.* **2011**, *39*, 717–732. [CrossRef]
6. Wang, J.; Men, J.; Zhang, Q.; Fan, D.; Zhang, Z.; Huang, C.-H. Seismic performance evaluation of a novel shape-optimized composite metallic yielding damper. *Eng. Struct.* **2022**, *268*, 114714. [CrossRef]
7. Sabelli, R.; Mahin, S.; Chang, C. Seismic demands on steel braced frame buildings with buckling-restrained braces. *Eng. Struct.* **2003**, *25*, 655–666. [CrossRef]
8. Xu, G.; Guo, T.; Li, A.; Wang, S.; Zhang, R.; Zhu, R.; Xu, J. Review on self-centering damper for seismic resilient building structures. *Structures* **2023**, *54*, 58–77. [CrossRef]
9. Christopoulos, C.; Tremblay, R.; Kim, H.J.; Lacerte, M. Self-centering energy dissipative bracing system for the seismic resistance of structures: Development and validation. *J. Struct. Eng.* **2008**, *134*, 96–107. [CrossRef]
10. Erochko, J.; Christopoulos, C.; Tremblay, R.; Kim, H.-J. Shake table testing and numerical simulation of a self-centering energy dissipative braced frame. *Earthq. Eng. Struct. Dyn.* **2013**, *42*, 1617–1635. [CrossRef]
11. Erochko, J.; Christopoulos, C.; Tremblay, R. Design and Testing of an Enhanced-Elongation Telescoping Self-Centering Energy-Dissipative Brace. *J. Struct. Eng.* **2015**, *141*, 04014163. [CrossRef]
12. Chou, C.-C.; Chung, P.-T. Development of cross-anchored dual-core self-centering braces for seismic resistance. *J. Constr. Steel Res.* **2014**, *101*, 19–32. [CrossRef]

13. Chou, C.-C.; Chen, Y.-C. Development of Steel Dual-Core Self-Centering Braces: Quasi-Static Cyclic Tests and Finite Element Analyses. *Earthq. Spectra* **2015**, *31*, 247–272. [CrossRef]
14. Chou, C.-C.; Tsai, W.-J.; Chung, P.-T. Development and validation tests of a dual-core self-centering sandwiched buckling-restrained brace (SC-SBRB) for seismic resistance. *Eng. Struct.* **2016**, *121*, 30–41. [CrossRef]
15. Wang, Y.; Zhou, Z.; Ge, H.; Yao, J.; Xie, Q. Experimental validation and numerical simulation of a dual-self-centering variable friction braced frame under strong ground motions. *J. Build. Eng.* **2022**, *56*, 104761. [CrossRef]
16. Xie, Q.; Zhou, Z.; Meng, S.-P. Experimental investigation of the hysteretic performance of self-centering buckling-restrained braces with friction fuses. *Eng. Struct.* **2020**, *203*, 109865. [CrossRef]
17. Xu, L.-H.; Fan, X.-W.; Li, Z.-X. Cyclic behavior and failure mechanism of self-centering energy dissipation braces with pre-pressed combination disc springs. *Earthq. Eng. Struct. Dyn.* **2017**, *46*, 1065–1080. [CrossRef]
18. Xu, L.; Fan, X.; Li, Z. Experimental behavior and analysis of self-centering steel brace with pre-pressed disc springs. *J. Constr. Steel Res.* **2017**, *139*, 363–373. [CrossRef]
19. Fan, X.-W.; Xu, L.-H.; Li, Z.-X. Behaviors Comparisons and Prediction of Pre-Pressed Spring Self-Centering Energy Dissipation Braces. *Int. J. Struct. Stab. Dyn.* **2018**, *18*, 1840006. [CrossRef]
20. Filiatrault, A.; Tremblay, R.; Kar, R. Performance evaluation of friction spring seismic damper. *J. Struct. Eng.-ASCE* **2000**, *126*, 491–499. [CrossRef]
21. Khoo, H.-H.; Clifton, C.; Butterworth, J.; MacRae, G.; Gledhill, S.; Sidwell, G. Development of the self-centering Sliding Hinge Joint with friction ring springs. *J. Constr. Steel Res.* **2012**, *78*, 201–211. [CrossRef]
22. Khoo, H.-H.; Clifton, C.; Butterworth, J.; MacRae, G. Experimental Study of Full-Scale Self-Centering Sliding Hinge Joint Connections with Friction Ring Springs. *J. Earthq. Eng.* **2013**, *17*, 972–997. [CrossRef]
23. Dolce, M.; Cardone, D.; Marnetto, R. Implementation and testing of passive control devices based on shape memory alloys. *Earthq. Eng. Struct. Dyn.* **2000**, *29*, 945–968. [CrossRef]
24. Qian, H.; Li, H.; Song, G.; Guo, W. Recentering Shape Memory Alloy Passive Damper for Structural Vibration Control. *Math. Probl. Eng.* **2013**, *2013*, 963530. [CrossRef]
25. Shi, F.; Saygili, G.; Ozbulut, O.E. Probabilistic seismic performance evaluation of SMA-braced steel frames considering SMA brace failure. *Bull. Earthq. Eng.* **2018**, *16*, 5937–5962. [CrossRef]
26. Shi, F.; Ozbulut, O.E.; Zhou, Y. Influence of shape memory alloy brace design parameters on seismic performance of self-centering steel frame buildings. *Struct. Control Health Monit.* **2020**, *27*, e2462. [CrossRef]
27. Shi, F.; Zhou, Y.; Ozbulut, O.E.; Cao, S. Development and experimental validation of anchorage systems for shape memory alloy cables. *Eng. Struct.* **2021**, *228*, 111611. [CrossRef]
28. Shi, F.; Zhou, Y.; Ozbulut, O.E.; Ren, F. Hysteretic response and failure behavior of an SMA cable-based self-centering brace. *Struct. Control Health Monit.* **2022**, *29*, e2847. [CrossRef]
29. Rayegani, A.; Soureshjani, O.K.; Alaee, S.A.M.; Mualla, I.H.; Nemati, F. Seismic Performance of Buildings Equipped with Four-Joint Rotational Friction Dampers in Mainshock–Aftershock Sequences. *J. Struct. Eng.* **2023**, *150*, 04023235. [CrossRef]
30. Li, Y.; Zhang, H.; Wang, J.; Yu, H.; Ma, K.; Zhang, X.; Ji, W.; Li, R. Experimental investigation on the seismic behavior of a novel self-centering friction damper. *J. Build. Eng.* **2023**, *76*, 107384. [CrossRef]
31. Chen, J.; Wang, W.; Fang, C. Manufacturing, testing and simulation of novel SMA-based variable friction dampers with enhanced deformability. *J. Build. Eng.* **2022**, *45*, 103513. [CrossRef]
32. Qiu, C.; Liu, J.; Du, X. Cyclic behavior of SMA slip friction damper. *Eng. Struct.* **2022**, *250*, 113407. [CrossRef]
33. Zheng, W.Z.; Tan, P.; Li, J.; Wang, H.; Liu, Y.H.; Xian, Z.B. Superelastic pendulum isolator with multi-stage variable curvature for seismic resilience enhancement of cold-regional bridges. *Eng. Struct.* **2023**, *284*, 115960. [CrossRef]
34. Zheng, W.Z.; Tan, P.; Zhang, Z.H.; Wang, H.; Sun, Z. Damping enhanced novel re-centering seismic isolator incorporating superelastic SMA for response control of bridges under near-fault earthquakes. *Smart Mater. Struct.* **2022**, *31*, 065015. [CrossRef]
35. Hussain, E.; Kalaycioglu, S.; Milliner, C.W.D.; Cakir, Z. Preconditioning the 2023 Kahramanmaras (Turkiye) earthquake disaster. *Nat. Rev. Earth Environ.* **2023**, *4*, 287–289. [CrossRef]
36. Lu, X.; Cheng, Q.; Xu, Z.; Xiong, C. Regional seismic-damage prediction of buildings under mainshock-aftershock sequence. *Front. Eng. Manag.* **2021**, *8*, 122–134. [CrossRef]
37. Raghunandan, M.; Liel, A.B.; Luco, N. Aftershock collapse vulnerability assessment of reinforced concrete frame structures. *Earthq. Eng. Struct. Dyn.* **2015**, *44*, 419–439. [CrossRef]
38. Wen, W.; Ji, D.; Zhai, C.; Li, X.; Sun, P. Damage spectra of the mainshock-aftershock ground motions at soft soil sites. *Soil Dyn. Earthq. Eng.* **2018**, *115*, 815–825. [CrossRef]
39. Yu, X.-H.; Li, S.; Lu, D.-G.; Tao, J. Collapse Capacity of Inelastic Single-Degree-of-Freedom Systems Subjected to Mainshock-Aftershock Earthquake Sequences. *J. Earthq. Eng.* **2020**, *24*, 803–826. [CrossRef]
40. Zhou, Z.; Xu, H.; Gardoni, P.; Lu, D.; Yu, X. Probabilistic demand models and fragilities for reinforced concrete frame structures subject to mainshock-aftershock sequences. *Eng. Struct.* **2021**, *245*, 112904. [CrossRef]
41. Lagoudas, D.C.; Mayes, J.J.; Khan, M.M. Simplified shape memory alloy (SMA) material model for vibration isolation. In Proceedings of the Smart Structures and Materials 2001 Conference, Newport Beach, CA, USA, 5–8 March 2001.
42. Brinson, L.C. One-Dimensional Constitutive Behavior of Shape Memory Alloys: Thermomechanical Derivation with Non-Constant Material Functions and Redefined Martensite Internal Variable. *J. Intell. Mater. Syst. Struct.* **1993**, *4*, 229–242. [CrossRef]

43. Auricchio, F.; Taylor, R.L.; Lubliner, J. Shape-memory alloys: Macromodelling and numerical simulations of the superelastic behavior. *Comput. Methods Appl. Mech. Eng.* **1997**, *146*, 281–312. [CrossRef]
44. *GB 50011-2010*; Code for Seismic Design of Buildings. China Architecture and Building Press: Beijing, China, 2016.
45. Vamvatsikos, D.; Cornell, C.A. Direct estimation of seismic demand and capacity of multidegree-of-freedom systems through incremental dynamic analysis of single degree of freedom approximation. *J. Struct. Eng.* **2005**, *131*, 589–599. [CrossRef]

buildings

Article

Shaking-Table Test and Finite Element Simulation of a Novel Friction Energy-Dissipating Braced Frame

Lijuan Yan [1,2] and Chunwei Zhang [1,3,*]

[1] School of Civil Engineering, Qingdao University of Technology, Qingdao 266033, China; lijuan.yan@qdc.edu.cn
[2] School of Civil Engineering, Qingdao City University, Qingdao 266100, China
[3] School of Marine Science and Engineering, South China University of Technology, Guangzhou 511442, China
* Correspondence: zhangchunwei@scut.edu.cn

Abstract: To enhance the effect of seismic mitigation in medium-sized buildings, this study introduced a novel friction damper within a braced frame, forming a friction energy-dissipating braced frame (FDBF). The seismic reduction mechanism of the FDBF was examined, and its performance was evaluated through shaking-table tests and finite element simulations. The hysteresis performance of the novel damper was assessed through low-cycle repeated loading tests, which yielded predominantly rectangular and full hysteresis curves, exemplifying robust energy dissipation capacity. The shaking-table tests of the FDBF indicated significant modifications in the dynamic characteristics of the original frame structure, which notably reduced the natural vibration period and enhanced the damping. Additionally, the FDBF remarkably reduced both acceleration and displacement responses during seismic excitation. Optimizing the orientation of the energy dissipation brace significantly improved seismic reduction efficiency. A dynamic time history analysis, employing finite element software, was conducted on the FDBF equipped with a friction energy dissipation brace at each level. Comparative analysis with both the moment-resistant frame and ordinary braced frame revealed that the FDBF substantially lowered the peak acceleration at the apex of the structure, achieving a reduction rate of 40–50%. Under both design and rare earthquake conditions, the FDBF demonstrated superior seismic mitigation capabilities, especially under rare earthquakes. Future studies should investigate various structural types with energy dissipation braces at different levels to identify the most efficient layout for the novel friction energy dissipation brace, thereby guiding relevant engineering practices.

Keywords: novel friction damper; energy-dissipating brace; shaking-table test; finite element simulation

1. Introduction

Frame structures are prevalently applied in medium- and high-rise buildings, as they provide clear force transmission pathways, flexible design, and cost-effectiveness. However, their significant limitation lies in lateral stiffness, which impedes effective interval displacement control during seismic events owing to inherent stiffness. Frame structures primarily address seismic impacts through the plastic deformation of their key structural components, which may induce permanent damage and reduce the overall seismic resilience [1]. In addressing this issue, numerous researchers have integrated energy-dissipating elements to absorb seismic forces, thus protecting the primary structure. The design philosophy of “moderate lateral stiffness with predominant energy dissipation through non-structural elements” [2,3] has evolved and become increasingly popular. A prominent example of this approach is the friction energy dissipation braced-frame structure.

In 1982, Pall and Marsh introduced the Pall-type friction energy-dissipation brace, featuring a four-link variable mechanism at the center to prevent buckling under horizontal seismic forces. This design facilitates energy dissipation through friction by incorporating a slide groove at the midpoint of the diagonal [3–5]. In 1985, Chen devised a friction shear hinge energy-dissipation brace, employing friction shear dampers at diagonal brace intersections [6,7]. Extensive subsequent research by Liu [8,9] and Zhou [10,11] led to the development of circular (square box) friction energy dissipation braces. These designs replaced the Pall-type four-link mechanism with a circular ring or square box, placing the friction damper at the center of the diagonal for energy dissipation [8–12]. Xian et al. [13,14] proposed a composite friction energy-dissipating brace, combining sliding friction dampers at the diagonal's center with rotating friction dampers at the four link corners. In 2003, Ou and Wu et al. [15–17] introduced a T-shaped core plate friction damper, an advancement of the Pall-type damper, substituting diagonal cross-shaped bars with T-shaped core plates.

The friction dampers previously mentioned are typically installed in the central section of diagonal braces and come in various forms. These dampers employ sliding friction for energy dissipation. However, their complex construction can increase the axial force on columns due to horizontal seismic forces [16,18,19]. This paper introduces a novel friction energy-dissipating braced frame (FDBF), as illustrated in Figure 1. The FDBF comprises a frame structure and an innovative friction-based energy-dissipating brace, featuring a new type of friction damper and braces.

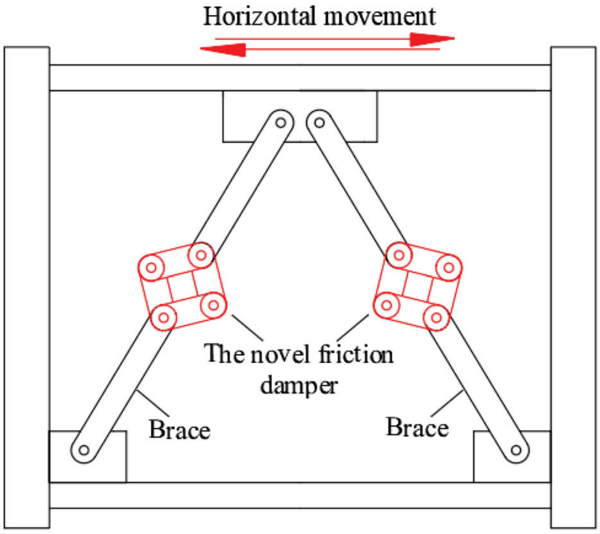

Figure 1. Novel friction energy-dissipating braced frame.

When subjected to horizontal seismic forces, the braces experience axial tension and compression, activating the damper. This leads to friction energy dissipation once the axial force reaches the slip force threshold of the new friction damper. The dissipation process involves the relative rotation of the connecting components and the friction pad, effectively reducing the displacement response of the structure during seismic events. The slip mechanism of the damper, designed to prevent compression buckling of the brace, allows the novel friction damper to adjust the absorbed length of the brace by deforming, keeping the slip force relatively constant despite increasing deformation. This design minimizes the additional axial force imparted to the column, thereby avoiding a gradual increase in column axial force. Additionally, this system offers several advantages, including straightforward construction, ease of installation, and flexibility, highlighting its practicality for seismic mitigation.

This article introduces and empirically investigates the working mechanism and hysteretic behavior of a new type of friction damper. Additionally, shaking-table tests and finite element simulations are conducted on the FDBF. The dynamic characteristics and seismic mitigation effects of the FDBF are thoroughly analyzed and assessed.

2. Study on Hysteretic Performance of the Novel Friction Damper

2.1. Theoretical Study

The innovative friction damper consists of six key components: a connecting plate, friction pad, steel disc, bolt washer, general bolts, and high-strength bolts, as illustrated in Figure 2. At the energy-dissipation end of the damper, each friction pad is securely attached using two connectors and fastened with high-tensile bolts under pre-pressure. To enable rotational movement between connectors at the loading end of the damper in response to external forces, ordinary discs, fixed with general bolts, are utilized in lieu of friction pads. Moreover, to modulate the energy-dissipating capacity of the friction pads, the steel disc at the loading end can be treated with a lubricant coating.

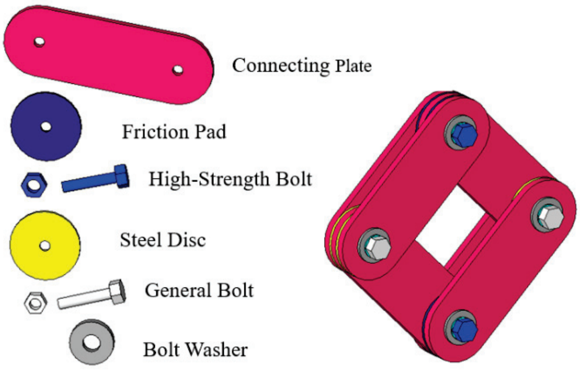

Figure 2. Novel friction damper construction.

Figure 3a,b illustrate the positive ($\Delta \geq 0$, Δ ranging from 0 to the maximum value and from the maximum value to 0) and negative ($\Delta < 0$, Δ ranging from 0 to the negative maximum value and from the negative maximum value to 0) displacements of the damper. These diagrams show that when a force, F, is applied to the loading end of the damper, relative rotation occurs between the connecting components and friction pads of the damper, causing frictional energy dissipation. As depicted in Figure 4, we can obtain: $x = L \sin \varphi$, then $dx = L \cos \varphi d\varphi$. Assuming that the displacement at the B (C) end of the damper is Δ ($dx = \Delta$) and the rotation angle of the damper is $\Delta\varphi$ ($d\varphi = \Delta\varphi$), we can obtain Equation (1) according to the principle of virtual work [20,21]:

$$2F\Delta = nM \cdot 2\Delta\varphi \tag{1}$$

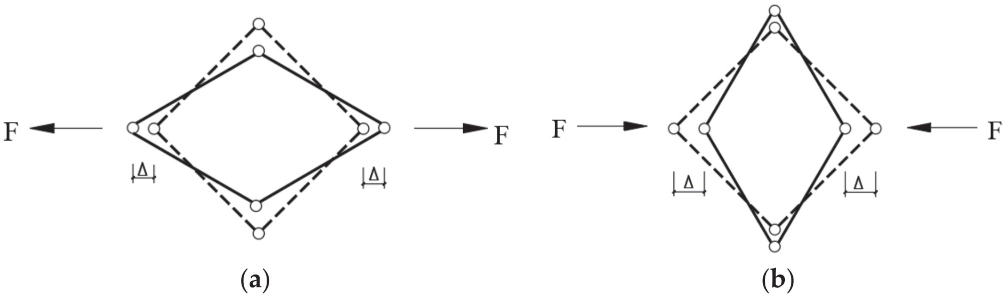

Figure 3. Mechanical model of damper.

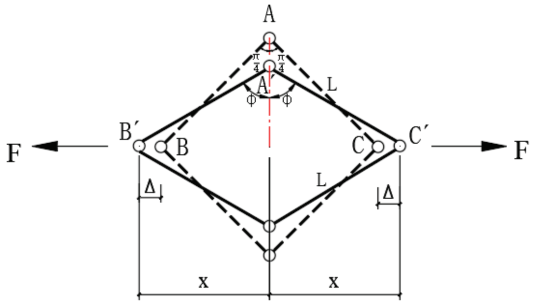

Figure 4. Stress diagram of isolator (positive).

Equation (2) can be obtained by substituting $\Delta = L\cos\varphi \cdot \Delta\varphi$ into Equation (1):

$$F = \frac{nM}{L\cos\varphi} \tag{2}$$

where M denotes the friction moment at the energy dissipation end of the damper, and n denotes the number of friction pads. The working principle of the friction pad is illustrated in Figure 5. When the rotational angle of the connecting plates is $\Delta\varphi$, the rotational angle of the friction pad is $\Delta\varphi$, and Equation (3) can be derived.

$$M = \iint \mu p_c r^2 d\varphi dr = \frac{2}{3}\mu P \frac{R_2^3 - R_1^3}{R_2^2 - R_1^2} \tag{3}$$

where P denotes the preload force of high-strength bolts, μ indicates the friction coefficient of the friction pads, n represents the number of friction pads, and R_1 and R_2 denote the inner and outer radii of the friction pads, respectively.

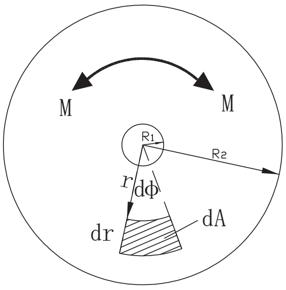

Figure 5. Working principle of friction pad.

Substituting Equation (3) into Equation (2), the theoretical formula for F–Δ is obtained for $\Delta \geq 0$ as follows:

$$F = \frac{2}{3L} n\mu P \frac{R_2^3 - R_1^3}{R_2^2 - R_1^2} / \sqrt{1 - \left(\frac{\sqrt{2}}{2} + \frac{\Delta}{L}\right)^2} \tag{4}$$

Similarly, Equation (5) can be obtained for $\Delta < 0$ as follows:

$$F = \frac{2}{3L} n\mu P \frac{R_2^3 - R_1^3}{R_2^2 - R_1^2} / \sqrt{1 - \left(\frac{\sqrt{2}}{2} - \frac{\Delta}{L}\right)^2} \tag{5}$$

From Equations (4) and (5), the theoretical F–Δ relationship of the novel friction damper is obtained, as displayed in Figure 6.

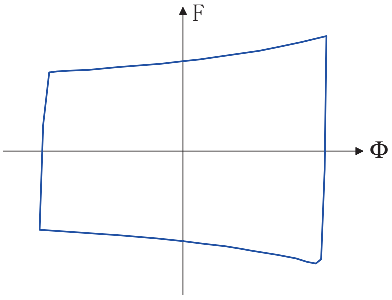

Figure 6. Theoretical hysteresis curve of *F*–Δ.

2.2. Experimental Study

2.2.1. Specimen Design

To more accurately replicate the actual performance of the new friction damper through a hysteresis curve, a reverse-cycle loading test was conducted at the structural laboratory of Qingdao University of Technology. Six specimen sets were designed, varying in preloading forces of high-strength bolts and friction pad materials, as detailed in Table 1. The specimens utilized grade 8.8 M12 high-strength bolts and Q345 steel for other damper components. According to the JGJ 82-2011 "Technical Specification for High-Strength Bolt Connections of Steel Structures" and the predetermined test conditions [22–25], the preloading force P of the high-strength bolts was set at 38 kN. The specimen identifiers were structured as follows: RFD-friction pad material-preloading force magnitude, with "N" representing non-asbestos composite material, "A" asbestos composite material, and "B" brass.

Table 1. Specimen parameters.

Specimens	Friction Pad Type	Pre-Tension (kN)	Torque (kN·m)
RFD-NA-0.5P	Non-asbestos composite	0.5P	0.78P
RFD-NA-P	Non-asbestos compound	P	1.56P
RFD-A-0.5P	Asbestos compound	0.5P	0.78P
RFD-A-P	Asbestos compound	P	1.56P
RFD-B-0.5P	Brass	0.5P	0.78P
RFD-B-P	Brass	P	1.56P

As depicted in Figure 7, the geometrical dimensions of all six sets of specimens were identical.

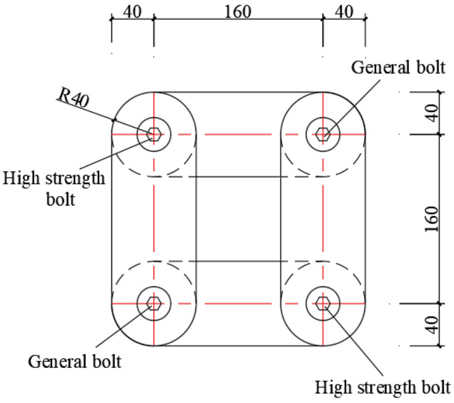

(**a**)

Figure 7. *Cont.*

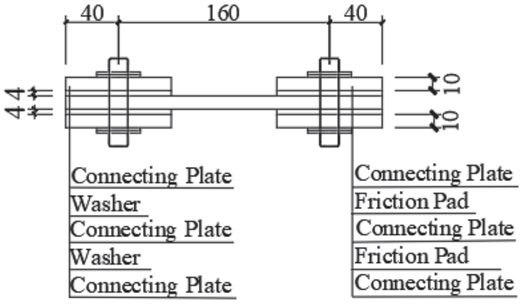

(**b**)

Figure 7. Geometric dimensions of specimens. (**a**) Elevation. (**b**) Side view.

2.2.2. Experimental Equipment and Loading Protocol

A 100-kN hydraulic servo loading MTS actuator, specifically engineered for horizontal linear loading, was employed in the experiment. One extremity of the square rotary friction damper was connected to the actuator, whereas the opposite end was linked to a limiting device. The MTS force and displacement sensors were used for real-time data collection. The loading apparatus is displayed in Figure 8a, and the experimental loading methodology is illustrated in Figure 8b. The displacement-controlled loading was adopted, and Figure 9 presents the test loading protocol.

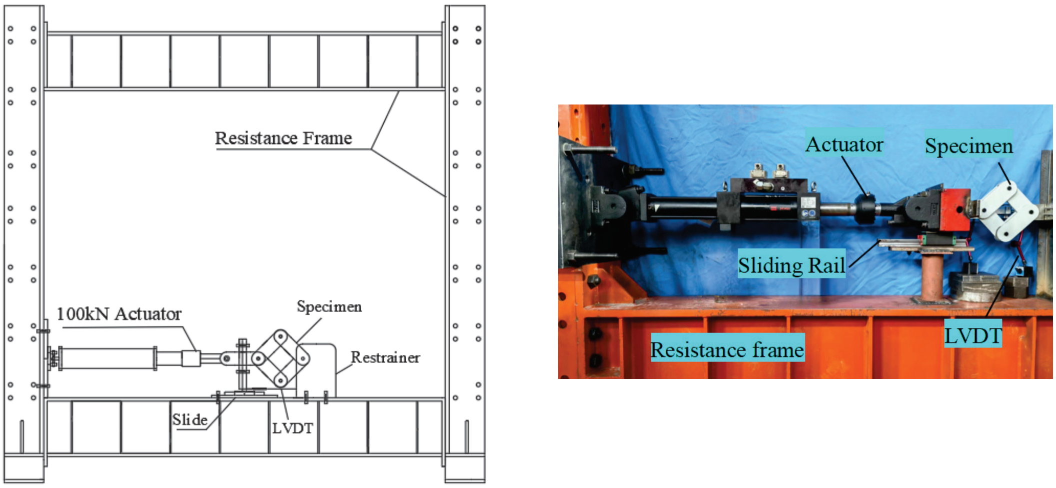

(**a**) (**b**)

Figure 8. Loading diagram and device.(**a**) Loading diagram. (**b**) Loading device.

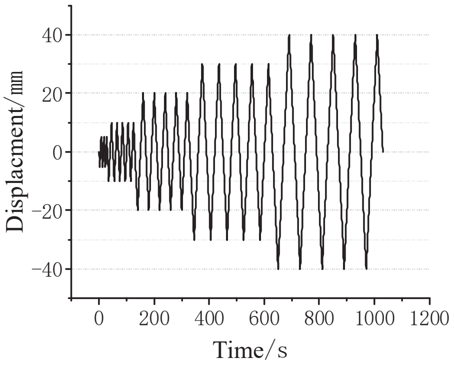

Figure 9. Loading protocol.

2.2.3. Experimental Results and Analysis

The primary parameters measured in this experiment included the displacement of the novel friction damper, the differential in displacement between the damper and the limit fixing device, and the variation in the sliding force of the damper. The displacement was quantified using displacement sensors, whereas the sliding force of the friction damper was measured using the force sensor of the actuator. These measurements facilitated the construction of the hysteresis curve of the friction damper, as depicted in Figure 10. This curve was predominantly rectangular and full. Even after 25 reciprocating displacement loading cycles, there was no significant degradation in stiffness, highlighting the robust energy-dissipation capacity of the damper. Moreover, the hysteresis curve of the damper was closely aligned with the theoretical analysis presented in Figure 6, affirming the general accuracy of the theoretical formula.

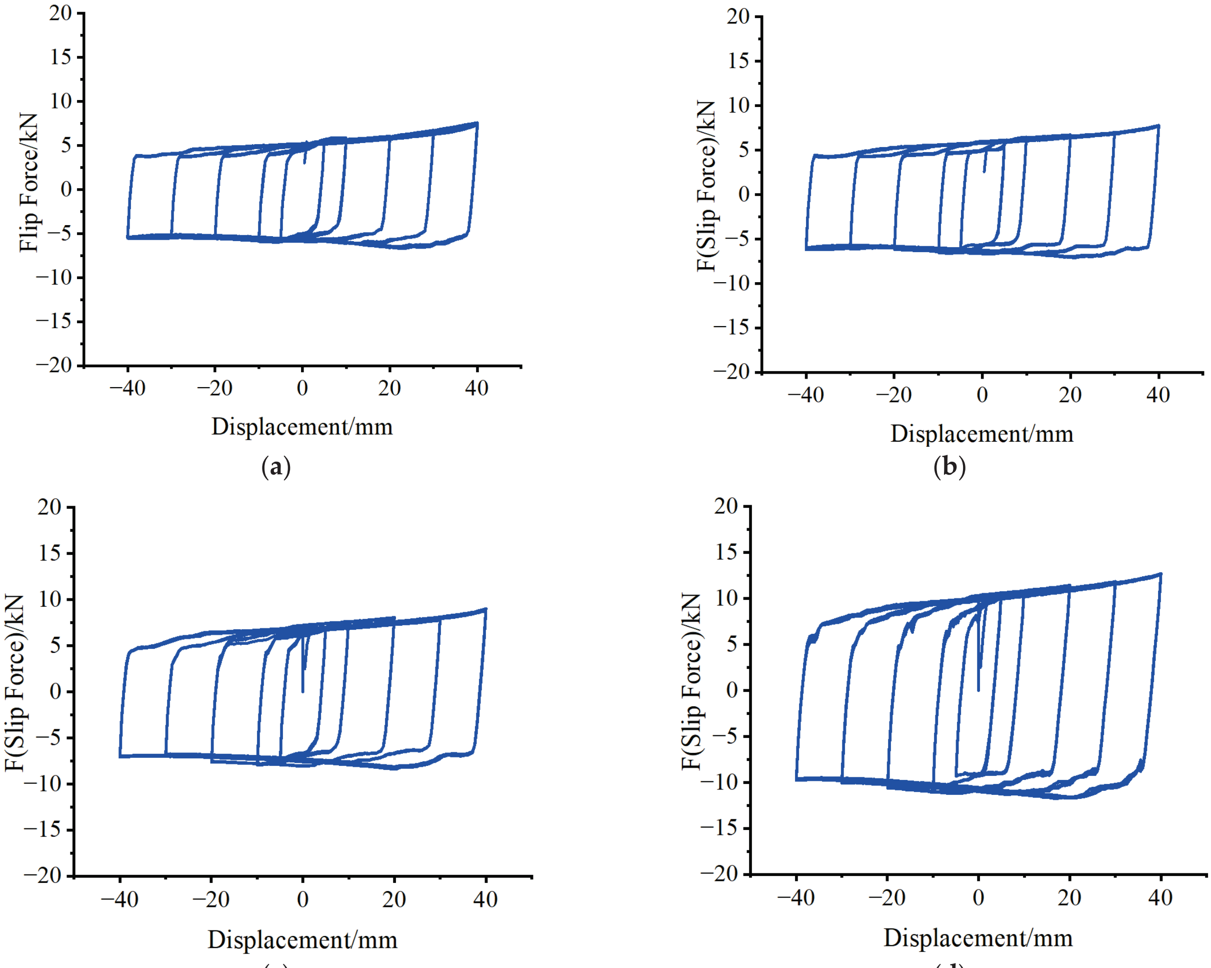

(**a**) (**b**)

(**c**) (**d**)

Figure 10. *Cont.*

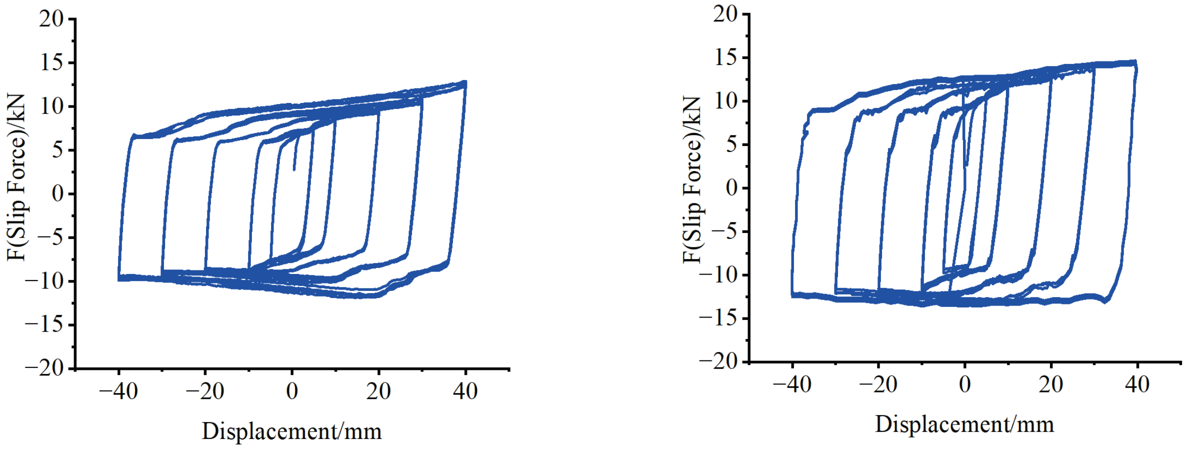

(**e**) (**f**)

Figure 10. Hysteresis curves. (**a**) RFD-NA-0.5P. (**b**) RFD-NA-P. (**c**) RFD-A-0.5P. (**d**) RFD-A-P. (**e**) RFD-B-0.5P. (**f**) RFD-B-P.

The sliding force *F* of the friction damper increases with a rise in the preloading force of the bolts, assuming constant friction-pad material. With identical preloading forces, the sliding force is minimized with non-asbestos composite material friction pads and maximized with brass. Therefore, the sliding force of the friction damper is influenced by both the preloading force of the bolts and the friction coefficient of the friction pad. Thus, different energy-dissipation capacities can be achieved by varying the preloading force of the bolts or employing different friction-pad materials for friction energy dissipation.

3. Study on Novel Friction Energy-Dissipating Braced Frame

3.1. Theoretical Study

Incorporating the friction damper into braces leads to the creation of a friction-based energy-dissipation structural system. Under horizontal seismic action, a mechanical analysis of the single-layer seismic damping structure can be performed, as depicted in Figure 1. This analysis produces a simplified diagram, displayed in Figure 11a, which divides the system into a single-layer frame structure and a dampening support section incorporating the damper. Figure 11b displays the energy-dissipation support, integrating the friction damper to augment energy dissipation and enhance the seismic performance of the structure.

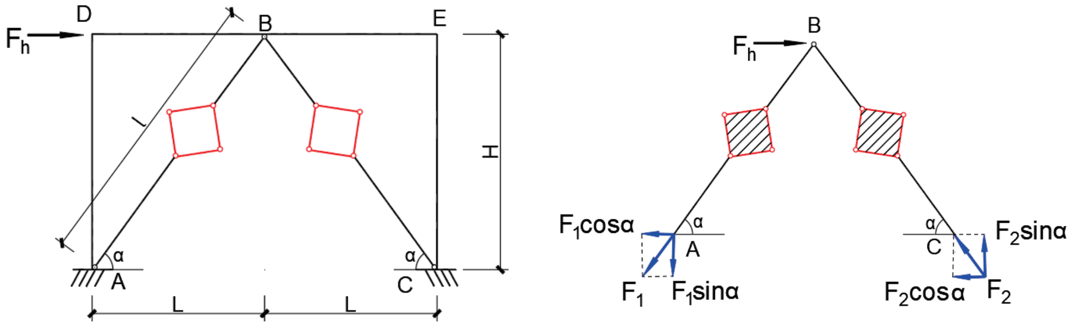

(**a**) (**b**)

Figure 11. Calculation diagrams and the brace. (**a**) Friction energy dissipating-braced frame. (**b**) Friction energy dissipating-brace.

When subjected to mild horizontal seismic forces, as indicated in Figure 11a, the AB rod remains in tension without deformation, whereas the AC rod experiences compression without collapsing. The energy-dissipation end of the friction damper remains static, and the energy-dissipation support is in an elastic stage. At this stage, the friction damper functions as a rigid body, rendering the energy-dissipation support similar to a conventional support. According to the principles of structural mechanics, the primary function of the support is to withstand the horizontal force [26–28].

$$F_1 = F_2 \tag{6}$$

$$F_h = F_1 cos\alpha + F_2 cos\alpha \tag{7}$$

When Equation (6) is substituted into Equation (7), we obtain $F_1 = \frac{1}{2cos\alpha}F_h$. Following the same reasoning, we can obtain $F_2 = \frac{1}{2cos\alpha}F_h$.

As the horizontal seismic force intensifies to a level where the AC compression support approaches buckling, the novel friction damper starts to rotate and engage, as illustrated in Figure 12. At this moment, the sliding force of the damper attains its maximum friction force. The internal force within the brace, provided by the support, can be computed as follows:

$$F_{sl} = \frac{1}{2cos\alpha}F_h \tag{8}$$

$$F_{sl} = \varphi A_b f_y \tag{9}$$

where φ denotes the stability coefficient of the compression support, A_b represents the cross-sectional area of the compression support, and f_y indicates the design value of the compressive strength of the steel material used for the support.

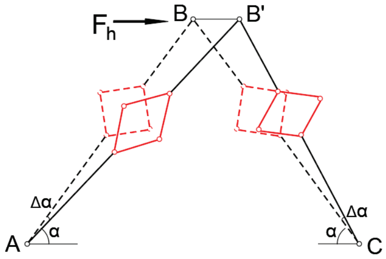

Figure 12. Energy-dissipating brace operation.

3.2. Shaking-Table Test

The experimental prototype is based on the initial-stage ATS-controlled benchmark model, incorporating studies [29–33]. It is a three-story, single-span steel-frame structure. The scaled-down model employed in this experiment has dimensions of 366 mm by 183 mm in plan, with a first-story height of 305 mm and subsequent stories each measuring 448 mm. The friction damper energy-dissipation brace was installed on the first story. The columns comprised 13 circular cylinders, and the base plate was firmly bolted to the shaking table. To adhere to the similarity criteria of the structural model, the friction damper was re-engineered, with dimensions presented in Figure 13. The frame model specimens were constructed according to the dimensions of each component, and the FDBF model specimens are exhibited in Figure 14.

3.2.1. Test Equipment and Loading Scheme

For the experiment, the Quanser Shake Table III, a bi-axial input vibration table measuring 71.1 cm × 71.1 cm, was utilized. Capable of handling a 100 kg load, it can generate a maximum seismic excitation level of 1 g. Both the X and Y directions have a stroke capability of 10.8 cm. Acceleration data were acquired using four Lord G-Link-200 sensors placed on the surface of the shaking table and at the center of each floor slab. Structural displacement signals were measured using Keyence CMOS IL series laser displacement sensors. The seismic performance was evaluated by comparing the lateral displacement and acceleration of both the FDBF and moment-resistant frame (MRF). The design response spectrum was formulated based on seismic intensity, site classification, and seismic design category, with the seismic intensity set at 8 degrees, site classification at Class II, and seismic design category at Group 2. The resulting design response spectrum is depicted in Figure 15.

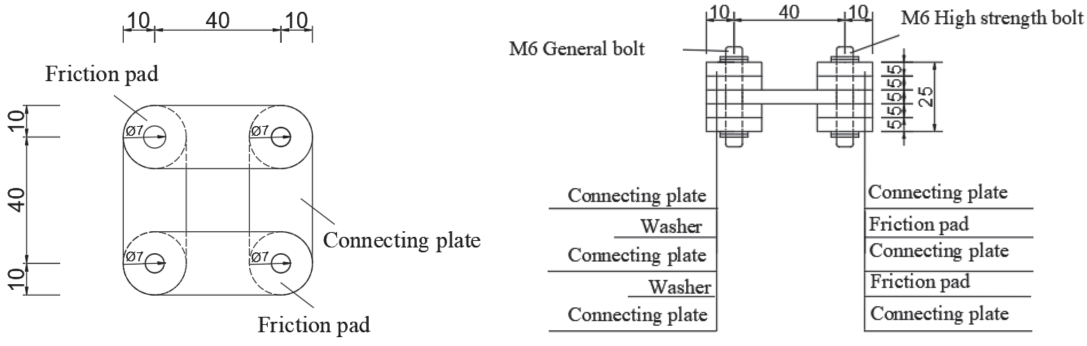

(**a**) (**b**)

Figure 13. Design details of the table-test friction damper model. (**a**) Elevation. (**b**) Side view.

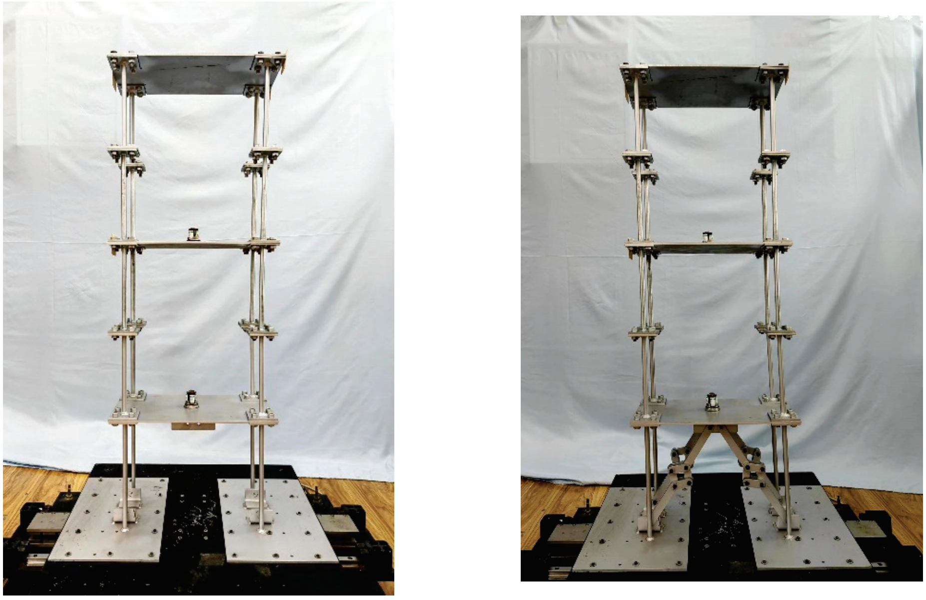

(**a**) (**b**)

Figure 14. Model specimens. (**a**) Frame model specimen. (**b**) Friction damper braced frame specimen.

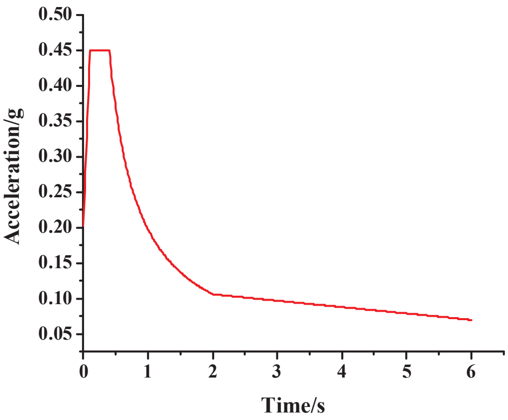

Figure 15. Design earthquake response spectrum.

Four seismic waves—the 1940 El Centro wave, 1979 El Centro wave, 1981 Salton Sea wave, and 1952 Taft wave—were selected for their spectral congruence with the structural period point. The peak values of these waves were adjusted to 0.2 g. A response spectrum analysis for each wave was then conducted and compared with the response spectrum from Code for Seismic Design of Buildings GB50011−2010(2016 Edition), as illustrated in Figure 16. The response spectra of these waves closely corresponded with the periods of the structure. The average response values of these waves were used to assess the seismic performance of the structure [34,35]. Owing to structural asymmetry, earthquake waves were applied independently in the X and Y directions. The structural model loading device is depicted in Figure 17.

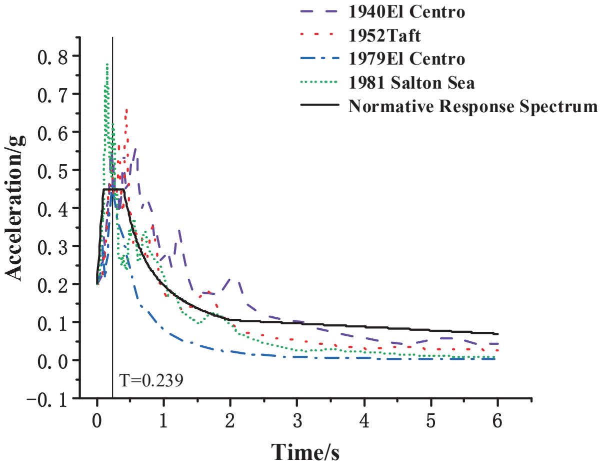

Figure 16. Earthquake wave response spectrum and design response spectrum.

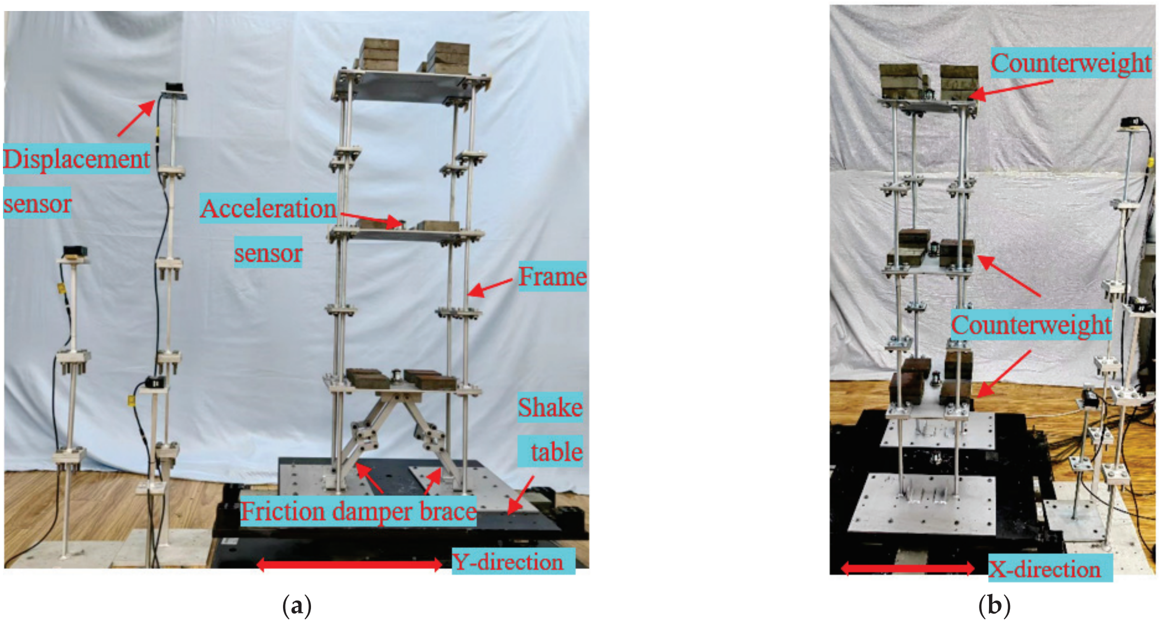

(**a**) (**b**)

Figure 17. Loading device for the structural model specimens (**a**) Loading device in Y-direction. (**b**) Loading device in X-direction.

3.2.2. Test Results and Analysis

(1) Natural frequency and damping ratio

Exposing both the MRF and FDBF to white noise excitation, ranging from 0 Hz to 8 Hz, with a 2-mm amplitude and conducting Fourier transformation on the resultant acceleration data facilitated the determination of the natural frequencies of both structures through frequency-response analysis. Subsequently, the damping ratios were determined using the half-power method based on the frequency-response function, as indicated in Table 2. The results revealed that the FDBF, equipped with friction energy-dissipating braces, exhibited higher damping ratios than the MRF, thereby improving its seismic resistance capabilities.

Table 2. Natural frequency and damping ratio.

Structure Model	Frame	FDBF
Natural frequency	3.1211 Hz	3.681 Hz
damping ratio	4.15%	4.77%

(2) Acceleration and displacement responses

The peak acceleration and displacement values for the top floor of both structures under seismic wave excitation are listed in Table 3. In the Y-direction, the FDBF exhibited reductions in peak acceleration values of 44.36%, 40.40%, 50.15%, and 48.75% compared to the MRF under the seismic waves of 1940 El Centro, 1979 El Centro, 1981 Salton Sea, and 1952 Taft, respectively. In the X-direction, these reductions were 29.3%, 27.5%, 9.09%, and 37.71%, respectively.

Table 3. Maximum top-floor acceleration and displacement.

Working Condition			1940 El Centro	1979 El Centro	1981 Salton Sea	1952 Taft
Frame	X-direction	Acceleration/g	0.215	0.291	0.143	0.236
		Displacement/mm	29.32	35.12	26.61	27.11
	Y-direction	Acceleration/g	0.390	0.656	0.401	0.359
		Displacement/mm	30.86	34.12	27.47	27.12
FDBF	X-direction	Acceleration/g	0.152	0.211	0.130	0.147
		Displacement/mm	29.04	34.07	26.01	26.03
	Y-direction	Acceleration/g	0.217	0.391	0.168	0.184
		Displacement/mm	28.02	31	25.68	25.21
Displacement-reduction ratio	X-direction	/	0.96%	3.08%	2.31%	4.15%
	Y-direction	/	10.14%	9.14%	6.97%	7.58%

Figures 18 and 19 present the time history responses of the top-floor accelerations in the Y- and X-directions for both structures influenced by the four seismic waves. The FDBF displayed a significantly lower acceleration response in the Y-direction compared to the MRF, whereas its response in the X-direction was modestly reduced. This suggests that the friction energy-dissipating brace is highly effective in its implemented direction, with a less pronounced damping effect in the unbraced direction. The displacement-reduction ratio is defined as the ratio of the maximum top-floor displacement of the FDBF to that of the MRF. According to Table 3, the displacement-reduction ratios in the Y-direction are 10.14%, 9.14%, 6.97%, and 7.58%, and in the X-direction, they are 0.96%, 3.08%, 2.31%, and 4.15%, respectively. These findings indicate that the novel friction energy-dissipating brace significantly reduces the displacement response of the MRF, with a maximum reduction ratio reaching up to 10.14%. Figures 20–22 reveal that the displacements at each level of the FDBF are consistently lower than those of the MRF, with the ratio of inter-story displacement at each FDBF level being less than one.

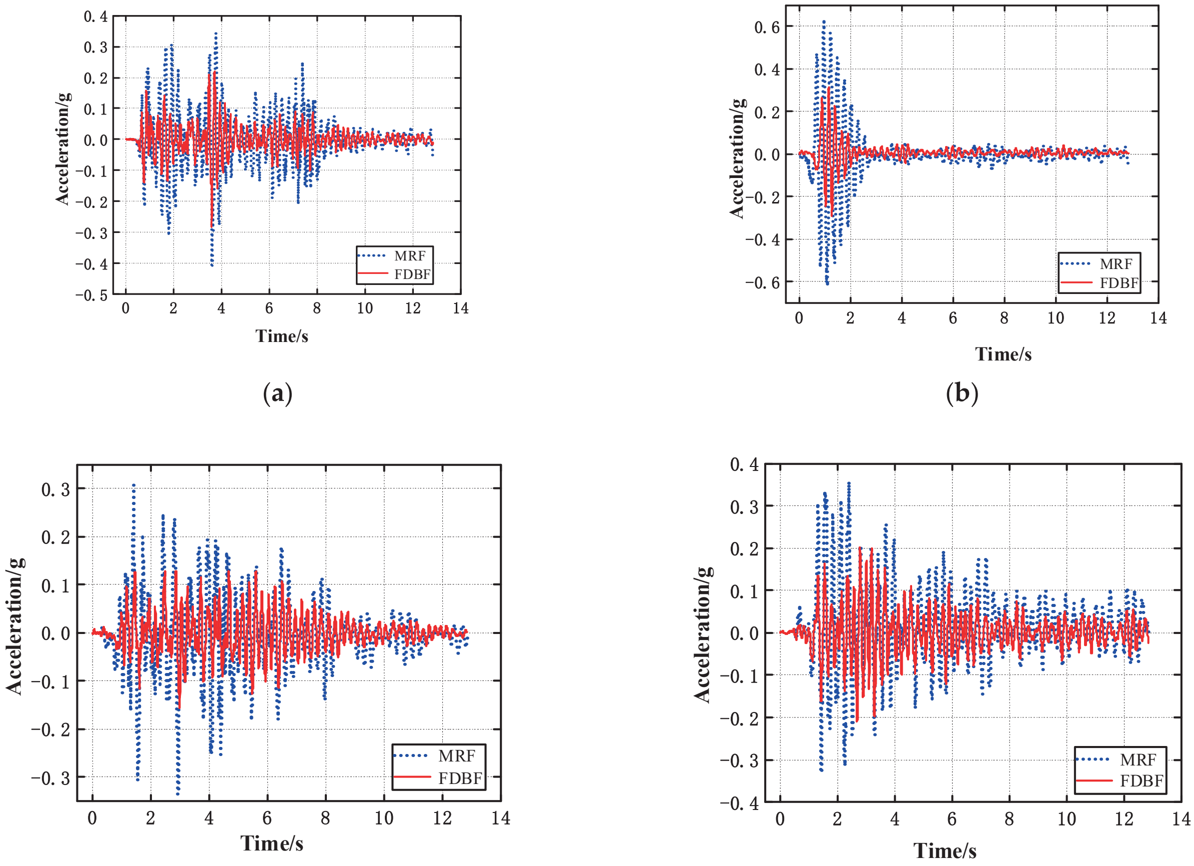

(**a**) (**b**)

(**c**) (**d**)

Figure 18. Acceleration–time histories of Y-direction seismic waves. (**a**) 1940 El Centro. (**b**) 1979 El Centro. (**c**) 1981 Salton Sea. (**d**) 1952 Taft.

(3) Acceleration amplification factor β

The acceleration amplification factor denotes the ratio of the maximum acceleration at the top of the structure to the maximum acceleration on the shaking table, illustrating the amplification effect of the top-floor acceleration during an earthquake. The data were collated, and the acceleration amplification factor in the Y-direction was calculated for both structures under the impact of four seismic waves; these findings are presented in Table 4. For comparative purposes, the acceleration amplification factor is plotted as a bar graph in Figure 23.

Table 4. Acceleration amplification factor β.

Earthquake	MRF			FDBF		
	Table Acceleration/g	Top-Floor Acceleration/g	β	Table Acceleration/g	Top-Floor Acceleration/g	β
1940 El Centro	0.176	0.390	2.22	0.172	0.217	1.26
1979 El Centro	0.255	0.656	2.57	0.219	0.391	1.78
1981 Salton Sea	0.192	0.401	2.09	0.213	0.398	1.73
1952 Taft	0.183	0.359	1.96	0.182	0.184	1.01

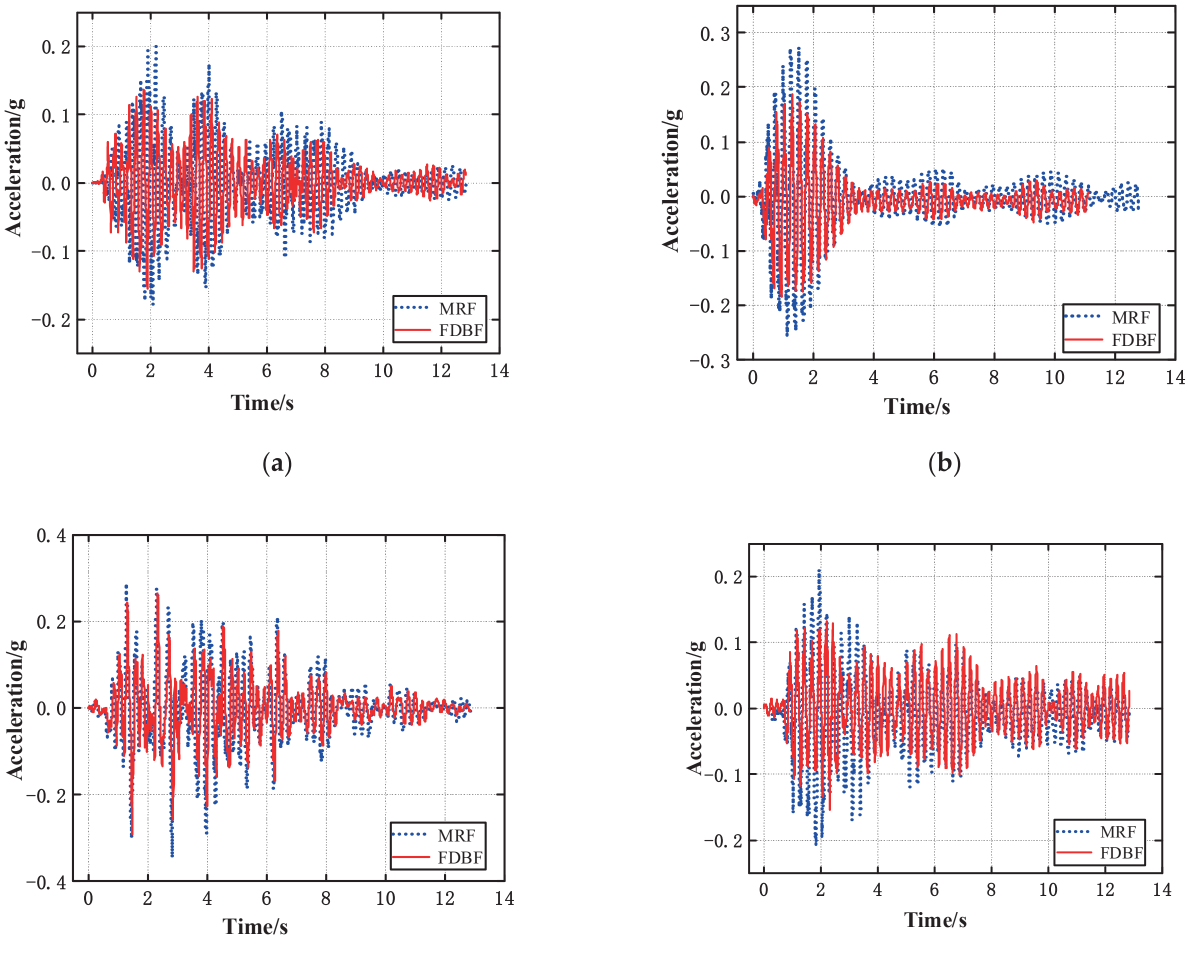

(**a**)

(**b**)

(**c**)

(**d**)

Figure 19. Acceleration–time histories of X-direction seismic wave. (**a**) 1940 El Centro. (**b**) 1979 El Centro. (**c**) 1981 Salton Sea. (**d**) 1952 Taft.

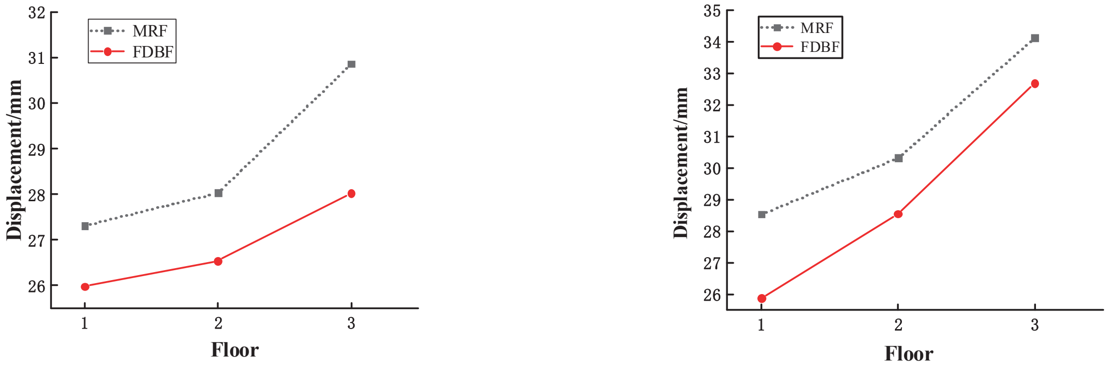

(**a**)

(**b**)

Figure 20. *Cont.*

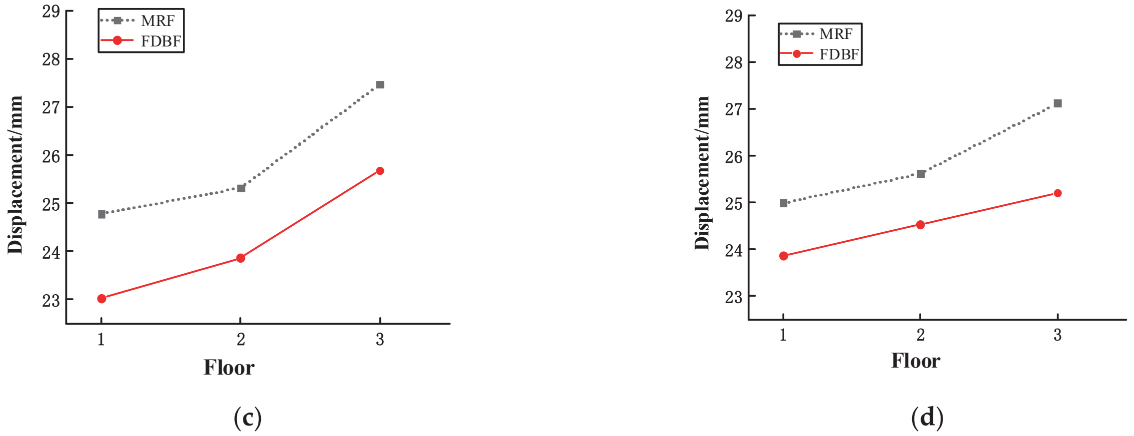

Figure 20. Maximum floor displacement of Y-direction seismic wave. (**a**) 1940 El Centro. (**b**) 1979 El Centro. (**c**) 1981 Salton Sea. (**d**) 1952 Taft.

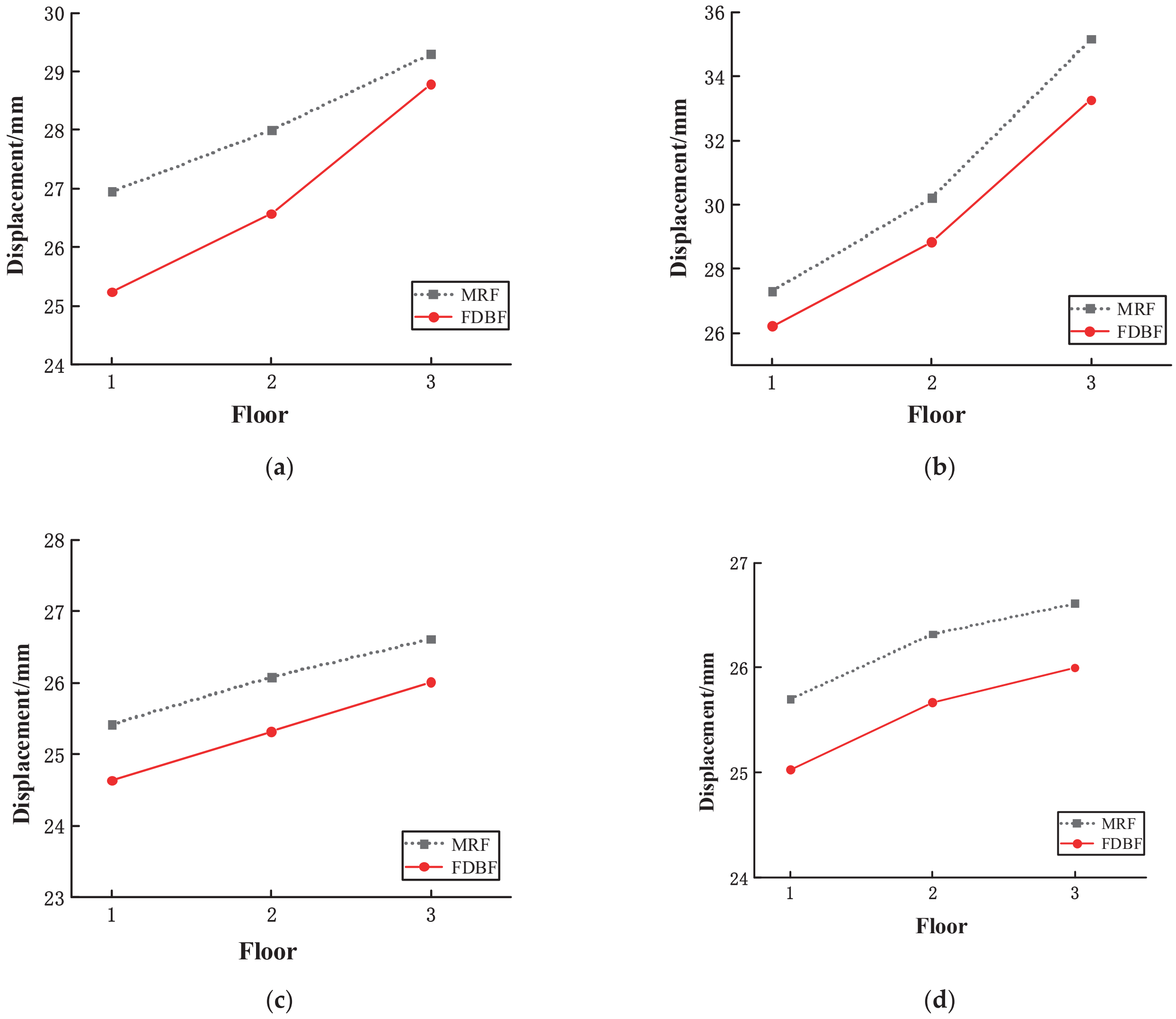

Figure 21. Maximum floor displacement of X-direction seismic wave. (**a**) 1940 El Centro. (**b**) 1979 El Centro. (**c**) 1981 Salton Sea. (**d**) 1952 Taft.

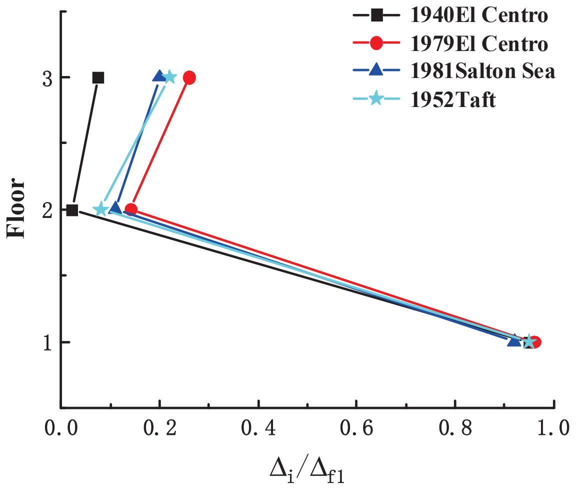

Figure 22. Ratio of inter-story displacement between each floor of FDBF and MRF on the first floor.

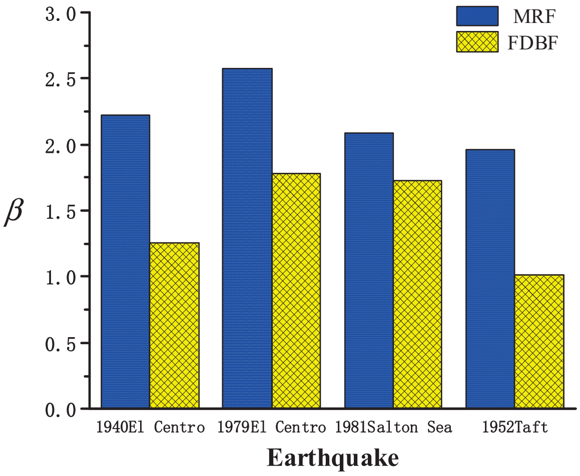

Figure 23. Acceleration amplification factor β.

Table 4 and Figure 23 reveal that the acceleration amplification factor of the FDBF is consistently lower than that of the MRF and remains below two. This observation highlights the crucial role of the friction energy-dissipating brace in mitigating seismic effects within the framed structure.

4. Finite Element Simulation

To comprehensively assess the seismic-reduction impact of the FDBF, the shaking-table test results were compared with finite element simulations conducted on the MRF, BMRF, and FDBF using ABAQUS 6.14 software. The acceleration–time and displacement–time responses of these three structures were contrasted under earthquake excitation, demonstrating the seismic mitigation efficiency of the FDBF.

4.1. Finite Element Model Verification

Finite element models of both the experimental MRF and FDBF were developed in ABAQUS. A modal analysis was performed to determine the natural frequencies of the two structures. Table 5 presents a comparison between the simulated outcomes and experimental data, showing relative closeness with differences ranging from 2% to 5%. This suggests that the finite element model effectively replicates the experimental specimen.

Table 5. Comparison of natural frequencies (top three modes)/Hz.

Mode	**MRF**			**FDBF**		
	1	**2**	**3**	**1**	**2**	**3**
Test	3.121	3.334	5.15	3.681	3.892	6.061
Finite	3.046	3.257	5.061	3.503	3.798	5.996

After the modal analysis, damping parameters were incorporated into the models. The 1940 El Centro earthquake wave was then applied at the base of the structures, and the top-floor acceleration response in the Y-direction was compared with experimental results, as illustrated in Figure 24. The comparative analysis indicated commendable consistency in acceleration responses between the FDBF and MRF, demonstrating the proficiency of the finite element model in simulating the experimental model.

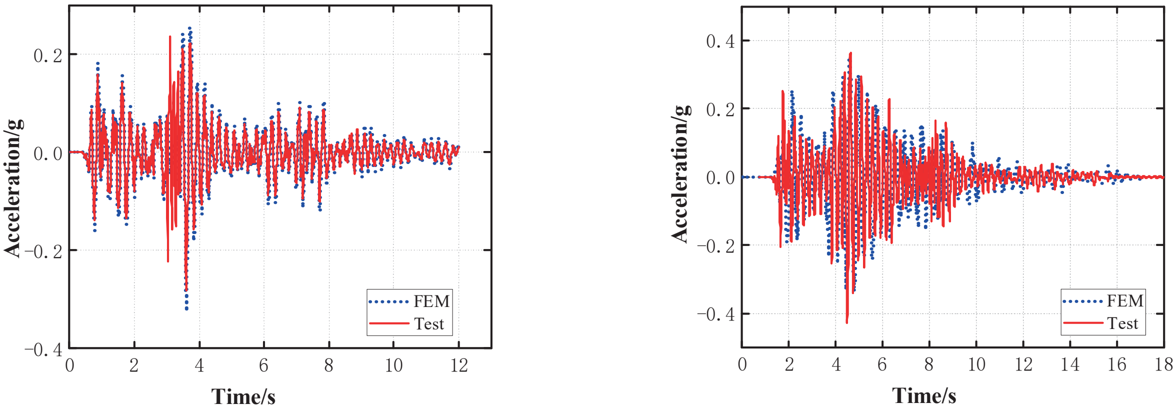

(**a**) (**b**)

Figure 24. Comparison of acceleration–time histories (**a**) FDBF. (**b**) MRF.

4.2. Finite Element Model

The three model sets included the MRF, BMRF, and FDBF with energy-dissipating braces on each floor, as illustrated in Figure 25. The original structure was a five-story, one-span, center-supported steel-frame structure. The finite element models represented a scaled-down version of this prototype, focusing on a single five-story span. The column spacing in the X- and Y-directions was 450 mm and 540 mm, respectively, with a story height of 225 mm and a floor thickness of 2 mm. Columns and supports were modeled using beam elements, while floor slabs employed shell elements.

In the numerical model, the damper is using a full scale of the damping mechanism. The length and width of the damper connecting plates in the numerical model are the same as those in the experimental model. The thickness of the connecting plates and friction plates is 2 mm, different from the experimental model. This is due to the fact that the thickness of the slabs is different in the two models. Considering the connection installation between the braces and the floor slabs, different thicknesses are used. The damping devices were modeled with solid elements. The bases of the columns were fixed, eliminating displacements and rotations. The interaction between the friction pads and connectors was defined as surface-to-surface contact, employing penalized tangential contact and rigid normal contact. General contact was applied for interactions between other components. Except for the friction pads and high-strength bolts, Q345 steel was used for the model components.

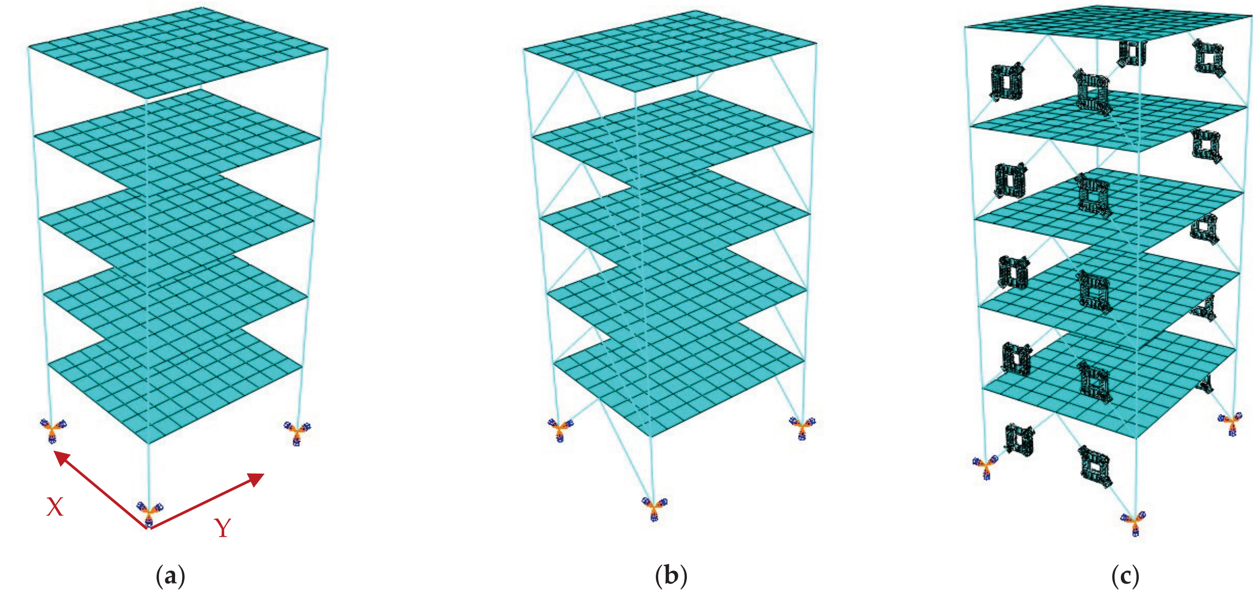

Figure 25. Different finite element models for various structures. (**a**) MRF. (**b**) BMRF. (**c**) FDBF.

4.3. Modal Analysis

Modal analysis was conducted on three structures: MRF, BMRF (ordinary braced frames), and FDBF. This analysis aimed to identify the mode shapes and frequencies for the top three modes. The specific frequencies for each mode are presented in Table 6. An examination of these results indicates that both the BMRF and FDBF exhibit higher frequencies compared to the MRF. Notably, the FDBF demonstrates lower frequencies than the BMRF, suggesting that the integration of the energy-dissipating brace alters the structural stiffness, which is beneficial for seismic energy dissipation relative to ordinary supports.

Table 6. Natural frequencies of MRF, BMRF, and FDBF (top three modes)/Hz.

Mode	**1**	**2**	**3**
MRF	1.227	1.243	1.706
BMRF	1.487	5.704	13.382
FDBF	1.476	5.611	13.256

4.4. Acceleration Response

Seismic waves, namely, the 1940 El Centro, 1979 El Centro, 1981 Salton Sea, and 1952 Taft earthquakes, were applied to the structural models. The peak accelerations for these waves were set to 0.21 g, 0.21 g, 0.19 g, and 0.18 g, respectively. The top-level acceleration–time history curves for these three structures are illustrated in Figure 26. The BMRF structure exhibited the highest acceleration response, followed by the MRF, whereas the base-isolated FDBF structure displayed the smallest acceleration response. Therefore, the novel friction energy-dissipating brace can effectively dissipate seismic energy and possesses significant damping properties.

To assess the amplification effect of top-level acceleration under identical seismic waves, the acceleration amplification factors of the models were calculated. The results are detailed in Table 7. The MRF displayed the highest amplification factor, followed by the BMRF, both exceeding 2.0, signifying a considerable amplification effect on the top-level acceleration in these structures. The base-isolated FDBF structure exhibited a maximum amplification factor of 1.17 and a minimum of 1.05, demonstrating its efficacy in reducing the top-level acceleration response and underscoring its damping capabilities.

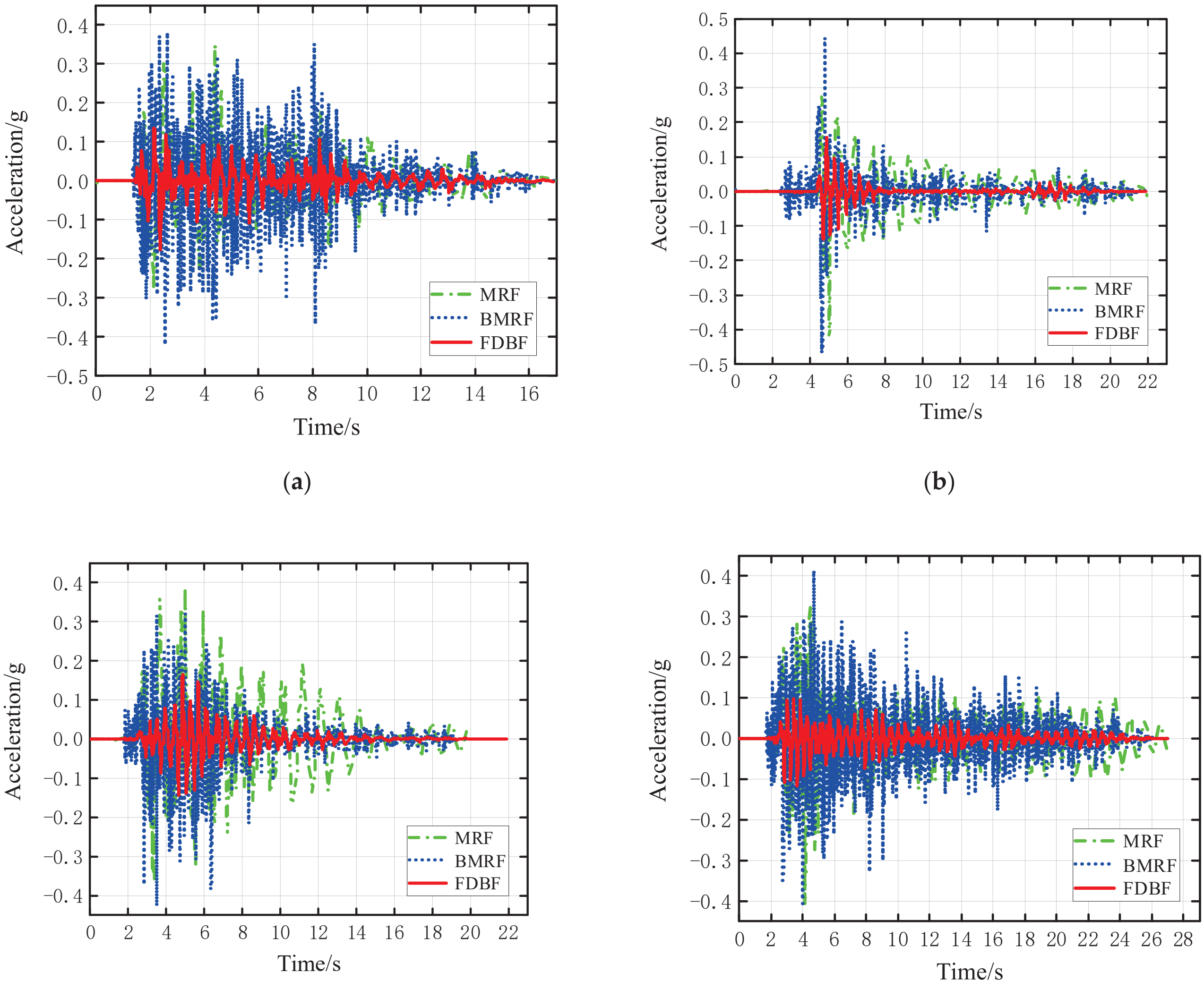

(**a**)

(**b**)

(**c**)

(**d**)

Figure 26. Comparison of acceleration–time histories of the three structures under seismic excitation. (**a**) 1940 El Centro. (**b**) 1979 El Centro. (**c**) 1981 Salton Sea. (**d**) 1952 Taft.

Table 7. Acceleration amplification factor β (acceleration unit (g)).

Earthquake	**MRF**			**BMRF**			**FDBF**		
	Ground Acceleration	**Top-Level Acceleration**	β	**Ground Acceleration**	**Top-Level Acceleration**	β	**Ground Acceleration**	**Top-Level Acceleration**	β
1940 El Centro	0.181	0.398	2.20	0.173	0.348	2.01	0.149	0.175	1.17
1979 El Centro	0.213	0.467	2.19	0.201	0.423	2.11	0.150	0.157	1.05
1981 Salton Sea	0.194	0.427	2.20	0.192	0.389	2.02	0.164	0.187	1.14
1952 Taft	0.180	0.414	2.30	0.179	0.403	2.25	0.166	0.176	1.06

Comparing the acceleration responses of the three structural models, the amplification factors from Table 6 are represented as a bar chart in Figure 27. As observed, the top-level acceleration-response peak of the FDBF structure, equipped with friction energy-dissipating braces, decreased by 40–50% compared to the MRF. The BMRF structure, with regular supports, achieved a decrease of approximately 15–25% compared to the MRF. Furthermore, the FDBF structure exhibited a reduction of approximately 35–50% compared to the BMRF structure. These findings demonstrate that the FDBF has a substantial vibration-damping effect.

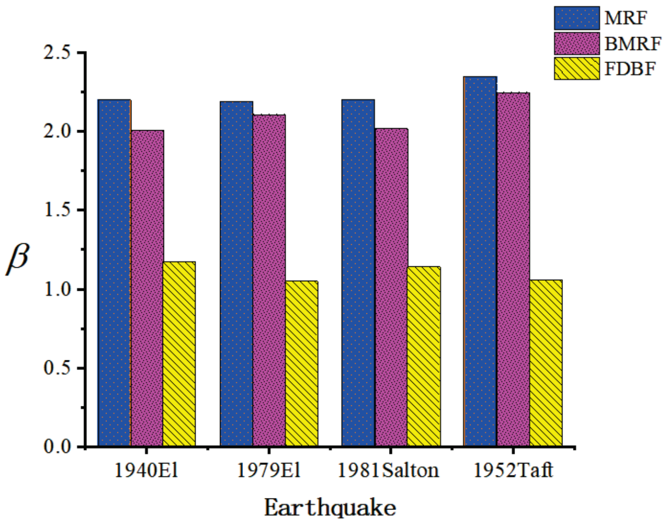

Figure 27. Acceleration amplification factors for the three structures.

4.5. Displacement-Reduction Rate α

The displacement-reduction rate is defined as the ratio between the maximum displacement of a seismically isolated structure and the maximum displacement of the same structure without isolation, typically a pure frame structure. This rate is crucial in assessing the seismic performance of the isolated structure, where a higher displacement-reduction ratio signifies improved damping efficacy and a smaller displacement response. To evaluate the seismic performance of both the BMRF and FDBF structures under various seismic excitations, a time history analysis was conducted using seismic waves with peak accelerations adjusted in accordance with the "Code for Seismic Design of Buildings GB50011–2010 (2016 Edition)" [36] for different design ground motion intensities. The peak accelerations were set to 0.14 g, 0.40 g, and 0.63 g, simulating SLE (Service-Level Earthquake) intensity 9, OBE (Operating Basis Earthquake) intensity 9, and MCE (Maximum Credible Earthquake) intensity 9, respectively. The structures were analyzed under these modified seismic waves.

Table 8 outlines the maximum displacement peaks and displacement-reduction ratios α for the FDBF, BMRF, and MRF under the influence of four different seismic waves with a peak acceleration of 0.14 g. Under SLE intensity 9, the displacement-reduction ratio of the FDBF structure is similar to that of the BMRF. This is primarily due to the fact that, during minor seismic events, the ordinary braces of the BMRF remain in an elastic state, and the friction dampers in the FDBF are not yet operational, rendering the energy-dissipating brace equivalent to an ordinary brace.

Table 8. Peak displacement (mm) of MRF, FDBF and BMRF (SLE intensity 9).

Working Condition	1940 El Centro	1979 El Centro	1981 Salton Sea	1952 Taft
MRF	7.08	10.75	8.06	7.33
FDBF	1.31	1.76	1.73	1.88
α/%	81.5	83.6	78.5	74.3
BMRF	1.23	1.66	1.72	1.99
α/%	82.6	84.6	78.7	72.8

Table 9 outlines the maximum displacement peaks and displacement-reduction ratios α for the FDBF, BMRF, and MRF under the influence of seismic waves with a peak acceleration of 0.40 g. Here, the displacement-reduction ratios of the BMRF are markedly lower than those of the FDBF under OBE intensity 9. This is due to the fact that, under OBE intensity 9, the new type of friction damper becomes active, and the energy-dissipating braces reduce structural displacement by absorbing seismic energy. Moreover, the ordinary brace enters a compression-yielding state, leading to a significant decrease in the lateral stiffness of the structure and an increase in displacement.

Table 9. Peak displacement (mm) of MRF and FDBF (OBE intensity 9).

Working Condition	1940 El Centro	1979 El Centro	1981 Salton Sea	1952 Taft
MRF	12.74	19.35	14.51	13.19
FDBF	4.91	8.48	8.02	5.29
$\alpha/\%$	61.4	56.2	44.7	59.9
BMRF	8.37	12.72	12.03	7.94
$\alpha/\%$	34.2	34.3	17.1	39.8

Table 10 outlines the peak displacements and displacement-reduction ratios for the FDBF, BMRF, and MRF under rare earthquake conditions. The data indicate that the displacement-reduction ratios for the FDBF structure exceed 60% across various seismic wave excitations during rare earthquakes. The displacement reduction rate of the BMRF structure is consistently below 10%, with its maximum displacement essentially mirroring that of the MRF structure. This reflects the yielding of ordinary braces under MCE intensity 9. Conversely, the FDBF structure demonstrates effective damping effects owing to the operational friction dampers, exhibiting robust seismic mitigation performance.

Table 10. Peak displacement (mm) of MRF, FDBF and BMRF (MCE intensity 9).

Working Condition	1940 El Centro	1979 El Centro	1981 Salton Sea	1952 Taft
MRF	21.16	30.1	25.01	25.65
FDBF	7.44	8.99	8.73	8.98
$\alpha/\%$	64.8	69.9	65.1	65.0
BMRF	19.99	27.95	23.02	24.35
$\alpha/\%$	5.53	7.14	8.01	5.07

Figure 28 illustrates the peak displacements of the FDBF and MRF. The peak dis placements of the FDBF are significantly smaller than that of the MRF under SLE, OBE and MCE intensity 9, and the reduction is more significant under MCE intensity 9. It shows that the FDBF shows good damping effect and the damping effect is better under rare earthquakes.

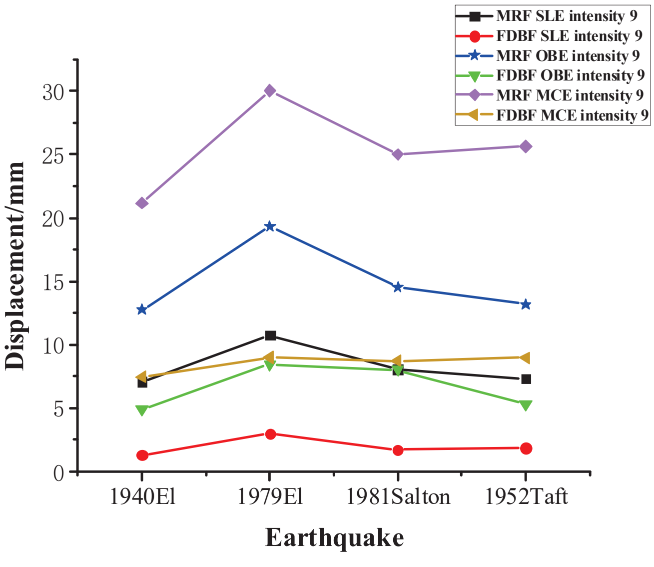

Figure 28. The peak displacements of the MRF and FDBF.

To illustrate the damping impact of the FDBF under earthquake conditions more effectively, the displacement reduction rates α from Tables 8–10 are visualized in Figure 29. As shown in the figure, at SLE intensity 9, the displacement reduction rates of both the FDBF and BMRF structures are similar, reflecting comparable seismic mitigation effects. At OBE intensity 9, the displacement reduction rate of the FDBF structure surpasses that of the BMRF structure. This difference arises as ordinary braces start to yield, leading to a decrease in stiffness. Concurrently, the new friction dampers become active, adjusting the brace length through their deformation to prevent brace compression. During MCE intensity 9, the BMRF structure loses nearly all of its seismic mitigation effectiveness owing to brace yielding and damage. In contrast, the displacement reduction rates of the FDBF structure exceed 60% as the deformations of the dampers in the energy-dissipating braces become more pronounced under severe seismic actions, effectively dissipating seismic energy and yielding superior seismic mitigation results.

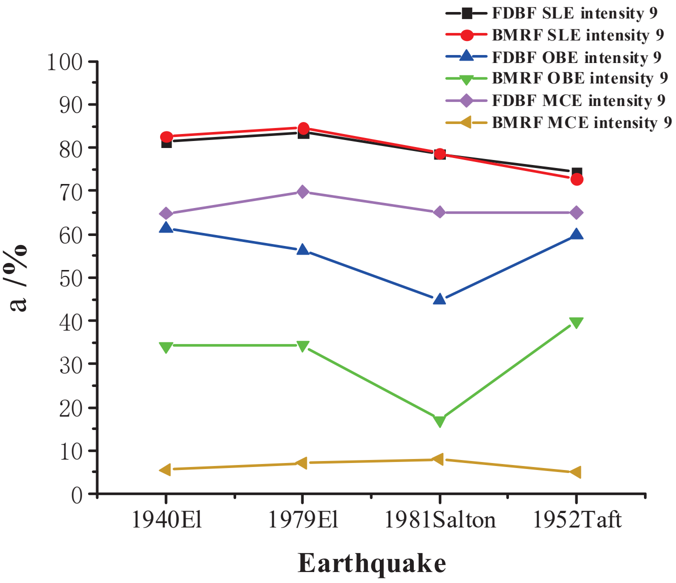

Figure 29. Displacement-reduction ratios α of the FDBF and BMRF.

5. Conclusions

A novel friction damper was proposed, and its hysteresis performance was examined. Shaking-table tests and finite element simulation analyses of the friction energy-dissipating braced frame structure, equipped with the new friction damper, were conducted. These tests evaluated the acceleration and displacement responses of the FDBF and MRF structures under seismic wave excitation. Finite element software enabled a comparative analysis of the seismic performance of the MRF, BMRF, and FDBF structures. The following conclusions were drawn:

(1) The hysteresis curve of the new friction damper is predominantly rectangular and complete, showing no significant stiffness degradation after repeated loadings. This indicates a stable and efficient energy dissipation capacity.

(2) Shaking-table tests revealed that the friction energy dissipation support at the bottom layer modified the dynamic characteristics of the original structure. Under seismic wave excitation, the peak acceleration at the top layer of the FDBF was reduced by 40–50% compared to the MRF, demonstrating a substantial seismic damping effect.

(3) With identical seismic wave excitation, the amplification factor of the peak top acceleration for both the MRF and BMRF exceeded 2, whereas that for the FDBF ranged between 1.05 and 1.17. This suggests a more significant seismic damping effect in the FDBF structure compared to the BMRF structure. During SLE intensity 9 earthquakes, the displacement-reduction rate of the FDBF was comparable to that of the

BMRF. However, under OBE and MCE intensity 9 earthquakes, the energy dissipation capacity of the BMRF diminished due to brace yielding, whereas the displacement-reduction rate of the FDBF was between 45 and 61% and between 60 and 70% under OBE and MCE intensity 9 earthquakes, respectively. This demonstrates the effectiveness of FDBF in damping both OBE and MCE earthquakes, with superior seismic mitigation performance during rare earthquakes.

This study did not examine certain factors affecting the seismic performance of friction dissipative braced frame structures, such as the placement and number of friction dissipative braces and the threshold slip force of the new friction dampers. Subsequent research can delve into these aspects in greater depth to provide further insights into the engineering application of this system.

Author Contributions: Conceptualization, L.Y. and C.Z.; methodology, C.Z.; software, L.Y.; validation, L.Y. and C.Z.; formal analysis, L.Y. and C.Z.; writing—original draft preparation, L.Y.; writing—review and editing, L.Y. and C.Z.; funding acquisition, C.Z. All authors have read and agreed to the published version of the manuscript.

Funding: This research was financially supported by the Ministry of Science and Technology of China (Grant No. 2019YFE0112400), the Department of Science and Technology of Shandong Province (Grant No. 2021CXGC011204).

Data Availability Statement: The data presented in this study are available on request from the corresponding author. The data are not publicly available due to the research on this topic is continuing.

Conflicts of Interest: The authors declare no conflict of interest.

References

1. Zhou, F. Development and application of isolation, energy dissipation, and structural control technology. *World Earthq. Eng.* **1989**, *4*, 16–20.
2. Jaisee, S.; Yue, F.; Ooi, Y.H. A state-of-the-art review on passive friction dampers and their applications. *Eng. Struct.* **2021**, *235*, 112022. [CrossRef]
3. Weining, S.; Xueli, W.; Zhanfei, W. Experimental study on mechanical properties of the steel friction discs used in a rotational friction damper. *Structures* **2021**, *29*, 1808–1818.
4. Pall, S.A.; Marsh, C. Response of friction damped braced frames. *J. Struct. Div. ASCE* **1982**, *108*, 1313–1323. [CrossRef]
5. Pall, A.S.; Marsh, C.; Fazio, P. Friction joints for seismic control of large panel structures. *PCI J.* **1980**, *25*, 38–61. [CrossRef]
6. Filiatrault, A.; Cherry, S. Performance evaluation of friction damped braced steel frames under simulated earthquake loads. *Earthq. Spectra* **1987**, *3*, 57–78. [CrossRef]
7. Chen, Z. Experimental research of a new type of energy dissipating bracing. *J. Build. Struct.* **1989**, *10*, 23–31.
8. Valente, M. Friction damper devices for seismic performance improvement of steel frames. *Int. Conf. Adv. Steel Struct.* **2012**, *1*, 58–70.
9. Wei, L.W.L. Study on table shaking test of RC frame model with friction energy-dissipation bracings. *J. Build. Struct.* **1997**, *18*, 29–37.
10. Hashemi, A.; Bagheri, H.; Zarnani, P.; Quenneville, P. Seismic performance of friction-damped steel frames integrated with resilient tension-only braces. *J. Constr. Steel Res.* **2021**, *176*, 106381. [CrossRef]
11. Zhou, Y. New Technology and System for Energy Consumption and Seismic Reduction in Buildings. PhD Thesis, Harbin Architecture University, Harbin, China, 1996.
12. Zhang, C.W. The active rotary inertia driver system for flutter vibration control of bridges and various promising applications. *Sci. China Technol. Sci.* **2023**, *66*, 390–405. [CrossRef]
13. Colajanni, P.; Papia, M. Seismic response of braced frames with and without friction dampers. *Eng. Struct.* **1995**, *17*, 129–140. [CrossRef]
14. Xian, Q. The Theoretical and Experimental Research on Energy Dissipating Brace Frame Structures. PhD Thesis, Hunan University, Changsha, China, 2000.
15. Naeem, A.; Kim, J. Seismic retrofit of structures using rotational friction dampers with restoring force. *Adv. Struct. Eng.* **2020**, *23*, 3525–3540. [CrossRef]
16. Wu, B.; Zhang, J.; Ou, J. Experimental study and numerical analysis of Pall friction damper. *J. Build. Struct.* **2003**, *24*, 7–13.
17. Ghasemi, M.; Zhang, C.; Khorshidi, H.; Zhu, L.; Hsiao, P.-C. Seismic upgrading of existing RC frames with displacement-restraint cable bracing. *Eng. Struct.* **2023**, *282*, 115764. [CrossRef]
18. Sheldon, C.; Yeda, L.; Xunan, Z. Damping characteristics of friction-damped braced frame and its effectiveness in the mega-sub controlled structure system. *Earthq. Eng. Eng. Vib.* **2007**, *6*, 171–181.

19. Liu, W.; Lian, W.; Li, S. Friction Dampers and Friction Damped Braced Frames. *J. Nanjing Archit. Civ. Eng. Inst.* **1994**, *29*, 9–16.
20. Wen, B.-P.; Zang, F.-C.; Zhang, H.-L.; Yang, D.L.; Wei, Y.H.; Chen, Y. Study on the seismic performance of a new type rotational friction damper. *Earthq. Resist. Eng. Retrofit.* **2022**, *44*, 76–81.
21. Mualla, I.H.; Belev, B. Analysis, design and applications of rotational friction dampers for seismic protection. *Arch. J. Civ. Eng. Env. Arch.* **2016**, *62*, 335–346. [CrossRef]
22. Xiaoqi, Y.; Yan, W.; Haibin, Z.; Liwei, M. Experimental study on hysteretic performance of rotating friction damper. *Ind. Arch.* **2020**, *50*, 151–157.
23. Javidan, M.M.; Kim, J. Seismic retrofit of soft-first-story structures using rotational friction dampers. *J. Struct. Eng.* **2019**, *145*, 04019162. [CrossRef]
24. Wei, G.; Hengchao, X. Performance of a novel rotational frictional damper. *Struct. Eng.* **2018**, *34* (Suppl. S1), 54–58.
25. Wei, G.; Chen, Z.; Xu, X.; Dan, B. Pseudo dynamic Hybrid Simulation of High-Speed Railway Bridge-Track System with Rotational Friction Damper. *Int. J. Struct. Stab. Dyn.* **2020**, *20*, 2040014.
26. Kim, J.; Choi, H.; Min, K.W. Use of rotational friction dampers to enhance seismic and progressive collapse resisting capacity of structures. *Struct. Des. Tall Build.* **2011**, *20*, 515–537. [CrossRef]
27. Monir, H.S.; Zeynali, K. A modified friction damper for diagonal bracing of structures. *J. Constr. Steel Res.* **2013**, *87*, 17–30. [CrossRef]
28. Wang, G.; Wang, Y.; Yuan, J.; Yang, Y.; Wang, D. Modeling and experimental investigation of a novel arc-surfaced frictional damper. *J. Sound. Vib.* **2017**, *389*, 89–100. [CrossRef]
29. Soong, T.T.; Skinner, G.T. Experimental study of active structural control. *J. Engrg Mech. Div.* **1981**, *107*, 1057–1067. [CrossRef]
30. Spencer, B.F.; Dyke, S.J.; Deoskar, H.S. Benchmark problems in structural control: Part I—Active Mass Driver system. *Earthq. Engng Struct. Dyn.* **1998**, *27*, 1127–1139. [CrossRef]
31. Agrawal, A.K.; Nagarajaiah, S. Benchmark structural control problem for a seismically excited highway bridge: Phase I and II. *Struct. Control Health Monit.* **2009**, *16*, 503–508. [CrossRef]
32. Spencer, B.F.; Dyke, S.J.; Deoskar, H.S. Benchmark problems in structural control: Part II—Active tendon system. *Earthq. Engng Struct. Dyn.* **1998**, *27*, 1141–1147. [CrossRef]
33. Chin Hsiung, L.; Mualla, I.; Liao, W.I. Shaking-table test of a friction-damped frame structure. *Struct. Des. Tall Spec. Build.* **2004**, *1*, 13.
34. Wengang, Z.; Songshan, N.; Fei, P.; Yiqian, C. Selection of input ground motions for seismic fragility analysis considering structural nonlinear response. *J. Dyn. Control* **2023**, *21*, 80–86.
35. Mirzabagheri, S.; Sanati, M.; Aghakouchak, A.A.; Khadem, S.E. Experimental and numerical investigation of rotational friction dampers with multi units in steel frames subjected to lateral excitation. *Arch. Civ. Mech. Eng.* **2015**, *15*, 479–491. [CrossRef]
36. *GB50011−2010*; Code for Seismic Design of Buildings (2016 Edition). Construction Industry Press: Beijing, China, 2016.

buildings

MDPI

Article

Performance Evaluation of Inerter-Based Dynamic Vibration Absorbers for Wind-Induced Vibration Control of a Desulfurization Tower

Yang Li, Qinghua Zhang, Yanwei Xu, Jinlong Wen and Zhihao Wang *

School of Civil Engineering and Communication, North China University of Water Resources and Electric Power, Zhengzhou 450000, China; liyang202020@163.com (Y.L.); zqh@ncwu.edu.cn (Q.Z.); xuyanwei_v587@163.com (Y.X.); wenjinlong0819@126.com (J.W.)

* Correspondence: wangzhihao@ncwu.edu.cn

Abstract: High-rise flue gas desulfurization towers are susceptible to wind loads, which can cause instability and failure in the along-wind and across-wind directions. The tuned mass damper (TMD) has been widely applied in the wind-induced vibration control of high-rise structures. To enhance the control performance and reduce the auxiliary mass of TMD, this study focuses on inerter-based dynamic vibration absorbers (IDVAs) for controlling the vibration response of a desulfurization tower. The dynamical equations of the tower–IDVA systems are established under wind loads, and a parameter optimization strategy for IDVAs is proposed by using the genetic algorithm. The performance of the traditional TMD and six IDVAs in the vibration control of the tower are systematically compared. Numerical simulations demonstrate that both the TMD and IDVAs can substantially mitigate the vibration response of the tower. However, compared to the TMD with the same response mitigation ratio, more than 34% of the auxiliary mass can be reduced by two optimal IDVAs. In addition, the energy dissipation enhancement and lightweight effect of the two IDVAs are explained through parametric studies.

Keywords: high-rise structure; wind-induced vibration control; inerter-based dynamic vibration absorber; tuned mass damper

1. Introduction

Large-scale flue gas desulfurization towers, characterized as high-rise thin-walled steel structures, are critical devices used by petrochemical enterprises. Such structures are notably sensitive to wind loads due to their high flexibility and low damping [1,2]. At the bottom of the desulfurization tower, industrial exhaust gases undergo desulfurization, and a slender steel chimney is set up on the upper sections to raise the height of the smoke discharge. The variation in the sections weakens the stiffness and carrying capacity of the upper parts of the structure. As the high-rise structure with a circular cross-section, the desulfurization tower can easily suffer severe across-wind vortex-induced vibrations at certain wind speeds in addition to the along-wind fluctuating response [3–5]. Therefore, it is imperative to conduct research on the wind-induced vibration control of the tower.

Passive measures have been recognized as an effective approach [6,7]. As a typical dynamic vibration absorber, the tuned mass damper (TMD) has been widely adopted in engineering structures [8–10]. The optimal parameter design approach, which disregards the damping of the main structure proposed by Den Hartog [11], serves as the foundation for TMD parameter optimization. Brownjohn et al. [12] installed a monitoring system for TMDs, which allows the real-time display of the resulting vibration status and modal damping values. This system facilitates the adjustment of the TMD parameters, consequently enhancing its control performance. Elias et al. [13] designed a distributed multiple tuned mass damper, which achieves multimodal dynamic response control of the along-wind response of the chimney. Xiang et al. [14] performed a seismic design of the hysteretic damping tuned mass damper using the H_∞/H_2 optimization for undamped and damped structures, providing valuable references for designers. Theoretical analysis and experimental verification have demonstrated that the application of TMDs in reducing chatter during the turning of the thin-walled cylinder also shows a good control performance [15]. Vibration control analyses of a high-rise structure indicate the effectiveness of linearizing the equations of motion to obtain optimal control device parameters [16]. Moreover, the pendulum TMDs installed at the top of Shanghai Tower and Taipei 101 significantly mitigate the wind-induced vibrations, thereby improving the comfort levels of residents [17]. Testing research on the TMD system in the Shanghai tower indicates that it is highly suitable for controlling vibrations of structures with relatively small damping ratios [18]. However, the control performance of TMD relies considerably on its tuned mass, which may have adverse effects on the structure. Additionally, the large displacement of its mass block and the narrow frequency band limit the development of TMD [19]. Especially for high-rise structures with limited installation space, like desulfurization towers, the large auxiliary mass of the TMD increases the difficulty of its application.

In 2002, based on the force–current analogy, Smith [20] introduced a two-terminal mechanical device dubbed an inerter. This groundbreaking innovation has allowed new avenues for the vibration control strategies of high-rise structures [21,22]. Combined with a TMD, the inerter element can effectively reduce the auxiliary mass and improve the control performance of traditional dynamic vibration absorbers [23–25]. Alotta et al. [26] included a standard inerter-based device within a rhombus truss, which can tune the frequency of the vibration absorber by changing only the geometry of the rhombus truss. In terms of the vibration control of high-rise structures, Liang et al. [27] seismically controlled a mega-substructure system with a tuned inerter damper (TID) and showed an enhanced effect under optimal conditions relative to the traditional viscous damper and the TMD. With reference to a multiple tuned mass damper system, Chen et al. [28] developed a multiple tuned inerter-based damper system for controlling the seismic response, which demonstrated significant advantages. Marian et al. [29] proposed a tuned mass damper–inerter (TMDI) by combining a TMD with an inerter element in series. By leveraging the mass amplification effect of the inerter, the TMDI can perform better than the traditional TMD. Based on a constrained multi-objective evolutionary algorithm, Wang et al. [30] proposed an efficient inerter-based absorber parameter optimization scheme for the wind-induced vibration control of high-rise structures, and they applied it to the TMDI/TID in a 340-meter-high building. However, TID and TMDI require connections at both ends of the structure. Their control performance depends on the connection length of the inerter device, posing installation difficulties in high-rise tubular towers.

Different from TID and TMDI, inerter-based dynamic absorbers (IDVAs) connected to one end of the primary structure are expected to solve the connection problem of the inerter device. Replacing the viscous damper in a TMD with a tuned viscous mass damper [31], Garrido et al. [32] proposed a rotational inertia double tuned mass damper and demonstrated the advantages of it with respect to the TMD. Zhang et al. [33] installed a rotational inertia double tuned mass damper on wind turbines to control their in-plane vibration, establishing comprehensive numerical models and optimization algorithms. Building on this basis, Zhang et al. [34–36] combined a TMD with an inerter subsystem, leading to the development of a generalized tuned mass inerter system. Their findings suggested that the tuned mass inerter system could reduce the auxiliary mass and improve the control performance compared to TMD. Wen et al. [37], Su et al. [38], and Hu et al. [39] compared the performance levels of different combinations of IDVAs, as shown in Figure 1. These studies have verified the advantages of IDVAs over the traditional TMD, which were manifested in energy dissipation enhancement, a lightweight effect, and a wider effective frequency band.

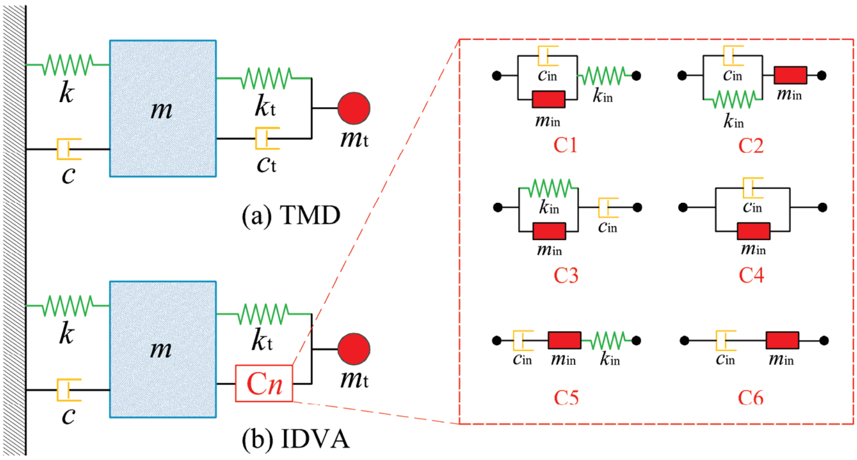

Figure 1. Schematic diagram of the tuned mass damper (TMD) and inerter-based dynamic vibration absorbers (IDVA) system: (**a**) TMD; (**b**) IDVA. (m, c, and k are the mass, damping, and stiffness of the main structure, respectively; m_t, c_t, and k_t are the tuned mass, damping, and tuned stiffness of the TMD, respectively; and m_{in}, c_{in}, and k_{in} are the inertance coefficient, damping, and stiffness of the inerter subsystems, respectively).

Given the limited space at the top of the tower, it is necessary to investigate the lightweight effects of different vibration absorbers. However, the specific effectiveness of different IDVAs in controlling the wind-induced vibration of the desulfurization towers are not clear. Additionally, in the parameter design of the vibration absorbers, the distinct wind-induced response characteristics of cylindrical structures in the along-wind and across-wind directions should be considered. The present study aims to provide an optimal solution for the wind-induced vibration control of the desulfurization tower and investigate the control performances of different IDVAs.

To this end, the control performances of six IDVAs on the wind-induced vibration of a desulfurization tower are systematically evaluated and compared. The organization of this paper is as follows. First, a numerical model of the tower is established, and the transfer functions are derived. Second, an optimal parameter design strategy for the IDVAs is established. Third, the control performances of a TMD and six IDVAs on the tower are compared. Finally, a parametric study is carried out to further analyze the control performance enhancement and lightweight effect of two optimal IDVAs.

2. Tower–IDVA Systems

2.1. Model of the Desulfurization Tower

The desulfurization tower is 85 meters tall and divided into five sections. The tower is mainly made of Q235 steel, with an elastic modulus of 2.06×10^5 MPa, a density of 7.85 g/cm^3, and a Poisson's ratio of 0.3. The thickness of the tower body decreases with increasing height, ranging from 1.6 cm to 2 cm. The dimensions of the segmental structures of the tower are shown in Table 1 and Figure 2a.

Table 1. Inner diameter and thickness values of each section of the tower.

Segment	I	II	III	IV	V
Inside diameter/m	7.700	7.700/5.760	5.760	2.700	2.700
Thickness/m	0.020	0.020/0.016	0.016	0.016	0.016

The desulfurization tower is regarded as a cantilever beam structure with the base fully constrained. A finite element model, comprising 32 elements, is established using the Beam188 element in ANSYS, as shown in Figure 2b. To validate the accuracy of the simplified beam element model, a solid model is established using the Solid95 element, as shown in Figure 2c. The parameters of dynamic characteristics and mode shapes of the two models are compared in Table 2 and Figure 3, respectively. The comparison reveals minimal discrepancies between the beam element model and the solid model. Conservatively, the first two modal damping ratios for the desulfurization tower are set as 0.5% [13,40]. To enhance computational efficiency, the structural mass matrix, stiffness matrix, and damping matrix of the beam element model are extracted to construct a numerical model of the tower for subsequent analysis.

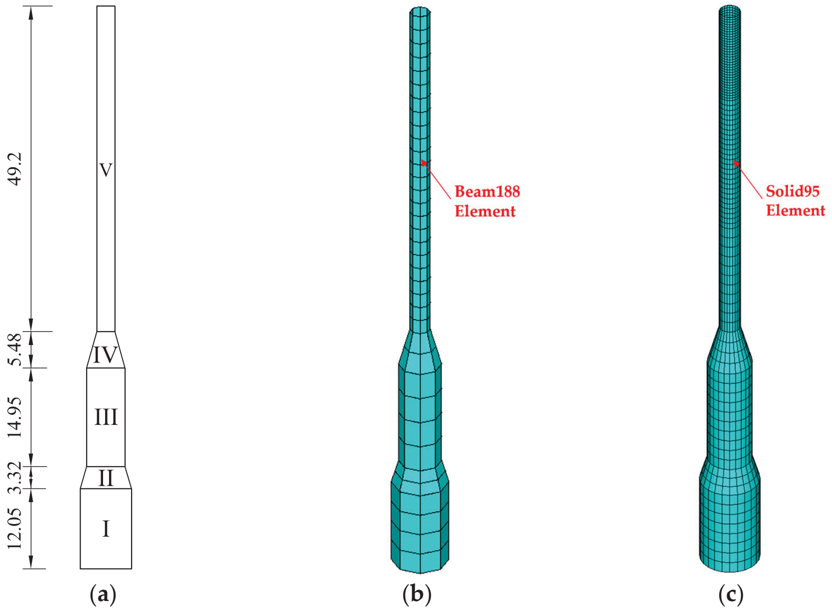

Figure 2. Comparison of the desulfurization tower models: (**a**) Height of each segment; (**b**) The beam element model; (**c**) The solid element model.

Table 2. Natural vibration frequencies and periods of the tower.

Mode	Frequency (Beam199/Solid95)	Period (Beam188/Solid95)	Error
1st	0.908/0.888	1.101/1.126	2.3%
2nd	4.192/4.160	0.239/0.241	0.8%
3rd	9.156/9.050	0.109/1.111	1.2%

Note: Error = (Beam model frequency – Solid model frequency)/Solid model frequency × 100%.

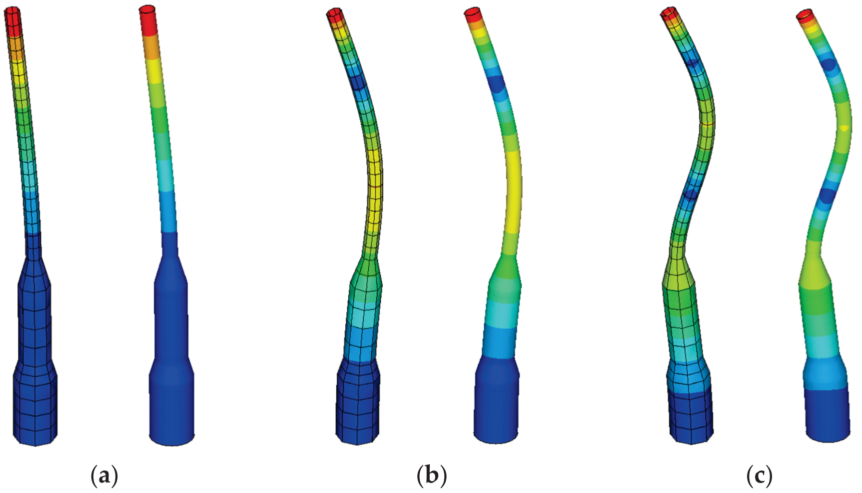

Figure 3. Comparison of the first three mode shapes: (**a**) The first mode; (**b**) The second mode; (**c**) The third mode.

2.2. Equations of the Tower–IDVA System

The desulfurization tower is simplified into a generalized system:

$$m = \boldsymbol{\Phi}^{\mathrm{T}}\boldsymbol{M}\boldsymbol{\Phi};\ c = \boldsymbol{\Phi}^{\mathrm{T}}\boldsymbol{C}\boldsymbol{\Phi};\ k = \boldsymbol{\Phi}^{\mathrm{T}}\boldsymbol{K}\boldsymbol{\Phi}, \tag{1}$$

where $\boldsymbol{M}$, $\boldsymbol{C}$, and $\boldsymbol{K}$ represent the mass matrices, damping matrices, and stiffness matrices, respectively; and $\boldsymbol{\Phi}$ represents the mode shape function of the desulfurization tower. In this study, only the first mode is considered in wind-induced vibration control.

The analytical model of the desulfurization tower–IDVA system under wind loads is shown in Figure 4. Cn may represent any inerter subsystem of the different configurations C1~C6, as shown in Figure 1. If Cn is replaced by a damping element c_{t}, it represents the TMD system. The dynamical equation for the tower–TMD system is Equation (2), and the equations for the six tower–IDVA systems are represented as Equations (3)–(8):

$$\begin{cases} m\ddot{x} + c\dot{x} + c_{\mathrm{t}}(\dot{x} - \dot{x}_{\mathrm{t}}) + kx + k_{\mathrm{t}}(x - x_{\mathrm{t}}) = f(t) \\ m_{\mathrm{t}}\ddot{x}_{\mathrm{t}} + c_{\mathrm{t}}(\dot{x}_{\mathrm{t}} - \dot{x}) + k_{\mathrm{t}}(x_{\mathrm{t}} - x) = 0 \end{cases}; \tag{2}$$

$$\begin{cases} m\ddot{x} + c\dot{x} + kx + k_{\mathrm{t}}(x - x_{\mathrm{t}}) + k_{\mathrm{in}}(x - x_{\mathrm{in}}) = f(t) \\ m_{\mathrm{t}}\ddot{x}_{\mathrm{t}} + m_{\mathrm{in}}(\ddot{x}_{\mathrm{t}} - \ddot{x}_{\mathrm{in}}) + c_{\mathrm{in}}(\dot{x}_{\mathrm{t}} - \dot{x}_{\mathrm{in}}) + k_{\mathrm{t}}(x_{\mathrm{t}} - x) = 0; \\ m_{\mathrm{in}}(\ddot{x}_{\mathrm{in}} - \ddot{x}_{\mathrm{t}}) + c_{\mathrm{in}}(\dot{x}_{\mathrm{in}} - \dot{x}_{\mathrm{t}}) + k_{\mathrm{in}}(x_{\mathrm{in}} - x) = 0 \end{cases} \tag{3}$$

$$\begin{cases} m\ddot{x} + m_{\mathrm{in}}(\ddot{x} - \ddot{x}_{\mathrm{in}}) + c\dot{x} + kx + k_{\mathrm{t}}(x - x_{\mathrm{t}}) = f(t) \\ m_{\mathrm{t}}\ddot{x}_{\mathrm{t}} + c_{\mathrm{in}}(\dot{x}_{\mathrm{t}} - \dot{x}_{\mathrm{in}}) + k_{\mathrm{t}}(x_{\mathrm{t}} - x) + k_{\mathrm{in}}(x_{\mathrm{t}} - x_{\mathrm{in}}) = 0; \\ m_{\mathrm{in}}(\ddot{x}_{\mathrm{in}} - \ddot{x}) + c_{\mathrm{in}}(\dot{x}_{\mathrm{in}} - \dot{x}_{\mathrm{t}}) + k_{\mathrm{in}}(x_{\mathrm{in}} - x_{\mathrm{t}}) = 0 \end{cases} \tag{4}$$

$$\begin{cases} m\ddot{x} + c\dot{x} + c_{\mathrm{in}}(\dot{x} - \dot{x}_{\mathrm{in}}) + kx + k_{\mathrm{t}}(x - x_{\mathrm{t}}) = f(t) \\ m_{\mathrm{t}}\ddot{x}_{\mathrm{t}} + m_{\mathrm{in}}(\ddot{x}_{\mathrm{t}} - \ddot{x}_{\mathrm{in}}) + k_{\mathrm{t}}(x_{\mathrm{t}} - x) + k_{\mathrm{in}}(x_{\mathrm{t}} - x_{\mathrm{in}}) = 0; \\ m_{\mathrm{in}}(\ddot{x}_{\mathrm{in}} - \ddot{x}_{\mathrm{t}}) + c_{\mathrm{in}}(\dot{x}_{\mathrm{in}} - \dot{x}) + k_{\mathrm{in}}(x_{\mathrm{in}} - x_{\mathrm{t}}) = 0 \end{cases} \tag{5}$$

$$\begin{cases} m\ddot{x} + m_{\mathrm{in}}(\ddot{x} - \ddot{x}_{\mathrm{t}}) + c\dot{x} + c_{\mathrm{t}}(\dot{x} - \dot{x}_{\mathrm{t}}) + kx + k_{\mathrm{t}}(x - x_{\mathrm{t}}) = f(t) \\ m_{\mathrm{t}}\ddot{x}_{\mathrm{t}} + m_{\mathrm{in}}(\ddot{x}_{\mathrm{t}} - \ddot{x}) + c_{\mathrm{t}}(x_{\mathrm{t}} - x) + k_{\mathrm{t}}(x_{\mathrm{t}} - x) = 0 \end{cases}; \tag{6}$$

$$\begin{cases} m\ddot{x} + c\dot{x} + kx + k_{\mathrm{t}}(x - x_{\mathrm{t}}) + k_{\mathrm{in}}(x - x_1) = f(t) \\ m_{\mathrm{t}}\ddot{x}_{\mathrm{t}} + c_{\mathrm{in}}(\dot{x}_{\mathrm{t}} - \dot{x}_2) + k_{\mathrm{t}}(x_{\mathrm{t}} - x) = 0 \\ m_{\mathrm{in}}(\ddot{x}_2 - \ddot{x}_1) + c_{\mathrm{in}}(\dot{x}_2 - \dot{x}_{\mathrm{t}}) = 0 \\ m_{\mathrm{in}}(\ddot{x}_1 - \ddot{x}_2) + k_{\mathrm{in}}(x_1 - x) = 0 \end{cases}; \tag{7}$$

$$\begin{cases} m\ddot{x} + c\dot{x} + c_{\mathrm{in}}(\dot{x} - \dot{x}_{\mathrm{in}}) + kx + k_{\mathrm{t}}(x - x_{\mathrm{t}}) = f(t) \\ m_{\mathrm{t}}\ddot{x}_{\mathrm{t}} + m_{\mathrm{in}}(\ddot{x}_{\mathrm{t}} - \ddot{x}_{\mathrm{in}}) + k_{\mathrm{t}}(x_{\mathrm{t}} - x) = 0 \\ m_{\mathrm{in}}(\ddot{x}_{\mathrm{in}} - \ddot{x}_{\mathrm{t}}) + c_{\mathrm{in}}(\dot{x}_{\mathrm{in}} - \dot{x}) = 0 \end{cases}, \tag{8}$$

where x, x_{t}, and x_{in} represent the displacements of the tower, the tuned mass, and the inerter element, respectively, and $f(t)$ represents the generalized wind load.

As previous research on TMDs is relatively mature and the derivation processes of various configurations are similar, only the configuration C1 is taken as an example to demonstrate the derivation of the transfer functions and the frequency domain responses of the tower–IDVA systems.

First, the following dimensionless parameters are defined:

$$\mu_{\mathrm{t}} = m_{\mathrm{t}}/m;\ \mu_{\mathrm{in}} = m_{\mathrm{in}}/m_{\mathrm{t}};\ \xi_{\mathrm{in}} = c_{\mathrm{in}}/(2\sqrt{m_{\mathrm{t}}k_{\mathrm{t}}});\ v_{\mathrm{t}} = \omega_{\mathrm{t}}/\omega_0;\ v_{\mathrm{in}} = k_{\mathrm{in}}/k_{\mathrm{t}}, \tag{9}$$

where μ_{t} and μ_{in} represent the tuned mass ratio and inertance–mass ratio, respectively; ξ_{in} represents the nominal damping ratio of the inerter subsystem; v_{t} is the frequency ratio of C1, where ω_{t} and ω_0 represent the circular frequency of C1 and the desulfurization tower, respectively; and v_{in} is the nominal stiffness ratio of spring k_{in} in the inerter subsystem.

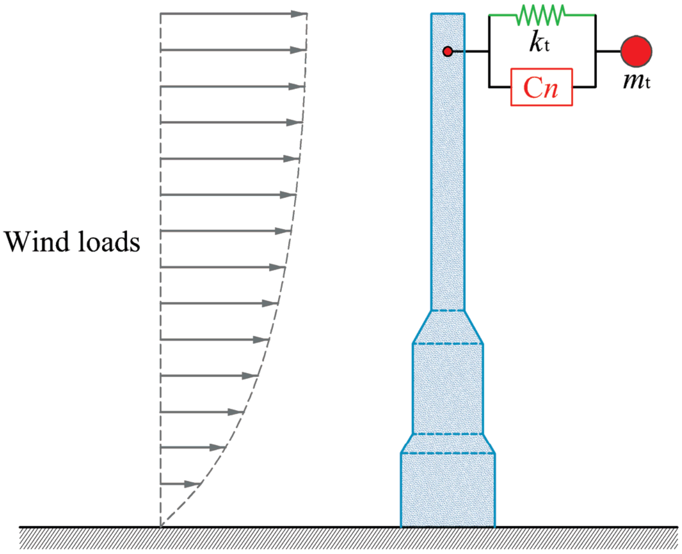

Figure 4. Analytical model of the desulfurization tower–IDVA system.

Accordingly, a substitution can be made for the mass, stiffness, and damping parameters in Equation (3):

$$m_t = \mu_t m;\ m_{in} = \mu_{in}\mu_t m;\ c = 2m\omega_0\xi_0;\ c_{in} = 2m\xi_{in}\mu_t v_t\omega_0;\ k = m\omega_0^2;\ k_t = \mu_t m(\omega_0 v_t)^2;\ k_{in} = v_{in}\mu_t m(\omega_0 v_t)^2, \tag{10}$$

where ξ_0 represents the first-order damping ratio of the desulfurization tower.

$$\boldsymbol{M}_1\ddot{\boldsymbol{X}} + \boldsymbol{C}_1\dot{\boldsymbol{X}} + \boldsymbol{K}_1\boldsymbol{X} = \boldsymbol{F}(t), \tag{11}$$

where $\boldsymbol{X} = [x, x_t, x_{in}]^T$, $\boldsymbol{F}(t) = [f(t)/m, 0, 0]^T$. The first modal mass matrices $\boldsymbol{M}_1$, damping matrices $\boldsymbol{C}_1$, and stiffness matrices $\boldsymbol{K}_1$ of C1 are represented as follows:

$$\begin{gathered}\boldsymbol{M}_1 = \begin{bmatrix} 1 & 0 & 0 \\ 0 & \mu_t + \mu_t\mu_{in} & -\mu_t\mu_{in} \\ 0 & -\mu_t\mu_{in} & \mu_t\mu_{in} \end{bmatrix};\ \boldsymbol{C}_1 = \begin{bmatrix} 2\xi_0\omega_0 & 0 & 0 \\ 0 & 2\xi_{in}\mu_t v_t\omega_0 & -2\xi_{in}\mu_t v_t\omega_0 \\ 0 & -2\xi_{in}\mu_t v_t\omega_0 & 2\xi_{in}\mu_t v_t\omega_0 \end{bmatrix}; \\ \boldsymbol{K}_1 = \begin{bmatrix} \omega_0^2(1 + \mu_t v_t^2 + v_{in}\mu_t v_t^2) & -\mu_t(\omega_0 v_t)^2 & -v_{in}\mu_t(\omega_0 v_t)^2 \\ -\mu_t(\omega_0 v_t)^2 & \mu_t(\omega_0 v_t)^2 & 0 \\ -v_{in}\mu_t(\omega_0 v_t)^2 & 0 & v_{in}\mu_t(\omega_0 v_t)^2 \end{bmatrix}\end{gathered} \tag{12}$$

Upon substituting the variables in Equation (10), the mass, stiffness, and damping matrices of C2~C6 can be found in Appendix A. If $f(t) = e^{i\omega t}$, $\boldsymbol{X} = \boldsymbol{H}(i\omega)\cdot e^{i\omega t}$, where $\boldsymbol{H}(i\omega) = [H_0(i\omega), H_t(i\omega), H_{in}(i\omega)]^T$, $H_0(i\omega)$, $H_t(i\omega)$, and $H_{in}(i\omega)$ represent the transfer functions of the main structure, the mass block. and the inerter element of the tower–C1 system, respectively. By substitution into Equation (11), the following equation is derived:

$$\begin{gathered}\boldsymbol{H}(i\omega) = \frac{1}{m}\cdot\left[-\omega^2\boldsymbol{M}_1 + i\omega\boldsymbol{C}_1 + \boldsymbol{K}_1\right]^{-1}\cdot[1,0,0]^T = \begin{bmatrix} A_{11} & A_{12} & A_{13} \\ A_{21} & A_{22} & A_{23} \\ A_{31} & A_{32} & A_{33} \end{bmatrix}^{-1}\begin{bmatrix} 1 \\ 0 \\ 0 \end{bmatrix} \\ \begin{cases} A_{11} = -\omega^2 + i2\omega\omega_0\xi_0 + \omega_0^2(1 + \mu_t v_t^2 + v_{in}\mu_t v_t^2) \\ A_{12} = -\mu_t(\omega_0 v_t)^2;\ A_{21} = A_{12} \\ A_{13} = -v_{in}\mu_t(\omega_0 v_t)^2;\ A_{31} = A_{13} \\ A_{22} = -\omega^2(\mu_{in} + \mu_t\mu_{in}) + i2\omega\xi_{in}\mu_t v_t\omega_0 + \mu_t(\omega_0 v_t)^2 \\ A_{23} = \omega^2\mu_t\mu_{in} - i2\omega\xi_{in}\mu_t v_t\omega_0;\ A_{32} = A_{23} \\ A_{33} = -\omega^2\mu_t\mu_{in} + i2\omega\xi_{in}\mu_t v_t\omega_0 + v_{in}\mu_t(\omega_0 v_t)^2 \end{cases}\end{gathered} \tag{13}$$

The root mean square of the displacement response of the tower–C1 system under wind load can be represented as follows:

$$\sigma_x = \sqrt{\int_{\omega_1}^{\omega_2} S_x(\mathrm{i}\omega)\mathrm{d}\omega} = \sqrt{\int_{\omega_1}^{\omega_2} |H_0(\mathrm{i}\omega)|^2 S_F(\mathrm{i}\omega)\mathrm{d}\omega}, \tag{14}$$

where ω_1~ω_2 represent the range of the integral frequency, and the integration is performed near the first-order frequency of the structure; $S_x(\mathrm{i}\omega)$ represents the response spectrum of the structure, and it is resolved using the pseudo excitation method [41], which has a relatively high computational efficiency; and $S_F(\mathrm{i}\omega)$ represents the load spectrum of the structure, which can be derived from the wind speed spectrum.

2.3. Optimal Design

For the along-wind vibration control, the minimum root-mean-square displacement response σ_x of the tower obtained from the frequency domain analysis or the minimum tuned mass ratio μ_t are taken as the optimization objectives. The genetic algorithm, a widely used computational method for optimizing damper parameters in design [10,42], is renowned for its global search capabilities and reduced likelihood of entrapment in local optima. Its ability to process multiple variables simultaneously enhances the computational efficiency, making it suitable for optimizing multiple computational parameters under a single objective. Therefore, the genetic algorithm is then used to optimize the IDVA parameters μ_in, ξ_in, v_t, and v_in under the specific $\mu_\mathrm{t,lim}$ or $\sigma_{x,\mathrm{lim}}$. The control performances of IDVAs can also be compared under varying μ_t. The control parameter settings of the genetic algorithm are as follows: the maximum evolution generation is set to 150 generations, the population size is 900, the crossover probability is 0.8, the mutation probability is 0.05, the proportion of the newly generated population is 0.25, and the calculation accuracy is 1×10^{-9}.

H_∞ control theory is renowned for high control accuracy and strong robustness, and it is suitable for the control of the single-order modal vibration of the structure [14,43]. The desulfurization tower is a cylindrical structure, and its vibration in the across-wind direction is dominated by single-order modal vortex resonance.

As a cylindrical high-rise structure, the across-wind response of the desulfurization tower is predominantly governed by vortex-induced resonance at a single modal frequency. It is feasible to simulate the vortex excitation by employing sinusoidal excitation (refer to Appendix B). The H_∞ optimization theory is typically employed for structural peak response suppression under harmonic/sinusoidal excitation [14,43,44]. Therefore, for the across-wind vibration control of the tower, based on the transfer function of the tower–IDVA system and the dimensionless parameters defined by Equation (9), the parameters of the IDVAs are optimized using the genetic algorithm and H_∞ performance index:

$$G(\mathrm{i}\omega) = \sup_{\omega} \tau_\mathrm{max}[H_0(\mathrm{i}\omega)], \tag{15}$$

where $G(\mathrm{i}\omega)$ represents the H_∞ norm of the six typical tower–IDVA systems, and τ_max represents the maximum singular value.

In summary, the parameter optimization of IDVAs for vibration control in the along-wind and across-wind directions of the desulfurization tower obtained from the above analysis is shown in Figure 5.

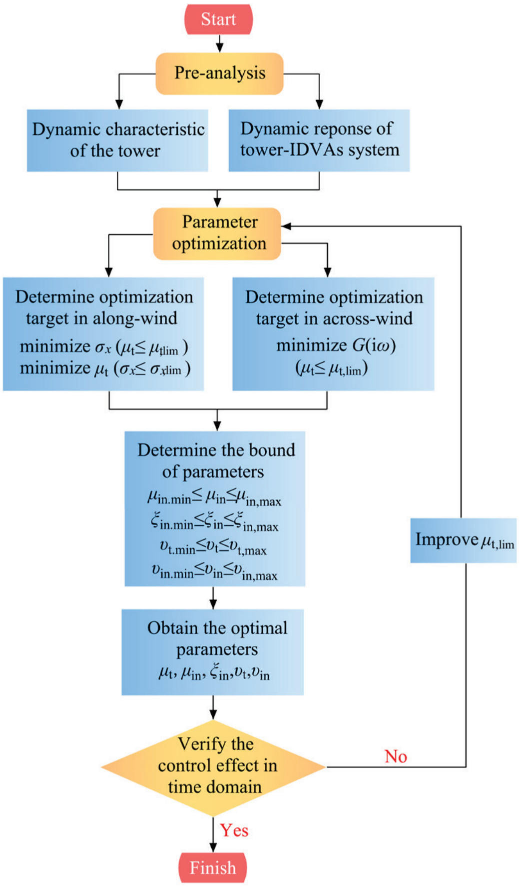

Figure 5. Parameter optimization of IDVAs for the desulfurization tower.

3. Evaluation of Wind-Induced Vibration Control

3.1. Comparative Analysis of H_∞ Performance

By setting the tuned mass ratios to $\mu_t = 2\%$ and $\mu_t = 5\%$, the genetic algorithm is used to search and optimize the four parameters of IDVAs, specifically μ_{in}, υ_t, υ_{in}, and ξ_{in}. The results, including the optimized parameters for the TMD calculated using the fixed point theory [9], are collated in Table 3. The frequency response curves of the TMD and six optimally designed IDVAs are performed in Figures 6 and 7, and the tuned mass ratios μ_t of the vibration absorbers are 2% and 5%, respectively.

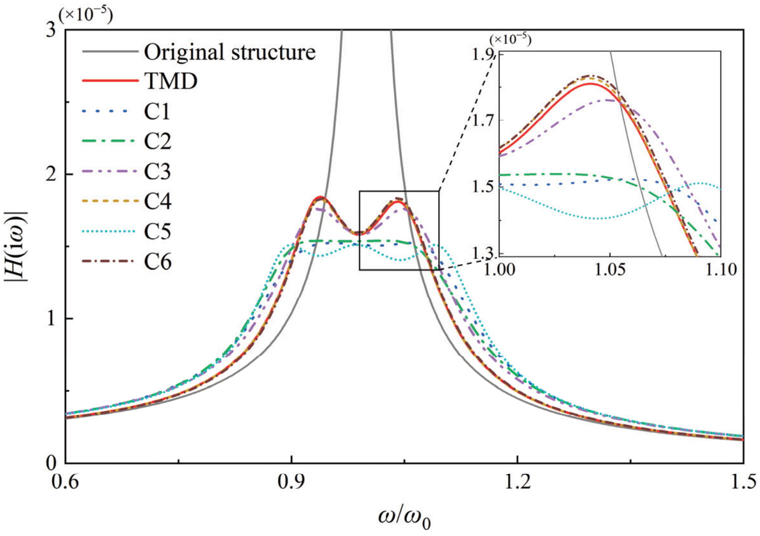

Figure 6. Comparison of frequency response curves ($\mu_t = 2\%$).

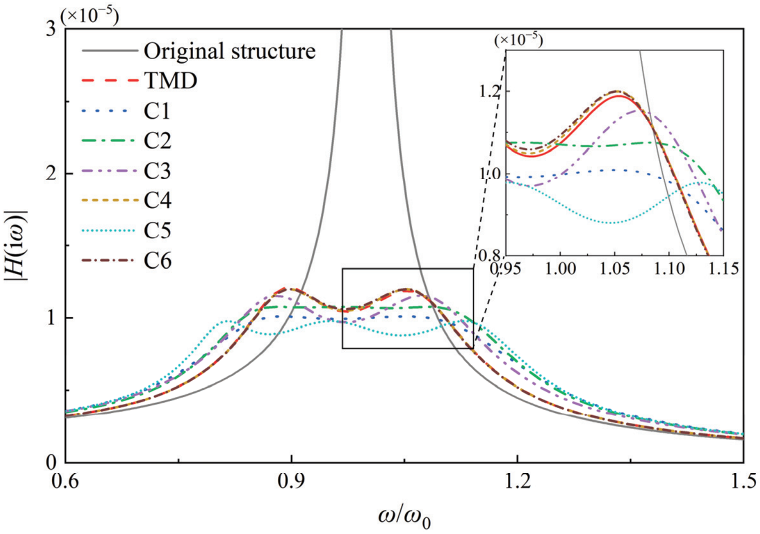

Figure 7. Comparison of frequency response curves (μ_t = 5%).

Table 3. Optimal H_∞ performance parameters of the TMD and IDVAs.

	μ_t (%)	μ_{in}	υ_t	υ_{in}	ξ_{in}
TMD	2	/	0.9794	/	0.0874 (ξ_t)
	5	/	0.9524	/	0.1336 (ξ_t)
C1	2	0.0646	0.9547	0.0738	0.0149
	5	0.1322	0.9060	0.1937	0.0548
C2	2	0.0683	0.9990	0.0621	0.0136
	5	0.0950	0.9705	0.0866	0.0176
C3	2	0.0038	0.9031	0.4170	0.1619
	5	0.0037	0.9013	0.8104	0.1520
C4	2	→0	0.9796	/	0.0862
	5	→0	0.9511	/	0.1346
C5	2	0.0413	0.9596	0.0438	0.0764
	5	0.1123	0.8978	0.1333	0.1156
C6	2	→+∞	1.0136	/	0.0975
	5	→+∞	0.9511	/	0.1359

Based on the comparison results of the frequency response curves and the optimal parameters of IDVAs, C1 and C5 exhibit the best H_∞ performance. When the mass ratio is 2%, the peak values of the frequency response curves of C1 and C5 can be reduced to below 80.02% and 80.43% of the traditional TMD, respectively. In addition, the H_∞ performance of C2 is also significantly superior to that of the TMD. The frequency response curve of C3 resides between that of C2 and TMD, resulting in a limited enhancement to the control performance. This indicates that in the inerter subsystem, the spring element is suitable for series connection with the inerter element and damping element. Furthermore, the inerter makes the effective frequency band of IDVAs wider than that of the TMD.

According to the results of parameter optimization, when the mass ratio μ_t is determined, C1, C2, C3, and C5 can obtain the optimal inertance–mass ratio μ_{in} within the set range. However, the optimal inertance–mass ratio μ_{in} of C4 is infinitely close to zero, while the optimal μ_{in} of C6 is close to positive infinity. Therefore, an additional analysis of the H_∞ performance of C4 is performed. The tuned mass ratio μ_t is set as 2%, and the inertance–mass ratio μ_{in} is varied. For each μ_{in}, the genetic algorithm is employed to find the optimal υ_t, υ_{in}, and ξ_{in} of C4. Figure 8a shows that the H_∞ performance under the control of C4 is optimal and equivalent to that of the TMD when μ_{in} is zero. As μ_{in}

gradually increases from 0 to 2, the peak of the frequency response curve continues to increase. This indicates that the inerter does not have a significant effect in C4, and C4 does not enhance the control performance of the TMD.

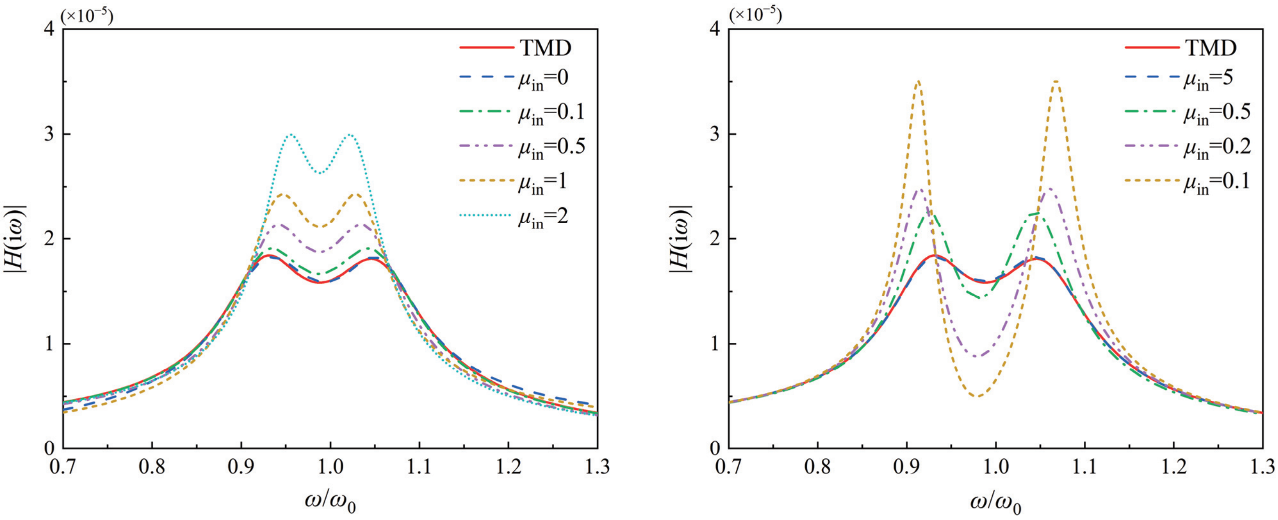

(**a**) (**b**)

Figure 8. Comparison of the frequency response curves by changing μ_{in}: (**a**) C4; (**b**) C6.

Similarly, the H_∞ performance analysis of C6 is performed, as shown in Figure 8b. The frequency response curves of C6 under various inertance–mass ratios μ_{in} are compared when μ_t = 2%. Contrary to C4, the control performance of C6 improves with increasing μ_{in}. The optimal frequency ratios υ_t and the damping ratios ξ_{in} of both C4 and C6 are similar to the optimal parameters of the TMD. By comparing C4, C6, and the traditional TMD, it can be determined that introducing only an inerter element, whether it is in parallel or series, cannot enhance the control performance of the TMD. For the IDVAs connected to one end of the primary structure, it is necessary to introduce another spring element within the inerter subsystem.

The subsequent vibration control analysis and the parametric study are no longer focused on C4 and C6. The variation trends of the optimal parameters of C1~C3 and C5 under different tuned mass ratios μ_t are shown in Figure 9. For an intuitive comparison, the dimensionless coefficients ξ_{in}, μ_{in}, υ_t, and υ_{in} of the IDVAs are calculated into c_{in}, m_{in}, k_t, and k_{in}, which can be used directly for engineering design through Equation (10). The range of the tuned mass ratio μ_t is set from 0.5% to 10%, and nine sets of H_∞ performance optimal parameters of C1, C2, C3, and C5 are further optimized.

As shown in Figure 9a,b, the damping coefficients c_{in} of C1 and C2 are relatively small, but their inertance mass m_{in} is the largest. This demonstrates that in the inerter subsystems of C1 and C2, the connection modes of the elements make the inerter more involved in vibration control. Moreover, these configurations achieve greater energy dissipation of the main structure because of their small damping coefficients. C3 has the largest damping coefficient and a small inertance mass, which indicates that in C3, the inerter element has not participated significantly in vibration control. This phenomenon is also the reason for the control performance of C3 compared to the other three configurations. The tuned mass m_{in} and damping coefficient c_{in} of C5 are relatively large, demonstrating that it achieves energy dissipation enhancement through its large damping by connecting the three elements in series in the inerter subsystem. This mechanism of energy dissipation is different from that of C1 and C2.

As shown in Figure 9c,d, the optimal stiffnesses k_t of the four IDVAs and TMD are relatively close, demonstrating that the introduction of the inerter subsystem has a minor impact on the stiffness of the TMD. In the inerter subsystems, the spring stiffness k_{in} of C3 is relatively large, while the k_{in} values of the remaining three IDVAs are fairly similar and significantly small.

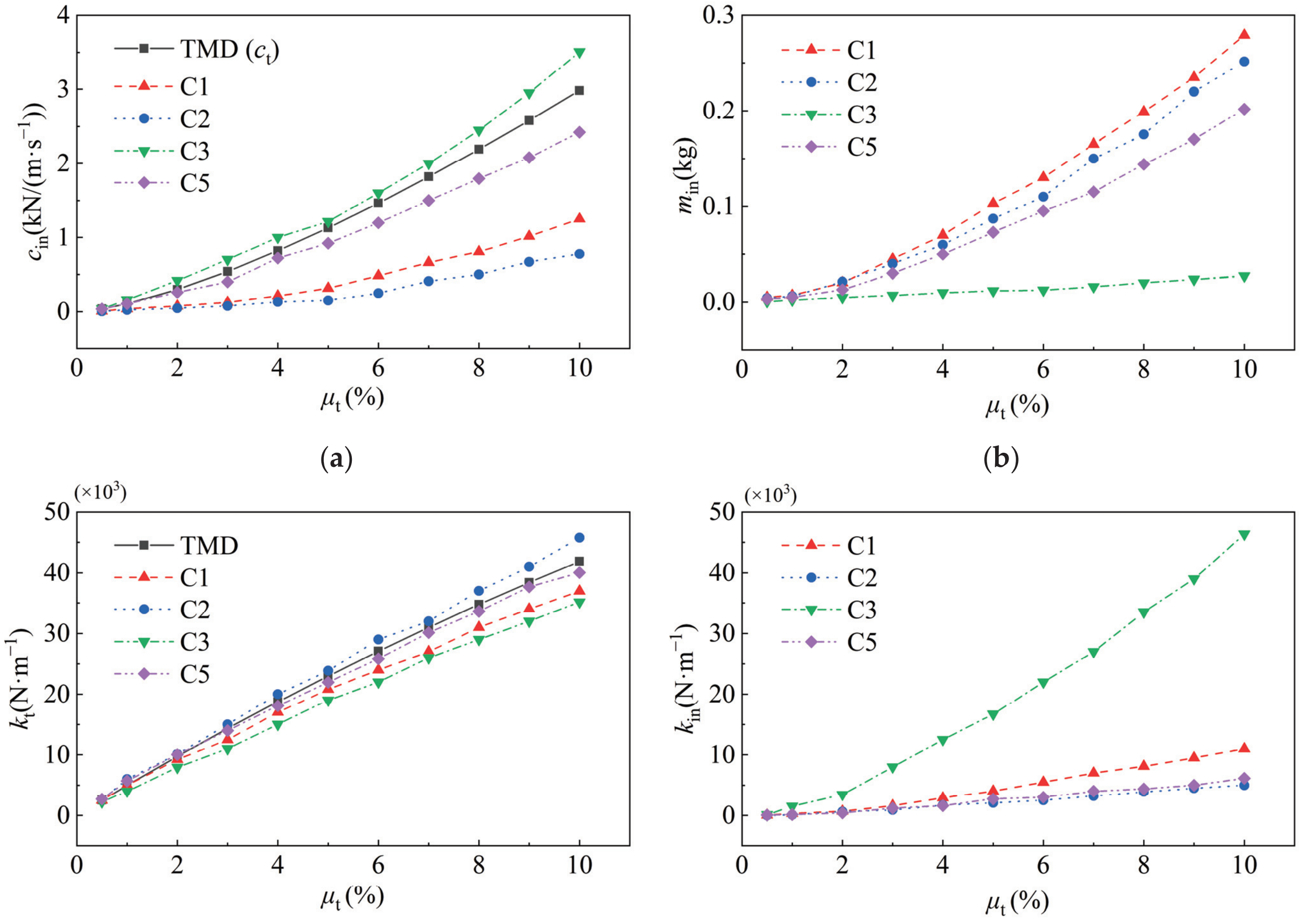

(**a**) (**b**)

(**c**) (**d**)

Figure 9. Variation laws of the optimal parameters of the IDVAs and TMD with the tuned mass ratio: (**a**) Optimal c_{in}; (**b**) Optimal m_{in}; (**c**) Optimal k_t; (**d**) Optimal k_{in}.

3.2. Along-Wind Vibration Control Analysis

The desulfurization tower is in the deltaic plain of the Yangtze River, where the basic wind pressure data corresponding to a 50-year return period are 0.40 kPa at a height of 10 meters. The along-wind load is represented by the Davenport spectrum [45], which is defined by Equation (16).

$$S_u(n) = \frac{2}{3}\frac{\sigma_u^2}{n}\frac{y}{(1+y^2)^{4/3}}, \tag{16}$$

where $S_u(n)$ represents the power spectrum of fluctuating wind; n represents the frequency; u represents the across-wind fluctuating wind speed; y represents the dimensionless frequency, $y = 1200n/\overline{u}_{10}$; $\overline{u}_{10} = 24.9$ m/s, representing the mean wind speed at an elevation of 10 m on the tower, which is derived through basic wind-pressure; and σ_u represents the root mean square of the fluctuating wind speed.

The optimal parameters of C1, C2, C3, and C5 can be obtained under the principle of minimizing the frequency domain displacement response σ_x in the along-wind direction. The IDVAs are then coupled with the numerical model of the tower for a comparative analysis of the control performance in the frequency domain and for verification in the time domain. To compare the control performances of the TMD and different IDVAs, the displacement response mitigation ratio γ is defined as:

$$\gamma = (1 - \sigma_{x,\text{controlled}} / \sigma_{x,\text{original}}) \times 100\%, \tag{17}$$

where $\sigma_{x,\text{original}}$ and $\sigma_{x,\text{controlled}}$ are the root-mean-square displacements of the tower in the frequency domain before and after the installation of the vibration absorber, respectively.

The relationships between the root-mean-square displacement response and the vibration mitigation ratio γ with respect to the mass ratio μ_t for the four typical IDVAs and TMD in application to the desulfurization tower are compared in Figure 10. The control performance of IDVAs on the along-wind vibration response of the desulfurization tower agrees with their H_∞ performance, demonstrating their advantages over the TMD. The control efficiency of the vibration absorbers is progressively improved with the increase in the mass ratio μ_t. However, once μ_t is larger than 5%, the increase rates of the vibration mitigation ratios progressively slow down. Therefore, in the subsequent time-domain vibration control analysis, the tuned mass ratios μ_t are all capped at 5%. The above results show that the H_∞ performance of C5 is superior to that of C1, but the advantage is not obvious. In the response control of the structure, the control ratios of the two configurations are even close. Therefore, subsequent analyses are carried out for both C1 and C5, and other IDVAs are no longer considered.

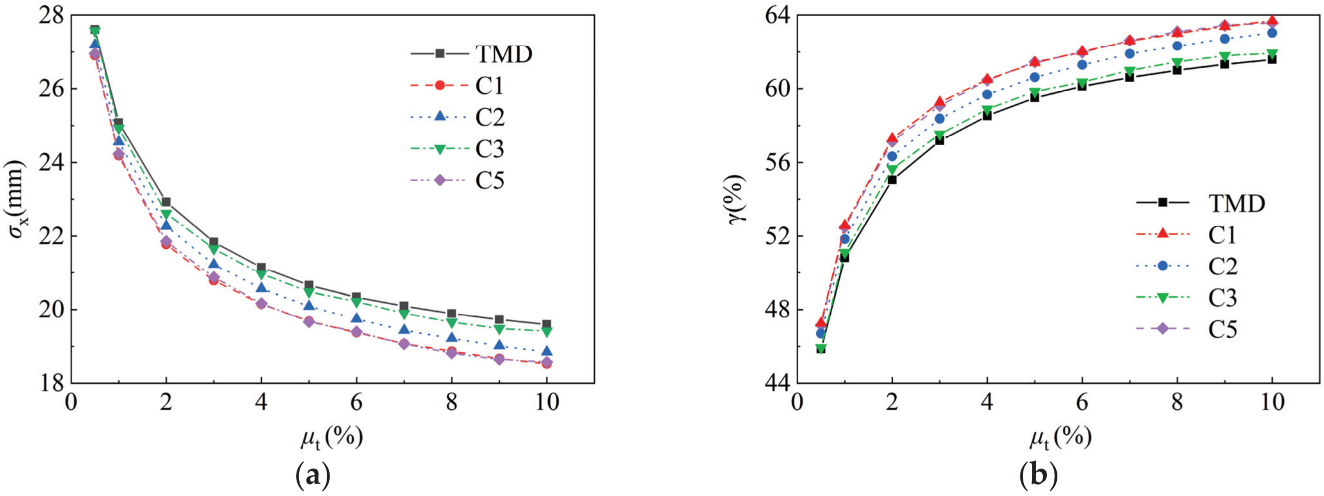

Figure 10. Comparison of along-wind responses in the frequency domain: (**a**) Root-mean-square responses; (**b**) Vibration mitigation ratios.

The simulation of the pulsating wind speed and wind load time is performed in accordance with the Davenport spectrum (Equation (16)) using the harmonic superposition method [13]. The along-wind speed curves of Elements 30, 31, and 32 at the top of the tower are shown in Figure 11, which demonstrate the spatial correlation of wind speed time history curves at these three locations. A comparison between the simulated wind speed spectrum and the target wind speed spectrum on the tower is further conducted in Figure 12, verifying the reliability of the simulated wind load.

A time-domain response analysis of wind-induced vibration in the along-wind direction of the tower is conducted, comparing the displacement and acceleration vibration control performance of C1, C5, and the TMD with μ_t = 2%. Figure 13 presents the time history response curves at the top (Element 32) of the tower. The analysis results also validate that the control performances of C1 and C5 are better than those of the TMD.

In addition to the enhancement of the control performance, the more significant advantage of C1 and C5 is that their auxiliary masses are smaller than that of the TMD. As depicted in the frequency domain analysis in Figure 10, C1 and C5 possess much smaller mass ratios than the TMD under the same displacement response mitigation ratio γ. To further validate the lightweight effects of C1 and C5, the frequency domain response mitigation ratio (γ = 59.21%) of the TMD (μ_t = 5%) is adopted as the objective, and the minimum mass ratios μ_t and other optimal parameters of C1 and C5 are designed again using the genetic algorithm. The results reveal that when μ_t = 3.3%, C1 and C5 can meet the vibration mitigation ratio, yielding an equivalent control performance with TMD when μ_t = 5%. The time domain response curves in Figure 14 corroborate this finding. For the identical control objective, C1 and C5 can achieve a 34% reduction in the auxiliary mass compared to the TMD.

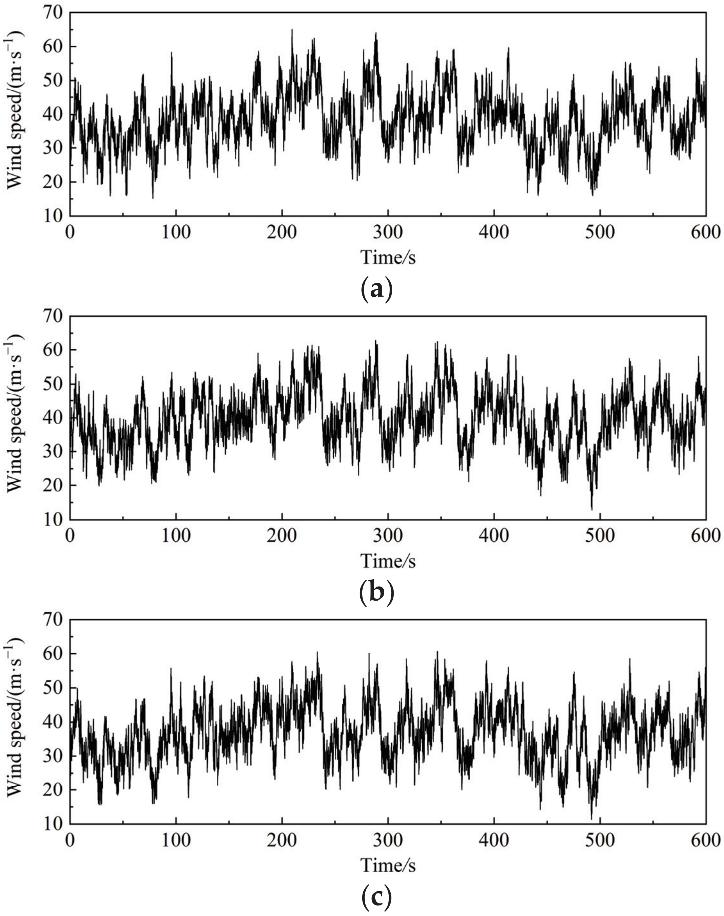

(**a**)

(**b**)

(**c**)

Figure 11. Time history curve of wind speed at the top of the desulfurization tower: (**a**) Element 32; (**b**) Element 31; (**c**) Element 30.

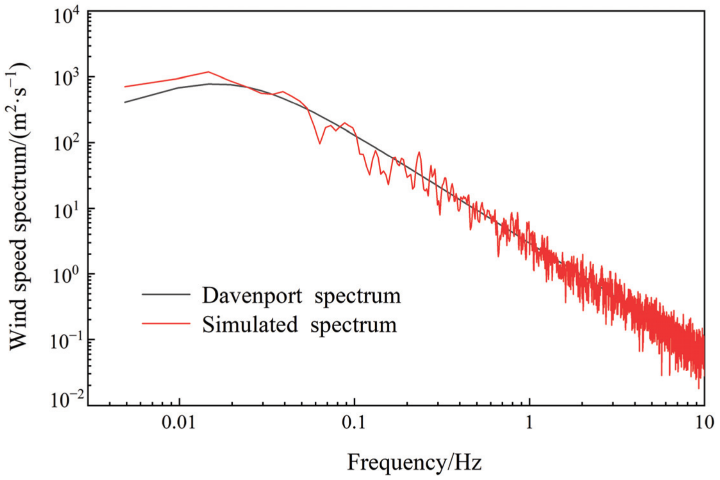

Figure 12. Wind speed spectrum comparison.

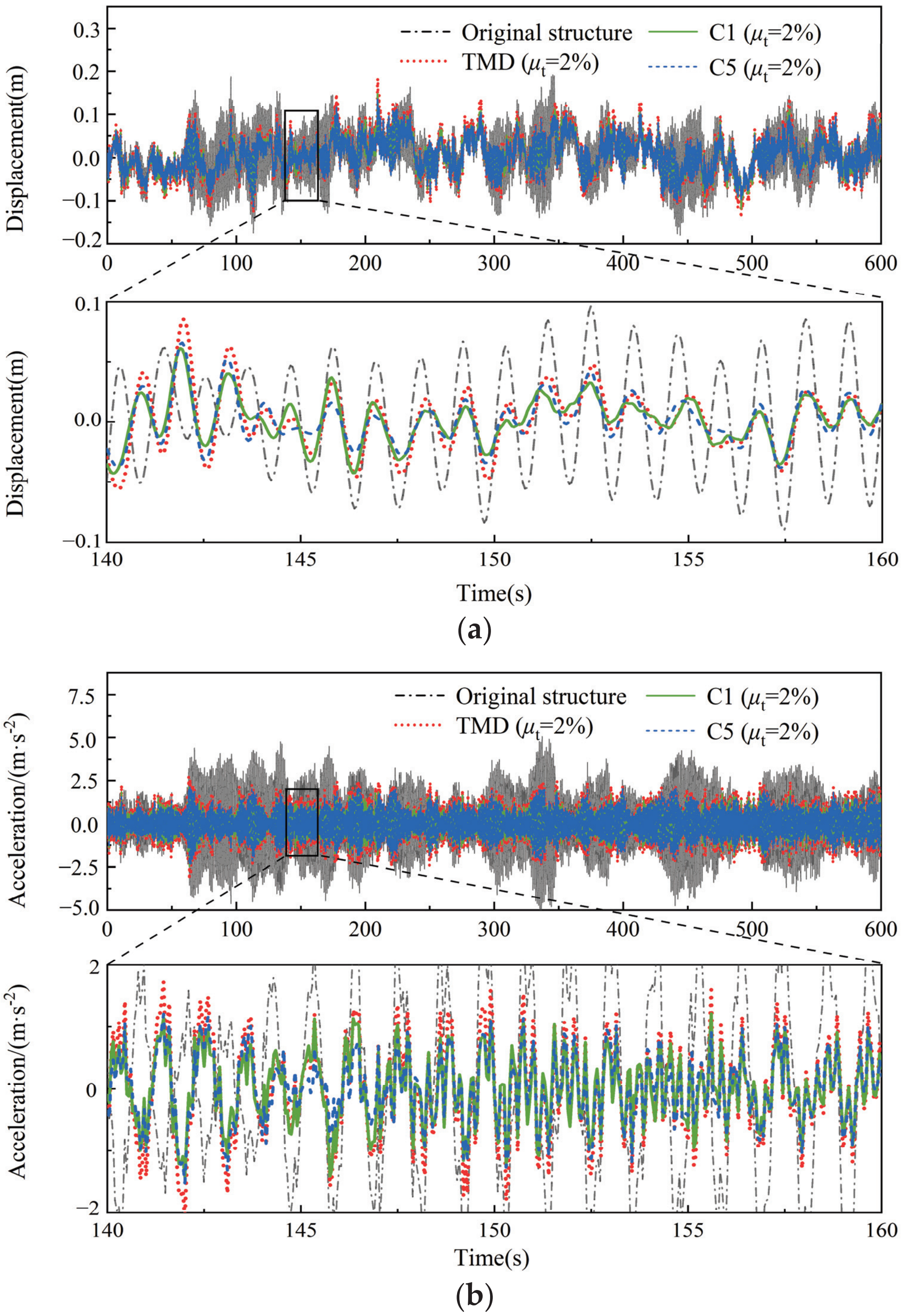

Figure 13. Comparison of the along-wind response of the desulfurization tower (μ_t = 2%): (**a**) Displacement response; (**b**) Acceleration response.

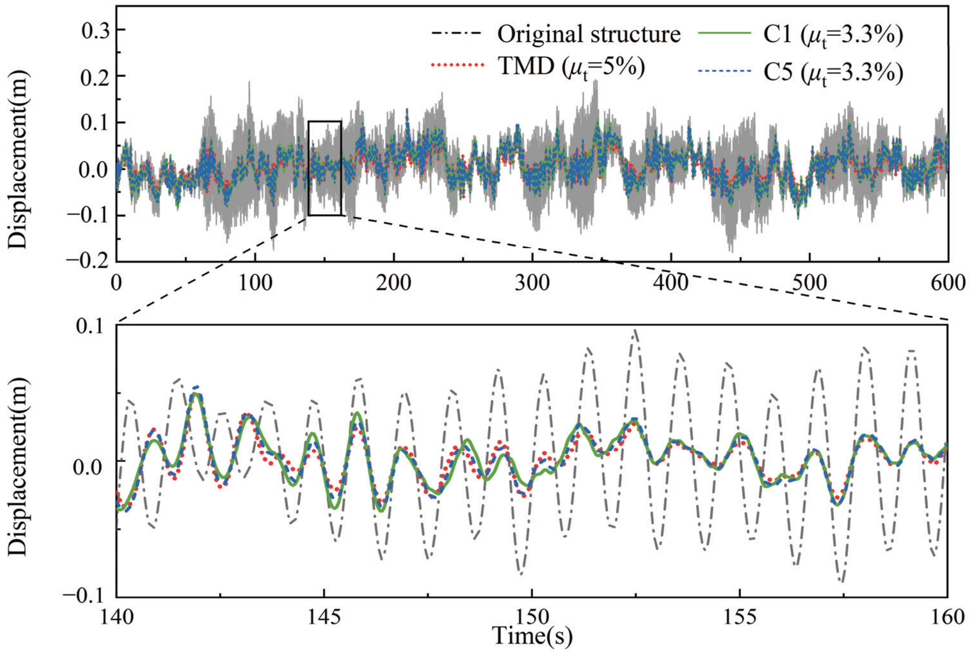

(**a**)

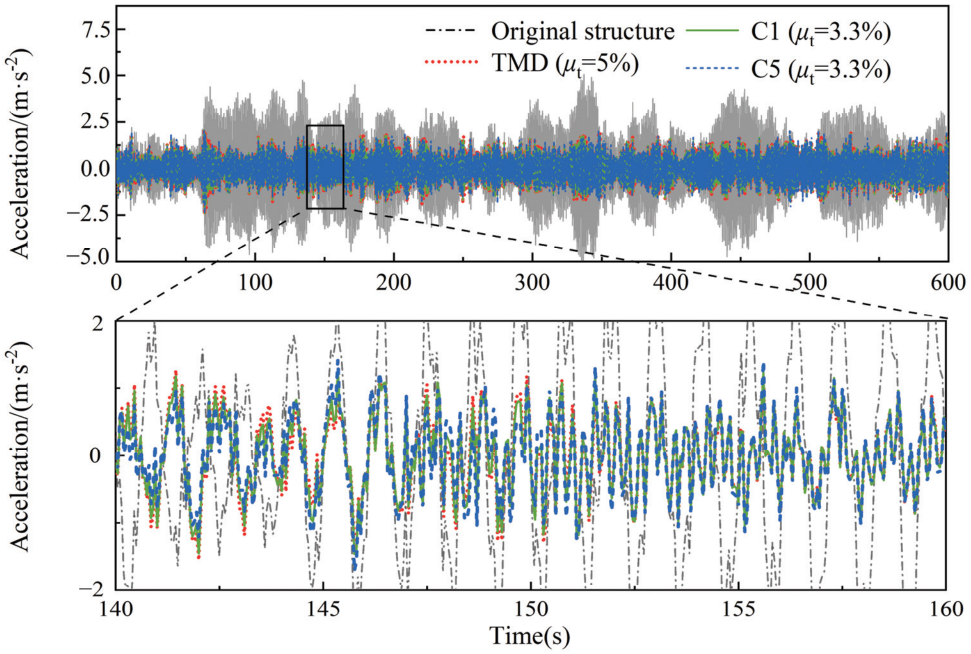

(**b**)

Figure 14. Comparison of the along-wind response of the desulfurization tower (γ = 59.21%): (**a**) Displacement response; (**b**) Acceleration response.

3.3. Across-Wind Vibration Control Analysis

The across-wind loads on high-rise structures are mainly composed of vortex excitation and across-wind turbulence. When vortex-induced resonance occurs, the impact of turbulence on the structural vibration can be neglected [5]; thus, only the vortex force is taken into account as the across-wind load. Taking into account the dimensions of various sections of the desulfurization tower, the Reynolds number, and the critical wind speed parameters, we refer to numerous standards [46–51] for the characteristics and modalities involved in vortex-induced resonance of the desulfurization tower. The detailed analysis process can be found in Appendix B. The results reveal that the upper part of the tower (Section V, Figure 1a) will be subject to vortex-induced resonant forces, leading to severe vortex-induced resonance, at its first-order critical wind speed. When vortex-induced resonance occurs, the wind speed at a height of 10 m is 11.7 m/s. The sinusoidal force proposed by Rumman [52] is applied to the upper section of the tower:

$$F_v(\mathrm{t}) = \frac{1}{2}\rho\overline{v}^2 A\mu_{\mathrm{L}}\sin(2\pi n_{\mathrm{s}}\mathrm{t}), \tag{18}$$

where $F_v(t)$ represents the vortex force; $\overline{v}$ represents the mean wind speed; n_{s} represents the vortex shedding frequency, which is taken as the first-order frequency of the tower; and μ_{L} represents the lift coefficient, which is set at 0.25 for a circular cross-section structure.

Time history response analysis is carried out to evaluate the performance of across-wind vibration control on the tower using a TMD (μ_{t} = 5%). The TMD yields a maximum vibration mitigation ratio of 93.51% for the top of the tower, resulting in a peak displacement response of 0.035 m at the tower top. Starting from 5%, the tuned mass ratios μ_{t} of C1 and C5 are gradually reduced in increments of 0.1%, and other parameters are optimally designed with the H_∞ performance index. When the tuned mass ratios of C1 and C5 are limited to 2.3%, the results of the time domain analysis show that the mitigation ratios for the largest across-wind displacement responses reach 93.46% and 93.52%, respectively. The control performance is approximately equivalent to that of the TMD under μ_{t} = 5%.

A comparative analysis in the time domain of TMD (μ_{t} = 2.3%, μ_{t} = 5%), C1 (μ_{t} = 2.3%), and C5 (μ_{t} = 2.3%) on the vibration control is carried out. Figure 15 shows the displacement responses at the top (Element 32) of the tower with different control devices installed. It verifies that the equivalent C1 and C5 can exhibit a consistent control performance relative to the TMD (μ_{t} = 5%), which is significantly superior to that of the TMD (μ_{t} = 2.3%). This finding indicates that when the tower experiences across-wind vortex-induced resonance, C1 and C5 based on H_∞ optimization exhibit superior vibration control performance. Compared to the along-wind vibration control, C1 and C5 reveal better results regarding the response mitigation ratios and the lightweight effects in the across-wind direction. Compared to the TMD under μ_{t} = 5%, C1 and C5 can reduce the auxiliary mass of the vibration absorber by 54%.

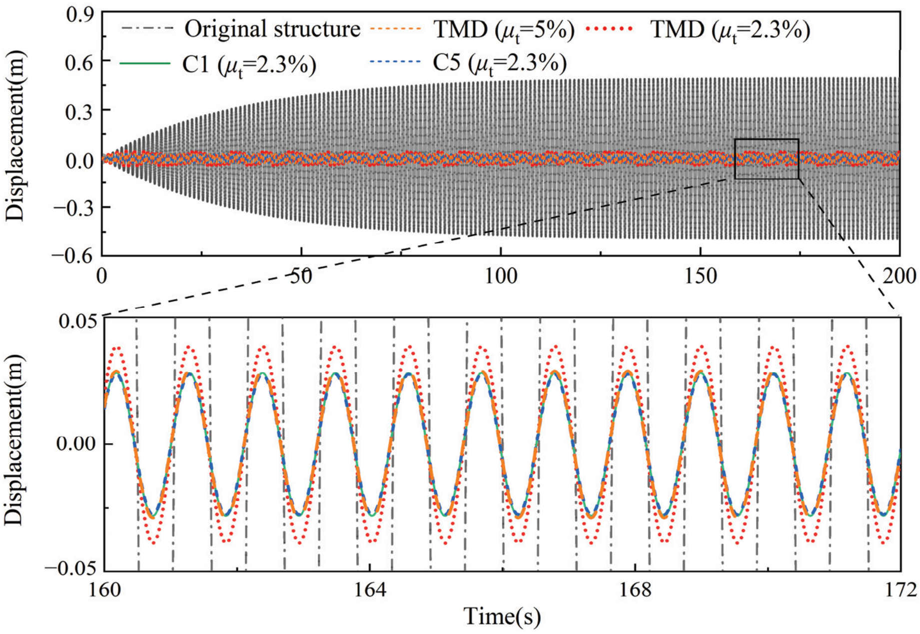

Figure 15. Comparison of the across-wind response of the desulfurization tower.

4. Parametric Study

Both the control devices C1 and C5 demonstrate a remarkable superiority in mitigating the along-wind and across-wind vibrations in the desulfurization tower. To further explore the principle of the control performance enhancement and lightweight effects of the inerter system, Figure 16 presents the hysteresis curves for the whole vibration absorber and damping elements of TMD, C1, and C5, all set at an identical mass ratio (μ_t = 2%). The hysteresis curves of C1 and C5 are observed to closely parallel those of the TMD. However, the hysteresis curve for the damping element in C1 shows a significant difference from those in C5 and the TMD. This difference is attributed to the inerter subsystem in C1, which can effectively amplify the displacement of the vibration absorber, leading to a significant enhanced energy dissipation. Additionally, the hysteresis curve for the damping element in C5 closely mirrors that of the TMD. In combination with the earlier parameter analysis results, it is evident that the inertance–mass ratio of C5 is smaller than that of C1, whereas its damping coefficient aligns closely with that of the TMD. This observation suggests that the energy dissipation mechanism of C5 aligns closely with that of the TMD. The difference is that the inerter element of C5 can increase the apparent mass through a series connection with a damping element, thereby realizing an enhancement in energy dissipation efficiency.

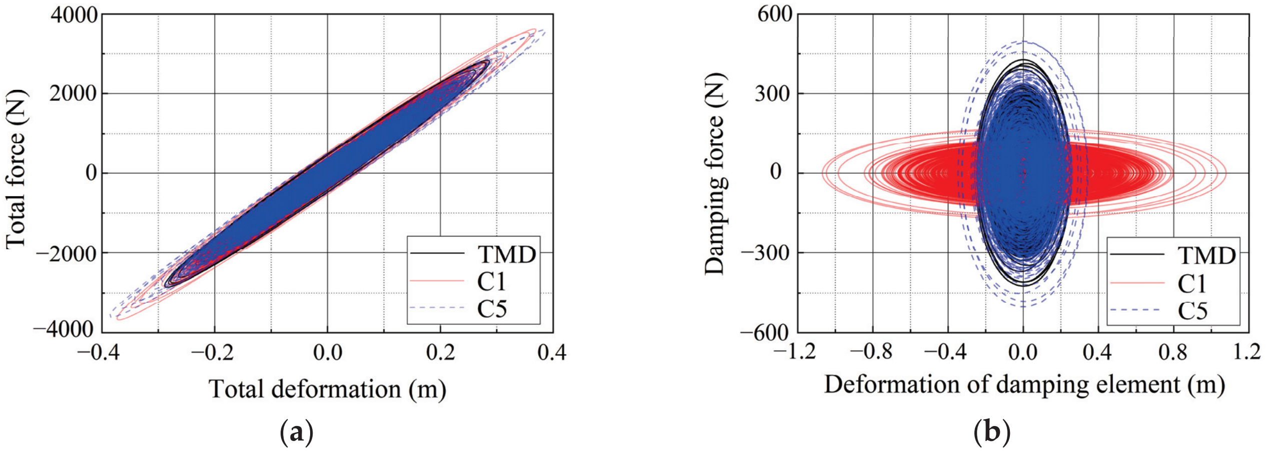

Figure 16. Hysteretic curves of the damping elements of the C1, C5, and TMD configurations: (**a**) Total hysteretic curves; (**b**) Hysteretic curves of the damping element.

Based on the optimized parameters of the control devices C1 and C5, a sensitivity analysis is conducted to evaluate the influence of various parameters including μ_{in}, μ_t, υ_{in}, and ξ_{in} on the displacement response mitigation ratio γ. In both Case 1 and Case 2, as depicted in Figures 17–20, the tuned mass ratios μ_t are set at 2% and 5%, respectively, with other primary optimal parameters referenced from Table 3. Figure 17 illustrates the influences of variations in μ_{in} and μ_t on the γ of C1. A comparative analysis of Figure 17a,b reveals that an increase in μ_t leads to a diminished sensitivity of C1 to changes in μ_{in}. This finding indicates that when m_t of C1 is relatively large, the role of the inerter system in vibration control gradually decreases. The increment of γ progressively decelerates with higher values of μ_t, consistent with the results obtained from Figure 10. Figure 18 presents the influences of υ_{in} and ξ_{in} on γ of C1 with μ_t values set at 2% and 5%, respectively. The outcomes demonstrate that the displacement response mitigation rate of C1 is insensitive to variations in the tuned stiffness, implying strong control robustness. This observation is consistent with the frequency response curve comparisons previously conducted.

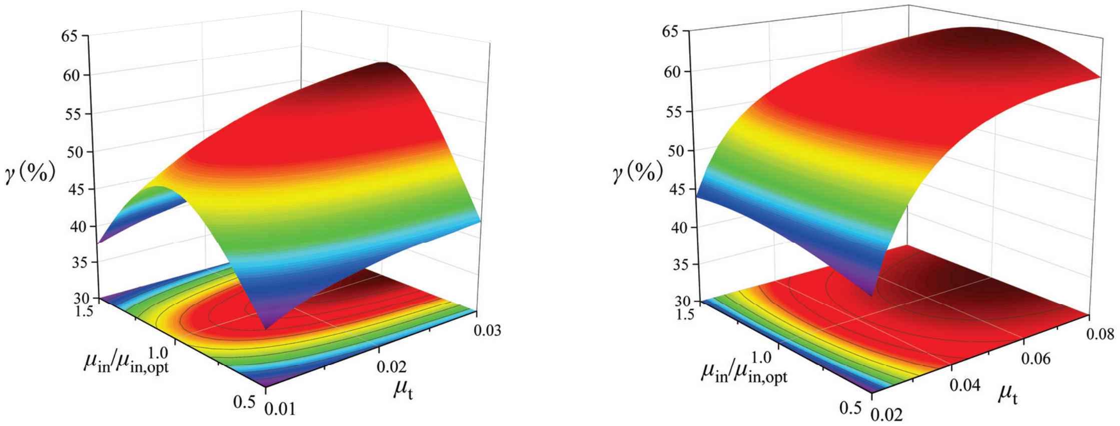

(**a**) (**b**)

Figure 17. Sensitivity analysis of the μ_t and μ_{in} of C1: (**a**) Case 1 (μ_t = 2%); (**b**) Case 2 (μ_t = 5%).

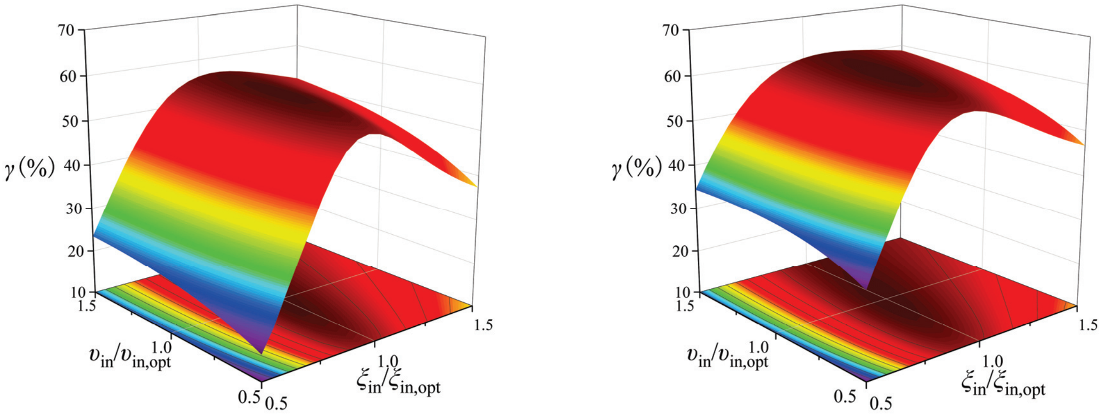

(**a**) (**b**)

Figure 18. Sensitivity analysis of the v_{in} and ξ_{in} of C1: (**a**) Case 1 (μ_t = 2%); (**b**) Case 2 (μ_t = 5%).

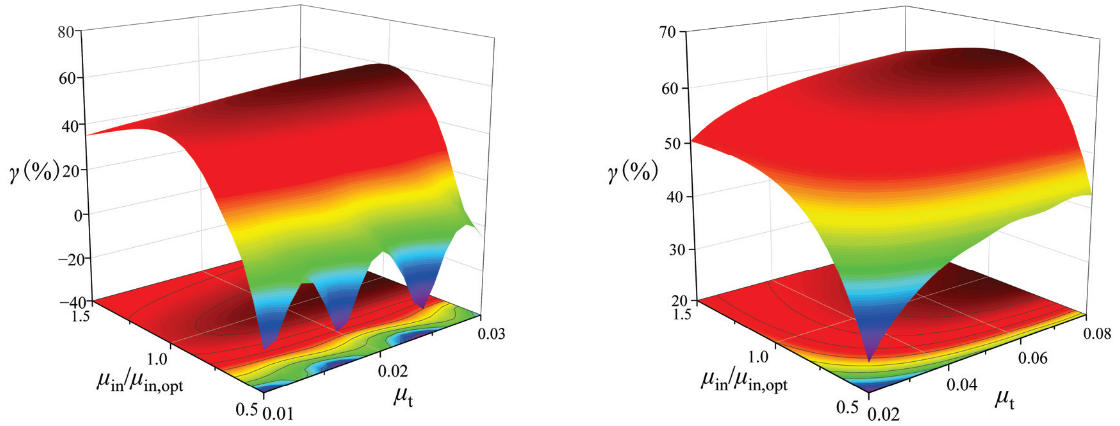

(**a**) (**b**)

Figure 19. Sensitivity analysis of the μ_t and μ_{in} of C5: (**a**) Case 1 (μ_t = 2%); (**b**) Case 2 (μ_t = 5%).

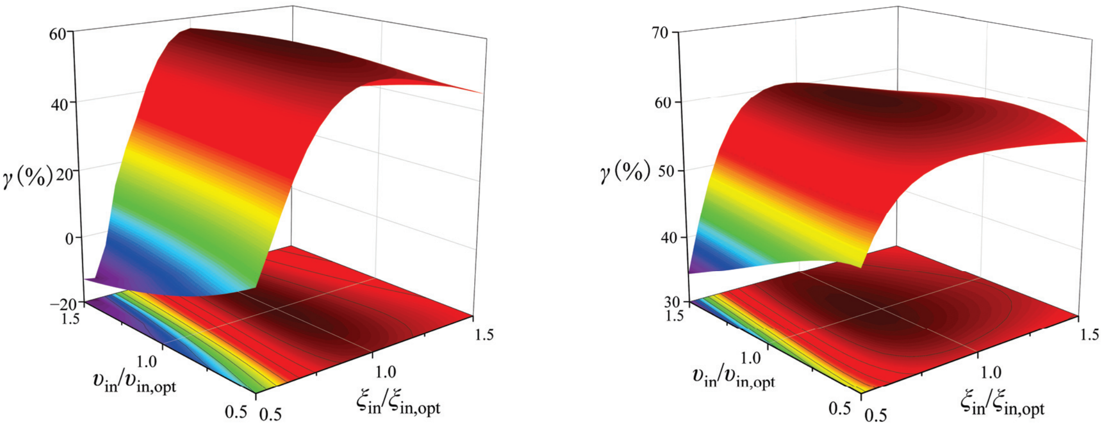

(**a**) (**b**)

Figure 20. Sensitivity analysis of the v_{in} and ξ_{in} of C5: (**a**) Case 1 (μ_t = 2%); (**b**) Case 2 (μ_t = 5%).

As depicted in Figure 19, compared to C1, the control performance of C5 exhibits greater sensitivity to variations in μ_{in}. This finding indicates that when the μ_t of C5 is relatively small, an excessively low μ_{in} may even lead to an adverse effect on the response mitigation capability. When the value of μ_{in} slightly exceeds its optimal value, its impact on the control performance of C5 is relatively insignificant. Figure 20 indicates a similar pattern of C5 and C1 regarding the influence of v_{in} and ξ_{in} on γ. The control performance of the two control devices exhibits greater sensitivity to variations in ξ_{in} but insensitivity to the variations in frequency within a certain range.

5. Conclusions

A study of IDVAs for the wind-induced vibration control of high-rise desulfurization towers is carried out. The transfer functions and displacement responses in the frequency domain of desulfurization tower–IDVA systems are derived and solved. Based on the vibration characteristics of the tower in both the along-wind and across-wind directions, the optimal design strategy for the IDVA parameters is established by using the genetic algorithm. The H_∞ performances and control efficiencies of the traditional TMD and six typical IDVAs are systematically compared. The principles of the energy dissipation enhancement and lightweight effects of the inerter in two optimal IDVAs are further elucidated through parametric analyses. The main conclusions are as follows:

1. C4 and C6, which only introduced an inerter element, cannot enhance the control performance of the TMD. It is necessary to add another spring element. The configurations C1, C2, C3, and C5 with three components—the spring, damper, and inerter—can enhance the H_∞ performance and expand the effective frequency band of the TMD when parallel with the tuning spring component. The configurations C1 and C5, where the spring element is in series with other components, have a relatively close control performance and are significantly superior to other configurations.
2. Under the along-wind loads, the application of C1 and C5 can reduce the tuned mass ratio of the TMD from 5% to below 3.3%, maintaining an equivalent vibration control performance for the tower. Under vortex excitation simulated by sinusoidal excitation in the across-wind direction, C1 and C5 demonstrate an even higher vibration mitigation ratio and greater lightweight effect. With mass ratios of 2.3%, C1 and C5 match the control performance of the TMD with a 5% tuned mass ratio, and their vibration mitigation ratio of the displacement response reaches 93.5%.
3. C1 features a high optimal inertance–mass ratio and a low damping ratio, and it achieves further energy dissipation through an increased displacement response of the damping element by paralleling it with the inerter element. C5 adopts a series connection of the inerter, damping, and stiffness elements, with a larger inertance–

mass ratio and an optimal damping coefficient close to that of the TMD, achieving further energy dissipation through the apparent mass enhancement of the inerter.

Author Contributions: Conceptualization, Y.L. and Z.W.; methodology, Y.L. and Q.Z.; software, Q.Z., Y.X. and J.W.; validation, Z.W., Q.Z. and Y.X.; formal analysis, Y.L.; investigation, Z.W.; resources, Z.W.; data curation, Y.L., Q.Z. and Y.X.; writing—original draft preparation, Y.L.; writing—review and editing, Z.W., Q.Z., Y.X. and J.W.; visualization, Y.L.; supervision, Z.W.; project administration, Z.W. and Q.Z.; funding acquisition, Z.W. All authors have read and agreed to the published version of the manuscript.

Funding: The authors greatly acknowledge the financial support from the National Natural Science Foundation of China (Grant No. 52378300 and 51878274).

Data Availability Statement: Data are contained within the article. Additional supporting data presented in this study are available upon request from the corresponding authors.

Conflicts of Interest: The authors declare no conflicts of interest.

Appendix A

Upon substituting the variables in Equation (10), the mass, damping, and stiffness matrices of the tower–C2 system can be expressed as:

$$\begin{gathered}\boldsymbol{M}_2=\begin{bmatrix}1+\mu_\mathrm{t}\mu_\mathrm{in} & 0 & -\mu_\mathrm{t}\mu_\mathrm{in}\\ 0 & \mu_\mathrm{t} & 0\\ -\mu_\mathrm{t}\mu_\mathrm{in} & 0 & \mu_\mathrm{t}\mu_\mathrm{in}\end{bmatrix};\ \boldsymbol{C}_2=\begin{bmatrix}2\xi_0\omega_0 & 0 & 0\\ 0 & 2\xi_\mathrm{in}\mu_\mathrm{t}v_\mathrm{t}\omega_0 & -2\xi_\mathrm{in}\mu_\mathrm{t}v_\mathrm{t}\omega_0\\ 0 & -2\xi_\mathrm{in}\mu_\mathrm{t}v_\mathrm{t}\omega_0 & 2\xi_\mathrm{in}\mu_\mathrm{t}v_\mathrm{t}\omega_0\end{bmatrix};\\ \boldsymbol{K}_2=\begin{bmatrix}\omega_0^2+\mu_\mathrm{t}(\omega_0v_\mathrm{t})^2 & -\mu_\mathrm{t}(\omega_0v_\mathrm{t})^2 & 0\\ -\mu_\mathrm{t}(\omega_0v_\mathrm{t})^2 & \mu_\mathrm{t}(\omega_0v_\mathrm{t})^2+v_\mathrm{in}\mu_\mathrm{t}(\omega_0v_\mathrm{t})^2 & -v_\mathrm{in}\mu_\mathrm{t}(\omega_0v_\mathrm{t})^2\\ 0 & -v_\mathrm{in}\mu_\mathrm{t}(\omega_0v_\mathrm{t})^2 & v_\mathrm{in}\mu_\mathrm{t}(\omega_0v_\mathrm{t})^2\end{bmatrix}\end{gathered}\tag{A1}$$

The matrices of the tower–C3 system can be expressed as:

$$\begin{gathered}\boldsymbol{M}_3=\begin{bmatrix}1 & 0 & 0\\ 0 & \mu_\mathrm{t}+\mu_\mathrm{t}\mu_\mathrm{in} & -\mu_\mathrm{t}\mu_\mathrm{in}\\ 0 & -\mu_\mathrm{t}\mu_\mathrm{in} & \mu_\mathrm{t}\mu_\mathrm{in}\end{bmatrix};\ \boldsymbol{C}_3=\begin{bmatrix}2\xi_0\omega_0+2\xi_\mathrm{in}\mu_\mathrm{t}v_\mathrm{t}\omega_0 & 0 & -2\xi_\mathrm{in}\mu_\mathrm{t}v_\mathrm{t}\omega_0\\ 0 & 0 & 0\\ -2\xi_\mathrm{in}\mu_\mathrm{t}v_\mathrm{t}\omega_0 & 0 & 2\xi_\mathrm{in}\mu_\mathrm{t}v_\mathrm{t}\omega_0\end{bmatrix};\\ \boldsymbol{K}_3=\begin{bmatrix}\omega_0^2+\mu_\mathrm{t}(\omega_0v_\mathrm{t})^2 & -\mu_\mathrm{t}(\omega_0v_\mathrm{t})^2 & 0\\ -\mu_\mathrm{t}(\omega_0v_\mathrm{t})^2 & \mu_\mathrm{t}(\omega_0v_\mathrm{t})^2+v_\mathrm{in}\mu_\mathrm{t}(\omega_0v_\mathrm{t})^2 & -v_\mathrm{in}\mu_\mathrm{t}(\omega_0v_\mathrm{t})^2\\ 0 & -v_\mathrm{in}\mu_\mathrm{t}(\omega_0v_\mathrm{t})^2 & v_\mathrm{in}\mu_\mathrm{t}(\omega_0v_\mathrm{t})^2\end{bmatrix}\end{gathered}\tag{A2}$$

The matrices of the tower–C4 system can be expressed as:

$$\begin{gathered}\boldsymbol{M}_4=\begin{bmatrix}1+\mu_\mathrm{t}\mu_\mathrm{in} & -\mu_\mathrm{t}\mu_\mathrm{in}\\ -\mu_\mathrm{t}\mu_\mathrm{in} & \mu_\mathrm{t}\mu_\mathrm{in}\end{bmatrix};\ \boldsymbol{C}_4=\begin{bmatrix}2\xi_0\omega_0+2\xi_\mathrm{in}\mu_\mathrm{t}v_\mathrm{t}\omega_0 & -2\xi_\mathrm{in}\mu_\mathrm{t}v_\mathrm{t}\omega_0\\ -2\xi_\mathrm{in}\mu_\mathrm{t}v_\mathrm{t}\omega_0 & 2\xi_\mathrm{in}\mu_\mathrm{t}v_\mathrm{t}\omega_0\end{bmatrix};\\ \boldsymbol{K}_4=\begin{bmatrix}\omega_0^2+\mu_\mathrm{t}(\omega_0v_\mathrm{t})^2 & -\mu_\mathrm{t}(\omega_0v_\mathrm{t})^2\\ -\mu_\mathrm{t}(\omega_0v_\mathrm{t})^2 & \mu_\mathrm{t}(\omega_0v_\mathrm{t})^2\end{bmatrix}\end{gathered}\tag{A3}$$

The matrices of the tower–C5 system can be expressed as:

$$\begin{gathered}\boldsymbol{M}_5=\begin{bmatrix}1 & 0 & 0 & 0\\ 0 & \mu_\mathrm{t} & 0 & 0\\ 0 & 0 & \mu_\mathrm{t}\mu_\mathrm{in} & -\mu_\mathrm{t}\mu_\mathrm{in}\\ 0 & 0 & -\mu_\mathrm{t}\mu_\mathrm{in} & \mu_\mathrm{t}\mu_\mathrm{in}\end{bmatrix};\ \boldsymbol{C}_5=\begin{bmatrix}2\xi_0\omega_0 & 0 & 0 & 0\\ 0 & 2\xi_\mathrm{in}\mu_\mathrm{t}v_\mathrm{t}\omega_0 & -2\xi_\mathrm{in}\mu_\mathrm{t}v_\mathrm{t}\omega_0 & 0\\ 0 & -2\xi_\mathrm{in}\mu_\mathrm{t}v_\mathrm{t}\omega_0 & 2\xi_\mathrm{in}\mu_\mathrm{t}v_\mathrm{t}\omega_0 & 0\\ 0 & 0 & 0 & 0\end{bmatrix};\\ \boldsymbol{K}_5=\begin{bmatrix}\omega_0^2+\mu_\mathrm{t}(\omega_0v_\mathrm{t})^2+v_\mathrm{in}\mu_\mathrm{t}(\omega_0v_\mathrm{t})^2 & -\mu_\mathrm{t}(\omega_0v_\mathrm{t})^2 & 0 & -v_\mathrm{in}\mu_\mathrm{t}(\omega_0v_\mathrm{t})^2\\ -\mu_\mathrm{t}(\omega_0v_\mathrm{t})^2 & \mu_\mathrm{t}(\omega_0v_\mathrm{t})^2 & 0 & 0\\ 0 & 0 & 0 & 0\\ -v_\mathrm{in}\mu_\mathrm{t}(\omega_0v_\mathrm{t})^2 & 0 & 0 & v_\mathrm{in}\mu_\mathrm{t}(\omega_0v_\mathrm{t})^2\end{bmatrix}\end{gathered}\tag{A4}$$

The matrices of the tower–C6 system can be expressed as:

$$\begin{aligned}
&\boldsymbol{M}_6=\begin{bmatrix} 1 & 0 & 0 \\ 0 & \mu_{\mathrm{t}}+\mu_{\mathrm{t}}\mu_{\mathrm{in}} & -\mu_{\mathrm{t}}\mu_{\mathrm{in}} \\ 0 & -\mu_{\mathrm{t}}\mu_{\mathrm{in}} & \mu_{\mathrm{t}}\mu_{\mathrm{in}} \end{bmatrix};\ \boldsymbol{C}_6=\begin{bmatrix} 2\xi_0\omega_0+2\xi_{\mathrm{in}}\mu_{\mathrm{t}}v_{\mathrm{t}}\omega_0 & 0 & -2\xi_{\mathrm{in}}\mu_{\mathrm{t}}v_{\mathrm{t}}\omega_0 \\ 0 & 0 & 0 \\ -2\xi_{\mathrm{in}}\mu_{\mathrm{t}}v_{\mathrm{t}}\omega_0 & 0 & -2\xi_{\mathrm{in}}\mu_{\mathrm{t}}v_{\mathrm{t}}\omega_0 \end{bmatrix}; \\
&\boldsymbol{K}_6=\begin{bmatrix} \omega_0^2+\mu_{\mathrm{t}}(\omega_0 v_{\mathrm{t}})^2 & -\mu_{\mathrm{t}}(\omega_0 v_{\mathrm{t}})^2 & 0 \\ -\mu_{\mathrm{t}}(\omega_0 v_{\mathrm{t}})^2 & \mu_{\mathrm{t}}(\omega_0 v_{\mathrm{t}})^2 & 0 \\ 0 & 0 & 0 \end{bmatrix}
\end{aligned} \tag{A5}$$

Appendix B

For the high-rise cylindrical desulfurization tower, it is necessary to determine their vortex-induced vibration characteristics by combining the Reynolds number, the critical wind speed, and the Strouhal number. The Reynolds number is calculated by the following equation:

$$Re = 69000vD, \tag{A6}$$

where v represents the wind speed, which can be defined as the critical wind speed of the structure; and D is the width of the structure. It should be noted that the tower has variable cross sections, leading to different D values and consequently diverse Re values.

When $Re \geq 3.5 \times 10^6$, the vortex shedding frequency is close to the structural natural frequency, indicating the potential cross-critical region strong wind resonance. In design, it is necessary to verify and check this index, and it should consider not only the first-order vibration mode of the structure but also the verification of the first 2–4 modes.

The critical wind speed of the desulfurization tower is calculated as:

$$v_{\mathrm{cr}} = f_{\mathrm{i}}D/S\mathrm{t}, \tag{A7}$$

where v_{cr} illustrates the i-th order critical wind speed of the tower; f_{i} represents the i-th order frequency of the structure; St represents the Strouhal number; and the St for the circular cylinder structure can be set as 0.2.

To clarify the across-wind vibration characteristics of the tower and prevent underestimation of the wind-induced response, resonance verification was deemed based on these calculations above and the structural dimensions of the tower. The verification results, for different codes, are shown in Table A1. Given the relative brevity of Section II and Section IV of the tower, verifications were principally conducted on Sections I, III, and V—the bottom, middle, and top of the tower, respectively.

Table A1. Across-wind resonance checking conditions.

Mode	Frequency (Beam199/Solid95)	Period (Beam188/Solid95)
Chinese codes [47,48]	$v_{\mathrm{cr}} < 1.2v_H$, and $Re \geq 3 \times 10^6$	Only Re and v_{cr} of Section III meet the requirements
Europe codes [49]	$v_{\mathrm{cr}} \leq 1.25v_H$, and $H/D > 6$	Only Section V needs to be calculated
Japanese codes [50]	$v_H/(f_1 \cdot D_{\mathrm{m}}) \geq 4.2$, and $H/D_m \geq 7$	Only Section V needs to be calculated
American codes [51]	$v_{\mathrm{cr}} < 1.2v_{Z\mathrm{cr}}$	Section III and Section V need to be calculated

Note: v_H is the wind speed at the top of each section of the structure; H and D are the height and width of each section of the structure, respectively; D_{m} is the cross-sectional diameter at 2/3 of the total height of the structure; $v_{Z\mathrm{cr}}$ is the wind speed at height Zcr, where Zcr = 0.5(z_1 + z_2), and z_1 and z_2 are the upper and lower height limits where the change in cross-sectional diameter is less than 30%, respectively. When the cross-sectional variation within the top 1/3 height range of the structure is less than 10%, Zcr can also be taken as 5/6 of the total height. To maintain clarity and consistency, symbols in different codes have been simplified and unified.

When the wind speed reaches the first-order critical wind speed, there is a potential for vortex-induced resonance in the upper part (Section V) of the tower. When the wind speed reaches the second-order critical wind speed, there is a potential for vortex-induced resonance in the middle part (Section III) of the tower. It is important to note that the critical wind speeds of higher orders exceed the maximum wind speed that may appear in the environment where the desulfurization tower is located, negating the need for further verification in these cases.

In addition, as shown in Table 1, a difference is observed between the results derived from Chinese codes and the other four codes. According to the Chinese codes, only the middle part of the tower necessitates calculation for vortex-induced resonance. For the upper part, the Reynolds number does not meet the verification conditions set by Chinese codes. Ignoring the impact of across-wind resonance in the upper part could potentially lead to wind-induced structural damage. Therefore, we conducted calculations for two different scenarios where Section V and Section III of the tower are subjected to vortex-induced forces.

In the theory of across-wind vibration analysis for high-rise cylindrical structures, the wind speed range of v_{cr}~1.3 v_{cr} along the height of the structure is usually defined as the lock-in zone. Considering a rather unfavorable situation, the two scenarios each designated Section V and Section III of the tower as the lock-in zone, with basic wind speeds at a height of 10 m set as v_{10} = 11.7 m/s and 24.9 m/s, respectively. In addition to the wake vortices in the lock-in zone, the response of the structure to crosswinds is also influenced by the incoming turbulent flow. Both influences on the tower were considered and calculated cumulatively. The schematic wind loads for the structure to crosswinds in both scenarios are shown in Figure A1.

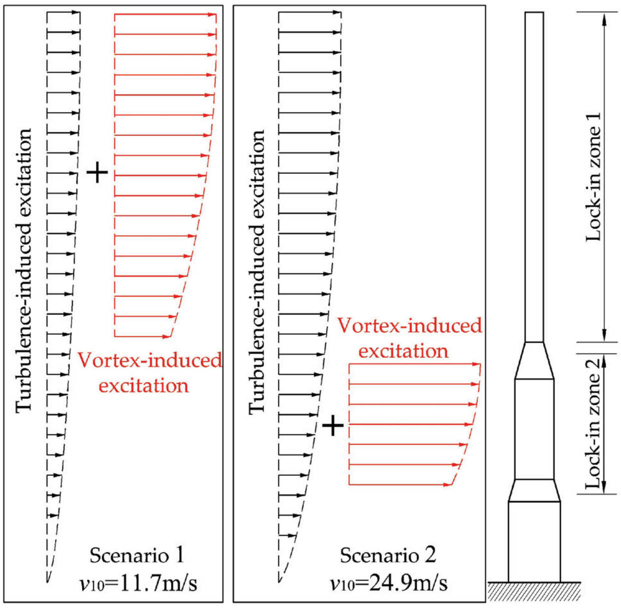

Figure A1. Across-wind load distribution.

For the vortex-induced forces of the desulfurization tower, the impact in non-lock-in zones is far less than that in lock-in zones, hence the sinusoidal force proposed by Rumman [52] is applied to the upper section of the tower:

$$F_v(\mathrm{t}) = \frac{1}{2}\rho\overline{v}^2 A\mu_{\mathrm{L}}\sin(2\pi n_{\mathrm{s}}\mathrm{t}), \tag{A8}$$

where $Fv(t)$ represents the vortex-induced excitation for each element; v is the average wind speed of that element; n_{s} represents the vortex shedding frequency, taken here as the first-order frequency of the tower; and μ_L is the lift coefficient, which for cylindrical structures is taken as 0.25.

The across-wind turbulence-induced excitation of the desulfurization tower can be analyzed under the theory of random vibrations. By opting for an across-wind pulsating wind power spectrum [53] as in Equation (A9), the simulation of the across pulsating wind speed process and the construction of the load vector are conducted.

$$S_v(n) = 3.1\frac{\sigma_v^2}{n}\frac{x}{(1+9.5x)^{5/3}}, \tag{A9}$$

where $Sv(n)$ is the power spectrum of the fluctuating wind in the across-wind direction; $x = n \cdot z/\overline{v}(z)$ is the dimensionless frequency; σ_v represents the root mean square of the fluctuating wind speed.

The wind-induced displacement and acceleration responses at the top of the structure in the across-wind direction are presented in Figure A2. The impact of turbulence-induced excitation is more significant in Scenario 2 due to the greater overall wind speed. However, given that the middle section accounts for less than 1/4 of the full height of the structure, even with the vortex-induced excitation, the overall response is still visibly smaller than that in Scenario 2. Therefore, the primary focus for across-wind vibration of the tower should be the scenario where the upper section is in the lock-in zone. Moreover, a comparison of the response curves from working Scenario 1 indicates that the sinusoidal force representing vortex-induced excitation plays a more dominant role over turbulence-induced excitation.

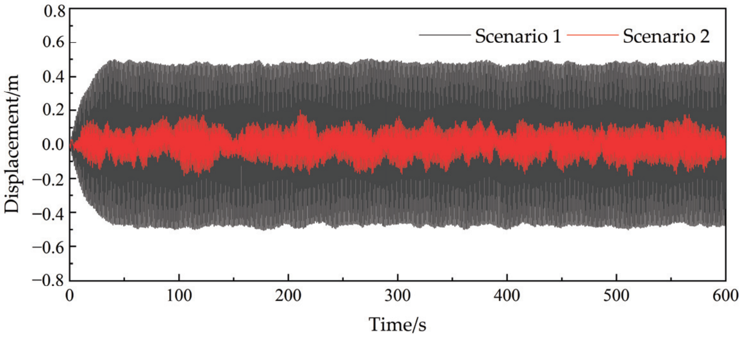

Figure A2. Displacement response in across-wind direction at the top of the tower.

From the comprehensive analysis above, it is evident that the across-wind vibration response of the desulfurization tower is predominantly due to first-mode vortex-induced resonance. Therefore, when calculating the vortex-induced vibration caused by across-wind, only the vortex-induced resonant force applied to the upper section of the structure is taken into account.

References

1. Kareem, A. Emerging frontiers in wind engineering: Computing, stochastics, machine learning and beyond. *J. Wind Eng. Ind. Aerodyn.* **2020**, *206*, 104320. [CrossRef]
2. Lorenzo, I.F.; Elena, B.C.; Rodríguez, P.M.; Parnás, V.B.E. Dynamic analysis of self-supported tower under hurricane wind conditions. *J. Wind Eng. Ind. Aerodyn.* **2020**, *197*, 104078. [CrossRef]
3. Lupi, F.; Niemann, H.J.; Höffer, R. A novel spectral method for cross-wind vibrations: Application to 27 full-scale chimneys. *J. Wind Eng. Ind. Aerodyn.* **2017**, *171*, 353–365. [CrossRef]
4. Han, Y.; Zhou, X.; Wang, L.; Cai, C.S.; Yan, H.; Hu, P. Experimental investigation of the vortex-induced vibration of tapered light poles. *J. Wind Eng. Ind. Aerodyn.* **2021**, *211*, 104555. [CrossRef]
5. Arul, M.; Kareem, A.; Kwon, K.D. Identification of vortex-induced vibration of tall building pinnacle using cluster analysis for fatigue evaluation: Application to Burj Khalifa. *J. Struct. Eng-ASCE* **2020**, *146*, 04020234. [CrossRef]
6. Kavyashree, B.G.; Patil, S.; Rao, V.S. Review on vibration control in tall buildings: From the perspective of devices and applications. *Int. J. Dyn. Control* **2020**, *9*, 1316–1331. [CrossRef]
7. Jafari, M.; Alipour, A. Methodologies to mitigate wind-induced vibration of tall buildings: A state-of-the-art review. *J. Build. Eng.* **2020**, *33*, 101582. [CrossRef]

8. Yang, F.; Sedaghati, R.; Esmailzadeh, E. Vibration suppression of structures using tuned mass damper technology: A state-of-the-art review. *J. Vib. Control* **2022**, *28*, 812–836. [CrossRef]
9. Den Hartog, J.P. *Mechanical Vibrations*; Courier Corporation: New York, NY, USA, 1985.
10. Colherinhas, G.B.; Morais, M.V.G.; Machado, M.R. Spectral model of offshore wind turbines and vibration control by pendulum tuned mass dampers. *Int. J. Str. Stab. Dyn.* **2022**, *22*, 2250053. [CrossRef]
11. Elias, S.; Matsagar, V. Research developments in vibration control of structures using passive tuned mass dampers. *Ann. Rev. Control* **2017**, *44*, 129–156. [CrossRef]
12. Brownjohn, J.M.W.; Carden, E.P.; Goddard, C.R.; Oudin, G. Real-time performance monitoring of tuned mass damper system for a 183 m reinforced concrete chimney. *J. Wind Eng. Ind. Aerod.* **2010**, *98*, 169–179. [CrossRef]
13. Elias, S.; Matsagar, V.; Datta, T.K. Along-wind response control of chimneys with distributed multiple tuned mass dampers. *Struct. Control Health Monit.* **2019**, *26*, e2275. [CrossRef]
14. Xiang, Y.; Tan, P.; He, H.; Yao, H.; Zheng, X. Seismic optimal design of hysteretic damping tuned mass damper (HD-TMD) for acceleration response control. *Acta Mech.* 2023. *published online*. [CrossRef]
15. Franco, L.G.T.; Morita, N.F.; Fong, H.F.A.; Carbajal, F.B.; Lopez, A.E.D.; Arreola, D.E.R. Oscillation attenuation in a building-like structure by using a flexible vibration absorber. *Mathematics* **2022**, *10*, 289. [CrossRef]
16. Nakano, Y.; Kishi, T.; Takahara, H. Experimental study on application of tuned mass dampers for chatter in turning of a thin-walled cylinder. *Appl. Sci.* **2021**, *11*, 12070. [CrossRef]
17. Bekdas, G.; Nigdeli, S.M. Mass ratio factor for optimum tuned mass damper strategies. *Int. J. Mech. Sci.* **2013**, *71*, 68–84. [CrossRef]
18. Lu, X.; Chen, J. Mitigation of wind-induced response of Shanghai Center Tower by tuned mass damper. *Struct. Des. Tall Spec. Build.* **2011**, *20*, 435–452. [CrossRef]
19. Xu, K.; Bi, K.; Ge, Y.; Zhao, L.; Han, Q.; Du, X. Performance evaluation of inerter-based dampers for vortex-induced vibration control of long-span bridges: A comparative study. *Struct. Control Health Monit.* **2020**, *27*, e2529. [CrossRef]
20. Smith, M.C. Synthesis of mechanical networks: The inerter. *IEEE Trans. Autom. Control* **2002**, *47*, 1648–1662. [CrossRef]
21. Wang, F.; Hong, M.; Chen, C. Building suspensions with inerters. *Proc. Inst. Mech. Eng. Part C J. Mech. Eng. Sci.* **2010**, *224*, 1605–1616. [CrossRef]
22. Lazar, I.F.; Neild, S.A.; Wagg, D.J. Using an inerter-based device for structural vibration suppression. *Earthq. Eng. Struct. Dyn.* **2014**, *43*, 1129–1147. [CrossRef]
23. Ma, R.; Bi, K.; Hao, H. Inerter-based structural vibration control: A state-of-the-art review. *Eng. Struct.* **2021**, *243*, 112655. [CrossRef]
24. Xu, T.; Li, Y.; Lai, T.; Zheng, J. A simplified design method of tuned inerter damper for damped civil structures: Theory, validation, and application. *Struct. Control Health Monit.* **2021**, *28*, e2798. [CrossRef]
25. Zhang, R.; Zhao, Z.; Pan, C.; Ikago, K.; Xue, S. Damping enhancement principle of inerter system. *Struct. Control Health Monit.* **2020**, *27*, e2523. [CrossRef]
26. Alotta, G.; Failla, G. Improved inerter-based vibration absorbers. *Int. J. Mech. Sci.* **2021**, *192*, 106087. [CrossRef]
27. Liang, Q.; Li, L.; Yang, Q. Seismic analysis of the tuned-inerter-damper enhanced mega-sub structure system. *Struct. Control Health Monit.* **2020**, *28*, e2568. [CrossRef]
28. Chen, H.; Bi, K.; Liu, Y.; Tan, P. Performance evaluation of multiple tuned inerter-based dampers for seismic induced structural vibration control. *Struct. Control Health Monit.* **2022**, *29*, e2860. [CrossRef]
29. Marian, L.; Giaralis, A. Optimal design of a novel tuned mass-damper–inerter (TMDI) passive vibration control configuration for stochastically support-excited structural systems. *Probabilist Eng. Mech.* **2014**, *38*, 156–164. [CrossRef]
30. Wang, Q.; Qiao, H.; Li, W.; You, Y.; Fan, Z.; Tiwari, N. Parametric optimization of an inerter-based vibration absorber for wind-induced vibration mitigation of a tall building. *Wind Struct.* **2020**, *31*, 241–253.
31. Ikago, K.; Sugimura, Y.; Saito, K.; Inoue, N. Modal response characteristics of a multiple degree-of-freedom structure incorporated with tuned viscous mass dampers. *J. Asian. Archit. Build.* **2012**, *11*, 375–382. [CrossRef]
32. Garrido, H.; Curadelli, O.; Ambrosini, D. Improvement of tuned mass damper by using rotational inertia through tuned viscous mass damper. *Eng. Struct.* **2013**, *56*, 2149–2153. [CrossRef]
33. Zhang, Z.; Høeg, C. Inerter-enhanced tuned mass damper for vibration damping of floating offshore wind turbines. *Ocean Eng.* **2021**, *223*, 108663. [CrossRef]
34. Zhang, R.; Cao, Y.; Dai, K. Response control of wind turbines with ungrounded tuned mass inerter system (TMIS) under wind loads. *Wind Struct.* **2021**, *32*, 573–586.
35. Zhang, R.; Zhao, Z.; Dai, K. Seismic response mitigation of a wind turbine tower using a tuned parallel inerter mass system. *Eng. Struct.* **2019**, *180*, 29–39. [CrossRef]
36. Zhang, L.; Xue, S.; Zhang, R.; Xie, L.; Hao, L. Simplified multimode control of seismic response of high-rise chimneys using distributed tuned mass inerter systems (TMIS). *Eng. Struct.* **2021**, *228*, 111550. [CrossRef]
37. Wen, Y.; Chen, Z.; Hua, X. Design and evaluation of tuned inerter-based dampers for the seismic control of MDOF structures. *J. Struct. Eng.* **2017**, *143*, 04016207. [CrossRef]
38. Su, N.; Peng, S.; Hong, N.; Xia, Y. Wind-induced vibration absorption using inerter-based double tuned mass dampers on slender structures. *J. Build. Eng.* **2022**, *58*, 104993. [CrossRef]

39. Hu, Y.; Chen, M.Z.Q. Performance evaluation for inerter-based dynamic vibration absorbers. *Int. J. Mech. Sci.* **2015**, *99*, 297–307. [CrossRef]
40. Li, S.; Liu, M.; Li, H.; Hui, Y.; Chen, Z. Effects of structural damping on wind-induced responses of a 243-meter-high solar tower based on a novel elastic test model. *J. Wind Eng. Ind. Aerod.* **2018**, *172*, 1–11. [CrossRef]
41. Lin, J.; Zhang, Y.; Li, Q.; Williams, F. Seismic spatial effects for long-span bridges, using the pseudo excitation method. *Eng. Struct.* **2004**, *26*, 1207–1216. [CrossRef]
42. Colherinhas, G.B.; Morais, M.V.G.; Shzu, M.A.M.; Avlia, S.M. Optimal pendulum tuned mass damper design applied to high towers using genetic algorithms: 2DOF modelling. *Int. J. Str. Stab. Dyn.* **2019**, *19*, 1950125. [CrossRef]
43. Liao, F.; Lu, Y.; Liu, H. Cooperative optimal preview tracking control of continuous-time multi-agent systems. *Int. J. Control* **2016**, *89*, 2019–2028. [CrossRef]
44. Kaveh, A.; Farzam, M.F.; Maroofiazar, R. Comparing H_2 and H_∞ algorithms for optimum design of tuned mass dampers under near-fault and far-fault earthquake motions. *Period. Polytech. Civ. Eng.* **2020**, *64*, 828–844. [CrossRef]
45. Davenport, A.G. The response of slender, line-like structures to a gusty wind. *Proc. Inst. Civ. Eng.* **1961**, *23*, 389–408. [CrossRef]
46. Wang, L.; Wang, Z.; Huang, N.; Fan, X.; Zhang, Z. Comparative analysis of cross-wind load code for high structures with circular sections. *Structures* **2022**, *43*, 117–1186. [CrossRef]
47. *NB/T 47041-2014*; Vertical Vessels Supported by Skirt. Standards Press of China: Beijing, China, 2014.
48. *GB/T 50051-2021*; Technical Standard for Chimney Engineering. China Planning Press: Beijing, China, 2021.
49. *BS EN 1991-3-2*; Eurocode 3: Design of Steel Structures: Part 3-2: Towers, Masts and Chimneys. European Committee for Standardization: Brussels, Belgium, 2006.
50. *AIJ 2004*; Recommendations for Loads on Buildings. Architectural Institute of Japan: Tokyo, Japan, 2004.
51. *ASME STS-1-2006*; Steel Stacks. The American Society of Mechanical Engineers: New York, NY, USA, 2006.
52. Holmes, J.D. *Wind Loading of Structures*, 3rd ed.; CRC Press: Boca Raton, FL, USA, 2018.
53. Simiu, E.; Yeo, D.H. *Wind Effect on Structures: Modern Structural Design for Wind*, 4th ed.; Wiley-Blackwell: Hoboken, NJ, USA, 2019.

buildings

Article

Multi-Objective Optimization Design of FRP Reinforced Flat Slabs under Punching Shear by Using NGBoost-Based Surrogate Model

Shixue Liang *, Yiqing Cai, Zhengyu Fei and Yuanxie Shen

School of Civil Engineering and Architecture, Zhejiang Sci-Tech University, Hangzhou 310018, China;
cyq9909@163.com (Y.C.); fzy01060020@163.com (Z.F.); shenyuanxiee@163.com (Y.S.)
* Correspondence: liangsx@zstu.edu.cn

Abstract: Multi-objective optimization problems (MOPs) in structural engineering arise as a significant challenge in achieving a balance between prediction accuracy and efficiency of the surrogate models, which are conventionally adopted as mechanics-driven models or numerical models. Data-driven models, such as machine learning models, can be instrumental in resolving intricate structural engineering issues that cannot be tackled through mechanics-driven models. This study aims to address the challenges of multi-objective optimization punching shear design of fiber-reinforced polymer (FRP) reinforced flat slabs by using a data-driven surrogate model. Firstly, this study employs an advanced machine learning model, namely Natural Gradient Boosting (NGBoost), to predict the punching shear resistance of FRP reinforced flat slabs. The comparisons with other machine learning models, design provisions and empirical theory models illustrate that the NGBoost model has higher accuracy in predicting the punching shear resistance. Additionally, the NGBoost model is explained with Shapley Additive Explanation (SHAP), revealing that the slab's effective depth is the primary factor affecting the punching shear resistance. Then, the formulated NGBoost model is adopted as a surrogate model in conjunction with the Non-Dominated Sorting Genetic Algorithm-II (NSGA-II) algorithm for multi-objective optimization design of FRP reinforced flat slabs subjected to punching shear. Through a case study, it is demonstrated that the Pareto-optimal set of the punching shear resistance and cost of the FRP reinforced flat slabs can be successfully obtained. By discussing the effects of design parameter changes on the results, it is also shown that increasing the slab's effective depth is a relatively effective way to achieve higher punching shear resistance of FRP reinforced flat slabs.

Keywords: FRP reinforced flat slabs; punching shear resistance; NGBoost; SHAP; multi-objective optimization; NSGA-II

1. Introduction

Fiber-reinforced polymers (FRPs) possess properties including a light weight, high strength and corrosion resistance. Among them, CFRP has higher mechanical and better fatigue and corrosion resistance while the durability of BFRP and GFRP may decrease in long-term alkaline environments [1–3]. In order to enhance the longevity of structures in a corrosive environment, FRP reinforcement can be employed as an alternative to steel bars in reinforced concrete structures [4–6]. In this regard, FRP reinforced concrete slabs can be served as prospective supplements to traditional reinforced concrete (RC) structures, owing to their superior durability and resistance to corrosions [7]. As for RC flat slab structures, particularly at the joints, they are susceptible to brittle punching failures, resulting in continuous collapse incidents (Figure 1) [8–10]. When it comes to FRP reinforced flat slab structures, since FRP reinforcement has a lower elasticity modulus and ductility compared to steel bars, they are more prone to brittle failure under punching shear [11]. Therefore, the punching shear resistance prediction and design optimization are the two most critical aspects in the research of FRP reinforced flat slabs, which are also prerequisites for the application of FRP reinforced concrete structures.

(**a**) (**b**) (**c**)

Figure 1. Collapse accident of reinforced slabs: (**a**) Piper's Row Car Park Collapse in the UK [8]; (**b**) Gretzenbach Underground Garage Collapses in Switzerland [9]; (**c**) Collapse of Florida Slab-Column-Structure Residential Building [10].

For the purpose of avoiding punching shear failure in FRP reinforced concrete flat slabs, researchers have conducted extensive experimental and theoretical studies. Matthys et al. [12] discovered that the punching shear strength of FRP reinforced slabs and RC slabs was similar under the same flexural stiffness. Bouguerra et al. [13] found that the thickness of FRP reinforced concrete slabs and the concrete's compressive strength had significant impacts on their punching shear capacity. Several researchers, including El Gandour et al. [14], El Gamal et al. [15] and Matthys et al. [12] modified the punching shear resistance models of FRP flat slabs based on the various theories. Nguyen et al. [16] put forward a punching shear strength model based on fracture mechanics, which took the size effect and effective slab-depth ratio into consideration. Ospina et al. [17] established a model that considered eccentric shear stress to determine the stiffness and punching shear resistance of FRP reinforced concrete slabs.

Since the structural design needs to take both the safety, usually represented as structural resistance, and cost into consideration, two or more conflicting optimization objectives such as these can be summarized as multi-objective optimization problems (MOPs) [18–20]. There can be only one set of equilibrium solutions for MOPs, described as the Pareto-optimal set, because it is impossible to achieve the optimal states for all objectives simultaneously [21]. Evolutionary algorithms (EAs) can obtain multiple optimal solutions and reduce the total computation time. Hence, it is considered as a viable strategy for addressing multi-objective optimization problems [22–24]. The common EAs used for multi-objective optimization include Particle Swarm Optimization (PSO) [25], Simulated Annealing (SA) [26], Sand Cat Swarm Optimization (SCSO) [27] and so on. Among these evolutionary optimization algorithms, the Non-Dominated Sorting Genetic Algorithm-II (NSGA-II) [28] stands out as one of the most influential and advanced multi-objective genetic algorithms. This algorithm has become one of the most prospective algorithms in multi-objective optimization problems due to its simplicity and effectiveness [29,30]. The fast non-dominated sorting approach proposed with NSGA-II simplifies the complexity of the non-dominated order. With the incorporation of the crowding operator and elitist strategy, NSGA-II demonstrates perfect performance in multi-objective evolutionary optimization [31].

Conventionally, two types of models can be adopted as surrogate models in multi-objective optimization. The first type is theoretical-derivation-based mechanical models, which have the advantages of straightforward expressions and high computational efficiency. However, their prediction accuracies are usually low due to the difficulties of considering all the influencing factors and the introduction of simplifications when predicting complex structural behaviors [32]. The second type is based on numerical models such as a nonlinear finite elements analysis (FEA), which simulates the complex structural behavior and combines with optimization algorithms to obtain accurate optimization results.

Steven et al. [33] developed the evolutionary structure optimization (ESO) method to optimize beams of a three-story RC frame structure. Li and Xie [34] developed the bidirectional evolutionary structural optimization (BESO) method for composite structures with varying material properties under tension and compression. However, the large computational requirement of FEA encounters some obstacles in MOP applications, especially for complex structures [35].

Machine learning (ML) approaches in structural performance prediction have been rapidly developed [36–40]. Due to the high prediction accuracy, good generalization performance and high efficiency, ML is particularly well suited for complex multi-objective optimization problems with the ability to achieve global optimization [41,42]. Therefore, an ML-surrogate-based multi-objective optimization design of FRP reinforced slabs is proposed in this study. The flowchart is given in Figure 2 as follows: firstly, this paper applies an advanced ML model, namely Natural Gradient Boosting (NGBoost), to predict the punching shear resistance of FRP reinforced flat slabs; secondly, the SHAP interpretable method is applied for influencing the factor analysis; thirdly, an NSGA-II-based multi-objective optimization for FRP reinforced flat slabs subjected to punching shear is proposed, in which the established NGBoost model is utilized as the surrogate model; and finally, the optimization results are examined to understand the impact of different design parameters. The innovations of this paper are as follows: 1, introduced innovative data-driven Natural Gradient Boosting (NGBoost) for predicting punching shear resistance of FRP reinforced flat slabs; 2, integrated an NGBoost-based surrogate model with Non-Dominated Sorting Genetic Algorithm-II (NSGA-II) for efficient multi-objective optimization, which obtains the Pareto-optimal set of punching shear resistance and cost for FRP reinforced flat slabs.

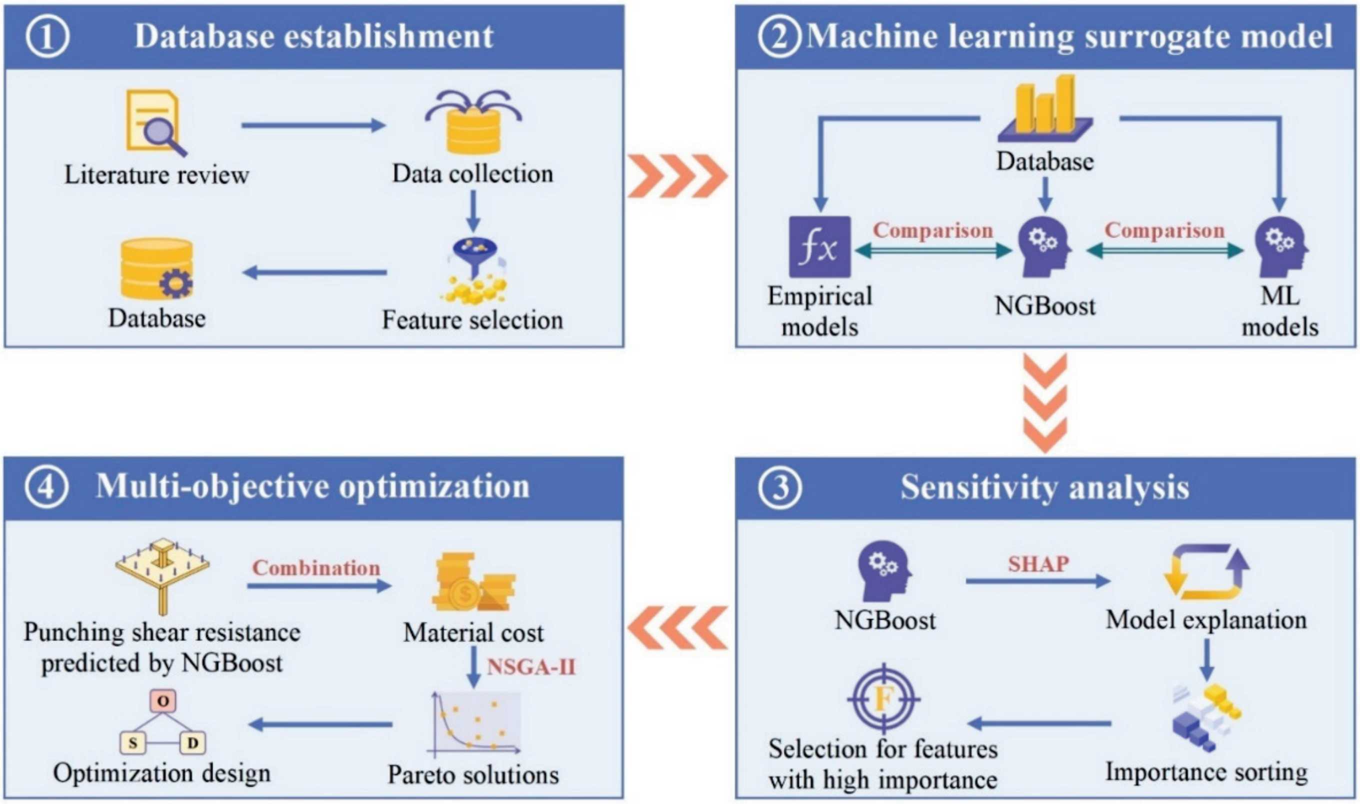

Figure 2. Workflow of the proposed optimization framework.

2. ML Model for Punching Shear Resistance Prediction

2.1. Experimental Dataset

A punching shear experimental dataset of 154 FRP reinforced slabs was gathered from relevant papers, which covers almost all currently published test data of FRP reinforced slabs. The complete dataset is provided in Appendix A. Through literature review [12,43,44], the shape of the column (s), area of the column (A), effective depth of the slab (h_0), cylinder concrete compressive strength (f_c'), FRP reinforcement's elasticity modulus (E_f) and FRP reinforcement ratio (ρ_f) are identified as the primary factors that influence the punching shear resistance of FRP reinforced concrete slabs (V). The statistical values of the six input parameters and one output parameter are presented in Table 1. Figure 3 shows the distribution of six input parameters and one output parameter. It can be seen that all parameters except s exhibit continuous distribution characteristics, which verifies that the samples selected in this paper have no significant deviation and are representative. The data size employed for ML modeling adheres to a widely recognized consensus, which asserts that the quantity of data should exceed 10 times the number of input parameters [45]. In this study, the dataset contains 154 experimental results and six input parameters; hence, the data size meets the requirement of ML modeling.

Table 1. Statistical values of dataset.

Design Parameters	s	A/cm^2	h_0/mm	f_c'/MPa	E_f/GPa	ρ_f/%	V/kN
Maximum	3	2025	284	118	230	3.76	1600
Minimum	1	4.91	45	22.16	28.4	0.15	45
Mean	/	740.65	164.50	43.51	71.15	0.98	365.96
Standard deviation	/	489.54	119.5	16.38	36.37	0.61	267.65

s = 1, 2 and 3 represent the shape of a column as square, circular and rectangular, respectively.

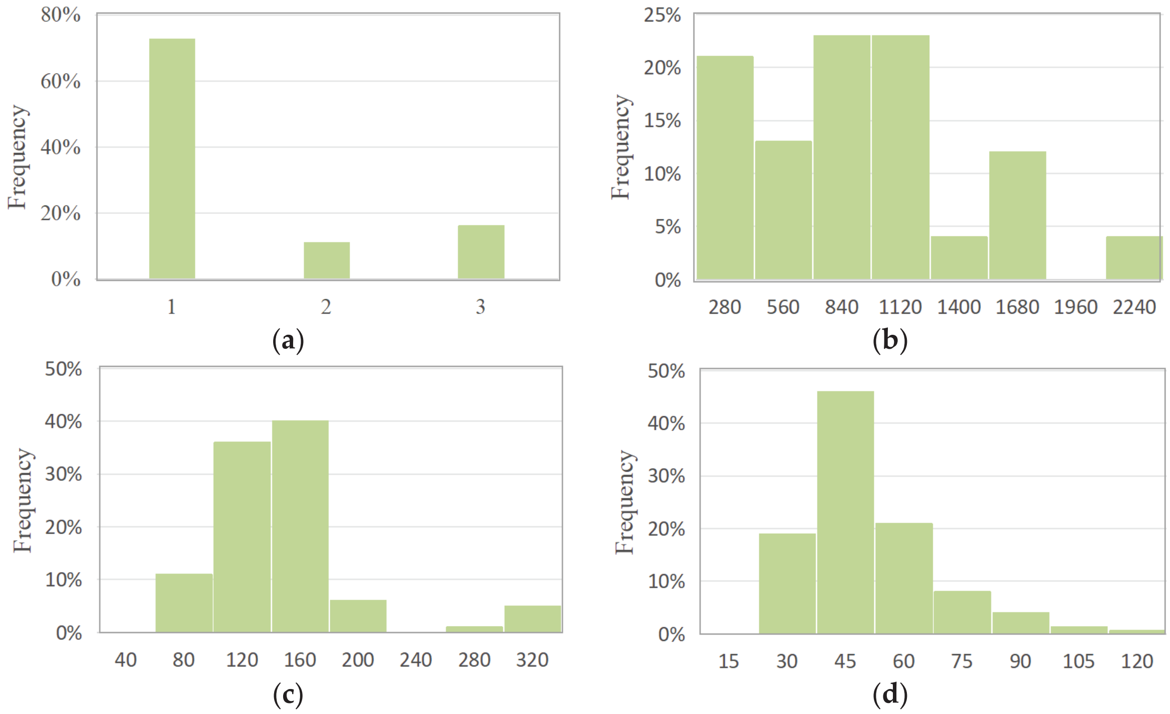

(**a**) (**b**) (**c**) (**d**)

Figure 3. *Cont.*

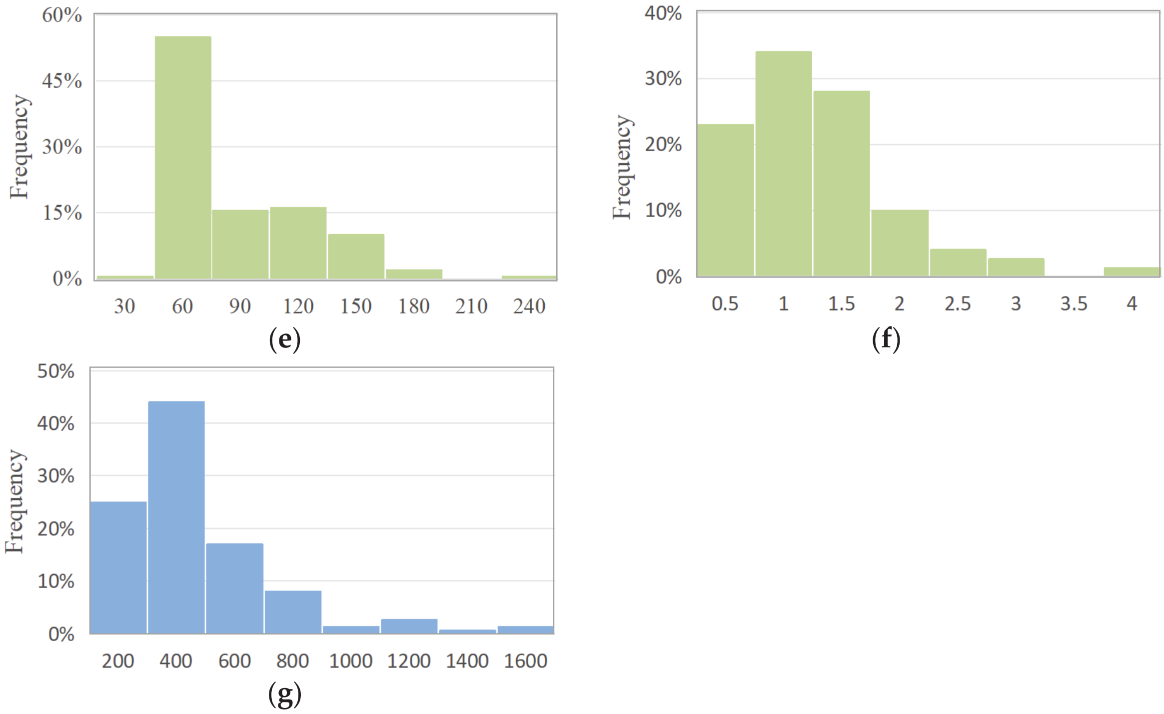

(e) (f) (g)

Figure 3. Distribution of 6 input parameters and 1 parameter. (**a**) s; (**b**) A; (**c**) h_0; (**d**) f_c'; (**e**) E_f; (**f**) ρ_f; (**g**) V.

By splitting the dataset into a training set and a testing set with an 8:2 ratio, it ensures an adequate number of training sets for model training and learning; meanwhile, the testing set is utilized to assess performance on new data and validate generalization ability of the model. From Table 1, noticeable variations can be observed in the numerical values of the different input parameters. Therefore, it becomes essential to normalize the dataset by scaling the input parameters within the range of [0, 1] to strengthen the convergence and precision of the model. The normalization is represented as

$$x_i^* = \frac{x_i - \min\limits_{1 \le j \le m} \{x_j\}}{\max\limits_{1 \le j \le m} \{x_j\} - \min\limits_{1 \le j \le m} \{x_j\}} \tag{1}$$

where x represents the parameter before processing; x^* represents the normalized parameter; m stands for the sample sizes; i is the i-th input parameter.

2.2. Natural Gradient Boosting (NGBoost)

NGBoost is a newly developed boosting approach [46], which applies a natural gradient-based boosting method composed of three parts: base learners, probability distribution types and scoring rules (Figure 4). This method directly acquires the full probability distribution in the output space, enabling probability prediction to measure uncertainty. It is shown that NGBoost provides eminent prediction performance in both deterministic and stochastic problems [47,48]. Figure 5 depicts the modeling process of NGBoost.

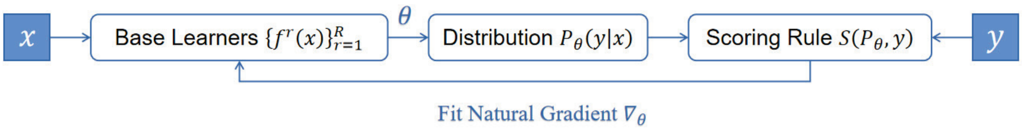

Figure 4. NGBoost offers modularity in terms of selecting the base learner, distribution and scoring rule.

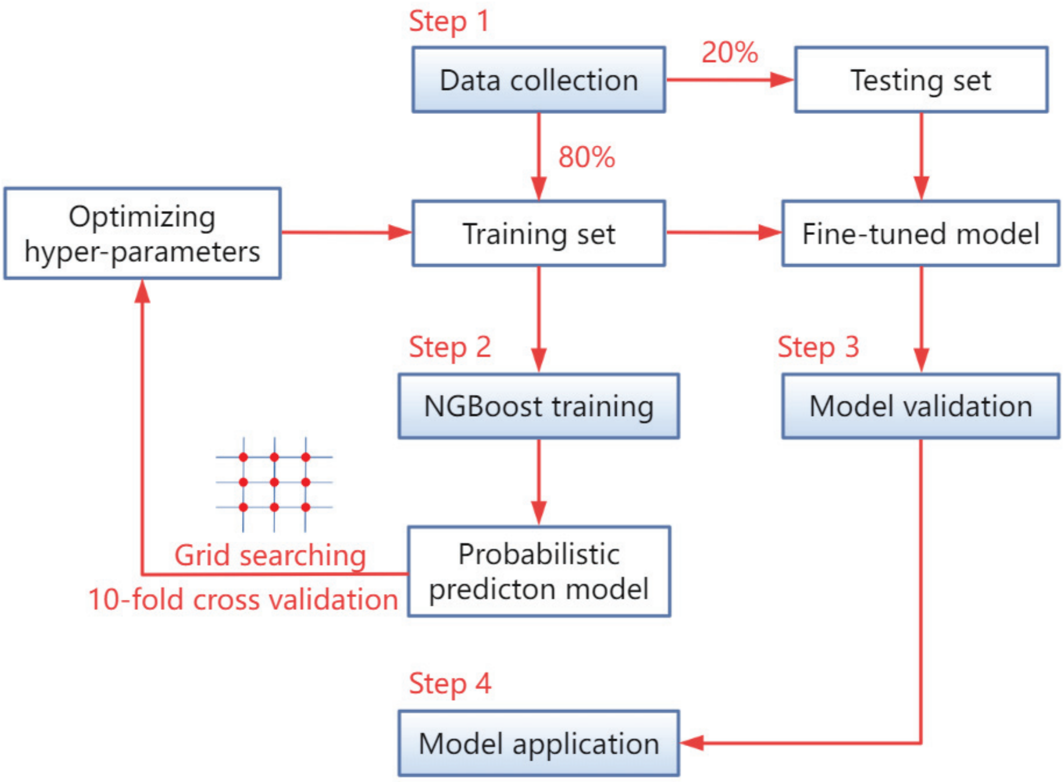

Figure 5. Implementation workflow of ML models (NGBoost).

In Section 2.1, the dataset for modeling is preliminarily established. The NGBoost algorithm is a derivative of the gradient boosting framework, which is an ensemble learning method that combines multiple base learners together to achieve better predictive performance. A decision tree is the common choice for the base learner, because it can effectively adapt to complex data patterns and improve predictive performance through the ensemble learning [49]. Unlike previously proposed ML methods, NGBoost can further obtain the probability distribution of the predicted results by utilizing a natural gradient instead of a conventional gradient. The definition of the natural gradient $\widetilde{\nabla}_\theta$ is shown in Equation (2):

$$\begin{aligned} \widetilde{\nabla}_\theta S(\theta,y) &= \lim_{\varepsilon\to 0} \underset{d:D_S(P_\theta,P_{\theta+d})=\varepsilon}{are\max} S(\theta+d,y) \\ &= \mathcal{I}_S(\theta)^{-1}\nabla_\theta S(\theta,y) \end{aligned} \tag{2}$$

where S represents the scoring rule; $D_S(P_\theta, P_{\theta+d})$ is the divergence of the scoring rule; $P_\theta = P(\theta|x,y)$ is the conditional probabilistic distribution that represents the prediction y for a new input x; $\mathcal{I}_S(\theta)$ is the Riemannian metric of the statistical manifold at parameter set θ [46].

One of the commonly used scoring rules is the maximum likelihood estimation (MLE), which is more suitable for probability predictions in complex resistance mechanisms compared to another commonly used scoring rule called the continuous ranked probability score (CPRS) [50]. The specific expression of the MLE scoring rule is shown in Equation (3) as

$$S(\theta,y) = \mathcal{L}(\theta,y) = -\log P(\theta|x,y) \tag{3}$$

where $\mathcal{L}$ represents the calculation of the MLE scoring rule.

All appropriate scoring rules should satisfy the following equation:

$$S(\theta,y) = \mathcal{L}(\theta,y) = -\log P(\theta|x,y) \tag{4}$$

Therefore, the Kullback–Leibler divergence (KL divergence, i.e., D_{KL}) of the MLE scoring rule can be obtained based on Equation (4) [51]:

$$\begin{aligned} D_{\mathcal{L}}(P_\theta, P_{\theta+d}) &= E_{y\sim P_\theta}[\mathcal{L}(P_{\theta+d}, y)] - E_{y\sim P_\theta}[\mathcal{L}(P_\theta, y)] \\ &= E_{y\sim P_\theta}\left(\log \frac{P_\theta}{P_{\theta+d}}\right) \\ &=: D_{KL}(P_\theta, P_{\theta+d}) \end{aligned} \tag{5}$$

Utilizing the new score and the gradient rule, multiple base learners can be trained through the gradient boosting framework to fit the parameters. The following text provides a description of the precise iteration procedure used with NGBoost. The learning algorithm first estimates a common initial distribution that minimizes the scoring rule S on the sum of response variables for all training samples and becomes the initial predicted parameter $\theta^{(0)}$. At iteration r, a set of base learners $f^{(r)}$ takes input x for predicting the output, which is then scaled based on the stage-specific scaling factors $\rho^{(r)}$ and a common learning rate η. As a result, after each iteration, the updated prediction parameter θ can be represented as

$$y|x \sim P_\theta(x), \theta = \theta^{(0)} - \eta \sum_{r=1}^{R} \rho^{(r)} \cdot f^{(r)}(x) \tag{6}$$

2.2.1. Other ML Models for Comparison

This section briefly introduces three ML methods and their modeling processes. Their prediction results will be compared with NGBoost in Section 2.2.3.

Random Forest (RF) [52] is an ensemble algorithm, which is composed of several base learners (Figure 6). The RF constructs multiple independent decision trees through random sampling and executes them in parallel to obtain prediction results.

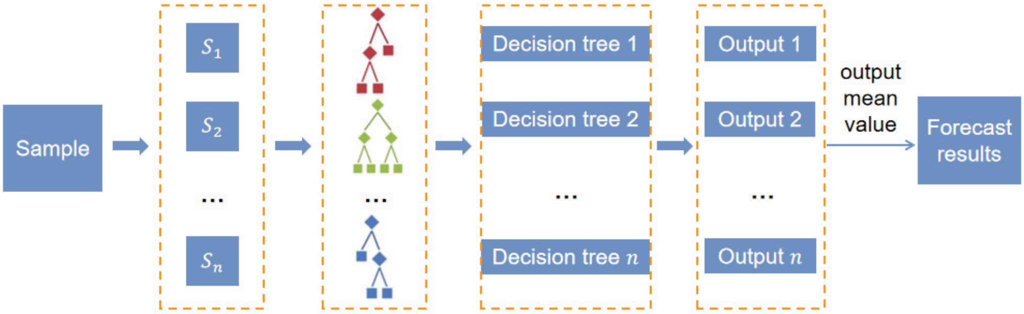

Figure 6. Implementation workflow of RF.

Adaptive Boosting (AdaBoost) [53] is also an ensemble learning algorithm (Figure 7). Firstly, the weight distribution of the training set is initialized. Then, the error rate and weight of each base learner are calculated, and the weight of the training samples is updated, until n base learners are trained. Finally, the prediction model is gained by combining strategies for prediction.

The support vector regression (SVR) [54] model can be simply understood that a spacer band ε is created on the two sides of the linear function and samples falling inside are not taken into account when calculating loss (Figure 8). By minimizing the total loss and maximizing the interval, an optimized model can be obtained.

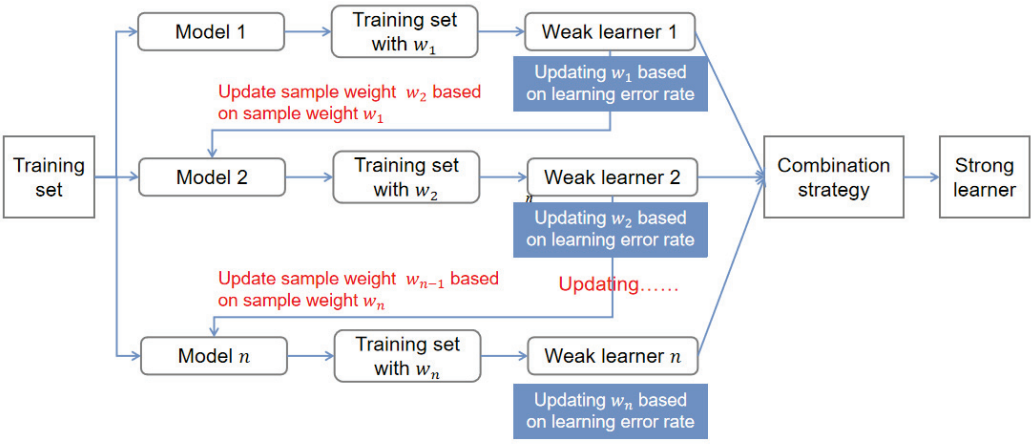

Figure 7. Implementation workflow of AdaBoost.

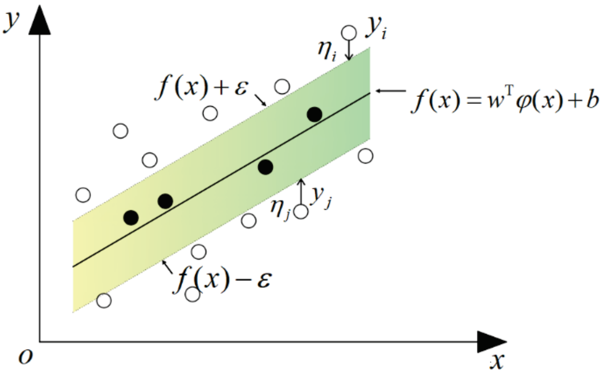

Figure 8. Implementation workflow of SVR.

2.2.2. Model Evaluation

To assess the prediction performance of the proposed models, three evaluation indexes, namely RMSE, MAE and R^2, are selected in Table 2.

Table 2. Model evaluation indexes.

Model Evaluation Index	Abbreviation	Equation	Explanations
Root Mean Square Error	RMSE	$\mathrm{RMSE} = \sqrt{\frac{1}{m}\sum_{i=1}^{m}\left(\hat{y}_i - y_i\right)^2}$	When the predicted value and the true value are in exact agreement, the value of RMSE/MAE is 0, indicating an excellent model. The value of RMSE/MAE rises as the error does as well.
Mean Absolute Error	MAE	$\mathrm{MAE} = \frac{1}{m}\sum_{i=1}^{m}\left\lvert\hat{y}_i - y_i\right\rvert$	
Coefficient of Determination	R^2	$R^2 = 1 - \frac{\sum_i\left(\hat{y}_i - y_i\right)^2}{\sum_i\left(\bar{y}_i - y_i\right)^2}$	The R^2 value, which ranges from 0 to 1, is a measure of the model's goodness fit. The larger the value, the better the model's fit.

m stands for the sample size, $\hat{y}_i$ represents the predicted value of the sample, $\bar{y}_i$ represents the mean value of all samples and y_i represents the true value of the sample.

2.2.3. Prediction Results

In the case of ML models, the goal of model training is to identify the optimal hyper-parameter within the provided search space. To achieve this objective, the search spaces for four ML models (i.e., SVR, RF, Adaboost and NGBoost) are presented in Table 3. The value range in this table encompasses the potential values for each hyper-parameter. In order to meticulously construct a prediction model with satisfactory performance, the grid searching method is employed to determine the appropriate hyper-parameters for each

ML model. Additionally, a 10-fold cross-validation approach is utilized to evaluate the outcomes of this selection process.

Table 3. Hyperparameters of 4 ML models.

ML Models	Optimal Hyper-Parameter
NGBoost	Base = default_tree_learner, Dist = Nomal, Score = MLE learning_rate = 0.2, Estimators = 300
AdaBoost	Max_depth = 5, n_estimators = 76, learning_rate = 0.85
RF	n_estimators = 20, min_samples_split = 2, min_samples_leaf = 1, n_jobs = 1
SVR	Epsilon = 1.26, C = 9923443, Gamma = 10.8

To conduct a more comprehensive evaluation of NGBoost's prediction accuracy, four empirical models, containing two design codes and two theoretical models, were selected for the comparison. The specifics of the empirical models are displayed in Table 4.

Table 4. Formulas of calculation of punching shear capacity.

Empirical Models	Formulas
ACI 440.15R-15 [55]	$V_1 = 0.8\sqrt{f_c'}b_{0,0.5h_0}(uh_0), u = \sqrt{2\rho_f d_f + \left(\rho_f d_f\right)^2} - \rho_f d_f, E_c = 4700\sqrt{f_c'}, d_f = \frac{E_f}{E_c}$
JSCE [56]	$V_2 = \beta_{h_0}\beta_e\beta_r f_{pcd} b_{0,0.5h_0} h_0/\gamma_b,\ \beta_e = \sqrt[3]{\left(100\rho_f E_f/E_s\right)} \leq 1.5$ $\beta_{h_0} = (1000/h_0)^{1/4} \leq 1.5,\ f_{pcd} = 0.2(f_c')^{1/2} \leq 1.2\text{MPa},\ \beta_r = 1 + 1/\left(1 + 0.25b_{0,0.5h_0}/h_0\right)$
El-Ghandour et al. [57]	$V_3 = 0.33\sqrt{f_c'} \times \sqrt[3]{\left(E_f/E_s\right)}b_{0,0.5h_0}h_0$
Ospina et al. [17]	$V_4 = 2.77 \times \sqrt[3]{\left(\rho_f f_c'\right)}\sqrt{\frac{E_f}{E_s}}b_{0,0.5h_0}h_0$

$b_{0,0.5h_0}$ is the perimeter of the critical section for slabs and footings at a distance of $0.5h_0$ away from the column face; $b_{0,1.5h_0}$ is the perimeter of the critical section for slabs and footings at a distance of $1.5h_0$ away from the column face; E_s is the elastic modulus of steel, with a value of 200 GPa; γ_b is the safety factor, with a value of 1.3.

Table 5 and Figure 9 demonstrate the prediction results of four ML models and four empirical models. It is depicted in Figure 9 that the prediction results generated with RF, Adaboost and NGBoost demonstrate good agreements with the experimental punching shear resistance; all the dots are closely distributed around the best fitting line. It is revealed in Table 5 that the NGboost model has the highest prediction accuracy among RF, Adaboost and NGBoost. In contrast, the SVR model performs poorly on the test set with an R^2 of 0.66. Additionally, it can be indicated that the Ospina et al. [17] prediction accuracy is the highest among empirical models with an RMSE, MAE and R^2 of 128.48, 82.65 and 0.77, respectively. However, the predicted accuracy is still lower than the NGBoost model, for which the RMSE, MAE and R^2 are 34.42, 16.81 and 0.98, respectively. Therefore, NGBoost demonstrates superior performance in predicting the FRP reinforced slabs' punching shear capacity compared to all the selected ML and empirical models.

Table 5. Prediction results of models.

ML	Training Set			Testing Set			Complete Dataset		
	RMSE	MAE	R^2	RMSE	MAE	R^2	RMSE	MAE	R^2
NGBoost	12.35	6.94	0.99	71.89	53.90	0.93	34.42	16.81	0.98
RF	34.47	22.61	0.98	103.16	74.26	0.85	55.69	34.99	0.96
AdaBoost	32.71	25.20	0.98	113.06	80.13	0.82	60.25	36.02	0.95
SVR	21.18	11.97	0.99	152.91	104.41	0.66	71.12	30.60	0.93
ACI 440.15R-15 [55]	250.84	194.49	0.09	278.02	214.24	0.01	256.54	198.47	0.08
JSCE [56]	152.72	111.74	0.66	165.95	121.24	0.65	155.48	113.65	0.66
El-Ghandour [57]	147.27	105.86	0.59	101.86	71.73	0.80	139.32	98.91	0.73
Ospina [17]	129.23	84.74	0.81	125.48	74.37	0.78	128.48	82.65	0.77

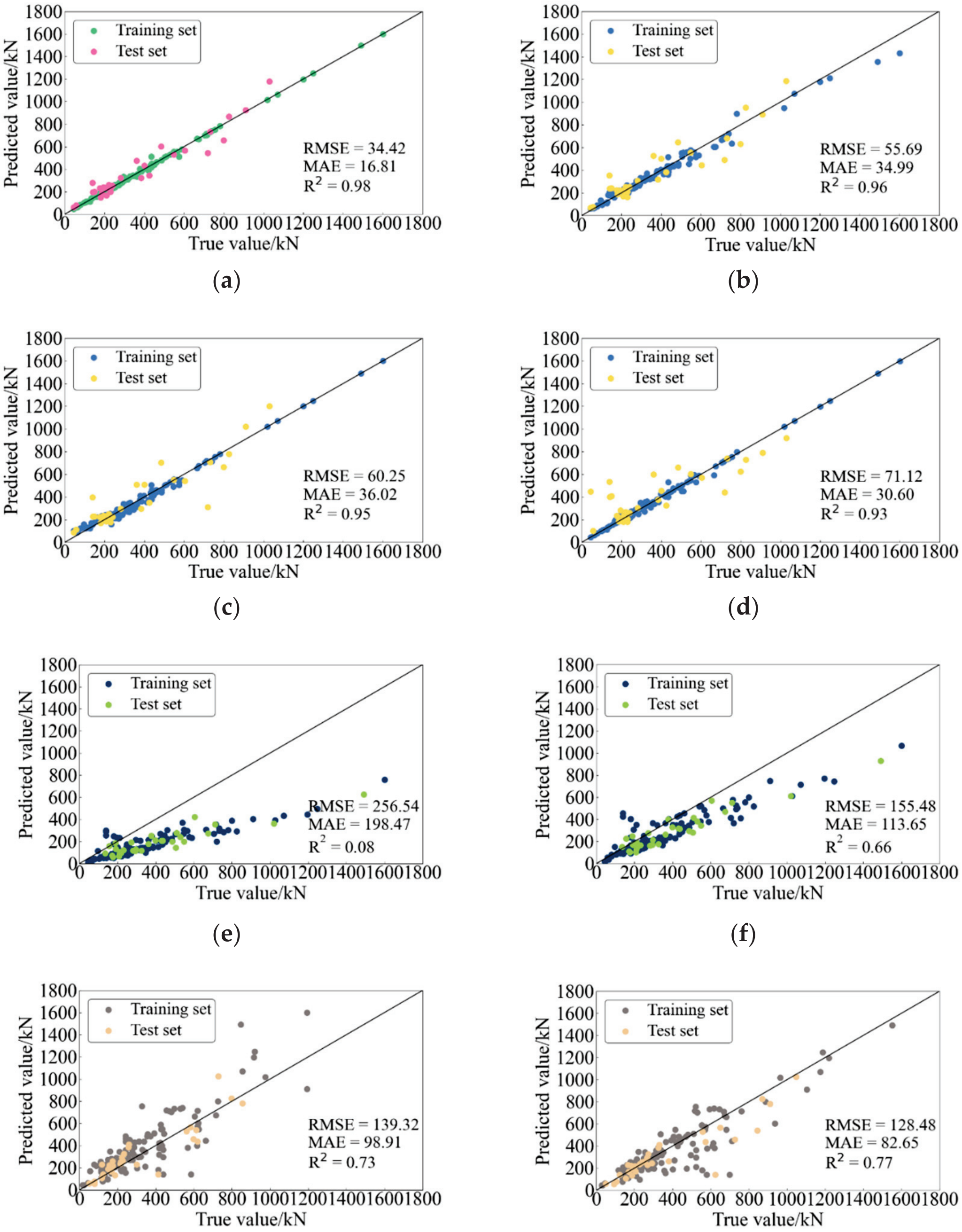

(**a**) (**b**)

(**c**) (**d**)

(**e**) (**f**)

(**g**) (**h**)

Figure 9. Results of prediction models: (**a**) NGBoost; (**b**) RF; (**c**) AdaBoost; (**d**) SVR; (**e**) ACI 440.15R-15 [55]; (**f**) JSCE [56]; (**g**) El-Ghandour [57]; (**h**) Ospina [17].

2.3. Parameter Sensitivity Analysis Based on SHAP

ML is commonly described as a black-box model that lacks the ability to elucidate the impact of input parameters on output parameters [58,59]. Therefore, this article introduces the Shapley Additive Explanation (SHAP) model for a sensitivity analysis of parameters, which helps explain the behavior of the NGBoost model, and identify which input parameters need attention and adjustment to improve model performance.

SHAP is an additive explanation model inspired by cooperative game theory [60]. The fundamental concept of SHAP is to compute input variables' marginal contribution, providing explanations for the 'black-box model' from both global and local perspectives [61]. The expression of SHAP can be given as

$$y_{pred}^{(i)} = y_{base} + \sum_{j}^{n'} f(x_{ij}) \tag{7}$$

where $f(x_{ij})$ is the SHAP value of x_{ij}, n' stands for the size of input variables; y_{base} is the baseline value of the entire model; $y_{pred}^{(i)}$ is the predicted value of sample x_i. Intuitively, $f(x_{i1})$ reflects the first input parameter's contribution to the prediction value y_{pred} in the x_i. If $f(x_{i1}) > 0$, it means that the predicted value is positively impacted by the input parameter and vice versa. The major benefit of the SHAP value lies in its ability to indicate the effect of input parameters, both positively and negatively, thus improving the interpretability of the model. Moreover, SHAP provides powerful data visualization functions to display the interpretation results of the prediction, making important contributions to explain complex ML models.

The parameter sensitivity analysis of FRP reinforced flat slabs is given as follows: (1) among all input parameters, the slab's effective depth h_0 has the greatest influence, far exceeding other influencing factors; (2) the second-ranked factor is the area of column A, with an importance of about 0.38% of h_0; (3) the following influential factors are FRP reinforcement ratio ρ_f, compressive strength of concrete f_c', elasticity modulus of FRP reinforcement E_f; (4) the shape of column s has the minimal influence.

The impact range and distribution of input parameters on the FRP reinforced flat slabs' punching shear capacity are displayed in Figure 10b. The x-axis represents the SHAP value observed using each parameter in a single sample in the dataset. Each point is colored from blue to red to indicate the magnitude of numerical changes from small to large. The parameters are listed on the y-axis in descending order of their significance in influencing the outcome. In Figure 10b, it is shown that when the h_0 reaches 400 or above, it almost solely determines the FRP reinforced flat slabs' punching shear capacity.

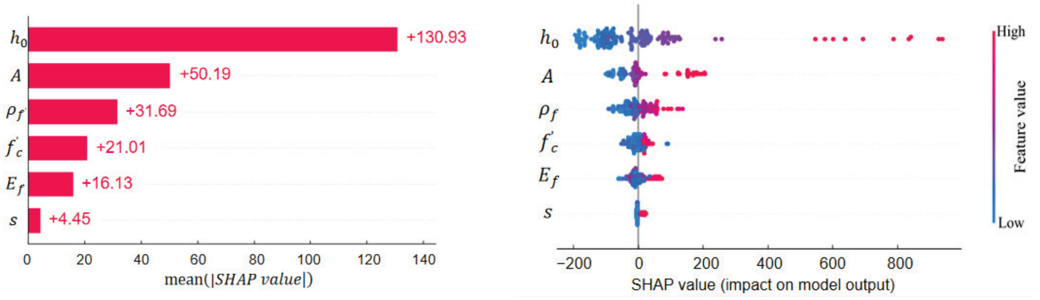

(**a**) (**b**)

Figure 10. Global interpretation of NGBoost model with SHAP: (**a**) SHAP feature importance; (**b**) SHAP summary plot.

3. Multi-Objective Optimization of FRP Reinforced Flat Slabs

3.1. NSGA-II Optimization

Non-Dominated Sorting Genetic Algorithm II (NSGA-II) [28] is a multi-objective genetic algorithm suitable for dealing with multi-objective optimization problems. It incorporates fast non-dominated sorting, crowding distance comparison and an elitist selection strategy into traditional genetic algorithms. The algorithm follows these steps: firstly, a random initial population N is created, and the initial generation offspring population is generated via selection, crossover and mutation operations; secondly, from the second generation onwards, the parent population and the offspring population are combined, and fast non-dominated sorting and crowding distance calculation are performed; thirdly, individuals suitable for selection are chosen to develop a new parent population based on non-dominated relationship and fitness sharing; finally, a new offspring population is created through basic genetic operations. This process is repeated until the termination condition is satisfied. The flowchart of this algorithm is depicted in Figure 11.

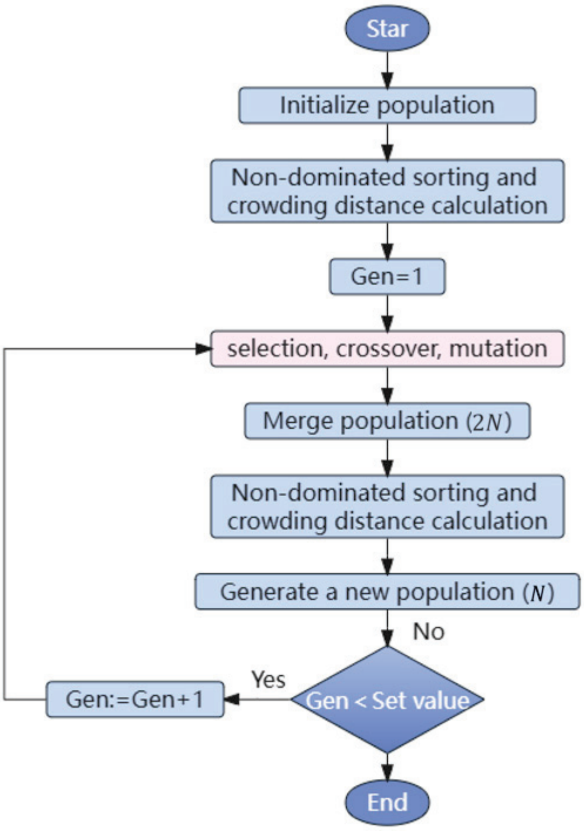

Figure 11. Flowchart of NSGA-II algorithm.

3.1.1. Fast Non-Dominated Sorting Approach

In MOPs, dominance is used to describe a solution that is not inferior to another solution in all objective functions. Throughout the population, individuals without dominant solutions are placed in set Rank 1, and then individuals in Rank 1 are removed from the set. The remaining individuals without dominant solutions are placed in set Rank 2 and so forth, until the population level is completely divided. Through fast non-dominated sorting, solutions can be brought nearer to the Pareto-optimal front (Figure 12).

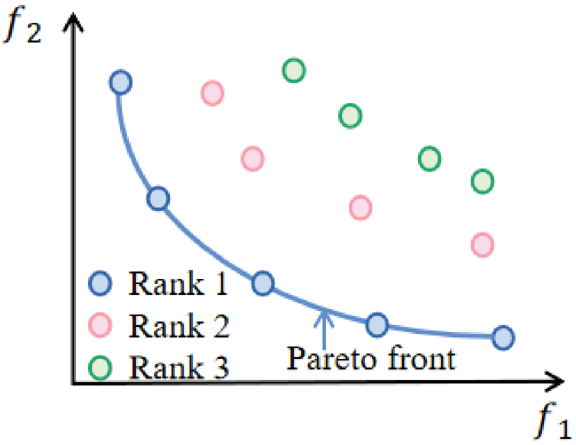

Figure 12. Dominance rank sorting.

3.1.2. Crowded-Comparison Approach

To achieve a more even distribution of obtained solutions in the objective space and cover the Pareto-optimal front as much as possible, the crowded-comparison approach is introduced. The individual crowding distance is illustrated in Figure 13, and the specific expression is shown in Equation (8):

$$i_d = \sum_{j=1}^{m_j}\left(\left|f_j^{i+1} - f_j^{i-1}\right|\right) \tag{8}$$

where i_d represents the crowding distance of point i, f_j^{i+1} represents the value of the objective function j at point $i+1$ and f_j^{i-1} represents the value of the objective function j at point $i-1$; m_j represents the number of objective functions.

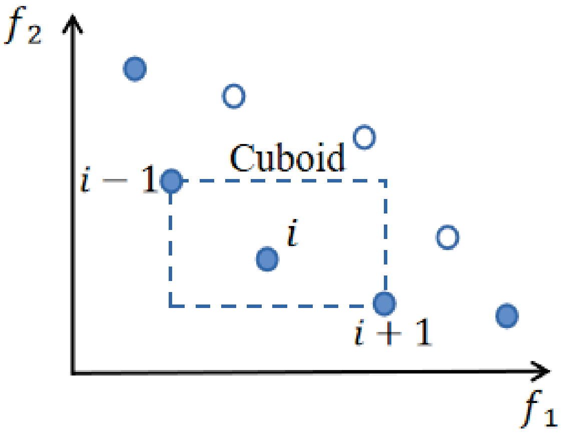

Figure 13. Illustration of crowding distance calculation.

3.1.3. Elitist Strategy

An elitist strategy preserves excellent solutions to accelerate the convergence speed of the algorithm. To begin with, the new population Q_t generated in t is combined with the parent population P_t to form the population R_t. Then, non-dominated sorting is performed and non-dominated sets Z_i are filled in new parent population P_{t+1} in rank order until the population size exceeds N. At this time, the crowding distance comparison operator is used to ensure that the population size in P_{t+1} remains at N. Lastly, a new offspring population Q_{t+1} is created through selection, crossover and mutation (Figure 14).

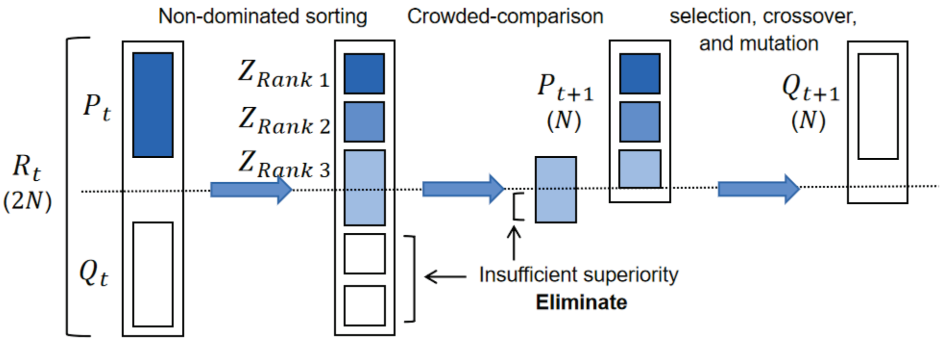

Figure 14. Illustration of elitist strategy.

3.2. Optimization Design of FRP Reinforced Flat Slabs

As mentioned earlier, the high-precision NGBoost prediction model has been successfully established and validated. Subsequently, this model will be used as a surrogate model for NSGA-II to conduct the optimization design for FRP reinforced flat slabs.

We took a set of experimental data [62] from the dataset as an example to conduct structural optimization design. To ensure that the optimized results meet the practical engineering's requirements, Chinese design code (GB 50010-2010 (2015)) [63] is applied in this paper for parameter value range determination. The range of the parameters are selected as follows: $s = 1, 2, 3$, $100\ \text{cm}^2 \le A \le 400\ \text{cm}^2$, $100\ \text{mm} \le h_0 \le 200\ \text{mm}$, $0.2 \le \rho_f \le 1.0$. Since the design parameters such as the size and depth of the slab and columns are the main consideration in this study, the material parameters of the concrete compressive strength and elasticity modulus of FRP reinforcement are chosen as constants as $f'_c = 28.32\text{MPa}$ and $E_f = 45.6\text{MPa}$. The punching shear resistance obtained with the NGBoost model is considered as the objective function f_1, while the material cost of the FRP reinforced slabs is deemed as function f_2. The calculation of objective function f_2 is shown in Equation (9) as

$$f_2(\text{cost}_{FRP}) = A \cdot \sqrt{A} \cdot 10^{-6} \cdot \text{cost}_1 + 1.5 \times 1.5 \cdot h_0 \cdot \text{cost}_1 + 1.5 \times 1.5 \times h_0 \cdot \gamma \cdot \rho_f \cdot 10^{-3} \cdot \text{cost}_2 \tag{9}$$

where cost_1 represents the price of concrete, with the price of approximately Chinese RMB $500/\text{m}^3$; γ denotes the density of FRP reinforcement ranging from $1250 \sim 2100\ \text{kg}/\text{m}^3$ and $2100\ \text{kg}/\text{m}^3$ is chosen as the representative; cost_2 represents the price of FRP reinforcement, which is about 8–12 times that of steel bars with a price of approximately RMB 40,000/t. The optimization design results of the selected FRP reinforced slab obtained by using NSGA-II are manifested in Figure 15.

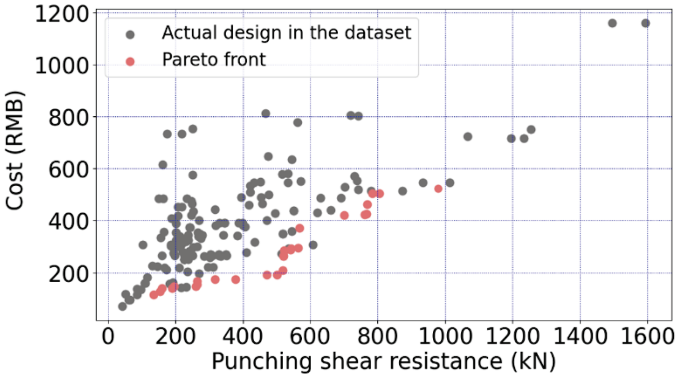

Figure 15. Optimization design results of FRP reinforced flat slabs.

Observing Figure 15, two objective functions, namely punching shear resistance and cost, can be found with a wide range of values, indicating that the optimization model has good generalization performance. In addition, all FRP reinforced slab data points are located above the Pareto-optimal set, suggesting that in the dataset, the material cost is higher than the optimization results of the optimization model. Therefore, the proposed optimization framework is effective in reducing the material cost of FRP reinforced slab design. In addition to obtaining the objective function values f_1 and f_2 of the Pareto solutions, the NSGA-II algorithm can also provide corresponding optimal parameter combination. In order to clearly illustrate the optimized design parameters and the resulting optimizations, three sets of samples among the Pareto solutions of Figure 15 are depicted in Table 6.

Table 6. Optimization samples.

Pareto Solutions	Objective Function $[f_1, f_2]$	Parameters $[s, A, h_0, f'_c, E_f, \rho_f]$
1	[180, 149]	[1, 240, 131, 28.32, 45.6, 0.20]
2	[467, 262]	[1, 165, 168, 28.32, 45.6, 0.23]
3	[719, 427]	[1, 171, 170, 28.32, 45.6, 0.74]

Figure 16 shows the impact of different parameter changes on Pareto solutions. As represented in Figure 16, within the same price range (y-axis), the slab's effective depth has the most significant influence on enhancing the punching shear resistance among the design parameters. When the cost ranges from RMB 150 to RMB 250, the increase in the area of the column and the reinforcement ratio increases the punching shear capacity by about 60 kN, while the increase in the slab's effective depth can increase the punching shear capacity by above 100 kN. But when the cost ranges from RMB 250 to RMB 350, the rise in the reinforcement ratio only provides a limited improvement of about 40 kN. In comparison, it can be seen that increasing the slab's effective depth is the most efficient method to balance economic effects and structural resistance requirements.

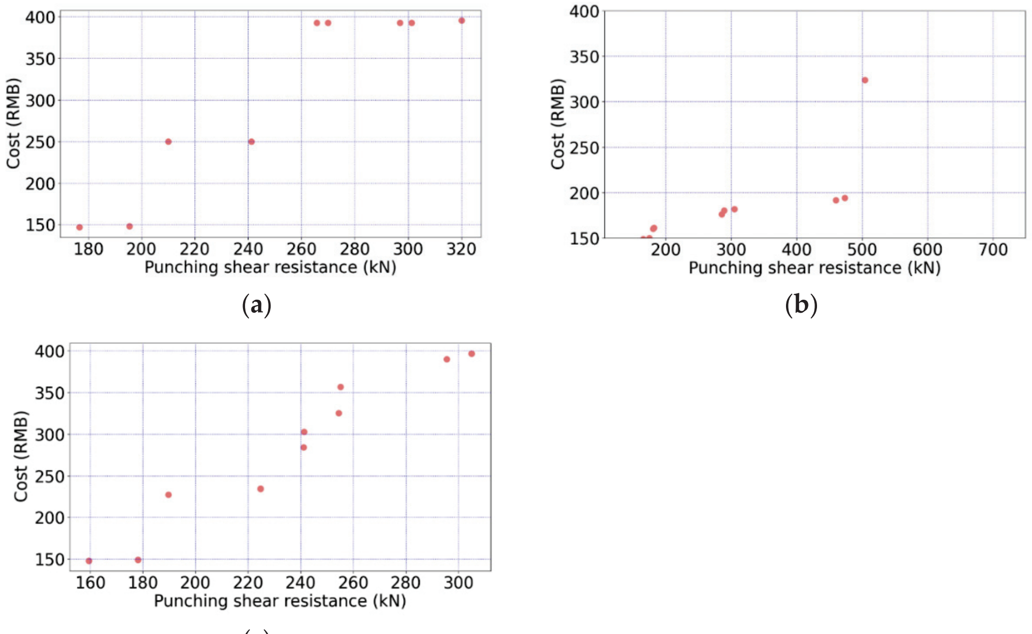

(**a**)

(**b**)

(**c**)

Figure 16. The impact of different parameter changes on the optimization results of FRP reinforced slabs: (**a**) A; (**b**) h_0; (**c**) ρ_f.

The analysis of optimization results reveals which design parameter has the greatest impact on the objective function, as well as which solution can meet the engineering design requirements. NSGA-II-based optimization results help to adjust the engineering design plan to achieve the optimal design goal. The design plan with the lowest cost and best performance can be chosen from the optimized results, or the design plan with the lowest cost can be selected while meeting the reliability requirements. By examining the impact of variations in design parameters on the results of NSGA-II, it is demonstrated that augmenting the effective depth of the slab is a feasible approach to substantially improve the punching shear resistance of flat slabs reinforced with FRP.

4. Conclusions

This paper introduces machine learning-based multi-objective optimization of FRP reinforced flat slabs subjected to punching shear, offering a new perspective on solving the multi-objective structural design optimization problems. Firstly, the NGBoost method is introduced to accurately predict the punching shear capacity of FRP reinforced slabs. Subsequently, the NGBoost model is served as the surrogate model in the multi-objective optimization. Finally, the NSGA-II algorithm is employed for multi-objective structural design optimization. Based on the ML prediction and multi-objective optimization results, conclusions can be summarized as follows:

(1) The proposed NGBoost model has superior prediction performance in predicting the punching shear resistance of FRP reinforced slabs, which shows the highest R^2 and lowest RMSE and MAE errors among the selected four ML models and four empirical models. The exceptional accuracy exhibited with NGBoost predictions renders it a highly advantageous surrogate model for multi-objective optimization applications.
(2) According to the analysis provided with SHAP, the slab's effective depth (h_0) has the greatest influence on the prediction results among all the six input parameters, followed by the FRP reinforcement ratio (ρ_f), the area of the column (A), the compressive strength of concrete (f_c') and the elasticity modulus of the FRP reinforcement (E_f), while the shape of the column (s) has the least effect.
(3) The proposed NSGA-II algorithm, which combines NGBoost as a surrogate model, achieves balance between punching shear capacity and cost. Through an analysis of the effects of design parameter variations on the multi-objective optimization results, it is shown that increasing the slab's effective depth is a viable strategy for significantly enhancing the punching shear resistance of FRP reinforced flat slabs.

Author Contributions: Conceptualization, S.L.; software, S.L. and Y.C.; validation, S.L., Y.C., Z.F. and Y.C.; formal analysis, S.L.; writing—original draft preparation, Y.C.; writing—review and editing, S.L.; visualization, Y.C. and Y.S.; supervision, S.L.; project administration, S.L. All authors have read and agreed to the published version of the manuscript.

Funding: This research was funded by Science Foundation of Zhejiang Province of China, grant number: LY22E080016; National Science Foundation of China, grant number: 51808499.

Data Availability Statement: Not applicable.

Acknowledgments: This study is supported by the Engineering Research Centre of Precast Concrete of Zhejiang Province. The help of all members of the Engineering Research Centre is sincerely appreciated. We would also like to express our sincere appreciation to the anonymous referee for valuable suggestions and corrections.

Conflicts of Interest: The authors declare that they have no known competing financial interests or personal relationships that could have appeared to influence the work reported in this paper.

Appendix A

The entire FRP reinforced slab dataset was uploaded to GitHub: https://github.com/YQing9909/Database/blob/main/Database of punching shear resistance of FRP reinforced concrete slabs.xlsx (accessed on 25 May 2023).

References

1. Xian, G.; Guo, R.; Li, C. Combined effects of sustained bending loading, water immersion and fiber hybrid mode on the mechanical properties of carbon/glass fiber reinforced polymer composite. *Compos. Struct.* **2022**, *281*, 115060. [CrossRef]
2. Aljidda, O.; Alnahhal, W.; Refai, A.E. Bond Durability of Near-Surface-Mounted BFRP and GFRP Bars in Aggressive Environments. *J. Compos. Constr.* **2023**, *27*, 4023055. [CrossRef]
3. Wu, J.; Zhu, Y.; Li, C. Experimental Investigation of Fatigue Capacity of Bending-Anchored CFRP Cables. *Polymers* **2023**, *15*, 2483. [CrossRef]
4. Wysmulsk, P. The analysis of buckling and post buckling in the compressed composite columns. *Arch. Mater. Sci.* **2017**, *85*, 35–41. [CrossRef]
5. Różyło, P. Failure analysis of beam composite elements subjected to three-point bending using advanced numerical damage. *Acta Mech. Autom.* **2023**, *17*, 133–144. [CrossRef]
6. Wysmulski, P. Non-linear analysis of the postbuckling behaviour of eccentrically compressed composite channel-section columns. *Compos. Struct.* **2023**, *305*, 116446. [CrossRef]
7. Zhang, Y.X.; Zhu, Y. A new shear-flexible FRP-reinforced concrete slab element. *Compos. Struct.* **2009**, *92*, 730–735. [CrossRef]
8. Wood, J. Pipers Row car park collapse: Identifying risk. *Concrete* **2003**, *37*, 29–31.
9. Miguel, F.R.; Muttoni, A.; Jakob, K. Strengthening of flat slabs against punching shear using post-installed shear reinforcement. *Aci. Struct. J.* **2010**, *107*, 434–442.
10. Lu, X.; Guan, H.; Sun, H.; Li, Y.; Zheng, Z.; Fei, Y.; Yang, Z.; Zuo, L. A preliminary analysis and discussion of the condominium building collapse in surfside, Florida, US, June 24, 2021. *Front. Struct. Civ. Eng.* **2021**, *15*, 1097–1110. [CrossRef]

11. Zou, X.; Lin, H.; Feng, P.; Bao, Y.; Wang, J. A review on FRP-concrete hybrid sections for bridge applications. *Compos. Struct.* **2021**, *262*, 113336. [CrossRef]
12. Matthys, S.; Taerwe, L. Concrete slabs reinforced with FRP grids. II: Punching resistance. *J. Compos. Constr.* **2000**, *4*, 154–161. [CrossRef]
13. Bouguerra, K.; Ahmed, E.A.; El-Gamal, S.; Benmokrane, B. Testing of full-scale concrete bridge deck slabs reinforced with fiber-reinforced polymer (FRP) bars. *Constr. Build. Mater.* **2011**, *25*, 3956–3965. [CrossRef]
14. El-Ghandour, A.W.; Pilakoutas, K.; Waldron, P. Punching shear behavior of fiber reinforced polymers reinforced concrete flat slabs: Experimental study. *J. Compos. Constr.* **2003**, *7*, 258–265. [CrossRef]
15. EI-Gamal, S.; El-Salakawy, E.; Benmokrane, B. Behavior of concrete bridge deck slabs reinforced with fiber-reinforced polymer bars under concentrated loads. *Aci. Struct. J.* **2005**, *102*, 727–735.
16. Nguyen-Minh, L.; Rovňák, M. Punching shear resistance of interior GFRP reinforced slab-column connections. *J. Compos. Constr.* **2013**, *17*, 2–13. [CrossRef]
17. Ospina, C.E.; Alexander, S.D.B.; Cheng, J.J.R. Punching of two-way concrete slabs with fiber-reinforced polymer reinforcing bars or grids. *Struct. J.* **2003**, *100*, 589–598.
18. Eiben, A.E.; Smith, J. From evolutionary computation to the evolution of things. *Nature* **2015**, *521*, 476–482. [CrossRef]
19. Jin, Y.; Miettinen, K.; Ishibuchi, H. Guest editorial evolutionary many-objective optimization. *IEEE Trans. Evolut. Comput.* **2018**, *22*, 1–2. [CrossRef]
20. Xu, G.; Ding, H.; Feng, Z. Optimal design of hydraulic excavator shovel attachment based on multiobjective evolutionary algorithm. *IEEE/ASME Trans. Mechatron.* **2019**, *24*, 808–819. [CrossRef]
21. Emmerich, M.T.M.; Deutz, A.H. A tutorial on multiobjective optimization: Fundamentals and evolutionary methods. *Nat. Comput.* **2018**, *17*, 585–609. [CrossRef] [PubMed]
22. Chand, S.; Wagner, M. Evolutionary many-objective optimization: A quick-start guide. *Surv. Oper. Res. Manag. Sci.* **2015**, *20*, 35–42. [CrossRef]
23. Falcón-Cardona, J.G.; Coello, C.A. Indicator-based multi-objective evolutionary algorithms: A comprehensive survey. *ACM Comput. Surv.* **2020**, *53*, 1–35. [CrossRef]
24. Liu, J.; Li, S.; Xu, C.; Ao, N.; Chen, Y.F. Automatic and optimal rebar layout in reinforced concrete structure by decomposed optimization algorithms. *Automat. Constr.* **2021**, *126*, 103655. [CrossRef]
25. Poli, R.; Kennedy, J.; Blackwell, T. Particle swarm optimization. *Swarm Intell-Us* **2007**, *1*, 33–57. [CrossRef]
26. Kirkpatrick, S.; Gelatt, C.D., Jr.; Vecchi, M.P. Optimization by Simulated Annealing. *Science* **1984**, *220*, 671–680. [CrossRef]
27. Seyyedabbasi, A.; Kiani, F. Sand Cat swarm optimization: A nature-inspired algorithm to solve global optimization problems. *Eng. Comput.* **2022**, *39*, 2627–2651. [CrossRef]
28. Deb, K.; Agrawal, S.; Pratap, A.; Meyarivan, T. A fast elitist non-dominated sorting genetic algorithm for multi-objective optimization: NSGA-II. In Proceedings of the 6th International Conference on Parallel Problem Solving from Nature (PPSN VI), Paris, France, 18–20 September 2000.
29. Leyva, H.A.; Bojorquez, E.; Bojorquez, J.; Reyes-Salazar, A.; Castorena, J.H.; Fernández, E.; Earthquake, M.A.B. design of reinforced concrete buildings using NSGA-II. *Adv. Civ. Eng.* **2018**, *2018*, 5906279.
30. Vo-Duy, T.; Duong-Gia, D.; Ho-Huu, V.; Vu-Do, H.C.; Nguyen-Thoi, T. Multi-objective optimization of laminated composite beam structures using NSGA-II algorithm. *Compos. Struct.* **2017**, *168*, 498–509. [CrossRef]
31. Liu, F.; Mu, S.; Lv, W.; Li, W.; Ge, T.; Li, L. LFM hybrid-coding waveform design of MIMO SAR based on NSGA-II. In Proceedings of the 2015 International Conference on Wireless Communications & Signal Processing (WCSP), Nanjing, China, 15–17 October 2015.
32. Wang, J.; Shen, W.; Wang, Z.; Yao, M.; Zeng, X. Multi-objective optimization of drive gears for power split device using surrogate models. *J. Mech. Sci. Technol.* **2014**, *28*, 2205–2214. [CrossRef]
33. Steven, G.; Querin, O.; Xie, M. Evolutionary structural optimisation (ESO) for combined topology and size optimisation of discrete structures. *Comput. Method Appl. Mech. Eng.* **2000**, *188*, 743–754. [CrossRef]
34. Li, Y.; Xie, Y.M. Evolutionary topology optimization for structures made of multiple materials with different properties in tension and compression. *Compos. Struct.* **2021**, *259*, 113497. [CrossRef]
35. Liu, W.; Yang, Y. Multi-objective optimization of sheet metal forming process using Pareto-based genetic algorithm. *J. Mater. Process. Tech.* **2008**, *208*, 499–506.
36. Fei, Z.; Liang, S.; Cai, Y.; Shen, Y. Ensemble machine-learning-based prediction models for the compressive strength of recycled powder mortar. *Materials* **2023**, *16*, 583. [CrossRef] [PubMed]
37. Liang, S.; Shen, Y.; Gao, X.; Cai, Y.; Fei, Z. Symbolic machine learning improved MCFT model for punching shear resistance of FRP-reinforced concrete slabs. *J. Build. Eng.* **2023**, *69*, 106257. [CrossRef]
38. Sandeep, M.S.; Tiprak, K.; Kaewunruen, S.; Pheinsusom, P.; Pansuk, W. Shear strength prediction of reinforced concrete beams using machine learning. *Structures* **2023**, *47*, 1196–1211. [CrossRef]
39. Shen, Y.; Wu, L.; Liang, S. Explainable machine learning-based model for failure mode identification of RC flat slabs without transverse reinforcement. *Eng. Fail. Anal.* **2022**, *141*, 106647. [CrossRef]
40. Shen, L.; Shen, Y.; Liang, S. Reliability Analysis of RC Slab-Column Joints under Punching Shear Load Using a Machine Learning-Based Surrogate Model. *Buildings* **2022**, *12*, 1750. [CrossRef]

41. Kookalani, S.; Cheng, B.; Xiang, S. Shape optimization of GFRP elastic gridshells by the weighted Lagrange ε-twin support vector machine and multi-objective particle swarm optimization algorithm considering structural weight. *Structures* **2021**, *33*, 2066–2084. [CrossRef]
42. Sun, S.; Cao, Z.; Zhu, H.; Zhao, J. A survey of optimization methods from a machine learning perspective. *IEEE Trans. Cybern.* **2019**, *50*, 3668–3681. [CrossRef]
43. Hassan, M.; Ahmed, E.; Benmokrane, B. Punching-shear strength of normal and high-strength two-way concrete slabs reinforced with GFRP bars. *J. Compos. Constr.* **2013**, *17*, 04013003. [CrossRef]
44. Min, K.H.; Yang, J.M.; Yoo, D.Y.; Yoon, Y.S. Flexural and punching performances of FRP and fiber reinforced concrete on impact loading. In *Advances in FRP Composites in Civil Engineering*; FRP Future Structures: Beijing, China, 2010; Volume 1.
45. Wang, H.; Yi, W.; Liu, Y. An innovative approach of determining the sample data size for machine learning models: A case study on health and safety management for infrastructure workers. *Electron. Res. Arch.* **2022**, *30*, 3452–3462. [CrossRef]
46. Duan, T.; Avati, A.; Ding, D.Y.; Thai, K.K.; Basu, S.; Ng, A.; Schuler, A. NGBoost: Natural Gradient Boosting for Probabilistic Prediction. *CoRR* **2019**, arXiv:1910.03225.
47. Chen, S.; Feng, D.; Wang, W.; Taciroglu, E. Probabilistic Machine-Learning Methods for Performance Prediction of Structure and Infrastructures through Natural Gradient Boosting. *J. Struct. Eng.* **2022**, *148*, 4022096. [CrossRef]
48. Ding, J.; Feng, D.; Brunesi, E.; Parisi, F.; Wu, G. Efficient seismic fragility analysis method utilizing ground motion clustering and probabilistic machine learning. *Eng. Struct.* **2023**, *294*, 116739. [CrossRef]
49. Wang, Y.; Wang, D.; Geng, N.; Wang, Y.; Yin, Y.; Jin, Y. Stacking-based ensemble learning of decision trees for interpretable prostate cancer detection. *Appl. Soft Comput. J.* **2019**, *77*, 188–204. [CrossRef]
50. Reason, L.M. Contrasting probabilistic scoring rules. *J. Stat. Plan. Infer.* **2013**, *143*, 1781–1790.
51. Dawid, A.P. The geometry of proper scoring rules. *Ann. Inst. Stat. Math.* **2007**, *59*, 77–93. [CrossRef]
52. Breiman, L. Random Forests. *Mach. Learn.* **2001**, *45*, 5–32. [CrossRef]
53. Freund, Y.; Schapire, R. Experiment with a new boosting algorithm. In Proceedings of the Thirteenth International Conference on International Conference on Machine Learning, Bari, Italy, 3–6 July 1996.
54. Corinna, C.; Vladimir, V. Support-vector networks. *Mach. Learn.* **1995**, *20*, 273–297.
55. ACI (American Concrete Institute). *Guide for the Design and Construction of Structural Concrete Reinforced with FiberReinforced Polymer Bars (ACI 440.15R-15)*; American Concrete Institute: Farmington Hills, MI, USA, 2015.
56. Machida, A. *Recommendation for Design and Construction of Concrete Structures Using Continuous Fiber Reinforcing*; Japan Society of Civil Engineers: Tokyo, Japan, 1997.
57. El-Ghandour, A.W.; Pilakoutas, K.; Waldron, P. New approach for punching shear capacity prediction of fiber reinforced polymer reinforced concrete flat slabs. In Proceedings of the International Symposium on Fiber Reinforced Polymer Reinforcement for Reinforced Concrete Structures, Baltimore, MD, USA, 31 October–5 November 1999.
58. Casalicchio, G.; Molnar, C.; Bischl, B. Visualizing the feature importance for black box models. In Proceedings of the Joint European Conference on Machine Learning and Principles and Practice of Knowledge Discovery in Databases, Dublin, Ireland, 10–14 September 2018.
59. Liang, S.; Shen, Y.; Ren, X. Comparative study of influential factors for punching shear resistance/failure of RC slab-column joints using machine-learning models. *Structures* **2022**, *45*, 1333–1349. [CrossRef]
60. Lundberg, S.M.; Lee, S. A unified approach to interpreting model predictions. In Proceedings of the 31st Annual Conference on Neural Information Processing Systems, Long Beach, CA, USA, 4–9 December 2017.
61. Onsree, T.; Tippayawong, N.; Phithakkitnukoon, S.; Lauterbach, J. Interpretable machine-learning model with a collaborative game approach to predict yields and higher heating value of torrefied biomass. *Energy* **2022**, *249*, 123676. [CrossRef]
62. Xiao, Z. Research on Punching Shear Performance of FRP Reinforced Concrete Two-Way Slabs under Central Concentrated Load. Ph.D. Thesis, Zhengzhou University, Zhengzhou, China, 2010.
63. *GB 50010-2010 (2015)*; Code for Design of Concrete Structures. China Architecture & Building Press: Beijing, China, 2016; pp. 28–30.

MDPI AG
Grosspeteranlage 5
4052 Basel
Switzerland
Tel.: +41 61 683 77 34

Buildings Editorial Office
E-mail: buildings@mdpi.com
www.mdpi.com/journal/buildings

MDPI

Academic Open
Access Publishing

mdpi.com

ISBN 978-3-7258-5730-2